MODELLING THE INTERCONNECTION OF THE OCEAN AND THE GREENLAND ICE SHEET

by

Laura Crystal Gillard

A thesis submitted in partial fulfillment of the requirements for the degree of

Doctor of Philosophy

Department of Earth and Atmospheric Sciences
University of Alberta

Abstract

The Greenland Ice Sheet (GrIS) is the largest freshwater reservoir in the Northern Hemisphere and continues to discharge large amounts of meltwater and icebergs into the ocean. The ice sheet has the potential to raise the sea-level by over 7 metres and impact ocean circulations. Greenland's marine-terminating glaciers (MtG) drain most of the ice sheet; therefore, ocean-induced undercutting of MtG has a strong control over the state of the ice sheet.

The understanding of the interconnection between the ocean and the GrIS is limited. Knowledge of the processes that drive the renewal of warm water in the deep troughs along the Greenland shelf that connect to fjords with MtG has not been studied for the entirety of the coastline. The influence that the GrIS may have on large-scale ocean features, such as the Labrador Sea convection and the Atlantic Meridional Overturning Circulation (AMOC), is still not completely understood. Furthermore, when forcing an ocean general circulation model, it is not clear which freshwater estimates of the GrIS to use over another or how different estimates may influence ocean processes.

Therefore, this thesis presents results from a suite of ocean model experiments, to investigate the complicated interactions between the ocean and the GrIS. This thesis first shows that the processes which drive the delivery of ocean heat respond differently by region to increasing GrIS meltwater, the origin of the warm water, how the water travels and is transformed, and local processes such as heat loss to the atmosphere. The Labrador Sea Water formation was impacted by a combination of altered lateral exchange from the shelf to the interior of the Labrador Sea as well as altered air-sea heat fluxes. An increase in vertical resolution, in the ocean model, generated unrealistic shallow mixed layer depths with a surface buoyancy cap that could not be broken. In order to break the buoyancy cap and generate a realistic mixed layer depth, a stronger heat loss was required at the surface of the ocean. Finally, based on a decade-long study period with an eddy-permitting ocean model, the GrIS meltwater and iceberg discharge did not have an impact on the Labrador Sea convection or the AMOC. However, ocean systems nearby the GrIS responded to varying freshwater flux estimates.

Preface

Chapter 3 of this thesis has been published as:

Gillard, L.C., X.Hu, P.G. Myers, M.H. Ribergaard, and C.M. Lee (2020), *Drivers for Atlantic-origin waters abutting Greenland*, The Cryosphere, 14(8), 2729–2753, https://doi.org/10.5194/tc-14-2729-2020.

P.G. Myers and myself designed the study and I carried all of the analysis. X. Hu developed the model configuration and performed three of the simulations. Y. Garcia-Quintana carried out the LowResNoStorm experiment. I prepared the manuscript with contributions from all co-authors. M.H. Ribergaard and C.M. Lee. provided comments on the manuscript, with C.M. Lee also providing Davis Strait data.

Chapter 4 of this thesis is being prepared for publication with authorship of Laura C. Gillard, Clark Pennelly, Helen L. Johnson, and Paul G. Myers. I was responsible for the analysis and ran all of the model experiments. C. Pennelly provided insight, manuscript edits, and performed some of the calculations: the heat flux at Cape Farewell, convective resistance, and buoyancy flux between the atmosphere and ocean surface. H.L. Johnson and P.G. Myers provided advice, insight, and manuscript edits.

Chapter 5 of this thesis is being prepared for publication with the authorship of Laura C. Gillard, Juliana M. Marson, Helen L. Johnson, and Paul G. Myers. I was responsible for the analysis and ran all of the model experiments. J.M. Marson taught me how to implement icebergs into the model and provide methods for analysis on iceberg variables and manuscript edits. H.L. Johnson provided insight to the project. P.G. Myers provided insight, advice and manuscript edits.

“It is our choices, Harry, that show what we truly are, far more than our abilities.”
- Albus Dumbledore, *Harry Potter and the Chamber of Secrets*

This thesis is dedicated to my teachers from all aspects of my life, thank you.

Acknowledgements

I would like to acknowledge my supervisor, Dr. Paul G. Myers, for his support and guidance throughout my graduate studies. Thank you for the many opportunities to collaborate with scientists, and travel all around the world.

Thank you to the ArcTrain program, for the knowledge gained, friendships made, and polar adventures had. Thank you Dr. Helen L. Johnson, who taught me to look at the bigger picture and continue to ask the question “Why?”. The time spent at the University of Oxford will forever be one to cherish.

To my colleagues at the University of Alberta: no matter how long our paths have crossed, thank you for your support, insight, and discussions. To Natasha, Laura, Yarisbel, Charlene, Andrew, Ran, Yiran, and Liam thanks for making our work environment a welcoming one. To Juliana, thank you for sharing your passion for icebergs with me. To Clark and Nathan, thank you for all the technical support you provided me, especially when I was first started running the model. To Xianmin Hu, the experience working with you was truly invaluable, and I will forever be grateful for your guidance and advice since the very beginning.

To my supportive friends, Maggie, Janelle, and Pippa: since our early years of our undergraduate degree, they remain to be the most supportive group of women one could ask for.

Thank you to my family. My parents, John and Concetta Gillard, who have always encouraged my curiosity and supported me to follow my passions. Thank you to my siblings, Christina, Jennifer, Jason, and Robert, for keeping me grounded, cheering me on, and being there since day one.

Vincent, who truly knows what this means to me and what it took for me to get here. You have read countless of pages and have been by my side every step of the way, I cannot thank you enough.

Contents

List of Figures

List of Tables

Chapter 1

Introduction

Since the 1950s, humans and their ventures have caused the climate system to warm (Abram et al., 2019). Ocean currents and the cryosphere are pivotal for the Earth to manage its climate. The ocean helps regulate the climate: it behaves as a carbon sink and stores anthropogenic carbon dioxide (Sarmiento and Gruber, 2002), and transports ocean heat poleward through large ocean circulations (Srokosz et al., 2012). In response to climate warming, Arctic temperatures experience a heightened increase compared to the rest of the world (Arctic Amplification) (Serreze and Francis, 2006). The cryosphere can amplify Arctic warming through albedo feedbacks, as well as increase the global mean sea level (Lindsay and Zhang, 2005; Shepherd et al., 2020). Therefore, communities that live near the Arctic and coastal environments will be at the highest risk for future climatic hazards from ocean and cryosphere change.

The Greenland Ice Sheet (GrIS) is the second-largest mass of fresh ice on Earth, with a volume of 2.74 ± 0.02 million Gt (Morlighem et al., 2017). The GrIS has been losing mass since the late 1990s (Rignot et al., 2008; Sasgen et al., 2020; van den Broeke et al., 2016). From 1992 to 2018 the GrIS has lost 3902 ± 342 Gt of fresh ice to the ocean and has contributed to a mean sea-level rise of 10.8 ± 0.9 millimetres (Shepherd et al., 2020). If the entire ice sheet were to melt, the global mean sea level could increase by 7.42 ± 0.05 metres (Morlighem et al., 2017).

In response to atmospheric warming the 2019 melt season showed a record mass loss rate of 532 ± 50 Gt/year (previously 464 ±- 62 Gt/year in 2012), even though the GrIS mass loss slowed in 2017 and 2018 (Sasgen et al., 2020; Tedesco and Fettweis, 2020). The unprecedented ice sheet mass loss in both 2012 and 2019 was due to similar atmospheric influences (Hanna et al., 2014; Sasgen et al., 2020; Tedesco and Fettweis, 2020). Over both summers a dominant high-pressure feature, associated with negative North Atlantic Oscillation (NAO) conditions, was persistent. This anticyclonic circulation advected warm southerly winds over the western coast of Greenland, which lead to record breaking air temperatures and widespread surface melting (98.6 % of the ice sheet in 2012 and 95.8 % in 2019) (Hanna et al., 2014; Nghiem et al., 2012; Tedesco and Fettweis, 2020). These two years show the extreme impact a warming atmosphere can have on the surface mass balance of Greenland. However, enhanced mass loss can come from the increasing presence of relatively warm ocean temperatures contacting the ice sheet (Holland et al., 2008; Jackson et al., 2014; Myers and Ribergaard, 2013; Straneo and Heimbach, 2013).

There are approximately 900 marine-terminating glaciers on the GrIS (Rastner et al., 2012) which drain $\sim$ 88 % of the ice sheet (Rignot and Mouginot, 2012). Marine-terminating glaciers began to rapidly retreat in the 1990's, when the mass loss of the GrIS began to increase (Rignot et al., 2008; Sasgen et al., 2020; Shepherd et al., 2020; van den Broeke et al., 2016). The retreat of marine-terminating glaciers can be caused by surface thinning (Csatho et al., 2014), glacier fjord geometry (Felikson et al., 2017; Fenty et al., 2016; Porter et al., 2014; Rignot et al., 2016a; Warren, 1991; Williams et al., 2017), state of the ice melange (Moon et al., 2015), subglacial discharge (Bartholomaus et al., 2016; Jenkins, 2011), and ocean temperature changes (Cai et al., 2017; Holland et al., 2008; Myers and Ribergaard, 2013; Rignot et al., 2016b; Straneo and Heimbach, 2013; Wood et al., 2018). Along the shelf break of Greenland, troughs extend from the coast supplying warm water through to the mouths of fjords. Depending on the structure of the water mass at the mouth of the fjord and the height of the fjord's sills, warm waters can access marine-terminating glaciers and accelerate their mass loss (Cai et al., 2017; Carroll et al., 2018; Gladish et al., 2015a; Rignot et al., 2010; Straneo et al., 2012; Wood et al., 2018). Undercutting of marine-terminating glaciers, due to warm ocean waters, is suggested to have a considerable influence on the grounding-line stability, iceberg calving, and overall mass balance of the GrIS (Rignot et al., 2015). Therefore, the ocean circulation and transport of oceanic heat near marine-terminating glaciers is a very important process to understand.

Along the west and east coasts of Greenland there are gateways between the Arctic and the North Atlantic Oceans (Figure 1.1). The North Atlantic Current transports warm water, from the Gulf Stream, across the North Atlantic Ocean. This Atlantic water reaches south of Iceland, where it either continues to travel northward across the Iceland - Scotland Ridge or enters the Irminger Sea, forming the Irminger Current circulating along Reykjanes Ridge. Northeast of Greenland modified Atlantic water is transported northward through Fram Strait, then travels cyclonically around the continental marines, providing the Arctic Ocean with additional heat (Polyakov et al., 2005).

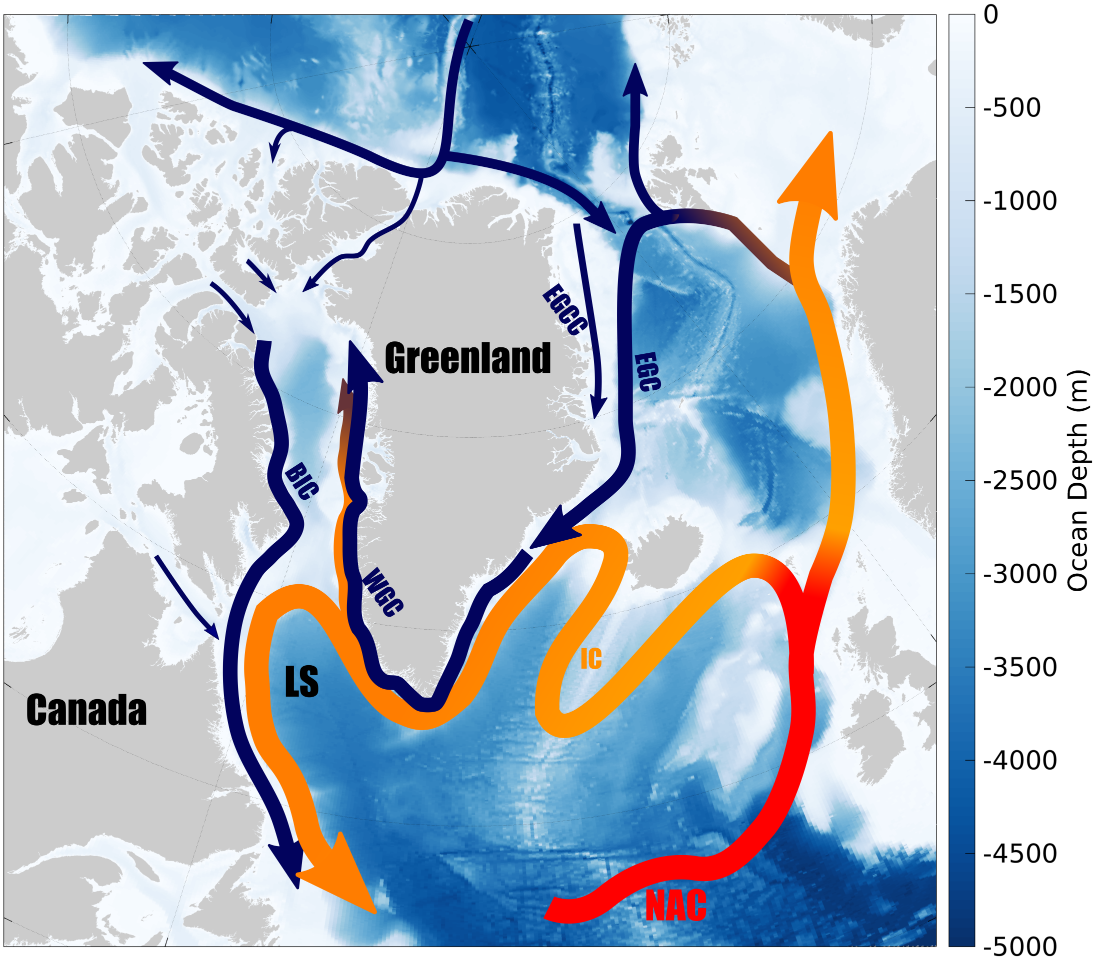

Figure 1.1: Realtively warm Atlantic waters are seen in red and change to orange as they get mixed and modified along the North Atlantic Current (NAC), Irminger Current (IC), and West Greenland Current (WGC). Arctic water and freshwater pathways are shown in blue lines. These currents include the East Greenland Coastal Current (EGCC), East Greenland Current (EGC), and Baffin Island Current (BIC). The Labrador Sea (LS) is located in the western Subpolar Gyre.

On the east side of the GrIS, polar water from the Arctic Ocean merges with Greenland meltwaters and travels southward along the east Greenland shelf as the East Greenland Costal Current (Bacon et al., 2002). Farther off the east Greenland shelf, the East Greenland Current travels southward (Aagaard and Carmack, 1989), and has been known to increase in strength and freshen the North Atlantic Ocean (de Steur et al., 2018). The East Greenland Coastal Current and the East Greenland Current bring relatively cold and low-saline waters to the south tip of Greenland, where the current rounds Cape Farewell. At Cape Farwell, the East Greenland Current merges with the warm, salty Irminger Current and becomes the West Greenland Current (WGC) (Pickart et al., 2005).

The WGC splits into two currents: one travels northward through Davis Strait into Baffin Bay along the west coast of Greenland and brings both buoyant (relatively fresh and cold) as well as modified Atlantic water (relatively salty and warm); and the other current travels westward at Davis Strait with more saline and warm waters, shedding eddies into the Labrador Sea or joining the southward flowing Baffin Island Current (Fratantoni and Pickart, 2007; Myers et al., 2009). The Baffin Island Current contains a mixture of polar water exported south through the Canadian Arctic Archipelago, melt from Greenland, and recirculated WGC waters (Tang et al., 2004). The Baffin Island Current travels south through Davis Strait and merges with the boundary current along the Labrador Shelf. The relatively fresh water exported south through Davis Strait flows along the Labrador Coast as the Labrador Current; the boundary current for the Labrador Sea (Myers et al., 2009; Straneo and Saucier, 2008).

The Labrador Sea is exposed to the mid-latitude storm track which transports strong cold westerlies off eastern Canada over the basin (Lau, 1988). Therefore, shifts in frequency and intensity of winter storms (i.e. winds and temperatures) alter the heat exchange between the atmosphere and the ocean (Marshall et al., 1998; Schulze et al., 2016; V*å*ge et al., 2009). Winter buoyancy loss at the surface of the ocean increases the density and initiates deep convection in the water column through plumes sinking to 1500 m or more (V*å*ge et al., 2009; Yashayaev and Loder, 2017). The Labrador Sea's convection produces the Labrador Sea Water (LSW) which is exported at depth through the North Atlantic Ocean (Talley et al., 2003).

The Labrador Sea convection strength can weaken due to weak atmospheric forcing (weak winds and mild winters) as well as an addition of buoyant waters in the interior of the Labrador Sea. Weak convection or large freshwater fluxes into the Labrador Sea create a buoyant cap on the surface of the water column. This limits the amount of heat loss that can occur at the surface. Without a strong heat loss to break this barrier, convection in subsequent years may be weaker (Schulze et al., 2016; Yashayaev and Loder, 2017).

The basin interior is restratifed after convection by a lateral exchange of heat and freshwater from the surrounding boundary currents (Straneo, 2006; Yashayaev and Loder, 2009). The water column stratifies due to the subsurface warming from the

Irminger Water producing a flux of heat and salt into the surface layers (Straneo, 2006) and the import of fresh surface boundary currents which contain both freshwater fluxes from the Arctic as well as the GrIS meltwater (Dukhovskoy et al., 2019). It has not yet been observed that the GrIS has had any impact on the Labrador Sea convection (Rhein et al., 2018; Yashayaev and Loder, 2017). However, several model studies have investigated the fate of GrIS meltwaters and icebergs, and those that originate off the south coast of the GrIS have been shown to accumulate in the Labrador Sea (e.g. Böning et al., 2016; Dukhovskoy et al., 2016; Gillard et al., 2016; Luo et al., 2016; Marson et al., 2018).

There is debate on the control that the LSW formation may have on the Atlantic Meridional Overturning Circulation (AMOC). The AMOC is a large-scale system of ocean currents and is a crucial component of the Earth's climate system due to its role in the uptake and redistribution of heat and carbon dioxide (Sarmiento and Gruber, 2002; Srokosz et al., 2012). Numerous ocean and climate modelling studies have shown the importance of the LSW formation in determining the variability and strength of the AMOC (e.g. Bailey et al., 2005; Feucher et al., 2019; Kuhlbrodt et al., 2007). However, a recent, short 21-month time series associated with the Overturning in the Subpolar North Atlantic Program (OSNAP) observing system suggested that the eastern sub-polar gyre, rather than the Labrador Sea, was largely responsible for setting the strength of the overturning in the sub-polar North Atlantic (Lozier et al., 2019). However, this OSNAP record is too short to draw definitive conclusions on LSW-AMOC linkages, requiring a longer decadal time scale. A climate model study Menary et al. (2020) also suggests the Labrador Sea may not have as much control over the variability and strength of the AMOC and calls to consider the role of convection that occurs in the eastern subpolar gyre (Irminger Sea) and the links between the basins. Nevertheless, LSW formation is still a crucial process for the ventilation of the deep ocean, transporting heat, nutrients, oxygen, and carbon dioxide from the surface layers to depth (Rhein et al., 2017).

This thesis is divided into six chapters and Chapter 1 discusses a brief introduction into the field and background pertaining the thesis. Chapter 2 describes the modelling framework used. Chapter 3, 4, and 5 are written as independent papers, each focusing on one objective mentioned below (1, 2, and 3, respectively). Chapter 6, the concluding chapter, summarizes the thesis main findings, discusses the significant and contributions to science, and future work.

1.1 Thesis Objectives

Objective 1: To examine the processes that drive the delivery of oceanic heat towards the coastline of Greenland through troughs that connect to fjords with marine-terminating glaciers.

Depending on the structure of the water mass at the mouth of a fjord and the height of the fjord's sills, warm waters can access marine-terminating glaciers and accelerate their mass loss (Cai et al., 2017; Gladish et al., 2015a; Straneo et al., 2012). On the northwest coast of Greenland the rapid retreat and disintegration of Jakobshavn Isbare's floating ice tongue has been attributed to an increase in heat content, deep bathymetry, and North Alantic Subpolar Gyre (NASPG) warming (An et al., 2017; Gladish et al., 2015b; Holland et al., 2008; Myers and Ribergaard, 2013). On the southeast coast of Greenland, Atlantic water off the shelf advects into the fjords that Helheim Glacier (Straneo et al., 2010) and Kangerlussuaq Glacier terminate into (Azetsu-Scott and Tan, 1997). On the northeast coast of Greenland, Nioghalvfjerdsbrae (79NG) has a floating ice tongue that abuts Hovgaard Ø. The most rapid melt occurs at the grounded front, south of Hovgaard Ø, where the ice tongue is thickest and is exposed to deeper and warmer waters (Mayer et al., 2000; Schaffer et al., 2017; Seroussi et al., 2011; Wilson and Straneo, 2015).

If the warm waters from the NASPG can reach transverse troughs along the Greenland Shelf, changes in the heat content of the NASPG may influence the state of marine-terminating glaciers on the GrIS (Holland et al., 2008; Myers and Ribergaard, 2013; Straneo and Heimbach, 2013). Ocean warming at intermediate depths could have the potential to increase ocean-induced undercutting of marine-terminating glaciers and may have a strong control over the future of the ice sheet. Therefore, Chapter 3 examines the processes that drive the delivery of oceanic heat towards the coastline of Greenland through troughs that connect to fjords with marine-terminating glaciers.

Objective 2: To investigate the response of the Labrador Sea Water formation due to atmospheric and lateral buoyancy fluxes.

To assess whether the GrIS freshwater flux can impact the Labrador Sea we need to make sure that models can accurately represent deep water formation. Ocean simulations at eddy-permitting resolutions, within the North Atlantic, have been plagued with a salinity drift. Models tend to produce mixed layers that are too deep compared with observations in the Labrador Sea (Rattan et al., 2010). Lower resolution models tend to overestimate LSW formation compared to models run at higher resolution

(Garcia-Quintana et al., 2019; Hirschi et al., 2020). The additional LSW can be due to under-representation of lateral transport of buoyant waters from the boundary currents, either through freshwater anomalies or by the warm salty subsurface Irminger Waters (Rattan et al., 2010; Treguier et al., 2005). Chapter 4 will investigate the response of the convective strength and the formation of LSW due to changes in lateral exchanges from the shelf to the interior of the Labrador Sea, air-sea heat fluxes, and vertical resolution, in an eddy-permitting forced ocean model.

Objective 3: To explore the consequences of using various estimates of the Greenland Ice Sheet's freshwater flux in an ocean model.

Many GrIS freshwater flux products exist; however, it is not clear which product will produce results comparable to observations in an ocean model or how changes in the product may influence ocean processes. In the past, ocean model studies have used incomplete GrIS freshwater flux (FWF) data, which included only runoff and excluded icebergs. Some ocean modelling studies that did not have an iceberg module, Dukhovskoy et al. (2016) and Gillard et al. (2020), combined the solid and liquid FWF as one liquid flux. However, these studies do not tell the whole story of the GrIS FWF impact on the ocean as they are not capturing the behaviour of solid ice discharge (icebergs). Marson et al. (2018) used an iceberg module, wherein icebergs account for 54 % of the total mass loss on the GrIS, estimated by Bamber et al. (2012). Marson et al. (2018) explored the fate of icebergs and found that most icebergs ($\sim$60 %) that crossed into the Labrador Sea interior were generated from the southeast coast. Marsh et al. (2018) showed the first attempt for forecasting icebergs, showing the need for studies to focus on implementing icebergs into an ocean model as the increase in calving of icebergs from GrIS will be important for navigation in the Arctic and Sub-Arctic ocean. The majority of the above-listed studies are based on numerical models. Their results are directly influenced by the amount, distribution and type of discharge prescribed as forcing fields. Chapter 5 uses a consistent model framework, and explores different Greenland freshwater flux products, for liquid runoff and iceberg discharge, and look at the ocean's response.

Bibliography

Aagaard, K. and Carmack, E. C. (1989). The role of sea ice and other fresh water in the Arctic circulation. *Journal of Geophysical Research: Oceans*, 94(C10):14485–14498.

Abram, N., Gattuso, J.-P., Prakash, A., Cheng, L., Chidichimo, M., Crate, S., Enomoto, H., M., G., Gruber, N., Harper, S., Holland, E., Kudela, R., Rice, J., Steffen, K., and von Schuckmann, K. (2019). 2019: Framing and Context of the Report . *IPCC Special Report on the Ocean and Cryosphere in a Changing Climate*.

An, L., Rignot, E., Elieff, S., Morlighem, M., Millan, R., Mouginot, J., Holland, D. M., Holland, D., and Paden, J. (2017). Bed elevation of Jakobshavn Isbrae, West Greenland, from high-resolution airborne gravity and other data. *Geophysical Research Letters*, 44(8):3728–3736. 2017GL073245.

Azetsu-Scott, K. and Tan, F. C. (1997). Oxygen isotope studies from Iceland to an East Greenland Fjord: behaviour of glacial meltwater plume. *Marine Chemistry*, 56(3):239 – 251. Modern Chemical and Biological Oceanography: The Influence of Peter J. Wangersky.

Bacon, S., Reverdin, G., Rigor, I. G., and Snaith, H. M. (2002). A freshwater jet on the east Greenland shelf. *Journal of Geophysical Research: Oceans*, 107(C7):5–1–5–16.

Bailey, D. A., Rhines, P. B., and Häkkinen, S. (2005). Formation and pathways of North Atlantic Deep Water in a coupled ice–ocean model of the Arctic–North Atlantic Oceans. *Climate Dynamics*, 25:497–516.

Bamber, J., Van Den Broeke, M., Ettema, J., Lenaerts, J., and Rignot, E. (2012). Recent large increases in freshwater fluxes from Greenland into the North Atlantic. *Geophysical Research Letters*, 39(19).

Bartholomaus, T. C., Stearns, L. A., Sutherland, D. A., Shroyer, E. L., Nash, J. D., Walker, R. T., Catania, G., Felikson, D., Carroll, D., Fried, M. J., and et al. (2016). Contrasts in the response of adjacent fjords and glaciers to ice-sheet surface melt in West Greenland. *Annals of Glaciology*, 57(73):25–38.

Böning, C. W., Behrens, E., Biastoch, A., Getzlaff, K., and Bamber, J. L. (2016).

Emerging impact of Greenland meltwater on deepwater formation in the North Atlantic Ocean. *Nature Geosci*, 9(7):523–527.

Cai, C., Rignot, E., Menemenlis, D., and Nakayama, Y. (2017). Observations and modeling of ocean-induced melt beneath Petermann Glacier Ice Shelf in northwestern Greenland. *Geophysical Research Letters*.

Carroll, D., Sutherland, D. A., Curry, B., Nash, J. D., Shroyer, E. L., Catania, G. A., Stearns, L. A., Grist, J. P., Lee, C. M., and de Steur, L. (2018). Subannual and Seasonal Variability of Atlantic-Origin Waters in Two Adjacent West Greenland Fjords. *Journal of Geophysical Research: Oceans*, 123(9):6670–6687.

Csatho, B. M., Schenk, A. F., van der Veen, C. J., Babonis, G., Duncan, K., Rezvanbehbahani, S., van den Broeke, M. R., Simonsen, S. B., Nagarajan, S., and van Angelen, J. H. (2014). Laser altimetry reveals complex pattern of Greenland Ice Sheet dynamics. *Proceedings of the National Academy of Sciences*, 111(52):18478–18483.

de Steur, L., Peralta-Ferriz, C., and Pavlova, O. (2018). Freshwater Export in the East Greenland Current Freshens the North Atlantic. *Geophysical Research Letters*, 45(24):13,359–13,366.

Dukhovskoy, D. S., Myers, P. G., Platov, G., Timmermans, M.-L., Curry, B., Proshutinsky, A., Bamber, J. L., Chassignet, E., Hu, X., Lee, C. M., and Somavilla, R. (2016). Greenland freshwater pathways in the sub-Arctic Seas from model experiments with passive tracers. *Journal of Geophysical Research: Oceans*.

Dukhovskoy, D. S., Yashayaev, I., Proshutinsky, A., Bamber, J. L., Bashmachnikov, I. L., Chassignet, E. P., Lee, C. M., and Tedstone, A. J. (2019). Role of Greenland Freshwater Anomaly in the Recent Freshening of the Subpolar North Atlantic. *Journal of Geophysical Research: Oceans*, 124(5):3333–3360.

Felikson, D., Bartholomaus, T. C., Catania, G. A., Korsgaard, N. J., Kjær, K. H., Morlighem, M., Noël, B., van den Broeke, M., Stearns, L. A., Shroyer, E. L., Sutherland, D. A., and Nash, J. D. (2017). Inland thinning on the Greenland Ice Sheet controlled by outlet glacier geometry. *Nature Geoscience*, 10:366–369.

Fenty, I., Willis, J. K., Khazendar, A., Dinardo, S., Forsberg, R., Fukumori, I., Holland, D., Jakobsson, M., Moller, D., Münchow, J. M. A., Rignot, E., Schodlok, M., Thompson, A. F., Tinto, K., Rutherford, M., and Trenholm, N. (2016). Oceans Melting Greenland: Early Results from NASA's Ocean-Ice Mission in Greenland . *Oceanography*, 29.

Feucher, C., Garcia-Quintana, Y., Yashayaev, I., Hu, X., and Myers, P. G. (2019). Labrador Sea Water Formation Rate and Its Impact on the Local Meridional Overturning Circulation. *Journal of Geophysical Research: Oceans*, 124(8):5654–5670.

Fratantoni, P. S. and Pickart, R. S. (2007). The western North Atlantic shelfbreak current system in summer. *Journal of Physical Oceanography*, 37(10):2509–2533.

Garcia-Quintana, Y., Courtois, P., Hu, X., Pennelly, C., Kieke, D., and Myers, P. G. (2019). Sensitivity of Labrador Sea Water Formation to Changes in Model Resolution, Atmospheric Forcing, and Freshwater Input. *Journal of Geophysical Research: Oceans*, 124(3):2126–2152.

Gillard, L. C., Hu, X., Myers, P. G., and Bamber, J. L. (2016). Meltwater pathways from marine terminating glaciers of the Greenland Ice Sheet. *Geophysical Research Letters*, 43(20):10,873–10,882.

Gillard, L. C., Hu, X., Myers, P. G., Ribergaard, M. H., and Lee, C. M. (2020). Drivers for Atlantic-origin waters abutting Greenland. *The Cryosphere*, 14(8):2729–2753.

Gladish, C., Holland, D., and Lee, C. (2015a). Oceanic boundary conditions for Jakobshavn Glacier. Part II: Provenance and sources of variability of disko bay and Ilulissat Icefjord waters, 1990-2011. *Journal of Physical Oceanography*, 45(1):33–63.

Gladish, C., Holland, D., Rosing-Asvid, A., Behrens, J., and Boje, J. (2015b). Oceanic boundary conditions for Jakobshavn Glacier. Part I: Variability and renewal of Ilulissat Icefjord waters, 2001-14. *Journal of Physical Oceanography*, 45(1):3–32.

Hanna, E., Fettweis, X., Mernild, S., Cappelen, J., Ribergaard, M., Shuman, C., Steffen, K., Wood, L., and Mote, T. (2014). Atmospheric and oceanic climate forcing of the exceptional Greenland Ice Sheet surface melt in summer 2012.

Hirschi, J. J.-M., Barnier, B., Böning, C., Biastoch, A., Blaker, A. T., Coward, A., Danilov, S., Drijfhout, S., Getzlaff, K., Griffies, S. M., Hasumi, H., Hewitt, H., Iovino, D., Kawasaki, T., Kiss, A. E., Koldunov, N., Marzocchi, A., Mecking, J. V., Moat, B., Molines, J.-M., Myers, P. G., Penduff, T., Roberts, M., Treguier, A.-M., Sein, D. V., Sidorenko, D., Small, J., Spence, P., Thompson, L., Weijer, W., and Xu, X. (2020). The Atlantic Meridional Overturning Circulation in High-Resolution Models. *Journal of Geophysical Research: Oceans*, 125(4):e2019JC015522. e2019JC015522 2019JC015522.

Holland, D. M., Thomas, R. H., De Young, B., Ribergaard, M. H., and Lyberth, B. (2008). Acceleration of Jakobshavn Isbrae triggered by warm subsurface ocean waters. *Nature Geoscience*, 1(10):659–664.

Jackson, R. H., Straneo, F., and Sutherland, D. A. (2014). Externally forced fluctuations in ocean temperature at Greenland glaciers in non-summer months. *Nature Geoscience*, 7(7):503–508.

Jenkins, A. (2011). Convection-driven melting near the grounding lines of ice shelves and tidewater glaciers. *Journal of Physical Oceanography*, 41(12):2279–2294.

Kuhlbrodt, T., Griesel, A., Montoya, M., Levermann, A., Hofmann, M., and Rahmstorf, S. (2007). On the driving processes of the Atlantic Meridional Overturning Circulation. *Reviews of Geophysics*, 45(2).

Lau, N.-C. (1988). Variability of the Observed Midlatitude Storm Tracks in Relation to Low-Frequency Changes in the Circulation Pattern. *Journal of the Atmospheric Sciences*, 45(19):2718–2743.

Lindsay, R. and Zhang, J. (2005). The Thinning of Arctic Sea Ice, 1988–2003: Have We Passed a Tipping Point? *Journal of Climate*, 18:4879–4894.

Lozier, M. S., Li, F., Bacon, S., Bahr, F., Bower, A. S., Cunningham, S. A., de Jong, M. F., de Steur, L., deYoung, B., Fischer, J., Gary, S. F., Greenan, B. J. W., Holliday, N. P., Houk, A., Houpert, L., Inall, M. E., Johns, W. E., Johnson, H. L., Johnson, C., Karstensen, J., Koman, G., Le Bras, I. A., Lin, X., Mackay, N., Marshall, D. P., Mercier, H., Oltmanns, M., Pickart, R. S., Ramsey, A. L., Rayner, D., Straneo, F., Thierry, V., Torres, D. J., Williams, R. G., Wilson, C., Yang, J., Yashayaev, I., and Zhao, J. (2019). A sea change in our view of overturning in the subpolar North Atlantic. *Science*, 363(6426):516–521.

Luo, H., Castelao, R. M., Rennermalm, A. K., Tedesco, M., Bracco, A., Yager, P. L., and Mote, T. L. (2016). Oceanic transport of surface meltwater from the southern Greenland Ice Sheet. *Nature Geoscience*.

Marsh, R., Bigg, G., Zhao, Y., Martin, M., Blundell, J. R., Josey, S., Hanna, E., and Ivchenko, V. (2018). Prospects for seasonal forecasting of iceberg distributions in the North Atlantic. *Nat Hazards*, 91:447–471.

Marshall, J., Dobson, F., Moore, K., Rhines, P., Visbeck, M., D'Asaro, E., Bumke, K., Chang, S., Davis, R., Fischer, K., Garwood, R., Guest, P., Harcourt, R., Herbaut, C., Holt, T., Lazier, J., Legg, S., McWilliams, J., Pickart, R., Prater, M., Renfrew, I., Schott, F., Send, U., and Smethie, W. (1998). The Labrador Sea Deep Convection Experiment. *Bulletin of the American Meteorological Society*, 79(10):2033–2058.

Marson, J. M., Myers, P. G., Hu, X., and Le Sommer, J. (2018). Using Vertically Integrated Ocean Fields to Characterize Greenland Icebergs' Distribution and Lifetime. *Geophysical Research Letters*, 45(9):4208–4217.

Mayer, C., Reeh, N., Jung-Rothenhäusler, F., Huybrechts, P., and Oerter, H. (2000). The subglacial cavity and implied dynamics under Nioghalvfjerdsfjorden Glacier, NE-Greenland. *Geophysical Research Letters*, 27(15):2289–2292.

Menary, M. B., Jackson, L. C., and Lozier, M. S. (2020). Reconciling the Relationship Between the AMOC and Labrador Sea in OSNAP Observations and Climate Models. *Geophysical Research Letters*, 47(18):e2020GL089793. e2020GL089793 10.1029/2020GL089793.

Moon, T., Joughin, I., and Smith, B. (2015). Seasonal to multiyear variability of glacier surface velocity, terminus position, and sea ice/ice mélange in northwest Greenland. *Journal of Geophysical Research: Earth Surface*, 120(5):818–833.

Morlighem, M., Williams, C. N., Rignot, E., An, L., Arndt, J. E., Bamber, J. L., Catania, G., Chauché, N., Dowdeswell, J. A., Dorschel, B., Fenty, I., Hogan, K., Howat, I., Hubbard, A., Jakobsson, M., Jordan, T. M., Kjeldsen, K. K., Millan, R., Mayer, L., Mouginot, J., Noël, B. P. Y., O'Cofaigh, C., Palmer, S., Rysgaard, S., Seroussi, H., Siegert, M. J., Slabon, P., Straneo, F., van den Broeke, M. R., Weinrebe, W., Wood, M., and Zinglersen, K. B. (2017). BedMachine v3: Complete Bed Topography and Ocean Bathymetry Mapping of Greenland From Multibeam Echo Sounding Combined With Mass Conservation. *Geophysical Research Letters*, 44(21):11,051–11,061.

Myers, P. G., Donnelly, C., and Ribergaard, M. H. (2009). Structure and variability of the West Greenland Current in Summer derived from 6 repeat standard sections. *Progress in Oceanography*, 80(1-2):93–112.

Myers, P. G. and Ribergaard, M. H. (2013). Warming of the polar water layer in Disko Bay and potential impact on Jakobshavn Isbrae. *Journal of Physical Oceanography*, 43(12):2629–2640.

Nghiem, S., Hall, D., Mote, T., Tedesco, M., Albert, M., Keegan, K., Shuman, C., DiGirolamo, N., and Neumann, G. (2012). The extreme melt across the Greenland Ice Sheet in 2012. *Geophys. Res. Lett.*, 39.

Pickart, R., Torres, D., and Fratantoni, P. (2005). The East Greenland Spill Jet. *Journal of Physical Oceanography*, 35.

Polyakov, I. V., Beszczynska, A., Carmack, E. C., Dmitrenko, I. A., Fahrbach, E., Frolov, I. E., Gerdes, R., Hansen, E., Holfort, J., Ivanov, V. V., Johnson, M. A., Karcher, M., Kauker, F., Morison, J., Orvik, K. A., Schauer, U., Simmons, H. L., Skagseth, y., Sokolov, V. T., Steele, M., Timokhov, L. A., Walsh, D., and Walsh, J. E. (2005). One more step toward a warmer Arctic. *Geophysical Research Letters*, 32(17).

Porter, D. F., Tinto, K. J., Boghosian, A., Cochran, J. R., Bell, R. E., Manizade, S. S., and Sonntag, J. G. (2014). Bathymetric control of tidewater glacier mass loss in northwest Greenland. *Earth and Planetary Science Letters*, 401:40 – 46.

Rastner, P., Bolch, T., Mölg, N., Machguth, H., Le Bris, R., and Paul, F. (2012). The first complete inventory of the local glaciers and ice caps on Greenland. *The Cryosphere*, 6(6):1483–1495.

Rattan, S., Myers, P. G., Treguier, A. ., Theetten, S., Biastoch, A., and Böning, C. (2010). Towards an understanding of Labrador Sea salinity drift in eddy-permitting simulations. *Ocean Modelling*, 35(1-2):77–88.

Rhein, M., Steinfeldt, R., Huhn, O., Sültenfuß, J., and Breckenfelder, T. (2018). Greenland Submarine Melt Water Observed in the Labrador and Irminger Sea. *Geophysical Research Letters*, 45(19):10,570–10,578.

Rhein, M., Steinfeldt, R., Kieke, D., Stendardo, I., and Yashayaev, I. (2017). Ventilation variability of Labrador Sea Water and its impact on oxygen and anthropogenic carbon: a review. *Philosophical Transactions of the Royal Society A: Mathematical, Physical and Engineering Sciences*, 375(2102):20160321.

Rignot, E., Box, J. E., Burgess, E., and Hanna, E. (2008). Mass balance of the Greenland ice sheet from 1958 to 2007. *Geophysical Research Letters*, 35(20).

Rignot, E., Fenty, I., Xu, Y., Cai, C., and Kemp, C. (2015). Undercutting of marine-terminating glaciers in West Greenland. *Geophysical Research Letters*, 42.

Rignot, E., Fenty, I., Xu, Y., Cai, C., Velicogna, I., Cofaigh, C. ., Dowdeswell, J. A., Weinrebe, W., Catania, G., and Duncan, D. (2016a). Bathymetry data reveal glaciers vulnerable to ice-ocean interaction in Uummannaq and Vaigat glacial fjords, west Greenland. *Geophysical Research Letters*, 43(6):2667–2674. 2016GL067832.

Rignot, E., Koppes, M., and Velicogna, I. (2010). Rapid submarine meting of the calving faces of West Greenland glaciers. *Nature Geoscience*, 3:187–191.

Rignot, E. and Mouginot, J. (2012). Ice flow in Greenland for the International Polar Year 2008-2009. *Geophysical Research Letters*, 39(11).

Rignot, E., Xu, Y., Menemenlis, D., Mouginot, J., Scheuchl, B., Li, X., Morlighem, M., Seroussi, H., den Broeke, M. v., Fenty, I., Cai, C., An, L., and Fleurian, B. d. (2016b). Modeling of ocean-induced ice melt rates of five west Greenland glaciers over the past two decades. *Geophysical Research Letters*, 43(12):6374–6382.

Sarmiento, J. and Gruber, N. (2002). Sinks for Anthropogenic Carbon. *Physics Today*, 55:30–36.

Sasgen, I., Wouters, B., Gardner, A., King, M., Tedesco, M., Landerer, F., Dahle, C., Save, H., and Fettweis, X. (2020). Return to rapid ice loss in Greenland and record loss in 2019 detected by the GRACE-FO satellites. *Commun Earth Environ*, 1(8).

Schaffer, J., von Appen, W.-J., Dodd, P. A., Hofstede, C., Mayer, C., de Steur, L., and Kanzow, T. (2017). Warm water pathways toward Nioghalvfjerdsfjorden Glacier, Northeast Greenland. *Journal of Geophysical Research: Oceans*, 122(5):4004–4020.

Schulze, L. M., Pickart, R. S., and Moore, G. W. K. (2016). Atmospheric forcing during active convection in the Labrador Sea and its impact on mixed-layer depth. *Journal of Geophysical Research: Oceans*, 121(9):6978–6992.

Seroussi, H., Morlighem, M., Rignot, E., Larour, E., Aubry, D., Ben Dhia, H., and Kristensen, S. S. (2011). Ice flux divergence anomalies on 79north Glacier, Greenland. *Geophysical Research Letters*, 38(9). L09501.

Serreze, M. and Francis, J. (2006). The Arctic Amplification Debate. *Climatic Change*, 76:241–264.

Shepherd, A., Ivins, E., Rignot, E., Smith, B., van den Broeke, M., Velicogna, I., Whitehouse, P., Briggs, K., Joughin, I., Krinner, G., Nowicki, S., Payne, T., Scambos, T., Schlegel, N., Geruo, A., Agosta, C., Ahlstrøm, A., Babonis, B., Barletta, V., Bjørk, A., Blazquez, A., Bonin, J., Colgan, W., Csatho, B., Cullather, R., Engdahl, M., Felikson, D., Fettweis, X., Forsberg, R., Hogg, A., Gallee, H., Gardner, A., Gilbert, L., Gourmelen, N., Groh, A., Gunter, B., Hanna, E., Harig, C., Helm, V., Horvath, A., Horwath, M., Khan, S., Kjeldsen, K., Konrad, H., Langen, P., Lecavalier, B., Loomis, B., Luthcke, S., McMillan, M., Melini, D., Mernild, S., Mohajerani, Y., Moore, P., Mottram, R., Mouginot, J., Moyano, G., Muir, A., Nagler, T., Nield, G., Nilsson, J., Noël, B., Otosaka, I., Pattle, M., Peltier, W., Pie, N., Rietbroek, R., Rott, H., Sørensen, L., Sasgen, I., Save, H., Scheuchl, B., Schrama, E., Schröder, L., Seo, K., Simonsen, S., Slater, T., Spada, G., Sutterley, T., Talpe, M., Tarasov, L., van de Berg, W., van der Wal, W., van Wessem, M., Vishwakarma, B., Wiese, D., Wilton, D., Wagner, T., Wouters, B., and Wuite, J. (2020). Mass balance of the Greenland Ice Sheet from 1992 to 2018. *Nature*, 579:233–239.

Srokosz, M., Baringer, M., Bryden, H., Cunningham, S., Delworth, T., Lozier, M., Marotzke, J., and Sutton, R. (2012). Past, Present, and Future Changes in the Atlantic Meridional Overturning Circulation. *Bulletin of the American Meteorological Society*, 93:1663–1676.

Straneo, F. (2006). Heat and freshwater transport through the central Labrador Sea. *Journal of Physical Oceanography*, 36(4):606–628.

Straneo, F., Hamilton, G., Sutherland, D., Stearns, L. A., Davidson, F., Hammill, M., Stenson, G. B., and A., R. (2010). Rapid circulation of warm subtropical waters in a major glacial fjord in East Greenland. *Nature Geosci*, 3(3):182–186.

Straneo, F. and Heimbach, P. (2013). North Atlantic warming and the retreat of Greenland's outlet glaciers. *Nature*, 504(7478):36–43.

Straneo, F. and Saucier, F. (2008). The outflow from Hudson Strait and its contribution to the Labrador Current . *Deep Sea Research Part I: Oceanographic Research Papers*, 55(8):926 – 946.

Straneo, F., Sutherland, D. A., Holland, D., Gladish, C., Hamilton, G. S., Johnson, H. L., Rignot, E., Xu, Y., and Koppes, M. (2012). Characteristics of ocean waters reaching Greenland's glaciers. *Annals of Glaciology*, 53(60):202–210.

Talley, L. D., Reid, J. L., and Robbins, P. E. (2003). Data-Based Meridional Overturning Streamfunctions for the Global Ocean. *Journal of Climate*, 16(19):3213–3226.

Tang, C. C. L., Ross, C. K., Yao, T., Petrie, B., DeTracey, B. M., and Dunlap, E. (2004). The circulation, water masses and sea-ice of Baffin Bay. *Progress in Oceanography*, 63:183–228.

Tedesco, M. and Fettweis, X. (2020). Unprecedented atmospheric conditions (1948–2019) drive the 2019 exceptional melting season over the Greenland ice sheet. *The Cryosphere*, 14(4):1209–1223.

Treguier, A. M., Theetten, S., Chassignet, E. P., Penduff, T., Smith, R., Talley, L., Beismann, J. O., and Böning, C. (2005). The North Atlantic Subpolar Gyre in Four High-Resolution Models. *Journal of Physical Oceanography*, 35(5):757–774.

van den Broeke, M. R., Enderlin, E. M., Howat, I. M., Kuipers Munneke, P., Noël, B. P. Y., van de Berg, W. J., van Meijgaard, E., and Wouters, B. (2016). On the recent contribution of the Greenland Ice Sheet to sea level change. *The Cryosphere*, 10(5):1933–1946.

V*å*ge, K., Pickart, R. S., Thierry, V., Reverdin, G., Lee, C. M., Petrie, B., Agnew, T. A., Wong, A., and Ribergaard, M. H. (2009). Surprising return of deep convection to the subpolar North Atlantic Ocean in winter 2007–2008. *Nature Geoscience*, 2:67–72.

Warren, C. R. (1991). Terminal environment, topographic control and fluctuations of West Greenland glaciers. *Boreas*, 20(1):1–15.

Williams, C. N., Cornford, S. L., Jordan, T. M., Dowdeswell, J. A., Siegert, M. J., Clark, C. D., Swift, D. A., Sole, A., Fenty, I., and Bamber, J. L. (2017). Generating synthetic fjord bathymetry for coastal Greenland. *The Cryosphere*, 11(1):363–380.

Wilson, N. J. and Straneo, F. (2015). Water exchange between the continental shelf and the cavity beneath Nioghalvfjerdsbrae (79 North Glacier). *Geophysical Research Letters*, 42(18):7648–7654.

Wood, M., Rignot, E., Fenty, I., Menemenlis, D., Millan, R., Morlighem, M., Mouginot, J., and Seroussi, H. (2018). Ocean-Induced Melt Triggers Glacier Retreat in Northwest Greenland. *Geophysical Research Letters*, 45(16):8334–8342.

Yashayaev, I. and Loder, J. W. (2009). Enhanced production of Labrador Sea Water in 2008. *Geophysical Research Letters*, 36(1).

Yashayaev, I. and Loder, J. W. (2017). Further intensification of deep convection in the Labrador Sea in 2016. *Geophysical Research Letters*, 44(3):1429–1438.

Chapter 2

Methods

2.1 Ocean Model

This thesis uses an ocean modelling framework of the Nucleus for European Modelling of the Ocean (NEMO). NEMO, developed by a European consortium, is used by departments in the Canadian government in a variety of applications including research and forecasting services in ocean and climate sciences. NEMO has three major components: Océan PArallélisé (OPA) for the ocean dynamics and thermodynamics (Madec, 2008), Louvain La-Neuve Ice Model (LIM) for the sea-ice dynamics and thermodynamics (Fichefet and Morales Maqueda, 1997), and Tracer in the Ocean Paradigm (TOP) for the online oceanic tracer transports.

This thesis includes work with two separate versions of NEMO, v3.4 and v3.6. The main modifications between the NEMO v3.4 and v3.6 are input and output server management, the open boundary set up, implicit bottom friction implemented to improve model stability, optimization with massive parallel processing (MPP) and implementation of injection of runoff at depth. Section 2.1 highlights key aspects of the model and further detail can be found in the NEMO v3.6 manual (Madec, 2008).

2.1.1 Underlying Principles

The ocean dynamics and thermodynamics in OPA are described using a set of primitive equations. These equations include the Navier-Stokes equations as well as a non-linear equation of state that couples temperature and salinity (the two active tracers) to the fluid velocity. The following assumptions (Figure 2.1) are applied for scale considerations of these primitive equations.

1. **Spherical Earth Approximation**
   The Earth is assumed to have a spherical shape rather than an ellipsoid. There-

fore, the geopotential surfaces are spheres and the local vertical gravity vector (g), combined with the centrifugal force from the Earth's rotation, is parallel with the earth's radius at a constant acceleration of 9.8 m/s^2.

2. **Thin-Shell Approximation**
   The depth of the ocean ($z \approx 4$ km) is smaller than the Earth's radius ($a \approx 6400$ km). Therefore, the Thin-Shell approximation neglects the depth of the ocean and $a+z$ is replaced by the constant value of a.

3. **Turbulent Closure Hypothesis**
   The effects of smaller-scale motions must be represented entirely in terms of large-scale patterns to close the equations. These effects appear in the Navier-Stokes equations, included in the subgrid-scale physics, as the divergence of turbulent fluxes.

4. **Boussinesq Hypothesis**
   Boussinesq models conserve volume with a reference density ($\rho_o = 1026$ kg/m^3) and neglect density variations except in their contribution to the buoyancy force. Since the steric effect, the expansion or contraction of the water column, is not explicitly represented attention is required to study the effect of the ocean acting on the sea level.

5. **Hydrostatic Hypothesis**
   The vertical pressure gradient and the buoyancy force are balanced to create the vertical momentum equation. The convective processes and vertical acceleration, from the Navier Stokes equations, are parameterized instead.

6. **Incompressibility Hypothesis**
   The flow is considered an incompressible fluid. Therefore, a controlled volume density (ρ) is constant ($\frac{D\rho}{Dt} = 0$). Combined with the continuity equation ($\frac{D\rho}{Dt} = -\rho\nabla \cdot \mathbf{U}$) results in the divergence of the three-dimensional velocity to equal zero ($\nabla \cdot \mathbf{U} = 0$).

The Navier-Stokes equations and the non-linear equation of state, in the orthogonal curvilinear coordinate system, includes a local upward unit vector (**k**) and two horizontal unit vectors (**i**,**j**) tangent to the geopotental surfaces. Therefore, the six primitive equations (momentum balance, hydrostatic equilibrium, incompressibility, the heat and salt conservation equations and equation of state) are written in the vector-invariant form:

$$\frac{\partial \mathbf{U_h}}{\partial t} = -\Big[(\nabla \times \mathbf{U}) \times \mathbf{U} + \frac{1}{2}\nabla(\mathbf{U}^2)\Big]_h - fk \times \mathbf{U_h} - \frac{1}{\rho_o}\nabla_h p + \mathbf{D^U} + \mathbf{F^U} \tag{2.1}$$

$$\frac{\partial p}{\partial z} = -\rho g \tag{2.2}$$

$$\nabla \cdot \mathbf{U} = 0 \tag{2.3}$$

$$\frac{\partial T}{\partial t} = -\nabla \cdot (T\ \mathbf{U}) + D^T + F^T \tag{2.4}$$

$$\frac{\partial S}{\partial t} = -\nabla \cdot (S\ \mathbf{U}) + D^S + F^S \tag{2.5}$$

$$\rho = \rho(T, S, p) \tag{2.6}$$

where $\mathbf{U}$ is the vector velocity, $\mathbf{U} = \mathbf{U}_h + w\mathbf{k}$ with the subscript h representing the horizontal vector, over the **i** and **j** plane. ∇ is the generalized derivative vector operator in **i**, **j**, and **k**) directions, t is time, z is the vertical coordinate, ρ is the in situ density given by the equation of state, ρ_o is a reference density, p is the pressure, $f = 2\Omega \cdot \mathbf{k}$ is the Coriolis acceleration, where Ω is the Earth's angular velocity vector, and g is the gravitational acceleration. $\mathbf{D^U}$, D^T, and D^S are parametrizations of small-scale physics for diffusion of momentum, temperature and salinity, and $\mathbf{F^U}$, F^T, and F^S surface forcing terms.

2.1.2 Boundaries

In the horizontal domain, the boundary conditions are set as solid walls (closed); therefore, the variables in the first and last rows and columns of the discretized fields are set to zero. For the ocean, boundaries are introduced at the ocean floor ($z = -H(i, j)$) and the height of the sea surface ($z = \eta(i, j, k, t)$) (Figure 2.2). The ocean surface is a linear free surface, where the sea surface height (η) may change in time but the thickness of the first vertical grid level is fixed. The model allows the ocean to exchange fluxes through these boundaries. These exchanges include heat, freshwater, salt and momentum through the coastline, sea ice, and the atmosphere.

An exchange of freshwater can occur between the land (coastline) and the ocean. The river runoff is injected and distributed equally within the top 30 m of the water

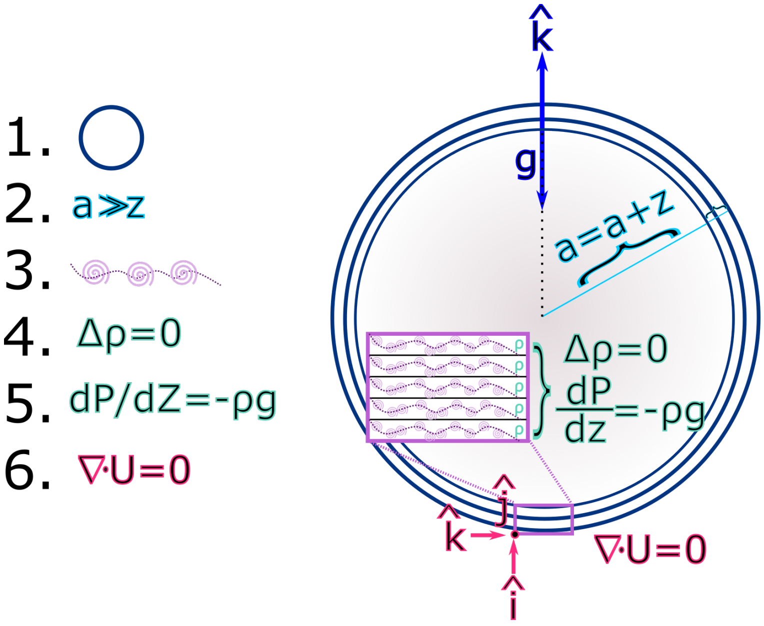

Figure 2.1: Six NEMO model assumptions are shown: 1. Spherical Earth, 2. Thin-Shell Approximation, 3. Turbulent Closure Hypothesis, 4. Boussinesq Hypothesis, 5. Hydrostatic Hypothesis, and 6. Incomprehensibility Hypothesis. The three dimensional vectors are $\hat{\imath}$, $\hat{\jmath}$ for the horizontal grid, and $\hat{k}$ for the vertical grid (represented as **i**, **j**, and **k**, in this thesis).

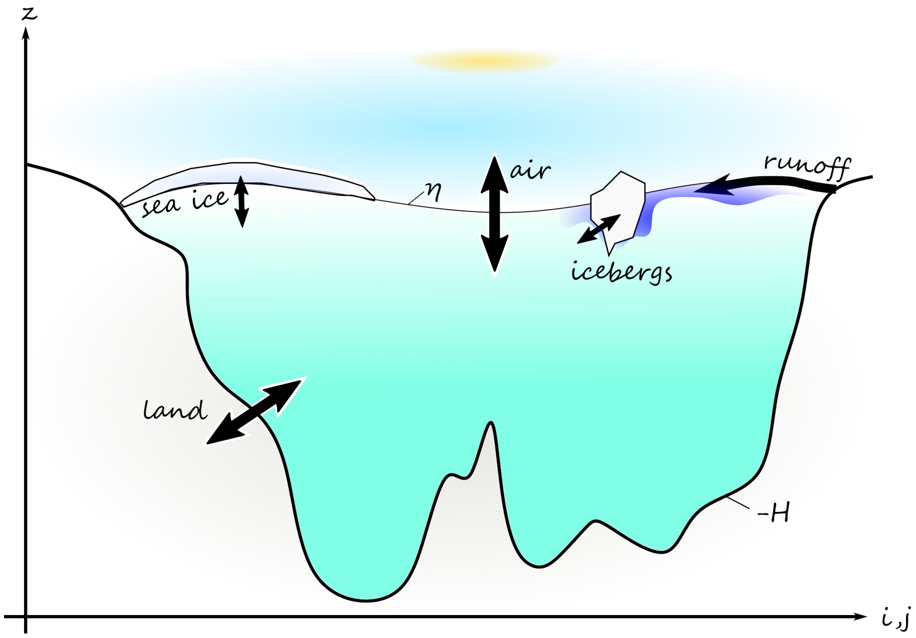

Figure 2.2: Introducing the type of NEMO model boundaries and optional interaction. η is the height of the sea surface, H is the depth of the ocean floor. Optional interaction include: land to ocean, sea ice to ocean, atmosphere to ocean, and freshwater input in forms of runoff (liquid) and icebergs (solid).

column. The runoff is assumed to be fresh (0 psu) and has the temperature of the ocean grid cell that received it. The linear free surface condition maintains a fixed volume of the ocean model domain with variations of the free surface. Therefore, the water column does not change by the addition of runoff but is instead diluted. A salt flux, which equals the volume of the runoff, is removed out of the model domain where the runoff was injected. Additionally, freshwater in the form of icebergs can be discharged into the ocean and this will be discussed more in Section 2.2.

There is no exchange of heat or salt fluxes between the ocean and the sea floor or coastline. Therefore, no flow can exist across the interface between the ocean and the sea floor or coastline. The velocity normal to the two solid boundaries (sea floor and coastline) is set to zero and therefore, the bottom velocity is parallel to the bottom. This kinematic boundary condition can be expressed as:

$$\omega = -\mathbf{U}_h \cdot \nabla_h \cdot H \tag{2.7}$$

where ω is the vertical velocity, $\mathbf{U}_h$ is the horizontal velocity, and H is the depth of the sea floor. However, the ocean can exchange momentum with the earth through frictional processes. Friction must be parameterized between the sea floor and coastline boundary conditions as the vertical and horizontal grid spacing are not fine enough to resolve such physics. It is parameterized in terms of modifying the turbulent fluxes ($\mathbf{D}^{\mathbf{U}}$ in Equation 2.1) using bottom and lateral boundary conditions, in which the simulations in this thesis use a non-linear quadratic bottom friction and a free slip lateral boundary condition. For the coastline, the tangential velocity at the coastline (”ghost” velocity point inside land area) is equal to the velocity just offshore the coastline, one grid cell over.

At the ocean’s surface, sea ice can melt or freeze, either supplying or removing salt from the ocean. Sea ice salinity is very low ($\sim$ 4 to 6 psu) compared to that of the ocean ($\sim$ 34 psu). This exchange is important and therefore, is not neglected in the model. The interface between the ocean and sea ice exchanges heat, salt, and momentum. Sea ice is floating upon the ocean surface and does not exert any pressure on the ocean. Underneath the sea ice, the ocean surface temperature is set to the freezing point.

The exchange of heat, salt, freshwater, and momentum also occur at the atmosphere and ocean interface. The displacement of the sea surface is thus governed by the kinematic surface condition:

$$\omega = \frac{\partial \eta}{\partial t} + \mathbf{U}_h|_{z=\eta} \cdot \nabla_h \eta + (P - E + R + I) \tag{2.8}$$

where P, E, R, and I represent precipitation, evaporation, runoff, and ice melt flux. The dynamic boundary condition leads to the continuity of pressure across the surface interface, $z = \eta$, which results in:

$$\frac{\partial \eta}{\partial t} = (P - E + R + I) - \nabla \cdot [(H + \eta)\mathbf{U}_h] \tag{2.9}$$

where the vertical averaged horizontal velocity is $\mathbf{U}_h = \frac{1}{H+\eta}\int_H^\eta \mathbf{U}_h dz$. Allowing the air-sea interface to move introduces external gravity waves (EGW) as a class of solution of the primitive equations. For this thesis, the focus is on processes that are at a relatively large scale, so a time-step of $O(1hour)$ is used. In the configurations used in this thesis, a linear filtered free surface model is used to solve the numerical stability problem that EGWs creates (Roullet and Madec, 2000). The linear filter introduces a damping term in the momentum equation (Equation 2.1):

$$\frac{\partial \mathbf{U}_h}{\partial t} = M - g\nabla\tilde{\rho}\eta - gT_c\nabla\left(\tilde{\rho}\frac{\partial \eta}{\partial t}\right) \tag{2.10}$$

where the first term on the right hand side of the equation, M, represents the Coriolis, the second term represents the hydrostatic pressure gradient, and the third term is the non-linear and viscous terms in the momentum balance in Equation 2.1. T_c is a parameter characterizing the force in time $T_c > \Delta t$, and $\tilde{\rho} = \rho/\rho_0$ is the dimensionless density (Roullet and Madec, 2000).

2.1.3 Curvilinear Z-Coordinate System

A coordinate transformation is required in order to represent dynamical processes on a sphere, to represent the earth. Curvilinear coordinates are used, which is a coordinate system derived from Cartesian coordinates by using a transformation to generate curved coordinate lines (Figure 2.3). Three orthogonal unit vectors are used in a spherical structure corresponding to the earth. Since the force of gravity is dominate in the equations of large scale motions, unit vector **k** represents local upward vector and (**i**,**j**) are orthogonal, and therefore tangent to the potential surfaces. To avoid a convergence at the North Pole, as spherical coordinates generate a singularity point close to the poles, the global orthogonal curvilinear ocean mesh is restructured to have a tri-pole transformation: two geometric poles with one over Canada and the other over Russia.

The geographical coordinate system is defined by latitude $\varphi(i, j)$, the longitude $\lambda(i, j)$ and the distance from the centre of the earth $(a + z(k))$ where a is the earth's radius and z the altitude above a reference sea level. The local deformation of the

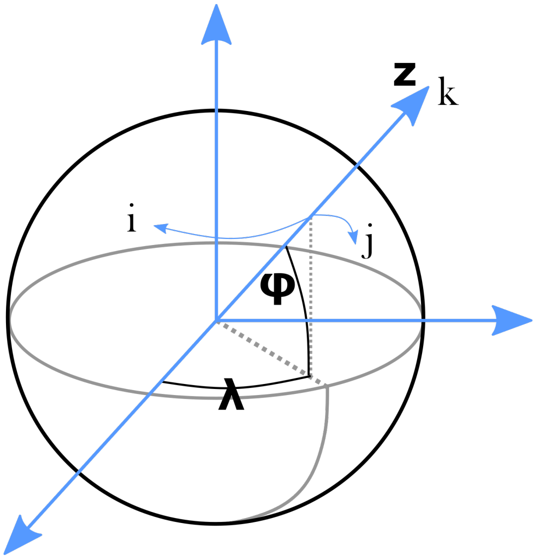

Figure 2.3: The representation of the geographical coordinate system (λ,φ and z) and the curvilinear coordinate system (**i**, **j** and **k**). Based on Madec (2008) Figure 2.2. The set of orthogonal curvilinear coordinates (i, j, k) on the sphere are associated with the positively oriented orthogonal set of unit vectors (**i**, **j**, **k**) connected to the Earth such that the unit vector **k** represents local upward vector and (**i**,**j**) are orthogonal to **k**.

curvilinear coordinate system is given by e_1, e_2, and e_3, the three scale factors. Each cell size is defined by horizontal scale factors (e_1, e_2) and a vertical scale factor (e_3). Partial derivatives of scale factors are evaluated by centre second order finite difference approximation.

$$e_1 = (a+z)\left[\left(\frac{\partial\lambda}{\partial i}cos\varphi\right)^2 + \left(\frac{\partial\varphi}{\partial i}\right)^2\right]^{1/2} \tag{2.11}$$

$$e_2 = (a+z)\left[\left(\frac{\partial\lambda}{\partial j}cos\varphi\right)^2 + \left(\frac{\partial\varphi}{\partial j}\right)^2\right]^{1/2} \tag{2.12}$$

$$e_3 = \left(\frac{\partial z}{\partial k}\right) \tag{2.13}$$

Given the thin shell approximation, the ocean depth is neglected when compared to the Earth's radius. Therefore, $a+z$, can be replaced by a. The resulting horizontal scale factors e_1, e_2 are independent of k while the vertical scale factor is a single function of k as **k** is parallel to **z**.

The ocean mesh is therefore defined by this transformation. The ocean mesh is classified as the Arakawa's C Grid (Figure 2.4). Cells are centred on scalar points of T, S, p, and ρ, with vector points u, v, and w defined in the centre of each face of the cell. At the centre of each vertical edge, the relative and planetary vorticity is defined, with the barotropic stream function at horizontal points overlying the vorticity points.

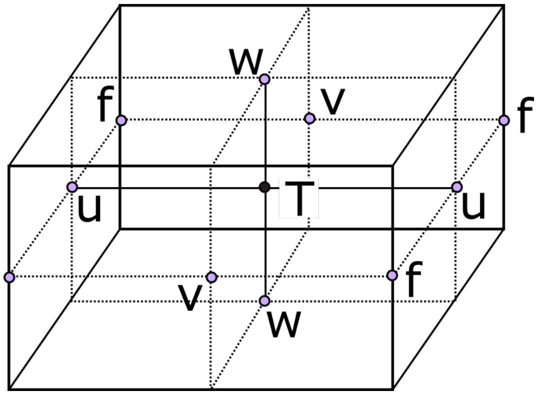

Figure 2.4: Arakawa's C Grid's arrangement of variables. T indicates scalar points (temperature, salinity, density, pressure, and horizontal divergence), (u, v, w) indicate vector points, and f indicates where planetary and relative vorticities are defined. Adapted from Madec (2008) Figure 4.1.

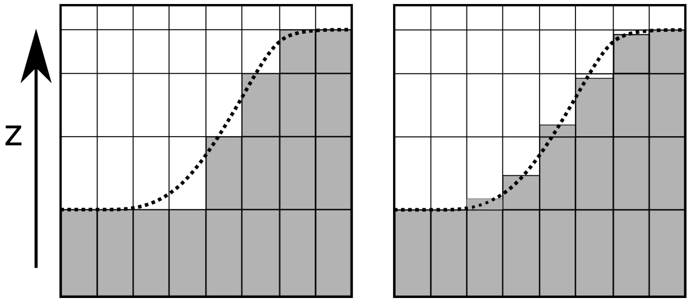

Figure 2.5: Vertical model grid with the traditional full step z-coordinate on the left, and partial step with z-coordinate on the right. Shaded cells represent the model bathymetry and the dashed lines represent the sea floor that is fed into the model. Based on Madec (2008) Figure 4.5.

For the vertical grid, the z-coordinate partial steps method is applied (Figure 2.5). The vertical column is divided into levels with a fixed thickness. However, the thickness of the bottom layer varies as a function of the geographical location and represents the bathymetry better than the traditional z-coordinate. The thickness of the bottom-most cells are determined by the input bathymetry product; therefore, improves the representation of the sea floor. The bathymetry product also defines the coastline. Recall that for the coastline, the tangential velocity at the coastline is equal to the velocity just offshore the coastline, one grid cell over. Thus, the vorticity is set to zero inside the land and at the coast.

2.1.4 Subgrid-Scale Physics

One of the largest hurdles ocean models have to overcome is representing the effects of small scale motions that the model is unable to capture (in both space and time). The advective terms in the primitive, Navier-Stokes, equations generate smaller-scale motions such as turbulent fluxes. To close the equations, the smaller scale motions must be represented in terms of large scale motion. Therefore small-scale motions are parameterized using the turbulent closure hypothesis, called subgrid-scale physics. Subgrid-scale terms for the momentum balance and heat and salt conservation equations ($\mathbf{D}^U$, D^S, and D^T, respectively) are divided into vertical and lateral components. For the horizontal, the eddy induced turbulent fluxes can be assumed to mix on slopes computed along neutral surfaces. An isoneutral second-order operator in three space directions is used. The lateral Laplacian tracer diffusive operator is defined by:

$$D_l^T = \nabla \cdot (A_l^T \mathscr{R} \nabla T) \text{ with } \mathscr{R} = \begin{pmatrix} 1 & 0 & -r_1 \\ 0 & 1 & -r_2 \\ -r_1 & -r_2 & r_1^2 + r_2^2 \end{pmatrix} \tag{2.14}$$

A_l^T is the lateral eddy diffusivity coefficient (for this thesis it is set as 300 m^2/s). For a z-coordinate with isoneutral diffusion, r_1 and r_2 are the slopes between the isoneutral and computational surfaces. Therefore the mixing is performed along neutral surfaces, gradients of ρ :

$$r_1 = \frac{e_3}{e_1}\left(\frac{\partial \rho}{\partial i}\right)\left(\frac{\partial \rho}{\partial k}\right)^{-1}, \; r_2 = \frac{e_3}{e_2}\left(\frac{\partial \rho}{\partial j}\right)\left(\frac{\partial \rho}{\partial k}\right)^{-1} \tag{2.15}$$

Lateral diffusion on momentum uses a fourth-order, geopotential operator. The lateral bilaplacian diffusive operator on geopotential surfaces for momentum is:

$$D_l^{\mathbf{U}} = \nabla_h \Big\{ \nabla_h \cdot \Big[A_l^m \nabla_h(\chi) \Big] \Big\} + \nabla_h \times \Big\{ \mathbf{k} \cdot \nabla \times \Big[A_l^m \nabla_h \times (\zeta \mathbf{k}) \Big] \Big\} \tag{2.16}$$

where A_l^m is the eddy coefficient and ζ and χ is defined as the relative vorticity (rotational part) and the divergence of the horizontal field:

$$\begin{aligned}\zeta = \nabla \times \bar{U} \cdot k &= \frac{1}{e_1 e_2}\left[\frac{\partial(e_2 v)}{\partial i} - \frac{\partial(e_1 u)}{\partial j}\right] \\ \chi = \nabla \cdot \bar{U}_h &= \frac{1}{e_1 e_2}\left[\frac{\partial(e_2 u)}{\partial i} + \frac{\partial(e_1 v)}{\partial j}\right]\end{aligned} \tag{2.17}$$

For the vertical subgrid-scale physics, the model resolution is always larger than the scale of vertical turbulence. Therefore turbulent motions are always parameterized. The vertical turbulent fluxes are assumed to depend linearly on the gradients of large-scale quantities such as turbulent heat flux, molecular diffusion and dissipation. The resulting vertical momentum and temperature and salinity tracer diffusive operators are of second-order differential equations:

$$\begin{aligned}\mathbf{D}_v^{\mathbf{U}} &= \frac{\partial}{\partial z}\left(A_v^m \frac{\partial \mathbf{U}_h}{\partial z}\right) \\ D_v^T &= \frac{\partial}{\partial z}\left(A_v^T \frac{\partial T}{\partial z}\right) \\ D_v^S &= \frac{\partial}{\partial z}\left(A_v^T \frac{\partial S}{\partial z}\right)\end{aligned} \tag{2.18}$$

where A_v^m and A_v^T are the vertical eddy viscosity and diffusivity coefficients, respectively. The eddy viscosity and diffusivity are set up for non-turbulent conditions as $10^{-4} m^2 s^{-1}$ and $10^{-5} m^2 s^{-1}$ respectively. For turbulent conditions, the vertical eddy viscosity and diffusivity coefficients are calculated using a Turbulent Kinetic Energy (TKE) closure scheme.

$$\begin{gathered}\bar{e} = 0.5(\overline{u'^2} + \overline{v'^2} + \overline{w'^2}) \\ \frac{\partial \bar{e}}{\partial t} = \frac{A_v^m}{e_3^2}\left[\left(\frac{\partial u}{\partial k}\right)^2 + \left(\frac{\partial v}{\partial k}\right)^2\right] - A_v^T N^2 + \frac{1}{e_3}\frac{\partial}{\partial k}\left[\frac{A_v^m}{e_3}\frac{\partial \bar{e}}{\partial k}\right] - c_\varepsilon \frac{\bar{e}^{3/2}}{l_\varepsilon} \\ A_v^m = c_k l_k \sqrt{\bar{e}} \\ A_v^T = \frac{A_v^m}{P_{rt}}\end{gathered} \tag{2.19}$$

where u',v', and w' are the turbulent component of velocity (deviations from the mean flow), N is the local buoyancy frequency, $c_\varepsilon = \sqrt{2}/2$ and $c_k = 0.1$ are constants, and P_{rt} is the Prandtl number (a function of the local Richardson number, R_i). The dissipation

(l_k) and mixing (l_ε) length scales are defined as:

$$\begin{gathered} l_k = l_\varepsilon = \sqrt{2\bar{e}}/N \\ \frac{1}{e_3}\left|\frac{\partial l}{\partial k}\right| \leq 1 \text{ with } l = l_k = l_\varepsilon \end{gathered} \tag{2.20}$$

Convection

In the vertical, static instabilities, where lighter potential densities are below denser ones, may occur generally due to air-sea fluxes and sea ice formation. Convective processes can re-establish the static stability of the water column. However, due to the coarse vertical grid and the hydrostatic assumption, convection must be parameterized. The model restores the static stability of the water column by the enhancement of vertical diffusion. This is done by increasing the values of the vertical eddy mixing coefficients in regions where the stratification is unstable, for momentum as well as both temperature and salinity tracers. This rapidly mixes away any instabilities.

Friction

The surface boundary condition on the momentum fluxes represents the stress exerted by the wind and sea ice.

$$A_v^m \left(\frac{\partial \mathbf{U}_h}{\partial z}\right) = \mathscr{F}_h^{\mathbf{U}} \tag{2.21}$$

where $\mathscr{F}_h^{\mathbf{U}}$ represents the downward flux of horizontal momentum outside the logarithmic turbulent boundary layer with a thickness on the order of 1 metre in the ocean. The logarithmic layer is never represented in the primitive equations. Therefore, $\mathscr{F}_h^{\mathbf{U}}$ must be parameterized. This thesis has chosen the non-linear bottom friction parameterization, which assumes that the bottom friction is quadratic:

$$\mathscr{F}_h^{\mathbf{U}} = \frac{A_v^m}{e_3}\frac{\partial \mathbf{U}_h}{\partial k} = C_D \sqrt{u_b^2 + v_b^2 + e_b}\, \mathbf{U}_h^b \tag{2.22}$$

where C_D is a drag coefficient, and e_b a bottom turbulent kinetic energy due to internal waves breaking and other short time scale currents. In this set up,
$C_D = 10^{-3}$ and $e_b = 2.5 \times 10^{-3}\ m^2 s^{-2}$, where $\mathbf{U}_h^b = (u_b, v_b)$ is the near bottom horizontal ocean velocity. Rotation between the interior velocity and bottom friction is neglected in the present release of NEMO.

The coefficients that control the strength of the non-linear bottom friction are computed as:

$$\begin{aligned} c_b^u &= -C_D\left[u^2 + (\bar{\bar{v}}^{i+1,j})^2 + e_b\right]^{1/2} \\ c_b^v &= -C_D\left[(\bar{\bar{u}}^{i,j+1})^2 + v^2 + +e_b\right]^{1/2} \end{aligned} \tag{2.23}$$

The surface boundary condition on momentum is the stress exerted by the wind and sea ice. At the surface, the momentum fluxes are prescribed as the boundary condition on the vertical turbulent momentum fluxes:

$$\left(\frac{A_v^m}{e_3}\frac{\partial \mathbf{U}_h}{\partial k}\right)\Big|_{z=1} = \frac{1}{\rho_o}\begin{pmatrix}\tau_u \\ \tau_v\end{pmatrix} \tag{2.24}$$

where (τ_u, τ_v) are the two components of the surface stress vector in the (i,j) coordinate system.

The surface stress of the ocean is exerted by the wind and sea ice and is computed by the CORE bulk formulae from Large and Yeager (2004):

$$\begin{aligned} \tau &= (f_i)\tau_{io} + f_o\tau_{as} \\ \tau_{io} &= \rho_o C_D|\mathbf{U}_i - \mathbf{U}_o|(\mathbf{U}_i - \mathbf{U}_o) \\ \tau_{ao} &= \rho_a C_D|\mathbf{U}_a - \mathbf{U}_o|(\mathbf{U}_i - \mathbf{U}_o) \end{aligned} \tag{2.25}$$

where subscripts a, o, and i refer to the atmosphere, ocean and sea ice components and io and ao denote the ice-ocean and air-ocean fluxes. $\tau = (\tau_u, \tau_v)$ is the surface stress, f_i is the fraction of ice cover over a grid point, $f_o = 1 - f_i$ is the fraction of the ocean grid point exposed to the atmosphere, the velocity, $\mathbf{U}_x = (u, v)$, is respect to the atmosphere (10-metre wind), ocean (first layer) and sea ice, and ρ is the density concerning atmosphere or ocean.

2.1.5 Time Domain

This section will include a description of NEMO's time-stepping method. NEMO uses a three level scheme that requires three arrays, a *before*, *now*, and *after* for each prognostic variable (u,v, T, or S):

$$x^{t+\Delta t} = x^{t-\Delta t} + 2\Delta t \ \mathrm{RHS}_x^{t-\Delta t,t,t+\Delta t} \tag{2.26}$$

where x represents the prognostic variables, RHS stands for the Right-Hand-Side of the corresponding equation, evolving in time, Δt is the time-step, which is defined as 1080 seconds (18 minutes) for the baroclinic component in this thesis, and the superscripts indicate the time at which each term is evaluated. To avoid instabilities in time-stepping with a complex and non-linear system of equations, the time-stepping calculation is performed in a single operation, rather than letting a prognostic variable evolve in time separately for each term in the equation.

For non-diffusive processes, such as momentum and tracer advection, pressure gradient and Coriolis terms, the Leapfrog scheme (Mesinger and Arakawa, 1976) is used for time-stepping. The Leapfrog scheme is a time centred scheme; therefore the RHS in Equation 2.26 is evaluated at t, the *now* time-step. It achieves second-order accuracy with just one right-hand side evaluation per time-step and does not artificially damp linear oscillatory motion or produce instability by amplifying the oscillations.

However, some disadvantages occur with the usage of the Leapfrog scheme such as a large phase-speed error, unsuitable for representing diffusive and Rayleigh damping processes. The scheme does allow the coexistence of a numerical and physical mode due to its leading third-order dispersive error. Therefore, a divergence of odd and even time-steps may occur. In order to prevent this error, a Robert-Asselin time filter is used (Asselin, 1972; Robert, 1966).

$$x_F^t = x^t + \gamma \left[x_F^{t-\Delta t} - 2x^t + x^{t+\Delta t} \right] \tag{2.27}$$

where, subscript F denotes filtered values and γ is the Asselin coefficient defined as 0.1 for this thesis.

As briefly mentioned before, the Leapfrog scheme cannot be used for diffusive and damping processes. Instead, a forward or backward time difference scheme is used. For the forward time difference scheme, D_x represents a diffusion term or tracer restoring term:

$$x^{t+\Delta t} = x^{t-\Delta t} + 2\Delta t \; D_x^{t-\Delta t} \tag{2.28}$$

This equation is diffusive in time and conditionally stable. Following conditions set by Griffies (2004), the stability of second and fourth-order horizontal diffusion schemes are:

$$A^h < \begin{cases} \dfrac{e^2}{8\Delta t} & \text{laplacian diffusion} \\ \dfrac{e^4}{64\Delta t} & \text{bilaplacian diffusion} \end{cases} \tag{2.29}$$

Here, the Laplacian operator is used for lateral diffusion for tracers and the Bilaplacian operator for lateral diffusion on momentum. For the vertical diffusion processes, a backward implicit time differencing scheme is used to overcome the strong constraint on the time-step that would be in place if using a forward time differencing scheme for numerical stability. This backward implicit time difference scheme is unconditionally stable, however diffusive:

$$x^{t+\Delta t} = x^{t-\Delta t} + 2\Delta t \ \mathrm{RHS}_x^{t+\Delta t} \tag{2.30}$$

2.2 Iceberg Module

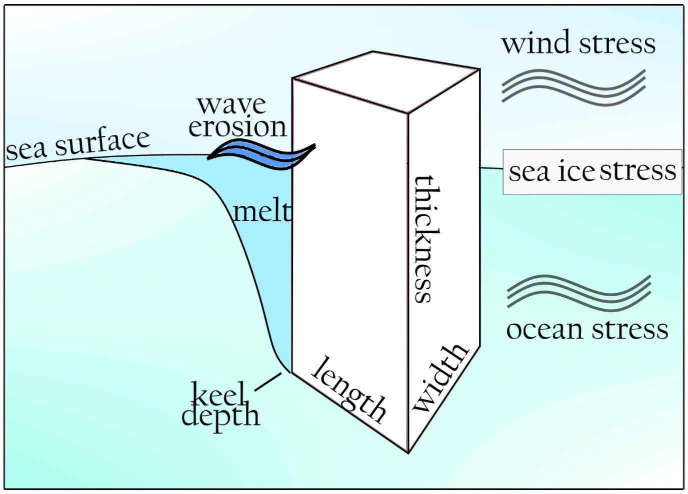

Figure 2.6: Illustration of the iceberg module's interactions with the atmosphere and ocean in NEMO. The melt plume from the iceberg is injected at the model's ocean surface layer.

The iceberg module used in NEMO is based on the original model of Bigg et al. (1996, 1997) and improvements from Gladstone et al. (2001); Marsh et al. (2015); Martin and Adcroft (2010), and Merino et al. (2016). Marsh et al. (2015) implemented the first iceberg module in NEMO. The iceberg module's physical behaviour (Figure 2.6) are controlled by a set of equations that are described in Martin and Adcroft (2010) and have been modified from Bigg et al. (1997) and Gladstone et al. (2001) to enhance numerical stability. However, a drawback was that the icebergs only interacted with the ocean surface layer. Merino et al. (2016) updated the module further and implemented a vertical integration which takes into account the influence of the vertical profiles of ocean currents and temperatures rather than just the sea surface temperature and surface velocities and slowed down icebergs at shallow bathymetry. Therefore, the following equations take into account a vertical integration from the surface to iceberg keel (Merino et al., 2016).

Icebergs are defined as cubes with total thickness T, length L and width W. The total thickness is divided into freeboard F, which is the height above the water level, and draught D, the submerged depth of the iceberg, with $T = F + D$, and $D = \rho/\rho_o T \simeq 0.8T$. In this thesis, the average density of icebergs $\rho = 850kg/m^3$ and the average density of sea water $\rho_o = 1026kg/m^3$. The momentum balance for an iceberg of mass M is comprised of:

$$M\frac{d\mathbf{v}}{dt} = -Mf \times \mathbf{v} + \tau_a + \tau_o + \tau_i + \mathbf{F}_r + \mathbf{F}_p \tag{2.31}$$

where subscripts a, o, and i refers to atmosphere, ocean and sea ice, respectively. The first term on the right-hand side of Equation 2.31 represents the Coriolis force with f as the Coriolis parameter and $\mathbf{v}$ is the 2 dimensional vector of the horizontal iceberg velocity. These other terms in this Equation 2.31 are the drag forces (τ) for air, ocean and sea ice, wave radiation force ($\mathbf{F}_r$) and the horizontal pressure gradient force ($\mathbf{F}_p$). These components are described as:

$$\tau_a = \rho_a\big[0.5\ c_{a,v}WF + c_{a,h}LW\big]\ |\mathbf{v}_a - \mathbf{v}|(\mathbf{v}_a - \mathbf{v}) \tag{2.31a}$$

$$\tau_o = \rho_o\big[0.5\ c_{o,v}W(D - T_i) + c_{o,h}LW\big]\ |\mathbf{v}_o - \mathbf{v}|(\mathbf{v}_o - \mathbf{v}) \tag{2.31b}$$

$$\tau_i = \rho_i\big[0.5\ c_{i,v}WT_i\big]\ |\mathbf{v}_i - \mathbf{v}|(\mathbf{v}_i - \mathbf{v}) \tag{2.31c}$$

where ρ_x is the density with respect to $x = \{a, o, i\}$, and $c_{x,v}$ and $c_{x,h}$ are the vertical and horizontal drag coefficients, where $c_{a,v}$ = 1.3, $c_{a,h}$ = 0.0055, $c_{o,v}$ = 0.9, $c_{o,h}$ = 0.0012 and $c_{i,v}$ = $c_{o,v}$. Sea ice can only act on the side walls of the iceberg and the drag force from the sea ice τ_i is relatively small since the thickness of T_i is much smaller than D for most of the iceberg's existence. The wave radiation force $\mathbf{F}_r$ and the pressure gradient force $\mathbf{F}_p$ are given by:

$$\mathbf{F}_r = \frac{1}{2}(\rho_o c_r g a) \cdot \min(a, F) \left[\frac{LW}{L+W}\frac{\mathbf{v}_a}{|(\mathbf{v}_a|}\right] \tag{2.31d}$$

$$\mathbf{F}_p = -Mg\nabla\eta \tag{2.31e}$$

where c_r is the wave radiation coefficient, g is the acceleration due to gravity, a is the wave amplitude and η is the sea surface slope.

The depth-integrated ocean velocity is defined from Merino et al. (2016) as:

$$\mathbf{v}_o = \frac{\int_{-\min(H_{\text{bat}},H_{\text{icb}})}^{0} \mathbf{v}_*(h)dh}{H_{\text{icb}}} \tag{2.31f}$$

where H_{bat} is the depth of the bathymetry at the grid point, H_{icb} is the thickness of the iceberg that is submerged, $\mathbf{v}_*(h)$ is the ocean velocity depending on the depth.

The mass balance of an iceberg is given by:

$$\rho \frac{d(LWT)}{dt} = \rho(-LWM_b - T(L+W)(M_e + M_v)) \tag{2.32}$$

where M_b, M_e, and M_v are the basal melt rate, wave erosion, and buoyancy convection, respectively. M_b is described as:

$$M_b = 0.58|\mathbf{v} - \mathbf{v}_b|^{0.8} \frac{\tilde{T}_b - \tilde{T}}{L^{0.2}} \tag{2.32a}$$

where $\mathbf{v}_b$ is the velocity of the ocean at the base of the iceberg (iceberg keel), $\tilde{T}_b$ is the temperature of the ocean at the iceberg keel, and $\tilde{T}$ is the temperature of the iceberg, assumed constant (-4^oC). M_e is described as:

$$M_e = \frac{1}{12} S_s \left(1 + cos\left[\pi A_i^3\right]\right)\left(\tilde{T}_s + 2\right) \tag{2.32b}$$

where A_i is the fractional sea ice area and $\tilde{T}_s$ is the sea surface temperature. S_s is the sea state (a function of the wind speed) which can be calculated by using the following equations:

$$S_s = \frac{3}{2}|\mathbf{v}_a - \mathbf{v}_o|^{\frac{1}{2}} + \frac{1}{10}|\mathbf{v}_a - \mathbf{v}_o| \tag{2.32c}$$

Finally, M_v can be expanded as:

$$M_v = \int_{-H\text{icb}}^{0} (7.62 \times 10^{-3} \tilde{T}_o(h) + 1.29 \times 10^{-3} \tilde{T}_o^2(h)) dh \tag{2.32d}$$

where $\tilde{T}_o(h)$ is the ocean temperature at depth h.

NEMO handles icebergs as Lagrangian particles (points in space). In order to reduce computational costs, icebergs are grouped in numbers that depend on their classification (i.e. size and mass ordered from 1 to 10) and modelled as a single particle (Martin and Adcroft, 2010). At each model time-step, a test is performed in the model to see if there is enough ice mass to calve a particle. When there is enough mass, a new iceberg is spawned and the total available mass reduces (Madec, 2008).

Icebergs mainly deteriorate due to erosion via wind, waves and currents, and melting on the bottom and sides; therefore, all other effects are negligibly small (Martin and Adcroft, 2010). Presently, the movement of icebergs cannot be stopped by a heavy pack of sea ice. Wave erosion not only leads to the melting of icebergs at the surface but can also cause icebergs to break down into smaller "child" icebergs, called bergy bits, which are assumed to travel with their parent iceberg (Martin and Adcroft, 2010). The wave erosion on icebergs uses a ratio in the iceberg module to determine the rate of liquid melt or production of bergy bits; the break down is taken from Marson et al. (prep) which implemented a division of 70% erosion to liquid melt and 30% to bergy bits. This division was a product of a rough estimate based on the limited observations of Savage (2001).

2.3 Sea Ice Model

This thesis focuses on the Arctic and North Atlantic Ocean and the communication between these two oceans. Therefore, this thesis benefits from the use of a full sea ice model coupled with the ocean model. The sea ice model used is the Louvain la Neuve sea ice model (LIM) (Fichefet and Morales Maqueda, 1997). There are two versions of the model available, LIM2 (Timmermann et al., 2005) and LIM3 (Vancoppenolle et al., 2009). This thesis will only use LIM2, as there needs to be further evaluation and tests before updating to LIM3 for the configuration set up used here. This section will discuss the details of the sea ice model's dynamic and thermodynamic processes as well as response to atmospheric forcing and techniques used to couple the sea ice model to the ocean model (Figure 2.7).

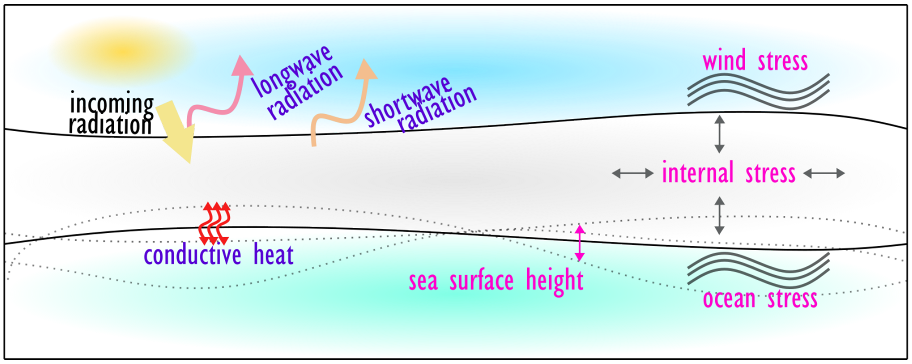

Figure 2.7: Sea ice model's dynamic (magenta) and thermodynamic (purple) processes. Dynamical processes (Equation 2.33) include wind, ocean and internal stresses and changes in sea surface height. Thermodynamical processes (Equation 2.34) include longwave and short wave radiation and conductive heat flux.

2.3.1 Sea Ice Dynamics

The sea ice model allows for ice consolidation and for leads and polynyas within the ice cover. The sea ice dynamics are set to move in a two-dimensional space. Ice motion is influenced by the winds and the ocean and the conservation of linear momentum (Bouillon et al., 2009) is used:

$$m\frac{\partial \mathbf{u}}{\partial t} = \nabla \cdot \sigma + A(\tau_a + \tau_o) - mf\mathbf{k} \times \mathbf{u} - mg\nabla\eta \tag{2.33}$$

where m is the ice mass per unit area, u is the ice velocity, σ is the internal stress tensor, A is the ice area fraction (concentration), f is the Coriolis parameter, $\mathbf{k}$ is the upward-pointing unit vector, g is the acceleration of gravity, and η is the sea surface elevation. τ_a is the wind stress, τ_o is the ocean stress. Therefore, this equation considers the motion of the ice due to wind, ocean stress, changes in sea surface height, earth's rotation, and sea ice deformation as a function of the sea ice internal stress.

Originally, LIM had the ice internal stress calculated based on the viscous-plastic (VP) formulation (Hibler, 1979). However, this method for solving VP dynamics was relatively slow and complicated. An alternative is the elastic-viscous-plastic (EVP) formulation of Hunke and Dukowicz (1997). This method was found to be simpler to program and can be solved explicitly in time, allowing for easier parallelization. The differences in VP and EVP formulation is how the method treats the sea ice rheology, how the sea ice flows and it's deformation under stress. A release of LIM2 using the EVP formulation Hunke and Dukowicz (1997) that has been successfully tested (Bouillon et al., 2009) and is used in this thesis.

In a steady-state, the internal stress of the EVP formulation converges to the VP formulation. This is because EVP formulation introduces a time dependence term. However static flow in EVP rheology is represented by an elastic deformation, which updates the ice stress on a shorter time-step, resolving elastic wave velocities. The internal stress is a function of divergence, horizontal tension, shearing strain rates, and the sea ice compressive strength. Where the sea ice compressive strength is defined by $P = P^{*}he^{C(1-A)}$, where h is the ice thickness per unit area, P^{*} is the ice strength (set as $2.3 \times 10^{4} N/m^{2}$ in this thesis), and C is the ice strength parameter (treated as constant 20).

2.3.2 Sea Ice Thermodynamics

This section will highlight specific processes within the sea ice thermodynamics. Further information can be found in Fichefet and Morales Maqueda (1997). The thermodynamic component of the sea ice model determines the growth and decay of ice in the vertical and horizontal. The sea ice is represented in three layers, a snow layer that can accumulate when the surface temperature is below the melting point, and two layers of sea ice with equal thickness.

First, lets define the internal temperatures of snow and ice:

$$\rho c_p \frac{\partial T}{\partial t} = G_h k \frac{\partial^2 T}{\partial z^2} \tag{2.34}$$

where T is temperature, t is time, and z is the vertical coordinate. For sea ice and snow, ρ is the density (900 kg/m^3 and 300 kg/m^3, respectively), c_p is specific heat (2093 $J/kg/K$). k is the thermal conductivity (2.0344 $W/m/K$ and 0.0398 $W/m/K$) for sea ice and snow, respectively. In this one-dimensional heat-diffusion equation, there is also a correction factor (G_h) that accounts for the variability of heat conduction corresponding to variations of sea ice thickness.

Secondly, the heat fluxes at the surface of the snow and ice are defined as a function of surface temperature ($B_{sf}(T_{sf})$). There is a balance of 5 components, incoming shortwave radiation (Q_{sw}), incoming longwave radiation (Q_{lw}), sensible (Q_H) and latent heat (Q_E), and conductive heat flux from below the surface (Q_c):

$$B_{sf}(T_{sf}) = Q_{sw} + Q_{lw} + Q_H + Q_E + Q_C \tag{2.35}$$

where the subscript *sf* refers to the top of the surface, either ice or snow. The first four flux components are defined by Large and Yeager (2004):

$$\begin{aligned} Q_{sw} &= (1 - i_o)(1 - \alpha)Q_i \\ Q_{lw} &= \varepsilon(Q_{dlw} - \sigma T_{sst}^4) \\ Q_H &= \rho_a c_p C_H (T_a - T_{sst})|\mathbf{u}_a - \mathbf{u}_o| \\ Q_E &= L\rho_a C_E (q_a - q_s(T_{sst}))|\mathbf{u}_a - \mathbf{u}_o| \end{aligned} \tag{2.36}$$

where i_o is the fraction of the net shortwave radiation that penetrates the snow or bare ice and is zero in the case of snow covered ice and α is the surface albedo (0.95). Q_i and Q_{dlw} is the downwelling shortwave (insolation) and long wave radiation, ε is the emissivitiy (0.97), σ is the Stefan-Boltzmann constant ($5.67 \times 10^{-8} kg/s^3K^4$), and T_{sst} is the sea surface temperature. Variables with subscript a denotes the variable at near surface (10 m); they include atmospheric density ρ_a ($\approx 1.22kg/m^3$), temperature T_a, specific humidity q_a, and wind velocity $\mathbf{u_a}$. C_H and C_E are the transfer coefficients of sensible and latent heat, L is the latent heat of vaporization of water ($\approx 2.5 \times 10^6 J/kg$), $\mathbf{u}_o$ is the current at the surface, and q_s is the saturated specific humidity.

If the heat balance generates the surface temperature (T_{sf}) to be above the melting point for snow and ice, then T_{sf} is held at that melting point and the excessive energy is balanced through melting snow or ice (Fichefet and Morales Maqueda, 1997):

$$\left(\frac{\partial h_{s,i}}{\partial t}\right)_{sf,abl} = -\frac{B_{sf}(T_{sf})}{L_{s,i}} \tag{2.37}$$

where h is the thickness of the ice, subscript (s,i) is for snow if it exists, or ice.

The final flux component in Equation 2.35 discusses the ice-ocean interface. At the ice-ocean interface, at the bottom of the ice slab, any extra energy between the conductive heat flux (Q_c) and heat flux from the ocean Q_{io} is used for ice accumulation or ablation, defined in Fichefet and Morales Maqueda (1997) as:

$$\left(\frac{\partial h_i}{\partial t}\right)_{io,acc-abl} = \frac{Q_c - Q_{io}}{L_i} \tag{2.38}$$

Lateral growth and decay of ice results in ice consolidation, or the existence of leads and polynyas. Ice concentration variable A is defined as the fraction of the grid cell covered by ice, with variations dependent on the heat budget of the open water (B_l):

$$\frac{\partial A}{\partial t} = (1-A^2)^{1/2}\frac{(1-A)B_l}{L_i h_0} \tag{2.39}$$

where h_0 is the thickness of ice growth in a lead. When B_l is greater than zero, all of the heat gained in the lead is used for melting sea ice from below using Equation 2.38. Additionally, it should be noted that other thermodynamic processes that the sea ice model includes are the storage of latent heat in brine pockets trapped in ice and the formation of snow ice under excessive loading.

2.3.3 Ice-Ocean Coupling

Sea ice provides a flux of momentum, salt and heat into the upper ocean. Therefore, the ocean model (OPA) and sea ice model (LIM2) must communicate and be coupled together. The sea ice model determines the surface boundary conditions of the upper ocean and the ocean model supplies the exchange of sensible heat at the ice-ocean interface. The net shortwave radiation at the ocean surface (Q_{swo}) will therefore be expressed as:

$$\begin{aligned} Q_{swo} &= AQ_{swbi} + (1-A)(1-\alpha_w)Q_{sw} \\ Q_{swbi} &= i_0(1-\alpha_{sf})Q_{sw}^{[-1.5(h_i-0.1)]} \end{aligned} \tag{2.40}$$

where Q_{swbi} is the shortwave radiation reaching the base of the ice cover, and α_w is the albedo of the open ocean (0.066).

As previously mentioned in Section 2.1.2, at the surface ocean, if sea ice is present the temperature of the surface is set to freezing point. If the ocean surface gains heat, the ocean model will supply the exchange of sensible heat to the ice. For the salt flux, the changes in sea ice contribute to the ocean surface:

$$\begin{aligned} Q_{salt} = S_m\left(\frac{\partial m_s}{\partial t}\right)_{abl} &+ (S_m - S_i)\left(\frac{\partial m_i}{\partial t}\right)_{acc-abl} \\ +(S_m - S_i)\left(\frac{\partial m_s}{\partial t} + \frac{\partial m_i}{\partial t}\right)_{si} &+ S_i\left(\frac{\partial m_s}{\partial t}\right)_{si} + S_m(AE - P_w) \end{aligned} \tag{2.41}$$

where S_m is the salinity of the mixed layer and S_i is the salinity of sea ice (6.0), m_s and m_i are the masses of snow and ice per unit area, E is the evaporation rate over the lead area, and P_w is the contribution of precipitation via rain and snow falling into open water and melting sea ice). The first term on the right-hand side is snowmelt, the second term is ice melt, the third term is salt rejection, the fourth term is an artificial flux which provides meteoric ice with adequate salinity, the fifth term is the balance between evaporation and precipitation.

2.4 Parameter List

Ocean Model Physical Constants

Symbol	Value	Description
g	9.8 m/s^2	acceleration of gravity
ρ_o	1026 kg/m^3	reference density of sea water
A_l^T	300 m/s^2	lateral eddy diffusivity coefficient
A_v^m	10^{-4}m^{2}s^{-1}	vertical eddy viscosity coefficient
A_v^T	10^{-5}m^{2}s^{-1}	vertical eddy diffusivity coefficient
C_D	10^{-3}	bottom drag coefficient
e_b	2.5×10^{-3} m^{2}s^{-2}	bottom turbulent kinetic energy
γ	0.1	Asselin coefficient

Icebergs Module Physical Constants

Symbol	Value	Description
ρ	850 kg/m^3	density of icebergs
$\tilde{T}$	-4 ^{o} C	temperature of an iceberg
$c_{a,v}$	1.3	atmospheric vertical drag coefficient
$c_{a,h}$	0.0055	atmospheric horizontal drag coefficient
$c_{o,v}$	0.9	ocean vertical drag coefficient
$c_{o,h}$	0.0012	ocean horizontal drag coefficient
$c_{i,v}$	$c_{o,v}$	sea ice vertical drag coefficient

Sea Ice Model Physical Constants

Symbol	Value	Description
P^*	2.3×10^4N/m^2	sea ice strength
C	20	sea ice strength parameter
ρ_i	900 kg/m^3	density of sea ice
ρ_s	300 kg/m^3	density of snow
c_p	2093 J/kg/K	specific heat capacity of sea ice
k_i	2.0344 W/m/K	thermal conductivity for sea ice
k_s	0.0398 W/m/K	thermal conductivity for snow
α	0.95	surface albedo for sea ice
α_w	0.066	albedo of the open ocean
ε	0.97	emissivitiy
σ	5.67×10^{-8} kg/ s^3 K^4	Stefan-Boltzmann constant
ρ_a	1.22 kg/m^3	density of the atmosphere
L	2.5×10^6 J/kg	latent heat of vaporization of water

Bibliography

Asselin, R. (1972). Frequency Filter for Time Integrations. *Monthly Weather Review*, 100(6):487–490.

Bigg, G. R., Wadley, M. R., Stevens, D. P., and Johnson, J. A. (1996). Prediction of iceberg trajectories for the North Atlantic and Arctic oceans. *Geophysical Research Letters*, 23(24):3587–3590.

Bigg, G. R., Wadley, M. R., Stevens, D. P., and Johnson, J. A. (1997). Modelling the dynamics and thermodynamics of icebergs. *Cold Regions Science and Technology*, 26(2):113 – 135.

Bouillon, S., Ángel Morales Maqueda, M., Legat, V., and Fichefet, T. (2009). An elastic–viscous–plastic sea ice model formulated on Arakawa B and C grids. *Ocean Modelling*, 27(3):174 – 184.

Fichefet, T. and Morales Maqueda, M. (1997). Sensitivity of a global sea ice model to the treatment of ice thermodynamics and dynamics. *Journal of Geophysical Research*, 102(C6):12609–12646.

Gladstone, R. M., Bigg, G. R., and Nicholls, K. W. (2001). Iceberg trajectory modeling and meltwater injection in the Southern Ocean. *Journal of Geophysical Research: Oceans*, 106(C9):19903–19915.

Griffies, S. (2004). Fundamentals of ocean climate models. *Princeton University Press*.

Hibler, W. D. (1979). A Dynamic Thermodynamic Sea Ice Model. *Journal of Physical Oceanography*, 9(4):815–846.

Hunke, E. C. and Dukowicz, J. K. (1997). An Elastic–Viscous–Plastic Model for Sea Ice Dynamics. *Journal of Physical Oceanography*, 27(9):1849–1867.

Large, W. G. and Yeager, S. G. (2004). Diurnal to decadal global forcing for ocean and sea-ice models: the datasets and flux climatologies.

Madec, G. (2008). NEMO ocean engine. *Note du Pole de modélisation*, (27).

Marsh, R., Ivchenko, V. O., Skliris, N., Alderson, S., Bigg, G. R., Madec, G., Blaker, A. T., Aksenov, Y., Sinha, B., Coward, A. C., Le Sommer, J., Merino, N., and Zalesny, V. B. (2015). NEMO-ICB (v1.0): interactive icebergs in the NEMO ocean model globally configured at eddy-permitting resolution. *Geoscientific Model Development*, 8(5):1547–1562.

Marson, J. M., C., G. L., Myers, P. G., and Le Sommer, J. (In prep). Prescribing Greenland discharge in ocean models: solid versus liquid and their corresponding impacts on the subpolar North Atlantic. *Ocean Modelling*.

Martin, T. and Adcroft, A. (2010). Parameterizing the fresh-water flux from land ice to ocean with interactive icebergs in a coupled climate model. *Ocean Modelling*, 34(3):111 – 124.

Merino, N., Sommer, J. L., Durand, G., Jourdain, N. C., Madec, G., Mathiot, P., and Tournadre, J. (2016). Antarctic icebergs melt over the Southern Ocean: Climatology and impact on sea ice. *Ocean Modelling*, 104:99 – 110.

Mesinger, F. and Arakawa, A. (1976). Numerical methods used in atmospheric models. *GARP Publication Series No. 17*, I:64.

Robert, A. J. (1966). The Integration of a Low Order Spectral Form of the Primitive Meteorological Equations. *Journal of the Meteorological Society of Japan. Ser. II*, 44(5):237–245.

Roullet, G. and Madec, G. (2000). Salt conservation, free surface, and varying levels: A new formulation for ocean general circulation models. *Journal of Geophysical Research: Oceans*, 105(C10):23927–23942.

Savage, S. (2001). *Aspects of Iceberg Deterioration and Drift*, pages 279–318. Springer Berlin Heidelberg, Berlin, Heidelberg.

Timmermann, R., Goosse, H., Madec, G., Fichefet, T., Ethe, C., and Dulière, V. (2005). On the representation of high latitude processes in the ORCA-LIM global coupled sea ice-ocean model. *Ocean Modelling*, 8(1-2):175–201.

Vancoppenolle, M., Fichefet, T., Goosse, H., Bouillon, S., Madec, G., and Morales Maqueda, M. (2009). Simulating the mass balance and salinity of Arctic and Antarctic sea ice. 1. Model description and validation. *Ocean Modelling*, 27(1):33 – 53.

Chapter 3

Drivers for Atlantic-origin waters abutting Greenland

Published in The Cryosphere (August, 2020). DOI: 10.5194/tc-14-2729-2020. Laura C. Gillard, Xianmin Hu, Paul G. Myers, Mads H. Ribergaard, and Craig M. Lee.

P.G. Myers and myself designed the study and I carried all of the analysis. X. Hu developed the model configuration and performed three of the simulations. Y. Garcia-Quintana carried out the LowResNoStorm experiment. I prepared the manuscript with contributions from all co-authors. M.H. Ribergaard and C.M. Lee. provided comments on the manuscript, with C.M. Lee also providing Davis Strait data.

Abstract

The oceanic heat available in Greenland's troughs is dependent on the geographic location of the trough, the water origin, and how the water is impacted by local processes along the pathway to the trough. This study investigates the spatial pattern and quantity of the warm water (with a temperature greater than $-1.5\,^{\circ}C$) brought to the shelf and into the troughs abutting the Greenland Ice Sheet (GrIS). An increase in ocean heat in these troughs may drive a retreat of the GrIS. Warm water that is exchanged from the trough into the fjord may influence the melt on the marine-terminating glaciers. Several regional ocean model experiments were used to study regional differences in heat transport through troughs. Results showed that warm water extends north into Baffin Bay, reaching as far north as the Melville Bay troughs. Melville Bay troughs experienced warming following 2009. From 2004 to 2006, model experiments captured an increase in onshore heat flux in the Disko Bay trough, coinciding with the timing of the disintegration of Jakobshavn Isbrae's floating tongue

and observed ocean heat increase in Disko Bay. The seasonality of the maximum onshore heat flux differs due to distance away from the Irminger Sea. Ocean temperatures near the north-west coast and south-east coast respond differently to changes in meltwater from Greenland and high-frequency atmospheric phenomena. With a doubling of the GrIS meltwater, Baffin Bay troughs transported ~ 20 % more heat towards the coast. Fewer storms resulted in a doubling of onshore heat through Helheim glacier's trough. These results demonstrate the regional variability of onshore heat transport through troughs and its potential implications to the GrIS.

3.1 Introduction

The Greenland Ice Sheet (GrIS), with the second largest storage of fresh ice on earth, has a glaciated cover of 1.81 million km^2 (Rastner et al., 2012). With the volume of ice reaching 2.96 million km^3, if the entire ice sheet were to melt, the sea level equivalent (SLE) would be ~ 7 m (Bamber et al., 2013). The GrIS recorded a maximum mass loss in 2012 with values reaching -446 ± 114 Gt/year, a SLE of $\sim 1.2 \pm 0.3$ mm/year, and has varied around ~ 1 mm/year SLE since (van den Broeke et al., 2016). Analysis of the the GrIS's mass loss and equivalent sea level rise (SLR) has shown that the GrIS has recently become a major source of global mean SLR (van den Broeke et al., 2016).

Meltwater originating off the south-west coast of the GrIS has been shown to circulate into the interior of the Labrador Sea (Böning et al., 2016; Dukhovskoy et al., 2016; Gillard et al., 2016; Luo et al., 2016). The Labrador Sea convection region is sensitive to changes in buoyancy, a balance between heat loss and freshwater input (Aagaard and Carmack, 1989; Straneo, 2006; Weijer et al., 2012). Thus, an increase in the accumulation of meltwaters in the Labrador Sea may affect and slow down deep convection (Böning et al., 2016; Weijer et al., 2012). A weakening of the deep water formation may impact the Atlantic Meridional Overturning Circulation (AMOC), influencing how the earth distributes heat, impacting sea ice production and concentration of dissolved gases such as oxygen and carbon dioxide, and altering ecosystems (Arrigo et al., 2017; Böning et al., 2016; Swingedouw et al., 2014; Weijer et al., 2012).

Numerous studies have focused on the causation of the increase in mass loss from the GrIS, such as atmospheric warming (Box et al., 2009) and synoptic wind patterns (Christoffersen et al., 2011). The annual mass balance of the GrIS has been persistently negative since the rapid retreat of marine-terminating glaciers began in 1995 (van den

Broeke et al., 2016). There are approximately 900 marine-terminating glaciers on the GrIS (Rastner et al., 2012) which drain ~ 88 % of the ice sheet (Rignot and Mouginot, 2012). Therefore, it is this type of glacier that has the greatest control over the fate of the ice sheet. Past studies have concluded that the influences affecting the dynamics of marine-terminating glaciers include glacier surface thinning (Csatho et al., 2014), glacier fjord geometry (Felikson et al., 2017; Fenty et al., 2016; Porter et al., 2014; Rignot et al., 2016a; Williams et al., 2017), state of the ice melange (Moon et al., 2015), subglacial discharge (Bartholomaus et al., 2016; Jenkins, 2011), and ocean temperature changes (Cai et al., 2017; Holland et al., 2008; Myers and Ribergaard, 2013; Rignot et al., 2016b; Straneo and Heimbach, 2013; Wood et al., 2018). Wood et al. (2018) showed that ocean warming at intermediate depths, below 200 m, has the potential to increase ocean induced undercutting.

The fluctuation of heat content in the North Atlantic Subpolar Gyre (NASPG) may have been the cause of ocean warming in fjords of marine-terminating glaciers (Holland et al., 2008; Myers and Ribergaard, 2013; Straneo and Heimbach, 2013). The NASPG contains a branch that travels northward across the North Atlantic Ocean to the West European Basins (Figure 3.1). Here, a branch travels westward, forming the Irminger Current circulating along Reykjanes Ridge. The Atlantic water that remains in the Irminger Current carries relatively warm and saline waters along the south-east coast of Greenland, while Polar waters from the Arctic Ocean and Greenland meltwaters from the East Greenland Current (EGC) and East Greenland Coastal Current merge to create a (mixed and modified) relative cold and low-saline current (Bacon et al., 2014). This current forms the West Greenland Current (WGC) near Cape Farewell. The WGC separates into two branches: one travels northward along the west coast of Greenland into Baffin Bay bringing with it both less saline, cold Polar water and relatively warm, saline, modified Atlantic water, and the second, warmer and more saline branch joins the southward flowing Baffin Island Current at Davis Strait (Fratantoni and Pickart, 2007; Myers et al., 2009). A portion of the NASPG branches off northward through the Iceland–Scotland Ridge, which separates the Norwegian Sea from the North Atlantic Ocean, as the Norwegian Atlantic Current (NwAC) (Beszczynska-Möller et al., 2012). Instead of recirculating in Fram Strait, a part of the NwAC can enter the Barents Sea, south of Spitzbergen or north through Fram Strait (Beszczynska-Möller et al., 2012). A large volume of water that travels through Fram Strait may recirculate directly in the strait and return south to the Nordic Seas (Beszczynska-Möller et al., 2012; Karcher et al., 2011). Another water source in Fram Strait may have originated from the Pacific Ocean (Aksenov et al., 2010; Hu and Myers, 2013). Pacific Water in Fram Strait is mainly the water mass entering the Arctic Ocean via the Bering Strait and delivered through the Transpolar route (Hu and Myers, 2013).

Along the shelf break of Greenland transverse troughs extend from the coast supplying warm water through to the mouths of fjords. Then depending on the structure of the water mass at the mouth of the fjord and the height of the fjord's sills, warm waters can access marine-terminating glaciers and accelerating their mass loss (Cai et al., 2017; Gladish et al., 2015b; Straneo et al., 2012). If the warm waters from the NASPG can reach these transverse troughs, changes in the heat content of the NASPG may influence the state of marine-terminating glaciers on the GrIS.

This study investigates the following questions: how is the heat flux through the troughs affected by ocean model resolution? What is the mean and variability of the heat flux through the troughs around Greenland? What are the processes that drive the variability of the flux?

3.2 Methods

3.2.1 Model description

A general circulation coupled ocean–sea ice model is utilized in this study. The fundamental modelling framework used is the Nucleus for European Modelling of the Ocean (NEMO) version 3.4 (Madec, 2008). The ocean component is based on Ocean Parallelise (OPA) and is used for ocean dynamics and thermodynamics. For sea ice dynamics and thermodynamics, Louvain la Neuve Ice Model (LIM2) is used (Fichefet and Morales Maqueda, 1997). The regional domain for the coupled ocean–sea ice model covers the Arctic and Northern Hemisphere Atlantic Oceans (ANHA), with two open boundaries: one at the Bering Strait and the other at the latitude of 20°S. All simulations start from January 2002 and are integrated to December 2016.

Initial and monthly open boundary conditions (temperature, salinity, horizontal velocities, and sea surface height) are derived from the $^1/_4{}^\circ$ Global Ocean Reanalyses and Simulations (GLORYS2V3) product (Ferry et al., 2008). The surface atmospheric forcing fields (10 m surface wind, two metre air temperature and humidity, downward shortwave and longwave radiation, and total precipitation) with a temporal resolution of one hour and spatial resolution of 33 km, are from the Canadian Meteorological Centres Global Deterministic Prediction System Reforecasts (CGRF), provided by

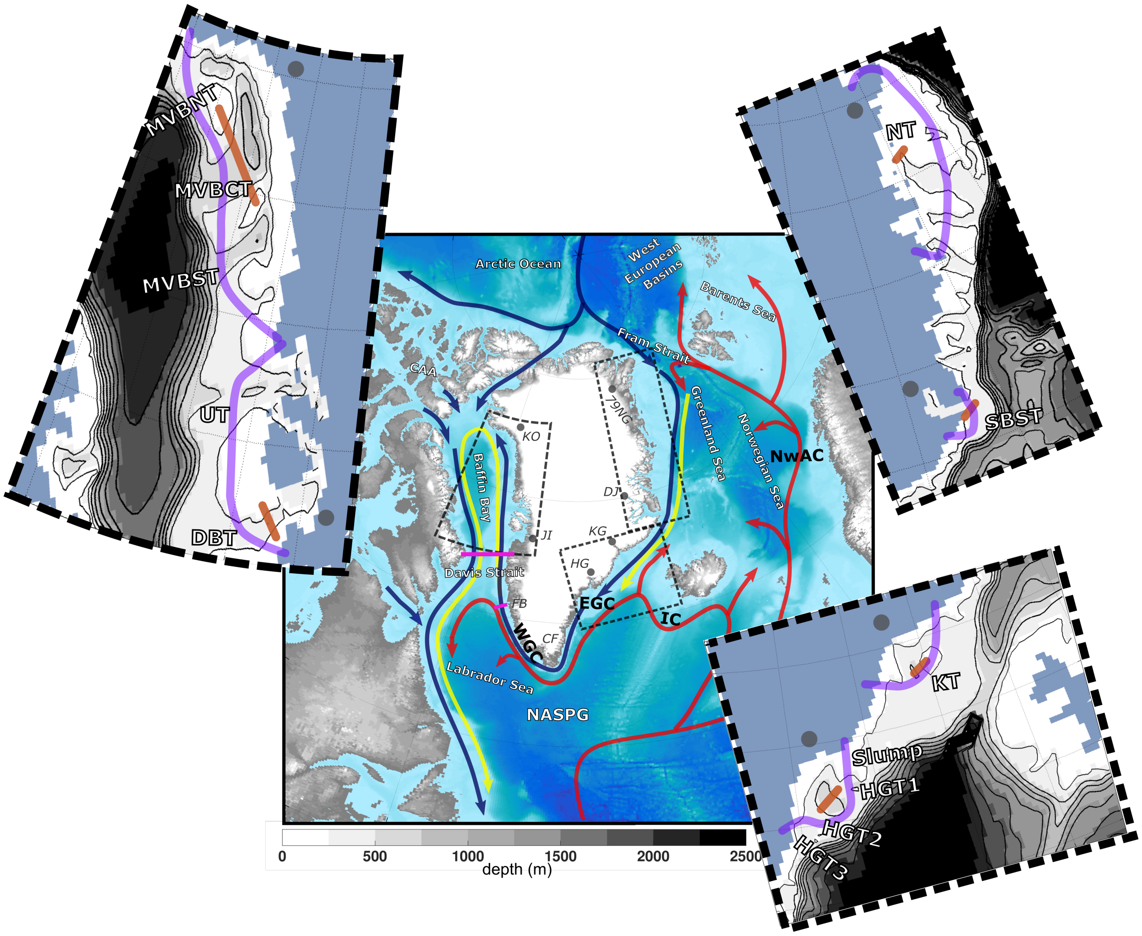

Figure 3.1: Ocean circulation around Greenland with relatively warm Atlantic waters are shown in red, modified Atlantic waters in yellow and the Arctic and freshwater pathways in blue lines. The large map's bathymetry and topography was generated using the ETOPO2v2 dataset (National Geophysical Data Cente, 2006). This map shows areas that will be discussed throughout this study such as the North Atlantic Subpolar Gyre (NASPG), Labrador Sea, Davis Strait (section drawn in magenta), Baffin Bay, Canadian Arctic Archipelago (CAA), Arctic Ocean, West European Basins, Norwegian Sea, Greenland Sea, Fram Strait, Cape Farwell (CF), and Fylla Bank (FB) (section drawn in magenta). Ocean currents (adapted from Hu and Myers (2013); Straneo et al. (2012)) that will be discussed are shown here, Irminger Current (IC), Norwegian Atlantic Current (NwAC), East Greenland Current (EGC), and West Greenland Current (WGC). The light grey circles show the locations of six marine-terminating glaciers. Kong Oscar (KO) that terminates into Melville Bay (MVB), Jakobshavn Isbrae (JI) that terminates into Disko Bay (DB), Helheim Glacier (HG), Kangerlussuaq Glacier (KG), Daugaard-Jensen Glacier that terminates into Scoresby Sund (SBS) and Nioghalvfjerdsbrae (79NG). The insets show a closer view of specific regions around Greenland. Starting from the top left, the west, south-east, and north-east coast. The insets show the model coastline, model bathymetry in metres (in grey shading and black contours), six sections of our analysis along the shelf in light purple, and sections of troughs (tan lines).

Environment and Climate Change Canada (Smith et al., 2014). The first two years of the model output are regarded as the adjustment from the initial GLORYS2V3 fields, which have already had over 10 years to evolve. Figure 3.2 shows the monthly summation of total kinetic energy (KE) in all layers of Baffin Bay, for the two experiments that will be discussed in detail in the next section, LowResControl and HighRes (Figs. 3.2a and b). The KE is low at the model start (January 2002) and increases abruptly after 2004 for the LowResControl experiment. For HighRes, the KE is fairly comparable for all years. HighRes also has more than an order of magnitude higher KE values compared to LowResControl. Figure 3.2 suggests that the spin-up of the large scale Baffin Bay circulation from the initial conditions takes one to two years, although it would take much longer for the deep layer and the interannual variation is not considered. Thus, only five–day averaged model output from 2004 to 2016 are analyzed in this study.

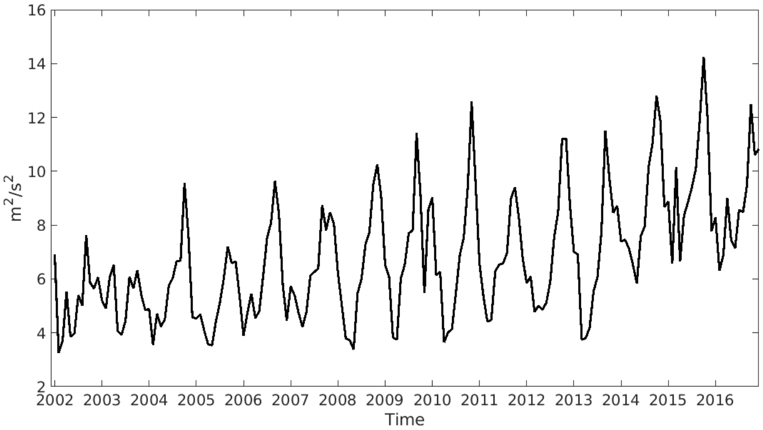

LowResControl (a)

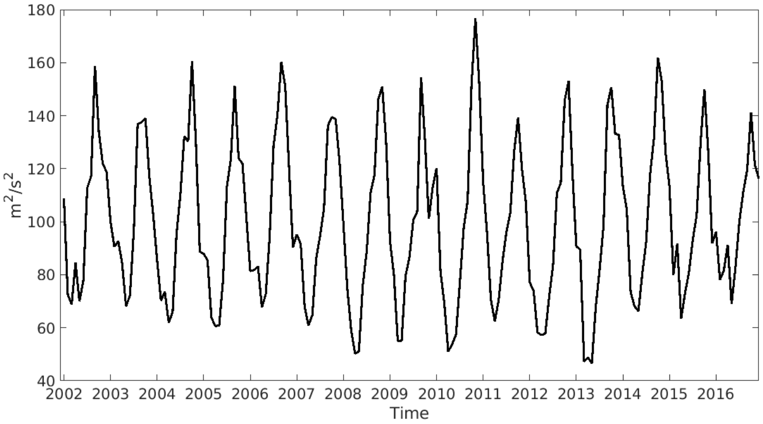

HighRes (b)

Figure 3.2: Monthly summation of total kinetic energy in Baffin Bay for two experiments, LowResControl and HighRes.

3.2.2 Sensitivity experiment set-up

Control experiment

The ANHA horizontal mesh grid is extracted from a global tripolar grid, ORCA (Barnier et al., 2007), at a $^1/_4{}^\circ$ resolution (hereafter referred to as LowResControl for low resolution) with a resolution ranging from $\sim$ 11 km to $\sim$ 15 km around Greenland. In the vertical, the LowResControl configuration uses the geopotential or z–level coordinate with a total of 50 levels. The layer thickness increases from 1.05 m at the surface level to 453.1 m in the last level (at a depth of 5958.3 m). Vertical high resolution is applied to the upper ocean, i.e., 22 levels for the top 100 m. Partial step (Bernard et al., 2006) is also enabled to better represent the sea floor. Bathymetry in LowResControl is taken from the existing global ORCA025 bathymetry (MEOM, 2013), which is based on a global relief model (ETOPO1) (Amante and Eakins, 2009) and a gridded bathymetric data set (GEBCO) (BODC, 2008) with modifications (Barnier et al., 2007).

This study will focus on the relatively large scale processes outside of the fjords (as fjords are not resolved in this configuration) with an assumption that meltwater will reach the ocean surface once out of the fjord (Figure 3.3). This assumption defines how Greenland discharge is added in the model, injected at the surface level then mixed into a 10 m thick layer. This approach is common in the present generation of ocean models at this horizontal scale, such as in Castro de la Guardia et al. (2015) and Dukhovskoy et al. (2016). Observations (Beaird et al., 2017, 2018) have shown that freshwater may not only be at the surface but be mixed and entrained with ambient waters and find a neutral buoyancy at depth. Therefore this stratification assumption in this model may be misrepresenting plume dynamics that occur in fjords and may need to be rethought in future studies.

The LowResControl simulation uses two interannual monthly runoff sources. Greenland's freshwater flux (tundra and ice sheet runoff) is provided by Bamber et al. (2012) for 2002 to 2010, and the 2010 runoff is repeated for the last 6 years of this study. The ice sheet runoff includes surface melt and melt at the front edge of a glacier. Runoff in the rest of the model domain (not including Greenland) is provided by Dai et al. (2009). The model used in this study does not have an iceberg module and so only the ice sheet and tundra runoff are included of Greenland's freshwater flux ($\sim$ 46 % of the total (Bamber et al., 2012)).

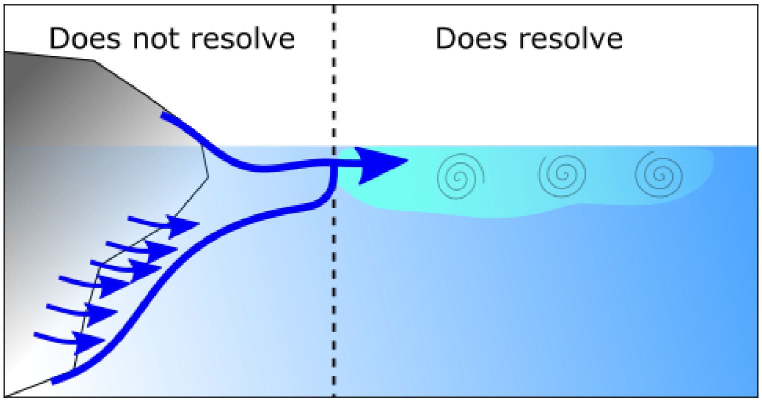

Figure 3.3: The schematic shows how the model injects meltwater. The left side of the figure shows what the model cannot resolve. This includes a glacier, small scale melting from the glacier, and the plume dynamics that occur along the face of the glacier. Instead, the model resolves larger-scale processes that occur along the coastline, and therefore, injects the meltwater from the GrIS at the first ocean model layer at the surface, which then is mixed over a thickness of 10 m.

Changes in resolution

How is heat flux through the troughs affected by ocean model resolution? A $^1/_{12}{}^\circ$ horizontal mesh grid is extracted from a global tripolar grid, ORCA (Barnier et al., 2007) (hereafter referred to as HighRes for high resolution) with a resolution ranging from ~ 3.5 km to ~ 5 km around Greenland. The vertical resolution remains identical to the LowRes, however, the HighRes bathymetry is built based on partly different sources. The bathymetry is generated by using ETOPO1 (Amante and Eakins, 2009) for the polar region, and the Global Predicted Bathymetry (Smith and Sandwell, 1997) from satellite altimetry and ship depth soundings for the rest of the domain. Therefore, given the difference in the sources of bathymetry data, downscaling HighRes will not reduce to LowRes. The HighRes configuration provides model fields at a finer scale that is not always visible in LowRes. This provides the potential for a better simulation of warm ocean currents travelling towards the GrIS via better representation of deep troughs. In addition, the model resolution also plays a role in simulating ocean mixing and mesoscale features such as eddies which bring warm water towards the GrIS shelf through the troughs. Note that, even at the $^1/_{12}{}^\circ$ resolution referred to as HighRes in this study, the majority of the fjords are still not resolved. HighRes has the same runoff and Greenland's freshwater flux setup as LowResControl. Given the numerical cost of HighRes, LowResControl is utilized for the sensitivity experiments.

Enhanced Greenland discharge experiment

How can changing Greenland's freshwater flux impact the heat flux through the troughs around Greenland? As Castro de la Guardia et al. (2015) showed, enhanced Greenland melt can change nearby ocean circulation, e.g., spinning up the circulation in Baffin Bay. Here we compare a pair of experiments (LowResControl and LowResDoubleMelt) with the more realistic spatial distribution and temporal varying Greenland freshwater flux to quantify the impact on warm waters flowing towards the marine-terminating glaciers through troughs.

LowResControl under-represents the total of Greenland's freshwater flux. Therefore, LowResDoubleMelt takes into account the solid mass discharge. LowResDoubleMelt has the identical setup as LowResControl, except for Greenland's freshwater flux. It is important to note that the entire solid discharge in LowResDoubleMelt is transformed into the liquid component (i.e., treated the same as the runoff). In addition, the ocean does not affect GrIS melting as the melting is prescribed and non-interactive. This results in roughly twice as much freshwater flux (hereafter called meltwater) (100 % Greenland's freshwater flux, broken down by $\sim$ 46 % runoff and total iceberg discharge $\sim$ 54 %) in LowResDoubleMelt compared to LowResControl (roughly 46 % of Greenland's freshwater flux, only including runoff). Therefore, the total meltwater added to LowResDoubleMelt had been roughly doubled and actually has a more realistic amount of meltwater than LowResControl. For this study, a comparison of the GrIS meltwater is made to demonstrate the ocean model's sensitivity to increased GrIS melt. How will ocean temperatures in troughs that terminate into Baffin Bay be impacted by an increase in GrIS melt?

High-frequency atmospheric event experiment

Previous studies (Garcia-Quintana et al., 2019; Holdsworth and Myers, 2015), have shown that high-frequency atmospheric phenomena, such as storms, barrier winds, fronts, and topographic jets, play an important role in ocean processes (e.g., deep convection in the Labrador Sea) in the study area. Jackson et al. (2014) reported that synoptic events can impact water properties and heat content within two large outlet fjords. Therefore they could impact shelf exchange and the renewal of warm waters to the GrIS. This study aims to go beyond Jackson et al. (2014)'s two fjords by considering the entire coast of Greenland.

We use the Kolmogorov–Zurbenko (KZ) filter method (Zurbenko et al., 1996) as

Table 3.1: ANHA-NEMO simulations used in this study. All experiments include interannual river discharge from Dai et al. (2009) except for the Greenland region, which is obtained by the Greenland Ice Sheet Freshwater Flux (GrIS FWF) provided by Bamber et al. (2012). All simulations use the same atmospheric forcing, CGRF (Smith et al., 2014), but with the winds and air temperature filtered in LowResNoStorms.

Simulation	**Resolution**	**Runoff**	**Atmospheric forcing**
LowResControl	$1/4^o$	50 % GrIS FWF	CGRF
HighRes	$1/12^o$	50 % GrIS FWF	CGRF
LowResDoubleMelt	$1/4^o$	100 % GrIS FWF	CGRF
LowResNoStorms	$1/4^o$	50 % GrIS FWF	CGRF Filtered

Eskridge et al. (1997) has shown that this filter has the same level of accuracy as the wavelet transformation method, however, is much easier to use. The KZ filter is based on an iterative moving average that removes high-frequency variations. We apply the moving average over a length of 10 days with one iteration as Garcia-Quintana et al. (2019) has done. Therefore, the removal of atmospheric variability that persisted for 10 days or less from the atmospheric forcing was done to drive a sensitivity simulation, called LowResNoStorms. LowResNoStorms has an identical setup as LowResControl, except for the KZ filter applied in the wind and air temperature fields. For more information regarding the methodology of the KZ filtering, please see Zurbenko et al. (1996) and Eskridge et al. (1997). A complete list of simulations used in this study is given in Table 3.1.

3.2.3 Mean flow and its fluctuation

To evaluate the ocean's heat that reaches onto the shelf and into the troughs, heat fluxes are calculated at six sections along the coast of Greenland (across one trough per section, as shown in purple and tan, respectively, in Figure 3.1). Section names and their associated trough names are seen in Figure 3.1. To calculate the fluctuation of the heat flux, the five-day average model output of both temperature (T) and velocity (U) normal to the section are treated as the full current. A moving average (Equation 3.2) was applied by averaging five model outputs (25 days) centered on a particular output (n) by taking outputs from two previous ($(n-2)$ and $(n-1)$), the centered (n), and two future ($(n+1)$ and $(n+2)$). A test has been previously done (not shown) for different averaging timescale of 85 days (roughly three months) and 185 days (roughly six months) and found that the different timescale averaging did not significantly change the results. Therefore, the mean of the temperature and velocity ($\overline{T}$, $\overline{U}$) have been taken over 25 days. The mean values were then subtracted from the full current to get the fluctuation component of the heat flux in Equation (3.3). Given Equation (3.3), ρ_0 is the reference density, Cp is the specific heat capacity of seawater, L is the length along the section direction x, $H(z,x)$ is the water depth along the section, and $U(t,z,x)$ is the velocity normal to the section.

To determine heat content and heat transport, a reference temperature has to be used. We considered using 0^oC, given glacial ice is fresh and 0^oC is the melting point for freshwater ice. However, there is a strong dependency on the freezing point on salinity and pressure. The boundary layer salinity is in general, not zero (Holland and Jenkins, 1999). Further, the pressure dependence of the freezing point is significant; even for freshwater at $\sim$ 700 m, the freezing point drops by half a degree. Thus, following a suggestion from a reviewer, and assuming moderate boundary layer salinities, we choose a reference temperature of $T_{ref} = -1.5^oC$ (271.65 K). Where there is little below-zero water, the choice of reference temperature will not make much difference. Where there are significant amounts of below-zero water, such as off north-east Greenland, our estimates then become a potential upper bound on the amount of heat available for glacial melting, assuming salinity and pressure have depressed the glacial freezing point from 0^oC. Therefore, T is the temperature in Celsius with T_{ref} taken into account and T_0 is the original model temperature field (Equation 3.1).

$$T = T_0 - T_{ref} \tag{3.1}$$

$$(\overline{U},\overline{T})_n = \frac{1}{5}\sum_{j=n-2}^{n+2}(U,T)_j \tag{3.2}$$

$$HeatFlux_{eddy}(t) = \rho_0 Cp \int_0^L \int_0^{H(x)} U(t,z,x)T(t,z,x) - \overline{U}(t,z,x)\overline{T}(t,z,x)dzdx \tag{3.3}$$

To see the importance of the fluctuation component of the flow around Greenland, the transient kinetic energy (TKE) was calculated using Equation (3.4). u and v are the five-day averaged model outputs of the zonal and the meridional velocity and $\overline{u}$ and $\overline{v}$ denotes the monthly mean averages.

$$TKE = \frac{(\overline{u^2} - \overline{u}^2) + (\overline{v^2} - \overline{v}^2)}{2} \tag{3.4}$$

3.2.4 Model evaluation

To continue with this study, a comparison was done to make sure that the model behaves similar to observations for West Greenland waters. The water mass structure at Fylla Bank is compared to observations from Ribergaard (2014). This section is chosen, as the WGC branches shortly after passing Fylla Bank, with a portion moving westward and joining the Labrador Current while the other portion continues north through Davis Strait. The Fylla Bank section is shown with a magenta line in Figure 3.1 (red in Figure 1 in Ribergaard (2014)). The observed temperature and salinity for June 14th, 2013 (Figure 31 in Ribergaard (2014)) are compared to the modeled averages for June 2013 (Figure 3.4). LowResControl (Figure 3.4a) had a similar water mass structure as the observations. In both observations and LowResControl, there was cooler water at the surface with a thickness of 50 m offshore and about 100 m thick, just off the west side of the bank (kilometre marker 45 in Figure 3.4a), with warmer water (greater than $3\,^{\circ}C$) below 100 m depth. The cold water layer in the LowResControl was slightly saltier with the depth of the modelled 34.2 isohaline similar to that of the observed 34 isohaline (Figure 31 in Ribergaard (2014)). For HighRes, the cold surface layer was thicker (Figure 3.4b) than in observations, where the $2\,^{\circ}C$ layer (contour in magenta) extended to about 100 m depth off the west side of Fylla Bank at kilometre marker 45. Similar to observations the $4\,^{\circ}C$ and warmer water mass starts below 200 m and slopes upwards towards the west. At a depth of $\sim$ 400 m HighRes is warmer than observations by $\sim\, 1\,^{\circ}C$. Overall, the modelled water mass structure compared well with the observations but with minor offsets in temperature and salinity. The model had a shallow fresh and colder surface layer in the west portion of the section that deepened towards Fylla Bank. Finally, the HighRes configuration had a much sharper and better-represented thermocline compared to the LowResControl configuration.

Moving northward to Davis Strait, the primary gateway for meltwater and heat exchange between Baffin Bay and the North Atlantic Ocean, we look at the model and the observations. A comparison was done with LowResControl and HighRes to the Curry et al. (2014) moored array data (see Figure 2 in Curry et al. (2014)). The monthly modelled temperature averaged over 2004 – 2010 at Davis Strait (Figure 3.5 and Figure 3.6) was compared to the mooring observations (Curry et al. (2014), their Figure 3(c)). July through to September LowResControl (Figure 3.5) captured the same structure of the West Greenland Slope Water (WGSW) and West Greenland Irminger Water (WGIW) as in the Curry et al. (2014) study. See Table 3.2 for water mass characteristics in Davis Strait. From March to June LowResControl showed WGIW and WGSW

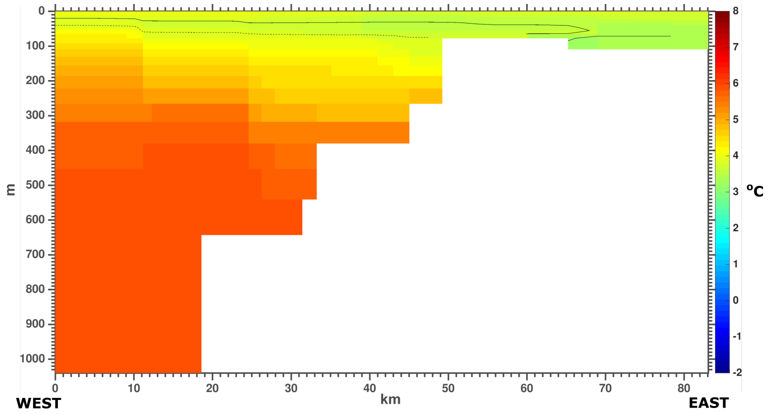

(a) LowResControl

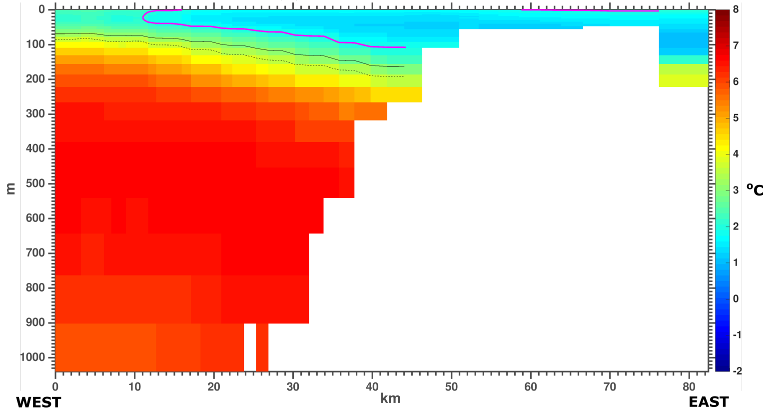

(b) HighRes

Figure 3.4: Average Fylla Bank temperature for June 2013 for (a) LowResControl and (b) HighRes. The magenta line shows the $2\,^{\circ}C$ isotherm, the black line is the 34.0 salinity isohaline, and the blacked dashed line is the 34.2 salinity isohaline.

cooler ($\sim 3\,^{\circ}C$) by about a degree than that of the observations ($\sim 4\,^{\circ}C$). LowResControl also had a tongue of relatively warm water from the WGIW protruding into the interior of Davis Strait at $\sim$ 200 km and $\sim$ 200 m depth. For HighRes (Figure 3.6), the structure was similar to that of LowResControl, with the protruding tongue at $\sim$ 200 km and $\sim$ 200 m depth. HighRes also had a similar structure to the observations for the WGSW from July to October. Note that compared to observation, the WGSW and WGIW seem to be about $1\,^{\circ}C$ warmer.

Table 3.2: Overview of Davis Strait's water masses. Potential temperature (θ) and salinity (S) characteristics are defined by Curry et al. (2011).

Davis Strait Water Masses	**Temperature Range**	**Salinity Range**
Polar Water	$\theta \leq 1^\circ C$	$S \leq 33.7$
West Greenland Irminger Water	$\theta > 2^\circ C$	$S > 34.1$
West Greenland Slope Water	$\theta < 7^\circ C$	$S < 34.1$
Transitional Water	$\theta \leq 2^\circ C$	$S > 33.7$

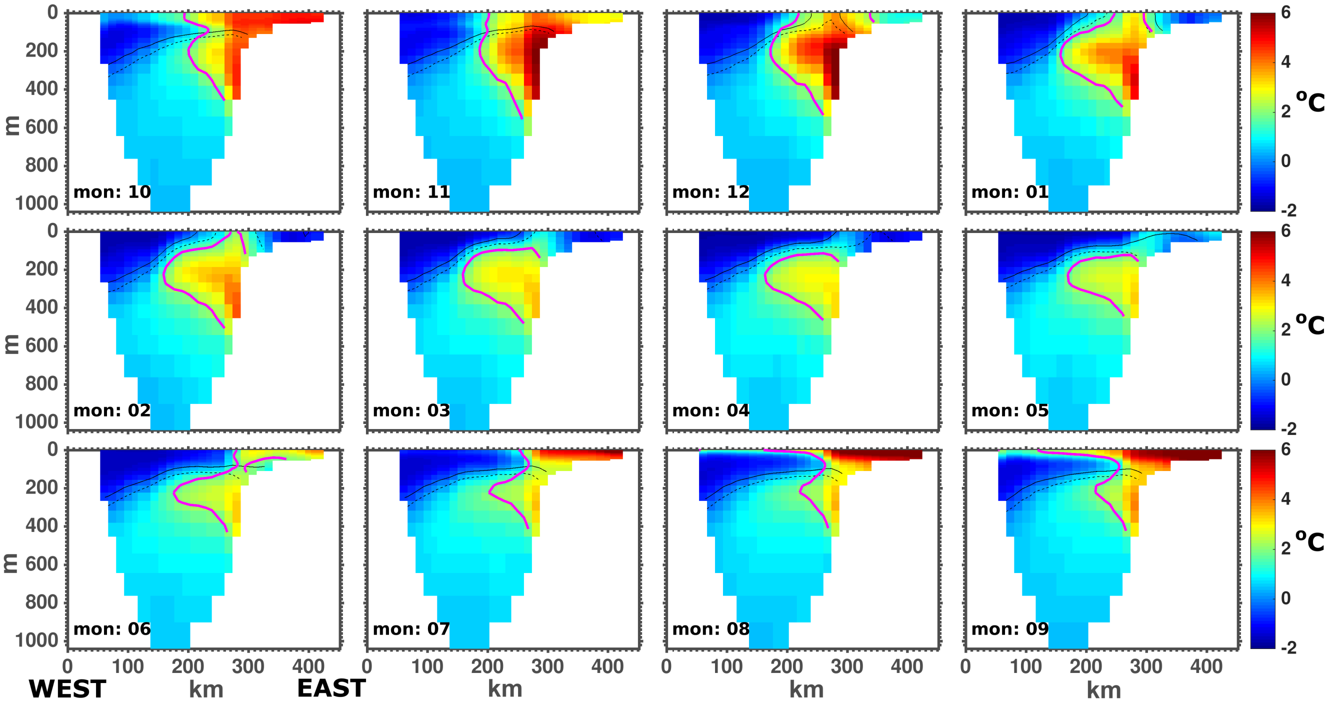

Figure 3.5: The monthly average temperature through the period of 2004 to 2010 at Davis Strait from LowResControl. The magenta line represents the $2^\circ C$ isotherm, the black line is the 34.0 salinity isohaline, and the blacked dashed line is the 34.2 salinity isohaline.

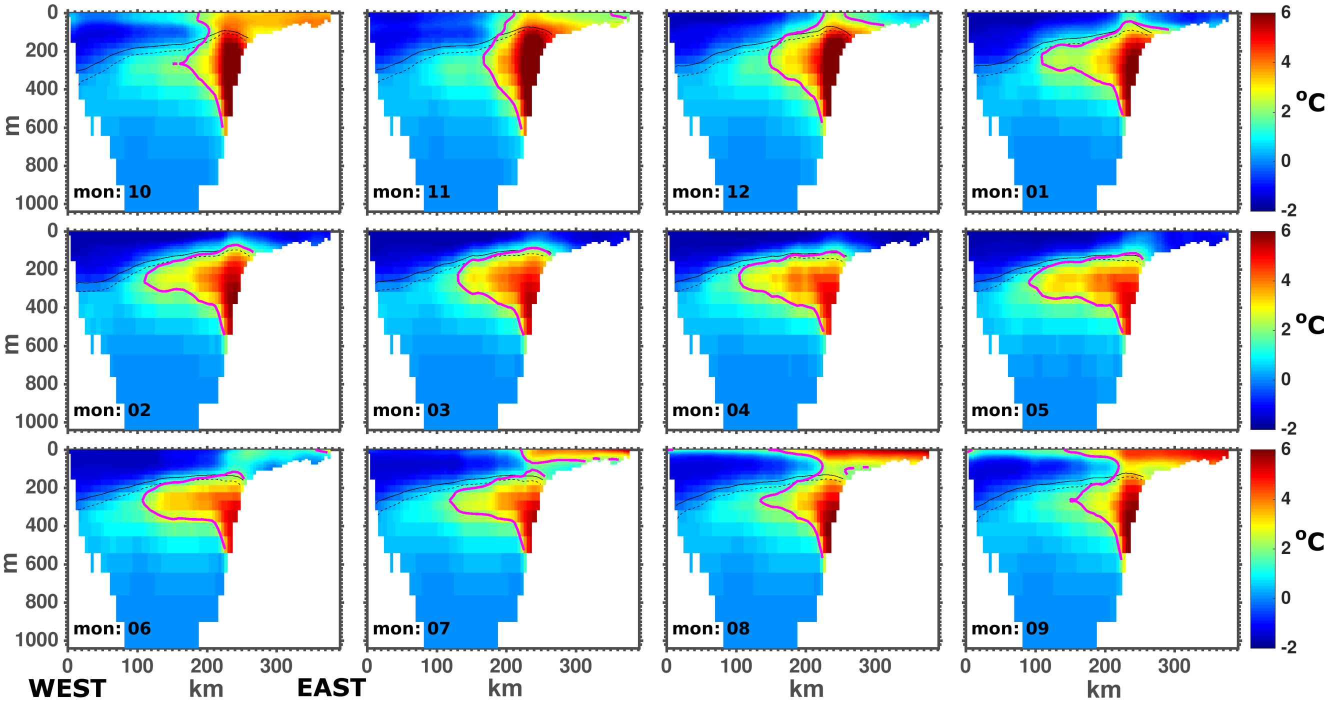

Figure 3.6: The monthly average temperature through the period of 2004 to 2010 at Davis Strait from HighRes. The magenta line represents the 2°C isotherm, the black line is the 34.0 salinity isohaline, and the blacked dashed line is the 34.2 salinity isohaline.

Curry et al. (2011) plotted a TS diagram (their Figure 3) showing the main water masses (Table 3.2) at Davis Strait, based on September 2004 and 2005 data along the mooring line. Curry et al. (2011)'s plot is repeated using all September and October observational data collected within $\sim$ 30 km of the Davis Strait sill, as part of the Davis Strait program, from 2004 to 2010 (Figure 3.7). Although the result is denser, the same general structure as in Curry et al. (2011) can be seen. HighRes and LowResControl are plotted similarly (September and October fields, for the same region as the observations, from 2004 to 2010). HighRes shows a similar structure for the WGIW and WGSW, while LowResControl's WGSW is warmer and its WGIW doesn't show the same tail-off to lower salinities with its transitional water between $2\,^{\circ}C$ and $0\,^{\circ}C$. Both runs show Polar Water with a salinity between 32.5 and 33.5, albeit about a degree warmer than the observations, with warming to $1\,^{\circ}C$ to $2\,^{\circ}C$ as the salinity drops to 31.

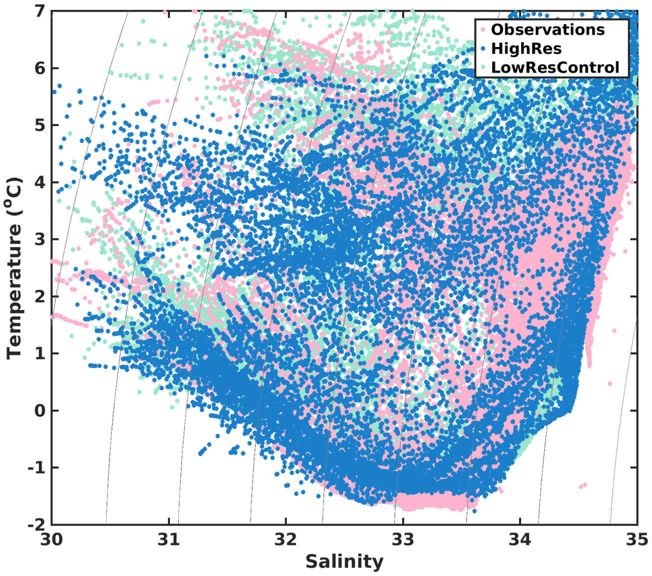

Figure 3.7: Temperature and salinity plot for the region around the Davis Strait sill ($\sim 30km$). Observations contain data collected by the Davis Strait program's fall mooring cruises. Observations are taken in fall months, late August to October, for years 2004 to 2010. Model fields are plotted the same for HighRes and LowRes Control (mid-September and mid-October fields, within $\sim 30km$ of the Davis Strait sill, from 2004 to 2010). Model fields are subsampled to a 1/2 degree grid to reduce the number of points plotted. Points with a salinity of less than 30 or more than 35, or warmer than $7\,^{\circ}C$ are excluded. Thin black curved lines are density in kg/m^3.

The LowResControl and HighRes volume transport from September 2004 to September 2013 (Figure 3.8) can satisfactorily represent the observations from the mooring array at Davis Strait (e.g. Curry et al. (2014, 2011)). Positive values indicate southward volume fluxes through Davis Strait, and negative values indicate northward transport. All model and observation output are plotted as the same 5-day average. The simulations underestimated the high-frequency peaks of transport from the observations (values approaching 6 Sv in some cases). The mean volume flux based on the Davis Strait moorings (Curry et al., 2014, 2011), calculated over the period of Sept 21, 2004, to Sept 30, 2013, is 1.6 Sv. Over the same period, the model transports are 1.2 Sv for LowResControl with a correlation of 0.54, significant at the 99 % level, and 1.2 Sv for HighRes with a correlation of 0.49. Yet many features, such as the reduction in transport at the end of 2010, are well simulated.

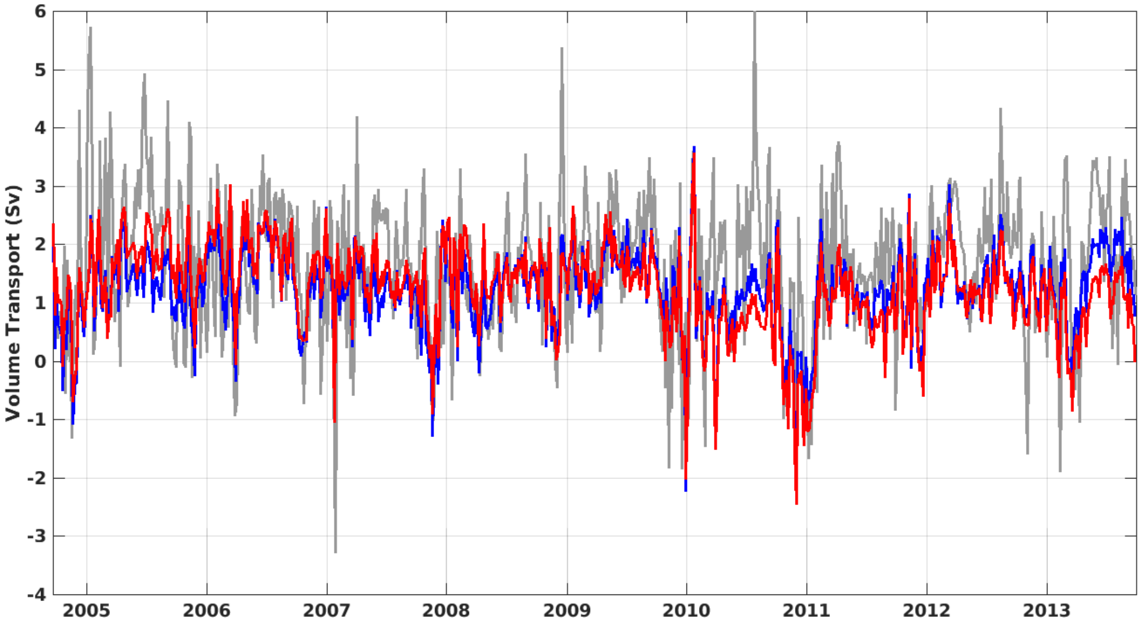

Figure 3.8: Volume flux through Davis Strait with HighRes (in red), LowResControl (in blue), and Davis Strait observations replotted from the mooring record discussed in Curry et al. (2014) (in grey). Positive values indicate southward volume fluxes through Davis Strait and negative values indicate the waters move northward. All fields, model and observation, are plotted as 5-day averages.

3.2.5 Study area

This study focuses on six sections around Greenland (Figure 3.1) with marine-terminating glaciers and deep bathymetric features. In Figure 3.9, the six sections are drawn (seen in light purple on the map inset Figure 3.1). HighRes model bathymetry is in grey and each section runs north to south on the x–axis starting at the left-hand side of the figure indicated by the zero kilometre marker. The rest of this section will compare the six sections and discuss how observed bathymetry from other studies compares to the HighRes model bathymetry (Figure 3.9).

In north-west Greenland, Kong Oscar is the fastest marine-terminating glacier, terminating into Melville Bay (Rignot and Kanagaratnam, 2006; Rignot and Mouginot, 2012). Twenty percent of the GrIS drainage volume is directed along glaciers that feed into Melville Bay, amounting to a discharge of $\sim$ 80 km^3/year (Rignot and Kanagaratnam, 2006). Located in north-east Baffin Bay (Figure 3.1), Melville Bay holds the widest and deepest Greenland cross shelf troughs. This system consists of three troughs: the North, Centre, and South Melville Bay Troughs (MVBTs: MVBNT, MVBCT, and MVBST). The MVBTs are 170 to 320 km long, 45 to 120 km wide and reach depths between 740 m to 1100 m with shallow banks (around 100 m below sea level) called inter–trough banks (Morlighem et al., 2017; Slabon et al., 2016). The HighRes bathymetry (seen in Figure 3.9a) is relatively shallow compared to the observations discussed. MVBNT is located at the kilometre markers 10 km to 120 km, MVBCT at 320 km to 450 km, and MVBST at 480 km to 580 km. The depths in the HighRes are about 400 m for MVBNT, reaching almost 700 m depth for MVBCT and MVBST.

Further south, on the west coast of Greenland, Jakobshavn Isbrae (JI) terminates into Disko Bay. The rapid retreat and disintegration of JI's floating ice tongue have been attributed to an increase in heat content, deep bathymetry, and NASPG warming (An et al., 2017; Gladish et al., 2015a; Holland et al., 2008; Myers and Ribergaard, 2013). Recent slowing down of JI's acceleration has been attributed to the glacier reaching a higher bed, high amounts of freshwater from the Canadian Arctic, a weak WGC, or a cold Baffin Bay current flooding the West Greenland Shelf and cooling in the Labrador and Irminger Seas (An et al., 2017; Gladish et al., 2015a; Joughin et al., 2012; Khazendar et al., 2019). In HighRes, the section drawn for Disko Bay (Figure 3.9b) shows two deep bathymetric features: the first trough, located at 100 km to 200 km, and the second trough at 380 km to 500 km, now called UT (Uummannaq Trough) and DBT (Disko Bay Trough), respectively. UT connects to Uummannaq Fjord and DBT connects into Disko Bay. Both UT and DBT reach depths of around 500 m, similar to observations found in Hogan et al. (2016). In a more recent data set provided by BedMachineV3, UT similarly reaches approximately 500 m but DBT is much deeper, reaching depths of 900 m (Morlighem et al., 2017).

In the south-east region, there are two major glaciers of interest: Helheim Glacier (HG) and Kangerlussuaq Glacier (KG). HG terminates at a depth of 700 m in Sermilik Fjord, which is approximately 900 m deep at the *U* shape mouth with the adjacent continental shelf, reaching depths of 350 m (Morlighem et al., 2017; Straneo et al., 2010). Temperature variability in Sermilik Fjord cannot be explained by local heating or surface fluxes. The temperature variability in the fjord is instead a result of the advection of warmer waters into the fjord, as warm waters are present on the shelf year-round, peaking from July to September (Straneo et al., 2010). In HighRes, the section for HG (Figure 3.9c) shows four unique features. The first one at kilometre marker 25 km to about 100 km shows a slumping of bathymetry reaching about 250 m in depth. Moving further south there are three deep troughs. The first trough is located at 120 km to 180 km, reaching depths surpassing 500 m, and the second and third troughs, located at 190 km to 260 km and 350 km to 375 km, respectively, reach depths closer to 700 m. Features will be referred to as Slump, HGT1, HGT2, and HGT3.

In the BedMachineV3 data set, Kangerlussuaq trough (KT) reaches depths closer to 800 m (Morlighem et al., 2017). Atlantic water occupies the deep waters of the KT and Kangerlussuaq Fjord (KF) (Azetsu-Scott and Tan, 1997). KF, similar to Sermilik Fjord has a deep open mouth, which could influence the Atlantic water transport that is observed there (Azetsu-Scott and Tan, 1997; Christoffersen et al., 2011; Inall et al., 2014). In HighRes, the section drawn for KT (Figure 3.9d) is drawn over an area with the maximum depth in the middle of the section, deeper than 600 m, at kilometre marker 175 km. The KT extends from 125 km to about 200 km.

In the north-east, Daugaard-Jensen Glacier terminates into Scoresby Sund and Nioghalvfjerdsbrae (79NG) terminates into the sound of Jøkelbugten. The BedMachineV3 shows depths of around 600 m (Morlighem et al., 2017). The HighRes section drawn for Scoresby Sund (Figure 3.9e) is outside of the opening of the coastline, from north to south, connecting fjord waters to the open ocean. The bathymetry here is smoother with fewer carved features. Instead, it shows a skewed *U* shape in this section. The maximum depth is reached at kilometre marker 120 km with a depth slightly greater than 500 m.

79NG has a floating ice tongue that abuts Hovgaard Ø, which divides the tongue into two sections (Wilson and Straneo, 2015). The most rapid melting occurs at the grounded (pinned) front, south of Hovgaard Ø, where the ice tongue is thickest and is exposed to deeper and warmer waters (Mayer et al., 2000; Seroussi et al., 2011; Wilson and Straneo, 2015). Schaffer et al. (2017) study showed that Atlantic Intermediate Water flows via bathymetric channels to the south of Hovgaard Ø at a pinned ice front, where there is a shorter pathway between the shelf and cavity, exposing the cavity to more shelf driven processes such as intermediary flows. The warm water is supplied from the warm water that resides in Norske Trough (NT) east of Hovgaard Ø (Figure 3.1) (Wilson and Straneo, 2015). Some of the relatively fresh glacially modified water is exported to the continental shelf via Dijmphna Sund, north of the glacier (Wilson and Straneo, 2015). In the BedMachineV3, NT reaches depths close to 600 m (Morlighem et al., 2017). The HighRes section drawn for 79NG (Figure 3.9f) is drawn from north to south. The HighRes bathymetry shows the deepest region exceeding depths of 300 m, though the majority of this section lies around 200 m.

3.3 Results and discussion

3.3.1 Onshore heat flux through coastal troughs

What is the significance of the deep troughs along Greenland's shelf to the supply of warm water to the fjords with marine-terminating glaciers? A look at the onshore heat flux through these troughs will be shown using HighRes, as the benefits of a higher horizontal resolution have been shown. However, given the numerical costs of the HighRes, LowResControl is utilized for the sensitivity experiments that will be discussed later in this paper.

West coast: mean state

A section was drawn for Melville Bay (Figure 3.9a), located on the north-west coast of Greenland, which shows three deep bathymetric troughs: the MVBNT, MVBCT, and MVBST (all troughs described in Sect. 3.2.5). At the north edge of all three troughs (kilometre marker 50 km, 330 km, and 500 km, for MVBNT, MVBCT, and MVBST, respectively) there is an offshore heat flux. At the south edge of all three troughs (kilometre marker 110 km, 450 km, and 560 km, for MVBNT, MVBCT, and MVBST, respectively) there is an onshore heat flux. This identified that the northward warm waters travelling along the west coast of Greenland are influenced by bathymetry and are steered eastward along the trough towards the coast.

MVBNT, the shallowest of the troughs, had the weakest onshore heat flux, barely exceeding 0 TW. MVBCT and MVBST transport increased between 2009 and 2010 and persisted in an anomalously high state for five years. For MVBNT there was an

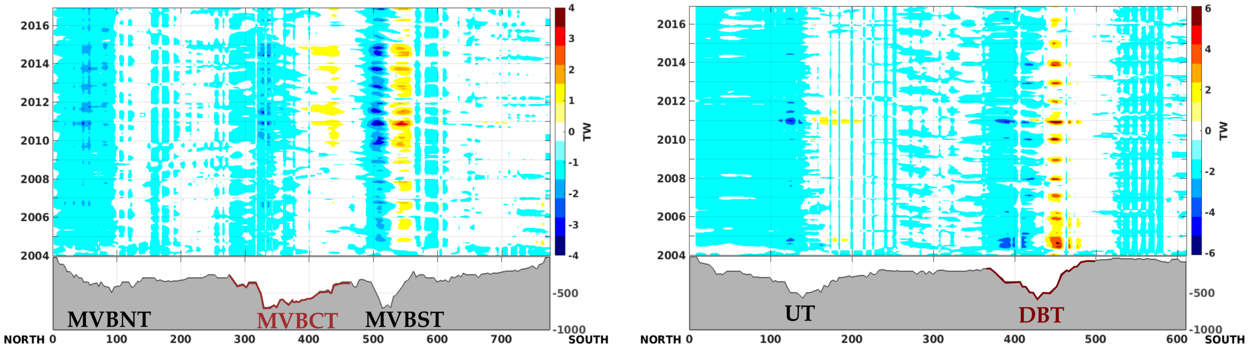

(a) Melville Bay Section (b) Disko Bay Section

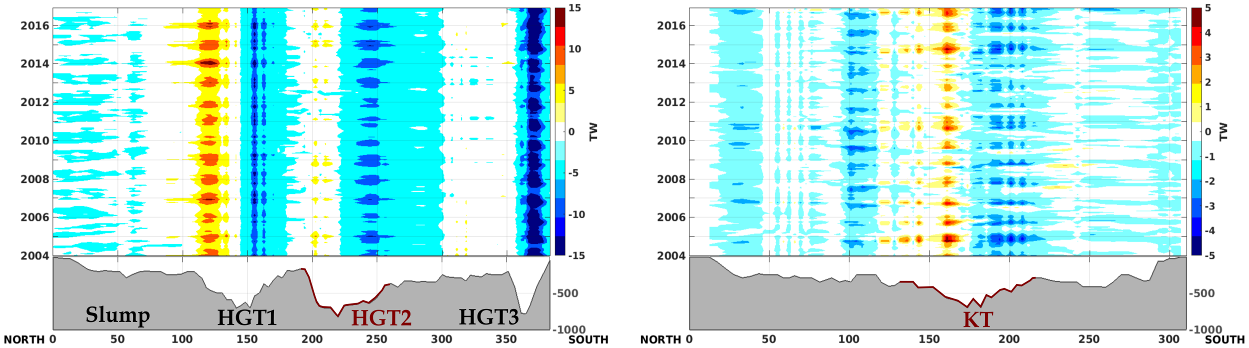

(c) Helheim Section (d) Kangerlussuaq Section

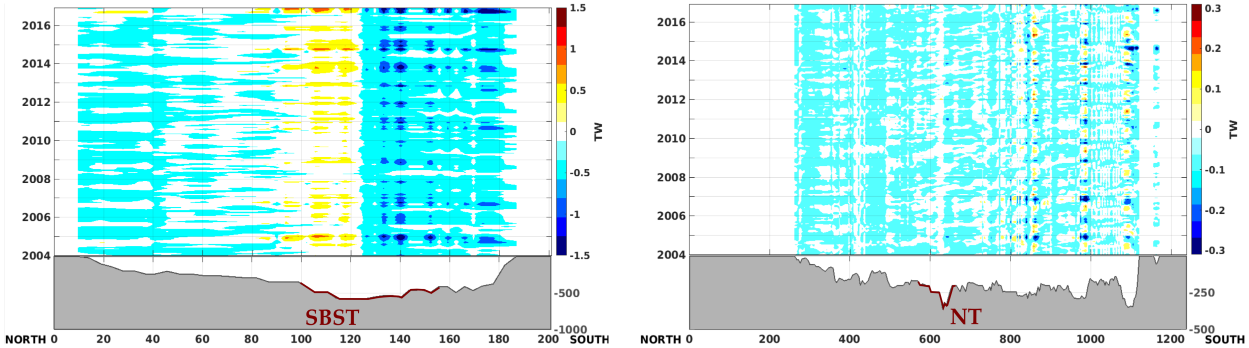

(e) Scoresby Sund Section (f) 79NG Section

Figure 3.9: This figure shows the entire ocean heat exchange (total flux) with respect to topography (in grey) within the time series of 2004 to the end of 2016 with the HighRes model output. These Hovmöller plots show the monthly average heat flux coming on or off the shelf in TW (into or out of the page respectively), through a section (sections drawn in light purple on the map inset Figure 3.1). Model bathymetry is in grey and the section runs north to south on the x-axis starting at the left-hand side of the figure indicated by the zero kilometre marker. Along the y-axis is the depth for the bathymetry and then time for the 2004 to 2016 period. Colours indicate direction and magnitude of the onshore or offshore heat flux. Positive numbers indicate the direction of onshore (into the page) and negative numbers indicate the direction of the heat flux offshore (out of the page). Colourbar limits change per location. In each section shows a highlighted trough, in dark red, which is selected for Figure 3.10 and Figure 3.11. Figure 3.1 indicates the exact location of the trough in the tan lines.

increase in onshore heat transfer for a brief period in 2010 (0.5 TW). At MVBCT an increase of heat flux started at the end of 2009 and reached a relatively stable value of 1 TW through to the end of 2015. For MVBST there was a more persistent interannual heat flux throughout the entire time period, increasing from 1 TW to 3 TW starting at the end of 2009. An increase in heat flux through troughs in northern regions of the Greenland shelf starting in 2009 for MVBCT and 2010 for MVBNT and MVBST was thus identified. A change of 1 TW is significant, as that increase in heat can potentially melt 3000 tons of ice per second. Thus, an increase in ocean heat presence in these troughs may have driven more melt from the glaciers that terminate in Melville Bay.

A section drawn for Disko Bay (Figure 3.9b), located on the west coast of Greenland, shows two deep troughs: UT and DBT. Both troughs showed an onshore heat flux at the south edge (kilometre marker about 180 km and 480 km, for UT and DBT, respectively) and an offshore heat flux at the north edge (kilometre marker 100 km to 120 km and 400 km to 420 km, for UT and DBT, respectively). This section, as well as the Melville Bay section showed that the ocean currents are influenced by the bathymetry and are steered eastward into the trough towards the coast.

There was an onshore heat flux into DBT in the early 2000s which was a consistently strong from 2004 to the end of 2007. Another increase in the heat flux (values showing 6 TW) were seen later on, reaching a maximum in 2010 and then decreased back towards 4 TW afterward. The increased heat flux in years of 2004 to 2006 coincided with the disintegration of the JI floating tongue and was within the period of observed oceanic heat increase in Disko Bay (from 1997 to 2007) (Holland et al., 2008). For UT there are pulses of onshore heat flux of about 1 TW throughout the period. Through 2010 to 2012 there are variable pulses (1 TW) with maximum in the winter of 2010–2011 with a value of 2 TW.

West coast: seasonal and interannual variation

The seasonality of the onshore heat flux is shown in MVBCT (Figure 3.10a). Late fall and early winter showed the maximum onshore heat flux with a peak in November. Through late winter to spring the onshore heat flux is weakest with the minimum in April. Years of 2004–2007, as indicated in a variety of blues in Figure 3.10, overall have less onshore heat flux. As time progressed the onshore heat flux increased. 2010, 2011 and 2014 (as indicated in colours of pale green and orange) showed the highest values of onshore heat flux reaching maximums of about 15 TW to 19 TW. This increase of heat flux indicates that more heat has been brought into MVBCT in more recent years. The lack of a summer peak at MVBCT, suggests seasonality is dominated by the subsurface warm layer. MVBCT heat flux seasonality seems to be dependent on both the seasonality of the volume flux and temperature (Figure 3.10b and Figure 3.10c), respectively, with a correlation of 0.96 and 0.89 (shown in Table 3.3).

Further south in DBT (Figure 3.10d), the fall and winter seasons have stronger onshore heat flux. However, earlier years (2004 to 2005) show above-average onshore heat flux in the summer. Maximum onshore heat flux was identified in July and August of 2004 and 2005 (reaching values around 10 TW to 15 TW). However, in other years, June and July have lower values of heat flux (hovering close to 4 TW). This warming event from 2004 to 2006 is also seen in DBT in Figure 3.9b. In 2010 there is a spike of onshore heat flux in December, reaching over 15 TW, then decreased in January (Figure 3.10d). Enhanced heat flux in 2011 is seen in UT and MVBST (Figs. 3.9a and b), indicating that the warming event is a large scale rather than a localized process. The timing of the onshore heat flux peak also undergoes large interannual variation (Figure 3.10d), which is likely driven by the volume flux of the inflow (Figure 3.10e)

Observations at Davis Strait show a temperature maximum starting around August/September continuing through to November/December (Curry et al., 2011; Grist et al., 2014). However, heat flux peaks in DBT occurred as early as June/July between 2004 and 2006 (Figure 3.10d), suggesting a larger influence from the warm surface waters in these months. As the years progressed in the model, the timing of the maximum heat flux was delayed until later in the year to between September to January, albeit with significant inter-annual variability. This timing coincided with the peak of warmest Irminger Water observed in Davis Strait. The timing was due to the advection time needed by the Irminger Sea water. Given they are farther north, the warm water reached Melville Bay later in the year than Disko Bay. This lag in the seasonal cycle of warm water is consistent with the Lagrangian trajectory-based study by Grist et al. (2014).

The results (Figure 3.10d) showed an early arrival of warm waters (June in 2004) occurred at the time when JI started to melted rapidly (Holland et al., 2008). This may, therefore, have been due to not only an increase in ocean heat flux but perhaps an arrival of warm waters earlier in the melt season impacting JI for a longer duration. DBT heat flux seasonality is more dependent on the seasonality of the temperature of the water mass and not as much as the seasonality of the volume flux (Figure 3.10f and Figure 3.10e), with a correlation of 0.64 with the volume flux and 0.83 for the temperature (shown in Table 3.3).

Table 3.3: This table shows a comparison for the entire time series (2004 to 2016) of the different troughs along the shelf of the GrIS: Melville Bay Central Trough (MVBCT), Disko Bay Trough (DBT), Helheim Glacier Trough 2 (HGT2), Kangerlussuaq Trough (KT), Scoresby Sund Trough (SBST), and Norske Trough (NT). These troughs can be identified in Figure 3.1. The second and third column shows the correlation between the heat flux with the volume flux and the average temperature ($\overline{T}$) across the section (shown in the black line in Figure 3.10). The fourth, fifth and sixth columns show the average percent of the heat flux moderated by fluctuations from three configurations, HighRes, LowResControl, LowResNoStorms. Column seven shows the correlation between the total heat flux (mean and fluctuation) from two configurations, HighRes, and LowResControl.

Troughs	**Correlations with Heat Flux**		**Percent of the Heat Flux Driven by the Fluctuations**			**Correlation between HighRes and LowResControl**
	Volume Flux	$\overline{T}$	HighRes	LowResControl	LowResNoStorms	
MVBCT	0.96	0.89	1%	1%	–	0.86
DBT	0.64	0.83	7%	6%	–	0.43
HGT2	0.95	-0.16	2%	13%	21%	0.77
KT	0.92	0.82	16%	17%	–	0.58
SBST	0.61	-0.66	76%	11%	–	0.98
NT	-0.24	0.76	24%	30%	–	0.83

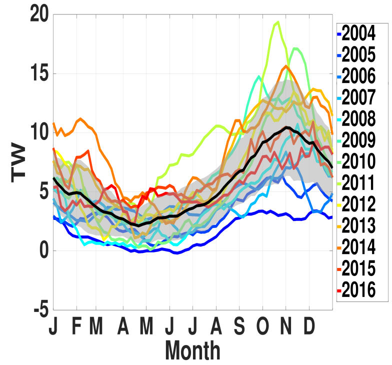

(a) MVBCT Heat Flux

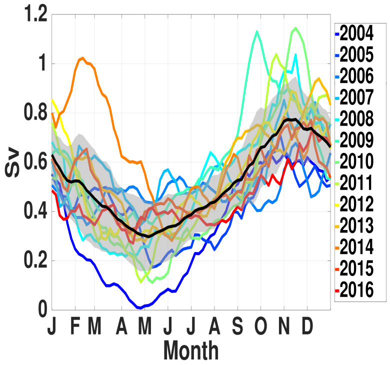

(b) Volume Flux

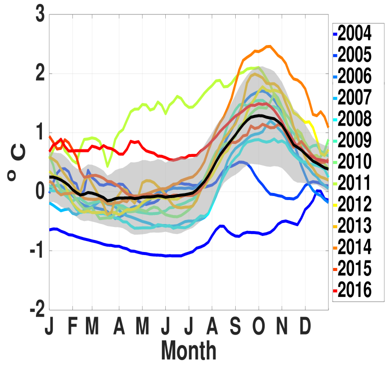

(c) Average Temperature

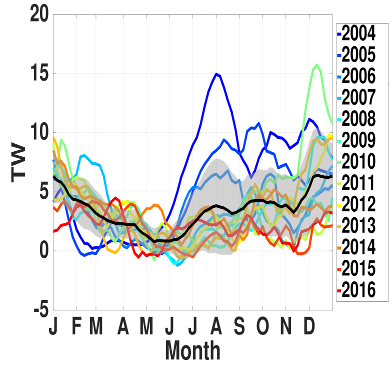

(d) DBT Heat Flux

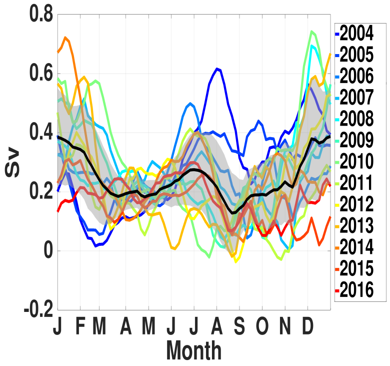

(e) Volume Flux

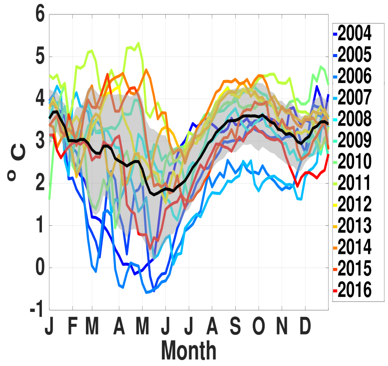

(f) Average Temperature

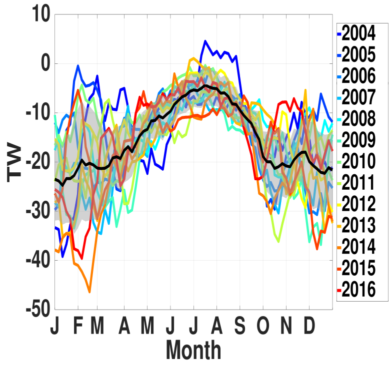

(g) HGT2 Heat Flux

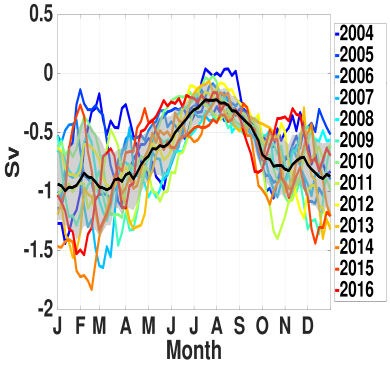

(h) Volume Flux

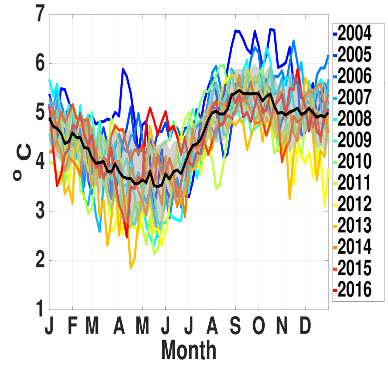

(i) Average Temperature

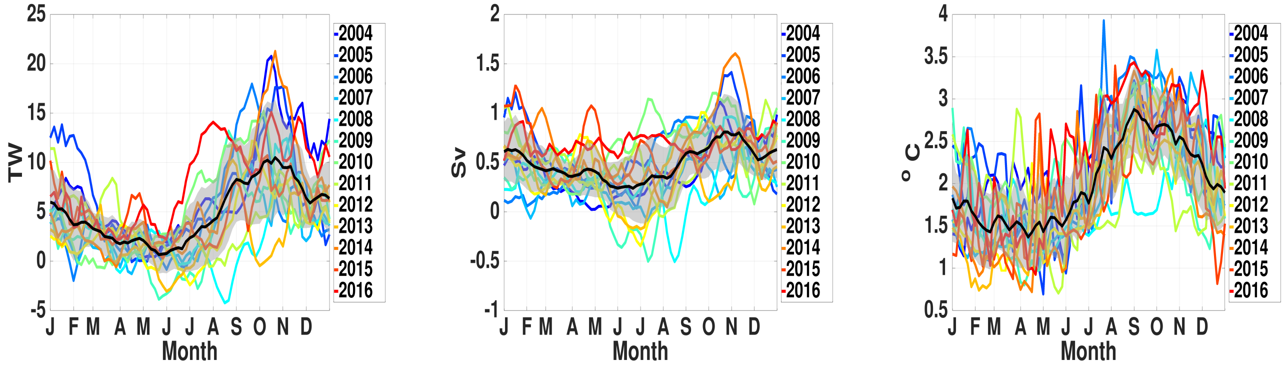

(j) KT Heat Flux (k) Volume Flux (l) Average Temperature

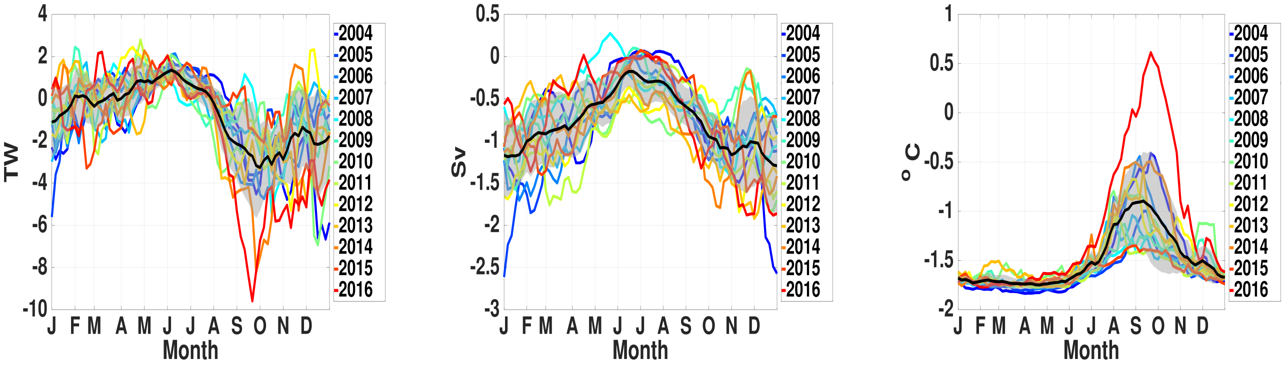

(m) SBST Heat Flux (n) Volume Flux (o) Average Temperature

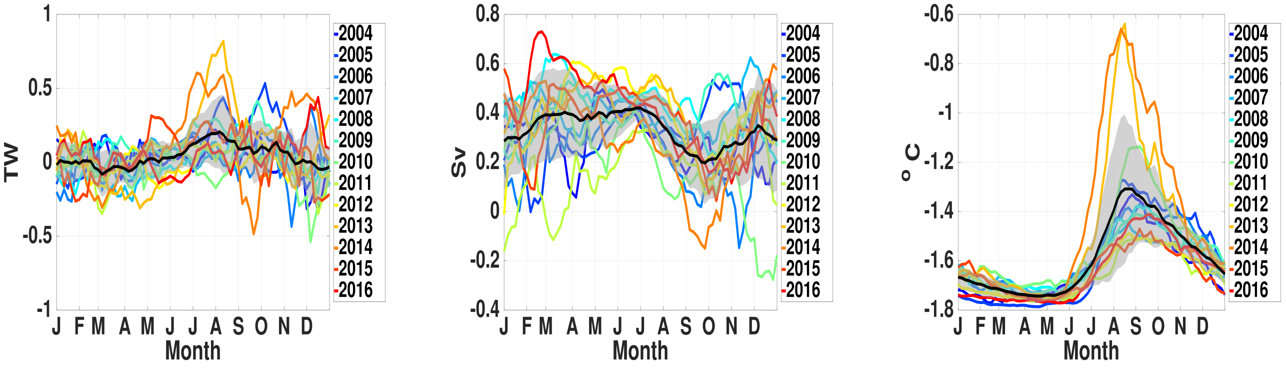

(p) NT Heat Flux (q) Volume Flux (r) Average Temperature

Figure 3.10: Seasonality of the heat flux (unit: TW, 1 TW= 10^{12} W), volume flux (unit: Sv, 1 Sv= $10^6 m^3 s^{-1}$) and section-averaged temperature (unit: $^\circ C$) in Melville Bay Central Trough (MVBCT), Disko Bay Trough (DBT), Helheim Glacier Trough 2 (HGT2), Kangerlussuaq Trough (KT), Scoresby Sund Trough (SBST), and Norkse Trough (NT) (locations shown in Figure 3.1) for each year from 2004 to 2016 (colour codes are shown in the legend). Note that the black line shows the mean of the 25-day moving window averages (Equation 3.3) over 2004 to 2016 with the standard deviation shown by the grey shading.

South-east coast: mean state

The section drawn for Helheim (Figure 3.9c) located off the south-east coast of Greenland, shows four unique features, Slump, HGT1, HGT2, and HGT3. At the north edge of the troughs in this section, HGT1 through to HGT3, (kilometre marker 100 km, 200 km, and 350 km) there is an onshore heat flux, and an offshore heat flux at the south edge (kilometre marker 175 km, 225 km, and 355 km). This identifies that there must be southward flowing warm water travelling along the south-east coast of Greenland, potentially drawn in from the Irminger Current, and the warm waters are again being bathymetrically steered westward along the trough towards the coast. Slump showed weak offshore heat flux, oscillating from 0 TW to ~ -0.5 TW, potentially associated with transient mixing and eddies.

The section that is drawn for KT (Figure 3.9d) highlights the extent of this trough. In the north portion of the section, from about 25 km to 100 km there is evidence of mixing of signals of onshore and offshore heat fluxes. At the 160 km mark, throughout the years, there is a onshore heat flux of greater than 2 TW and similar in magnitude is an offshore heat flux on the south edge of the trough. In the south portion of the section (from 225 km to 325 km) there is variability in the offshore heat flux in space and time.

South-east coast: seasonal and interannual variation

For HGT2 (Figure 3.10g) the sign of the heat flux is mostly negative (offshore), with the highest magnitude occurring between the period of August through to May. Offshore heat flux occurred all year round (except for short bursts in 2005) making this location unique compared to all other regions examined. Observations from a fjord in south-east Greenland (Sermilik Fjord) showed that water properties and heat content vary significantly on synoptic timescales throughout non-summer months (Jackson et al., 2014). Looking at HGT2 (Figure 3.10g), from October to March, there was large variability in the magnitude of the heat flux and also a decrease in average temperature (Figure 3.10i).

The seasonality of HGT2 heat flux is dominated by that of the volume flux (correlation of 0.95) (Figure 3.10h), while the seasonality of the averaged temperature is out of phase (correlation of $-$ 0.16) (Figure 3.10i). At KT (Figure 3.10j), the seasonality of heat flux seems to be dependent on both the seasonality of the volume flux and temperature (Figure 3.10k and Figure 3.10l), with a correlation of 0.92 and 0.82, respectively (Table 3.3). At KT, the peak of onshore heat flux occurred after August for most years with significant interannual variation. The stronger warming events were found in 2004, 2005, 2014, and 2016.

North-east coast: mean state

The section drawn for Scoresby Sund (Figure 3.9e), shows Scoresby Sund Trough (SBST). On the trough's north edge near the maximum depth, at kilometre marker 110 km there is a consistent signal for the onshore heat flux of more than 0.5 TW. The strongest offshore flux, at kilometre maker $120-180$ km, reaches -1.5 TW. The section for 79NG (Figure 3.9f), located in the north-east of Greenland, is drawn from north to south. We see little onshore heat flux, other than the odd short pulse of heat reaching 0.15 TW.

North-east coast: seasonal and interannual variation

At SBST (Figure 3.10m), the heat flux is around zero in the first half of the year. With inter-annual variability, most months can have either weak onshore or weak offshore heat transport. This changes in late summer and fall (August through November), when the heat transport is consistently offshore, reaching almost -10 TW in 2016. This is despite the water being warmest from July to November, with temperatures reaching $-0.5\,^{\circ}C$ (and $0.5\,^{\circ}C$ in 2016). Thus, the transports are offshore during this period. At NT (Figure 3.10p), the mean heat fluxes are around zero year round, with inter-annual variability meaning onshore or offshore fluxes in any given month and year, rarely exceeding an absolute of 0.5 TW in either direction. This is despite a strong seasonal signatures in temperatures, reaching $-1.4\,^{\circ}C$ to $-0.7\,^{\circ}C$, depending on the year in late Summer (August to October).

Summary of onshore heat flux through coastal troughs

Of these six regions the region closest to the Irminger Sea, HGT2, received the highest heat flux earliest in the year, from June to September. The results presented here showed heat flux calculated with a temperature reference of $-1.5\,^{\circ}C$. There appears to be a pattern that the two regions farther away from the NASPG on the west coast of Greenland (MVBCT and DBT), have a warm water peak later, potentially due to the later arrival of modified warm water from the Irminger Sea. DBT had the largest onshore ocean heat flux from July to December. Further north, a later arrival occurs at MVBCT (September through December). On the north-east coast of Greenland, warm water is received from the NwAC. The onshore heat flux through the three troughs peaked thusly: KT from August to November, followed by SBST from November to April and the NT peaked from September to January. Therefore, HGT2 could receive warm water first from the Irminger Sea, then the WGC reaches DBT then MVBCT and the NwAC reached KT, followed by SBST and NT.

Grist et al. (2014) had examined the propagation of the seasonal signal for Irminger water. This study found that the peak seasonal temperatures occur on the east coast of Greenland and west coast south of Davis Strait between August and December, similar to the south-east locations in this study showed (HGT2 and KT). Grist et al. (2014) are in agreement with our study that a lagged timing of the seasonal cycle for warm waters exists north of Davis Strait. In Davis Strait the temperature maximums occur during October to December (Curry et al., 2014) this would align with the timing of the arrival of sub-surface warm waters in the troughs along the west coast of Greenland, as flow from Davis Strait can take about a month to reach DBT and five to six months to reach MVBCT according to HighRes. The seasonality of heat flux through these troughs seems to correspond with the volume flux (HGT2, SBST) or average temperature (DBT and NT), and even both components in some cases (MVBCT, KT).

3.3.2 Contribution of the mean flow and its fluctuation

Examining the mean and fluctuation components of the flow will help identify what processes drive heat through the troughs (shown as tan lines in Figure 3.1). Table 3.3 shows the overall percentage of the heat flux transported by the fluctuating component of the flow. In general, these percentages are less than 10%, suggesting the fluctuating component is a minor player in the heat transport through Greenland's coastal troughs.

In Baffin Bay, consistent with the overall big picture view, the heat flux transported by the mean component peaks later in the year at 5 – 19 TW, based on HighRes. The general behaviour is similar in LowResControl, albeit with smaller peak fluxes. This may be related to HighRes being better able to represent the bathymetry and coastal flows, although the northward-flowing Atlantic Water at Davis Strait is also around $1\,^{\circ}C$ warmer in HighRes. DBT (Figure 3.11c. and Figure 3.11d) sees peak fluxes over 10 TW in 2004, 2005, 2009, and 2010. The peak heat fluxes for MVBCT (Figure 3.11a. and Figure 3.11b) were concentrated in the early 2010s, between the end of 2009 and 2014. For both of these locations, the fluctuation component rarely exceeds $0.1-0.2$ TW.

Warm water exchange into the troughs is very different in south-east Greenland as compared to Baffin Bay. At HGT2, the mean heat transport in HighRes is offshore, with peak transport of -30 to -35 TW (Figure 3.11e). The behaviour of the mean component in LowResControl is very different, with onshore heat transport reaching 10 TW in summer/autumn, balanced by offshore transport the rest of the year. Significant differences in cross-shelf transport between 1/4 and 1/12 degree simulations were also seen by Pennelly et al. (2019). At HGT2, the fluctuation component of the heat fluxes was smaller than the mean, reaching only $2-3$ TW at peaks, but is generally directed onshore (Figure 3.11f). Thus, here at HGT2, even though the fluctuation component is relatively small compared to the mean (Table 3.3), the difference in directions means it plays a key role in transporting heat towards this glacier fjord. This is consistent with Christoffersen et al. (2011), who showed strong wind events were important in bringing warm waters to the coast.

For KT, the mean flow still transports the most heat, mainly in summer/autumn with peak transports reaching $16-20$ TW in HighRes (substantially smaller in LowResControl) (Figure 3.11g). However, the mean transport becomes smaller or even reverses in winter, transporting heat offshore, with maximum peaks approaching -5 TW. Meanwhile, although intermittent, the transient component of the heat flux is generally onshore in HighRes, regularly exceeding 0.5 TW and approaching 1 TW (Figure 3.11h). This would be consistent with low-pressure systems propagating along the coast past KT, potentially linked to the Lofoten Low as suggested by Moore et al. (2014).

Moving to north-east Greenland, SBST stood out with the fluctuating component of the flow transporting about 76% of the heat flux at this location (Table 3.3). SBST has onshore heat flux, peaking at $2-3$ TW in HighRes (and little different in LowResControl), associated with the mean flow (Figure 3.11i). However, offshore heat flux peaks around -6 TW to -8 TW in HighRes, therefore, the heat flux direction switches from onshore to offshore. Additionally, there are occasionally strong peaks in the fluctuating component, exceeding 0.5 TW (Figure 3.11j). There are more peaks in the fluctuating component in recent years (2011 onwards) and this might be related to the reductions in sea ice in this region, or due to the presence of Pacific Water on the shelf (e.g. Dmitrenko et al. (2019)). The mean component dominates at NT, though switching offshore and onshore directions as well (-0.4 TW to-0.8 TW in HighRes; Figure 3.11k and Figure 3.11l).

The correlation of the heat flux between the HighRes and LowResControl for most of the troughs was high (SBST greater than 0.9, NT and MVBCT greater than 0.8, and HGT2 greater than 0.7, see Table 3.3). The LowResControl and HighRes compared well with observations (see Section 3.2.4). However, since running several high-resolution experiments are computationally expensive compared to lower resolution configurations, the LowResControl had been used for the sensitivity experiments which will be discussed later in this paper (Section 3.3.3 and Section 3.3.4).

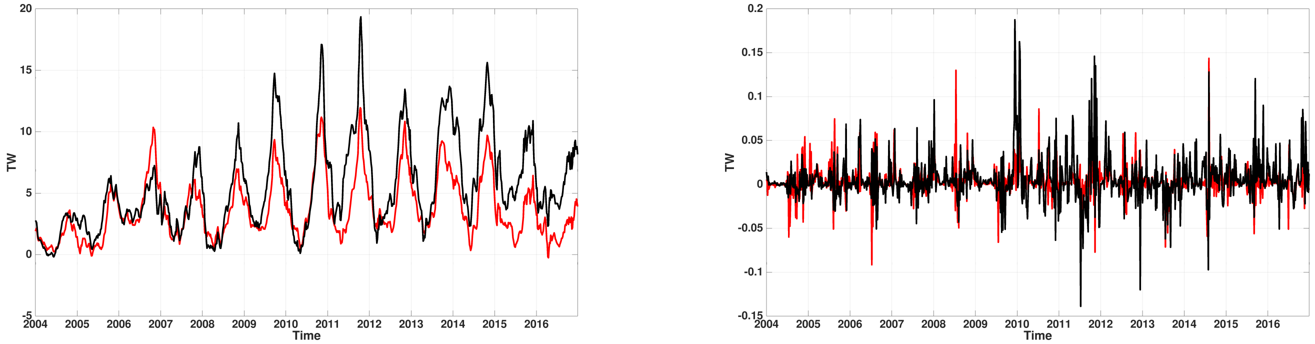

(a) MVBCT Mean

(b) MVBCT Fluctuation

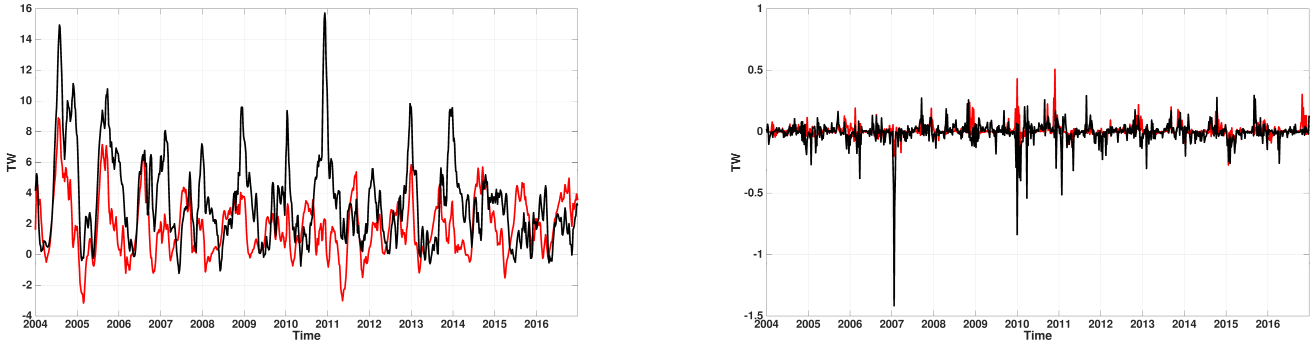

(c) DBT Mean

(d) DBT Fluctuation

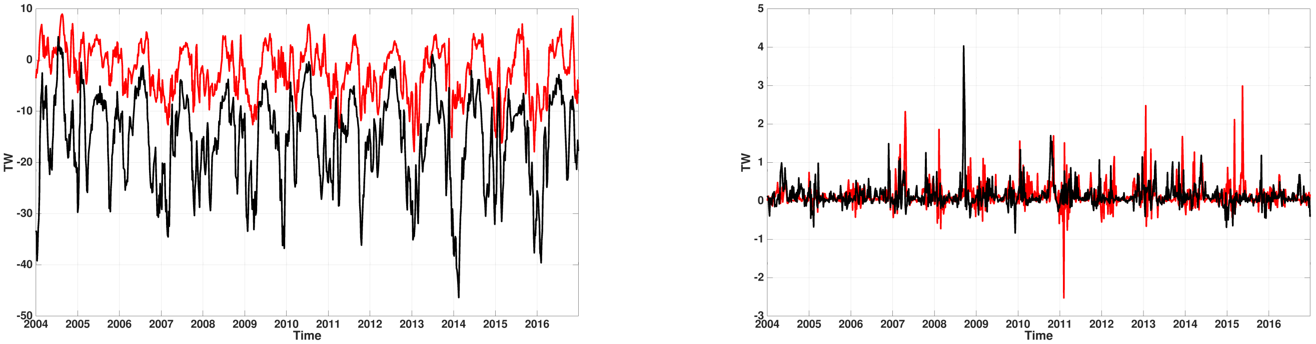

(e) HGT2 Mean

(f) HGT2 Fluctuation

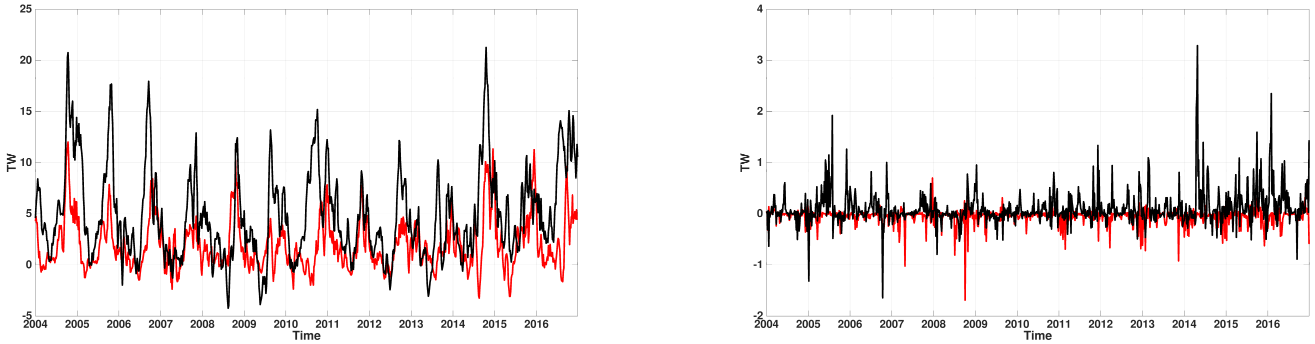

(g) KT Mean

(h) KT Fluctuation

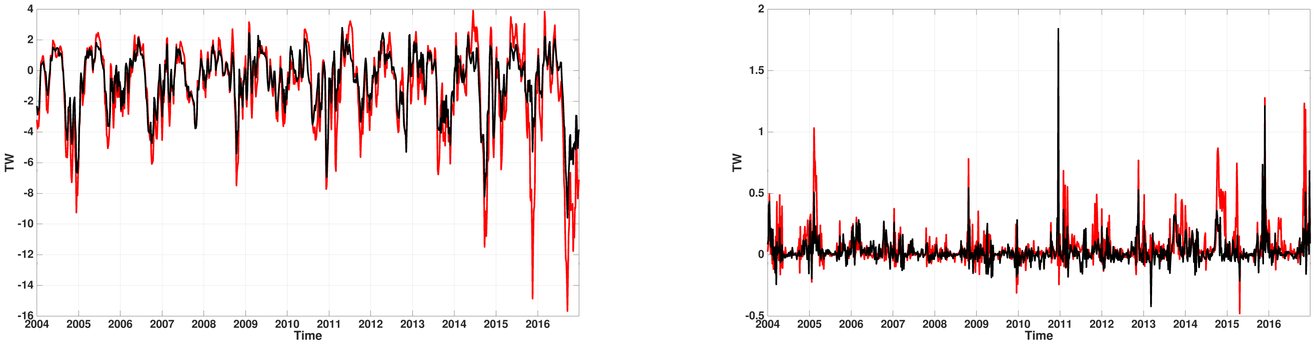

(i) SBST Mean

(j) SBST Fluctuation

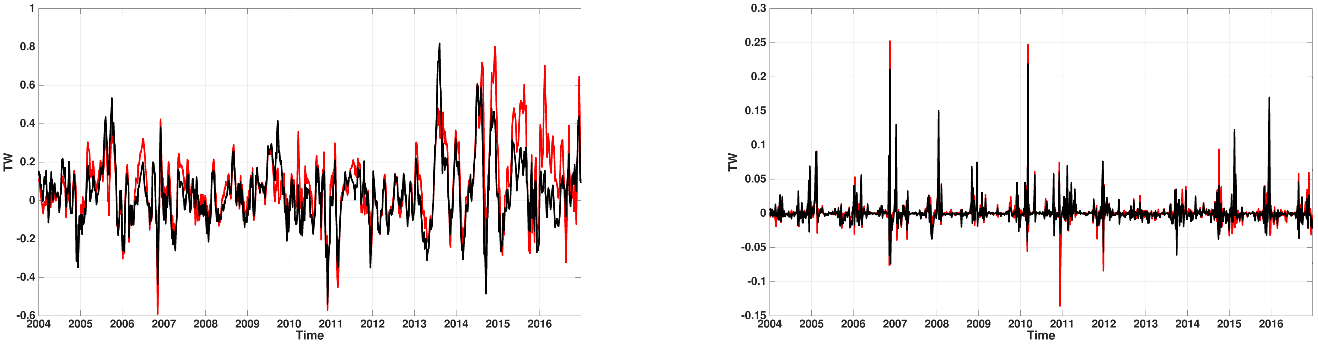

(k) NT Mean

(l) NT Fluctuation

Figure 3.11: Mean (left column) and fluctuating (right column) components of the heat flux (TW) from LowResControl (in red) and HighRes (in black). Plotted for the whole time series 2004 to 2016. Each row is for a different trough.

3.3.3 Impact of enhanced Greenland meltwater

Previous studies, from a variety of scales of modelling, have shown that enhanced freshwater discharge from the GrIS could increase the presence of heat near the ice sheet. For example, if GrIS melt increases it may add more energetic plume dynamics along a glacier face and increase the strength of the thermohaline circulation in fjords. Cai et al. (2017) showed in a 2–D model ran for one year, with ice shelf melt derived from observed melt rates for Petermann Glacier, that an increase in thermohaline circulation in the fjord could bring more heat and salt towards the ice sheet. Note that such fjord scale processes are not resolved by the model simulations presented in this paper. Outside of the fjord, Castro de la Guardia et al. (2015) and Grivault et al. (2017) had found enhanced meltwater from the GrIS could increase the heat content within the Baffin Bay. Enhanced runoff decreased surface salinity in Baffin Bay, particularly along the coast. Due to the halosteric effect, it led to a lift of the sea surface height on the shelf, and then an enhanced boundary current. This strengthened Baffin Bay's cyclonic gyre in the upper layer, which resulted in a stronger Ekman pumping that lifted the isopycnals and caused the shallowing of the warm water layer in Baffin Bay. Strengthening the WGC also brought more warm waters northward into Baffin Bay. The warming and lifting of the intermediate warm layer are clearly evident in the temperature field along the west Greenland coast (Figure 3.12) in LowResDoubleMelt. This study provides more realistic experiments and analysis on specific locations concerning troughs which connect to fjords with large marine-terminating glaciers. With an increase in GrIS melt, Baffin Bay's ocean heat content may increase. Thus increasing the potential for glaciers to continue to melt, impacting climate, SLR, and ecosystems.

For Melville Bay in LowResControl (Figure 3.12a), a warm core of water existed at depths 100 m to 400 m, with a maximum (kilometre marker 500 km) in MVBST reaching almost $2\,^{\circ}C$. In LowResDoubleMelt (Figure 3.12b), the warm water core temperature increased and MVBST reached temperatures closer to $3\,^{\circ}C$. The cold water layer in LowResDoubleMelt thinned more than in the LowResControl. For Disko Bay, both deep troughs (UT and DBT) held warmer water in LowResDoubleMelt ($3\,^{\circ}C$, Figure 3.12d) than in LowResControl ($\sim 2\,^{\circ}C$, Figure 3.12c). The maximum increase occurred in a warm core in both troughs, UT and DBT (at kilometre marker 150 km and 400 km), of a depth of 150 m to 350 m. The cooler water layer at the surface thinned in LowResDoubleMelt (Figure 3.12c). However, when examining average velocities normal to the section, for the entire period there was no clear trend that increasing the

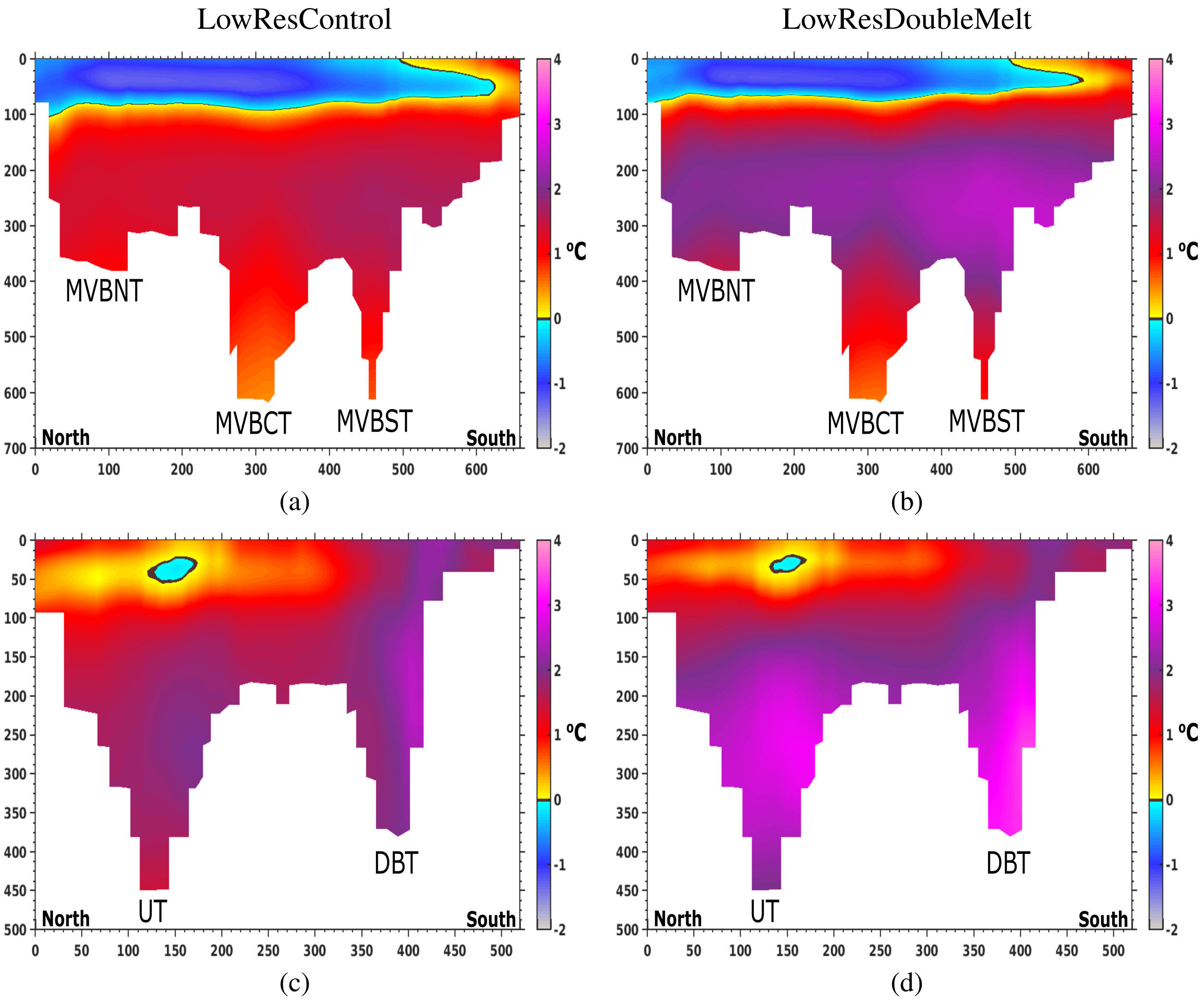

(a) (b)

(c) (d)

Figure 3.12: Temperature along two sections in the north-west of Greenland, Melville Bay Section and Disko Bay Section. For location of the sections, see Figure 3.1. Shown is the average temperature over the period of 2004 to 2016, with the model bathymetry in white (m) and the colours indicating the temperature of the water in $^{\circ}C$. The left column shows the results for LowResControl, and the right column shows the results for LowResDoubleMelt. The first row shows the section Melville Bay and the second row shows the section for Disko Bay.

meltwater strengthens the velocities.

This study found that Baffin Bay was a very unique system. Other regions around Greenland did not respond to an increase in the GrIS melt in the same way. With a doubling of the meltwater, the west sector had a 21 % increase in onshore heat flux (Table 3.4) but we saw a 6 % decrease in the north-east region and a 12 % decrease in the south-east region.

Table 3.4: This table shows the percentage of the difference between the onshore sum of yearly heat fluxes from three experiments, HighRes, LowResControl, LowResDoubleMelt from 2004 to 2016. West coast includes Melville Bay Central Trough (MVBCT) and Disko Bay Trough (DBT), south-east coast sector includes Helheim Glacier Trough 2 (HGT2) and Kangerlussuaq Trough (KT), and north-east coast includes Scoresby Sund Trough (SBST) and Norske Trough (NT). These troughs can be identified in Figure 3.1.

Troughs along the GrIS	**Changes in onshore heat (%)**
West Coast	
HighRes vs LowResControl	57%
LowResDoubleMelt vs LowResControl	21%
South-east Coast	
HighRes vs LowResControl	55%
LowResDoubleMelt vs LowResControl	6%
North-east Coast	
HighRes vs LowResControl	21%
LowResDoubleMelt vs LowResControl	12%

3.3.4 Impact of high-frequency atmospheric events

A question of how the atmospheric variability may impact the region of HG for renewing heat from the shelf has been discussed in previous observational studies (Christoffersen et al., 2011; Straneo et al., 2010). How does filtering out storms, where winds and the associated temperatures are impacted, affect the high frequency variability in south-east Greenland? A comparison of LowResControl and LowResNoStorms will be shown to examine this question.

Figure 3.13 shows the average TKE integrated over the entire depth for the south-east region with LowResControl and LowResNoStorms. A comparison was done for the north-west and north-east regions as well. However, the south-east region had the highest TKE as well as the strongest sensitivity to changes in atmospheric conditions. Therefore only the south-east region will be shown for further analysis. LowResControl (Figure 3.13a) had TKE values reaching 4×10^{-3} m^2 s^{-2}. However, LowResNoStorms TKE peaked at 2.5×10^{-3} m^2 s^{-2}, i.e., TKE is reduced by about half. Significant

TKE decrease close to HGT2 is seen on the shelf at depths less than 500 m (Figure 3.13a). By filtering out storms, the TKE strength decreased in the south-east region (Figure 3.13b).

Figure 3.13c and Figure 3.13d show the time series of the mean and fluctuation components of the heat flux for HGT2 with LowResControl and LowResNoStorms. The mean component has less onshore heat flux in the LowResControl than LowResNoStorms. The LowResNoStorms mean component of the onshore heat flux reached values closer to 10 TW in 2004 to the end of 2007. LowResControl had onshore heat flux values greater than 5 TW in 2004, 2007, 2010, 2015 and 2016. After 2011, both experiment's mean component rarely surpass 5 TW and the time series show more negative (offshore direction) heat flux values. LowResControl mean component shows more prominent offshore heat flux in 2013 to 2016, reaching maximums close to -18 TW , where LowResNoStorms has a weaker offshore mean heat flux, though similar values with LowResControl in 2014 (~ -15 TW). The fluctuation component of the heat flux is smaller with the LowResNoStorms. The fluctuation component moderated the heat flux more with storms (21% for the LowResControl vs 13% with LowResNoStorms, Table 3.3). Therefore, filtering storms decreased the fluctuation component of the heat flux as well as it's control over the total heat flux.

The integration of the mean component of the heat flux from 2004 to 2016 has been calculated and compared between LowResControl and LowResNoStorms. LowResNoStorms has a total energy accumulation of 1.24 GJ (1 GJ $= 1 \times 10^9$ J), where LowResControl had a total of -4.23 GJ. The total energy increase of ~ 5 GJ could have the potential to melt 15 tonnes of ice. LowResNoStorms has a 97 % increase of onshore component of the heat for this period of 4.3 GJ compared to LowResControl of 2.3 GJ. LowResNoStorms has a 52% decrease of offshore component of the heat for this period of -3.1 GJ compared to LowResControl of -6.4 GJ. HGT2 has more energy in the onshore direction in LowResNoStorms due to filtering out offshore winds and therefore decreasing offshore heat transport. A decrease in storms decreased the offshore winds (southward) and therefore less Ekman transport (upwelling) along the shelf. Less upwelling and offshore winds may decrease the offshore exchange of heat flux. As a result, fewer storms in this region may increase the overall onshore heat flux into HGT2.

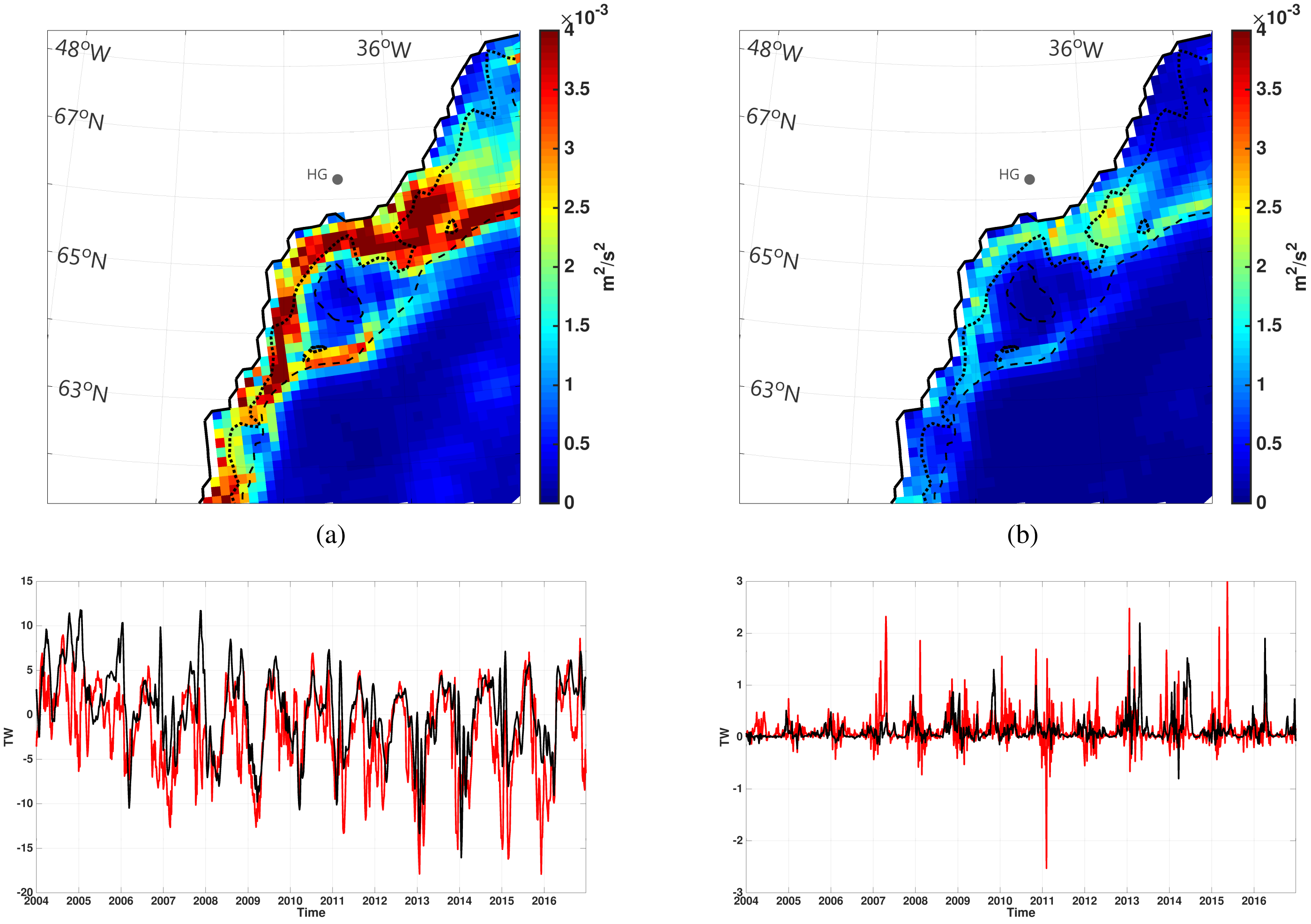

(a) (b)

(c) (d)

Figure 3.13: Comparison of filtering the atmospheric forcing in LowResNoStorms. (a) and (b) shows the Transient Kinetic Energy (TKE) integrated over the entire depth at the south-east region of Greenland for LowResControl (a) and LowResNoStorms (b). The TKE here is the average TKE for the period of 2004 to 2016. The thick dashed lines mark the bathymetry at 250 m and the thin dashed line marks the 500 m depth. (c) shows the mean heat flux and (d) shows the fluctuation component of heat flux through Helheim Glacier Trough 2 (HGT2) (location identified in Figure 3.1). The LowResNoStorms configuration in black solid lines, LowResControl configuration in red solid lines.

3.4 Conclusions

The oceanic heat available in Greenland's troughs is dependent on both the location of the trough, source of the warm water origin, how the water is transformed as it travels to the troughs, as well as local processes, such as heat loss to the atmosphere. It is important to understand the processes that bring this warm water to the shelf and into the troughs, as this water can be then exchanged into the fjords. Warm water present in fjords provides oceanic heat forcing on marine-terminating glaciers (Cai et al., 2017; Rignot et al., 2016b; Wood et al., 2018). To our knowledge, this is the first study looking at seasonal changes in heat flux in troughs that are connected to fjords with marine-terminating glaciers.

This study showed that the presence of warm water at depth can extend far north into Baffin Bay, reaching as north as Melville Bay and its subsequent troughs. Increased heat flux through the Melville Bay section is found from 2009 to the end of 2014. Therefore an associated increase in ocean heat presence in these troughs may have driven more heat to glaciers that terminate there. From 2004 to 2006, model experiments captured an increase in onshore heat flux in DBT, coinciding with the timing of the disintegration of JI floating tongue and within the period of observed oceanic heat increase in Disko Bay (from 1997 to 2007) (Holland et al., 2008).

The seasonality of the maximum onshore heat flux through all six regions was presented. The study looked at heat fluxes using a reference temperature of $-1.5\,^{\circ}C$ to consider the effects of boundary layer salinity and pressure on the freezing point (see Section 3.2.3 for further detail). Therefore the heat present in the troughs that we consider is not simply modified Irminger Water (although that will be the most important component off west Greenland). The seasonality of the maximum onshore heat flux through troughs around the GrIS differs as the distance between the Irminger Sea increases. Therefore, the influence of the Irminger Current may still present itself in these troughs as well as other warm waters. The seasonal peak of warm waters began in: June for HGT2, July for DBT, and September for MVBCT. Then for the areas receiving warm water from the NwAC: August for KT, November for SBS, and September to January for NT.

The south-east region had the highest TKE as well as the strongest sensitivity to changes in atmospheric conditions. The south-east coast of Greenland is impacted the most by the atmospheric filter (i.e. no storms). No storms resulted in a reduction of TKE ($\sim$ 50 %) and less offshore heat transport and therefore more onshore heat flux

(97 %) through the Helheim Glacier Trough 2 (HGT2).

It is imperative to try to understand how sensitive the ocean is to additional meltwater from Greenland. Baffin Bay is a unique system, as it responded to an increase in the GrIS melt in a different way than any other region around Greenland in this study. Troughs off the west coast of Greenland in Baffin Bay brought more heat (~ 20 %) towards the GrIS when the GrIS freshwater flux doubled. This study showed that a doubling of the GrIS melt may cause warming in Baffin Bay and an increase in heat flux through troughs, potentially escalating the melt of the GrIS, consistent with Castro de la Guardia et al. (2015) but now in a more realistic set–up with Greenland meltwater temporally and spatially distributed.

Since the model used in this study cannot resolve small scale processes such as fjord circulation, the exchange between fjords and troughs cannot be looked into. Instead, there is an assumption in place that the water characteristics that exist in the troughs will match those in the fjords due to the dynamics of cross-shelf exchanges (Jackson et al., 2014; Sutherland et al., 2014). Warming of ocean water in troughs may lead to a warming of ocean waters in fjords. Due to the model bathymetry underrepresenting the depth of these troughs, this study may be underestimating the amount of ocean heat available to enter these troughs. The study only looked at the impact of the freshwater flux from the GrIS. The inclusion of an iceberg model coupled with an ocean model (Marson et al., 2018) may give further insight into the heat and freshwater budget in regions of high GrIS discharge.

Acknowledgements

We would like to thank Yarisbel Garcia-Quintana for carrying out the LowResNoStorm experiment. We are grateful to the NEMO development team and the Drakkar project for providing the model and continuous guidance, and to Westgrid and Compute Canada for computational resources, where all model experiments were performed and archived (http://www.computecanada.ca). We gratefully acknowledge the financial and logistic support of grants from the Natural Sciences and Engineering Research Council (NSERC) of Canada. These include Discovery Grant (rgpin227438) awarded to Dr. P.G. Myers, Climate Change and Atmospheric Research Grant (VITALS - RGPCC 433898), and an International Create (ArcTrain - 432295). The author would like to thank the anonymous reviewers for their insightful comments and suggestions that have contributed to improving this paper.

Bibliography

Aagaard, K. and Carmack, E. C. (1989). The role of sea ice and other fresh water in the Arctic circulation. *Journal of Geophysical Research: Oceans*, 94(C10):14485–14498.

Aksenov, Y., Bacon, S., Coward, A. C., and Holliday, N. P. (2010). Polar outflow from the Arctic Ocean: A high resolution model study . *Journal of Marine Systems*, 83(1–2):14 – 37.

Amante, C. and Eakins, B. (2009). ETOPO1 1 Arc-Minute Global Relief Model: Procedures, Data Sources and Analysis. *NOAA Technical Memorandum NESDIS NGDC-24*.

An, L., Rignot, E., Elieff, S., Morlighem, M., Millan, R., Mouginot, J., Holland, D. M., Holland, D., and Paden, J. (2017). Bed elevation of Jakobshavn Isbrae, West Greenland, from high-resolution airborne gravity and other data. *Geophysical Research Letters*, 44(8):3728–3736. 2017GL073245.

Arrigo, K. R., van Dijken, G. L., Castelao, R. M., Luo, H., Rennermalm, A. K., Tedesco, M., Mote, T. L., Oliver, H., and Yager, P. L. (2017). Melting glaciers stimulate large summer phytoplankton blooms in southwest Greenland waters. *Geophysical Research Letters*, 44(12):6278–6285.

Azetsu-Scott, K. and Tan, F. C. (1997). Oxygen isotope studies from Iceland to an East Greenland Fjord: behaviour of glacial meltwater plume. *Marine Chemistry*, 56(3):239 – 251. Modern Chemical and Biological Oceanography: The Influence of Peter J. Wangersky.

Bacon, S., Marshall, A., Holliday, N. P., Aksenov, Y., and Dye, S. R. (2014). Seasonal variability of the East Greenland Coastal Current. *Journal of Geophysical Research: Oceans*, 119(6):3967–3987.

Bamber, J., Van Den Broeke, M., Ettema, J., Lenaerts, J., and Rignot, E. (2012). Recent large increases in freshwater fluxes from Greenland into the North Atlantic. *Geophysical Research Letters*, 39(19).

Bamber, J. L., Griggs, J. A., Hurkmans, R. T. W. L., Dowdeswell, J. A., Gogineni, S. P., Howat, I., Mouginot, J., Paden, J., Palmer, S., Rignot, E., and Steinhage, D. (2013). A new bed elevation dataset for Greenland. *The Cryosphere*, 7(2):499–510.

Barnier, B., Brodeau, L., Le Sommer, J., Molines, J.-M., Penduff, T., Theetten, S., Tréguier, A.-M., Madec, G., Biastoch, A., Böning, C. W., Dengg, J., Gulev, S. K., Bourdallé-Badie, R., Chanut, J., Garric, G., Alderson, S., Coward, A. C., De Cuevas, B., New, A. L., Haines, K., Smith, G. C., Drijfhout, S., Hazeleger, W., Severijns, C. A., and Myers, P. G. (2007). Eddy-permitting ocean circulation hindcasts of past decades. *CLIVAR Exchanges*, 12(42):8–10.

Bartholomaus, T. C., Stearns, L. A., Sutherland, D. A., Shroyer, E. L., Nash, J. D., Walker, R. T., Catania, G., Felikson, D., Carroll, D., Fried, M. J., and et al. (2016). Contrasts in the response of adjacent fjords and glaciers to ice-sheet surface melt in West Greenland. *Annals of Glaciology*, 57(73):25–38.

Beaird, N., Straneo, F., and Jenkins, W. (2017). Characteristics of meltwater export from Jakobshavn Isbræ and Ilulissat Icefjord. *Annals of Glaciology*, 58(74):107–117.

Beaird, N. L., Straneo, F., and Jenkins, W. (2018). Export of Strongly Diluted Greenland Meltwater From a Major Glacial Fjord. *Geophysical Research Letters*, 45(9):4163–4170.

Bernard, B., Madec, G., Penduff, T., Molines, J.-M., Treguier, A.-M., Le Sommer, J., Beckmann, A., Biastoch, A., Böning, C., Dengg, J., Derval, C., Durand, E., Gulev, S., Remy, E., Talandier, C., Theetten, S., Maltrud, M., McClean, J., and De Cuevas, B. (2006). Impact of partial steps and momentum advection schemes in a global ocean circulation model at eddy-permitting resolution. *Ocean Dynamics*, 56(5):543–567.

Beszczynska-Möller, A., Fahrbach, E., Schauer, U., and Hansen, E. (2012). Variability in Atlantic water temperature and transport at the entrance to the Arctic Ocean, 1997–2010. *ICES Journal of Marine Science: Journal du Conseil*.

BODC (2008). British Oceanographic Data Center's General Bathymetric Chart of the Oceans. http://www.gebco.net/data_and_products/gridded_bathymetry_data/.

Böning, C. W., Behrens, E., Biastoch, A., Getzlaff, K., and Bamber, J. L. (2016). Emerging impact of Greenland meltwater on deepwater formation in the North Atlantic Ocean. *Nature Geosci*, 9(7):523–527.

Box, J. E., Yang, L., Bromwich, D. H., and Bai, L. (2009). Greenland Ice Sheet surface air temperature variability: 1840–2007. *Journal of Climate*, 22(14):4029–4049.

Cai, C., Rignot, E., Menemenlis, D., and Nakayama, Y. (2017). Observations and modeling of ocean-induced melt beneath Petermann Glacier Ice Shelf in northwestern Greenland. *Geophysical Research Letters*.

Castro de la Guardia, L., Hu, X., and Myers, P. G. (2015). Potential positive feedback between Greenland Ice Sheet melt and Baffin Bay heat content on the west Greenland shelf. *Geophysical Research Letters*, 42(12):4922–4930.

Christoffersen, P., Mugford, R. I., Heywood, K. J., Joughin, I., Dowdeswell, J. A., Syvitski, J. P. M., Luckman, A., and Benham, T. J. (2011). Warming of waters in an East Greenland fjord prior to glacier retreat: Mechanisms and connection to large-scale atmospheric conditions. *Cryosphere*, 5(3):701–714.

Csatho, B. M., Schenk, A. F., van der Veen, C. J., Babonis, G., Duncan, K., Rezvanbehbahani, S., van den Broeke, M. R., Simonsen, S. B., Nagarajan, S., and van Angelen, J. H. (2014). Laser altimetry reveals complex pattern of Greenland Ice Sheet dynamics. *Proceedings of the National Academy of Sciences*, 111(52):18478–18483.

Curry, B., Lee, C., Petrie, B., Moritz, R., and Kwok, R. (2014). Multiyear volume, liquid freshwater, and sea ice transports through Davis Strait, 2004-10. *Journal of Physical Oceanography*, 44(4):1244–1266.

Curry, B., Lee, C. M., and Petrie, B. (2011). Volume, Freshwater, and Heat Fluxes through Davis Strait, 2004–05. *Journal of Physical Oceanography*, 41(3):429–436.

Dai, A., Qian, T., Trenberth, K. E., and Milliman, J. D. (2009). Changes in continental freshwater discharge from 1948 to 2004. *Journal of Climate*, 22(10):2773–2792.

Dmitrenko, I. A., Kirillov, S. A., Rudels, B., Babb, D. G., Myers, P. G., Stedmon, C. A., Bendtsen, J., Ehn, J. K., Pedersen, L. T., Rysgaard, S., and Barber, D. G. (2019). Variability of the Pacific-Derived Arctic Water Over the Southeastern Wandel Sea Shelf (Northeast Greenland) in 2015–2016. *Journal of Geophysical Research: Oceans*, 124(1):349–373.

Dukhovskoy, D. S., Myers, P. G., Platov, G., Timmermans, M.-L., Curry, B., Proshutinsky, A., Bamber, J. L., Chassignet, E., Hu, X., Lee, C. M., and Somavilla, R. (2016). Greenland freshwater pathways in the sub-Arctic Seas from model experiments with passive tracers. *Journal of Geophysical Research: Oceans*.

Eskridge, R. E., Ku, J. Y., Rao, S. T., Porter, P. S., and Zurbenko, I. G. (1997). Separating Different Scales of Motion in Time Series of Meteorological Variables. *Bulletin of the American Meteorological Society*, 78(7):1473–1484.

Felikson, D., Bartholomaus, T. C., Catania, G. A., Korsgaard, N. J., Kjær, K. H., Morlighem, M., Noël, B., van den Broeke, M., Stearns, L. A., Shroyer, E. L., Sutherland, D. A., and Nash, J. D. (2017). Inland thinning on the Greenland Ice Sheet controlled by outlet glacier geometry. *Nature Geoscience*, 10:366–369.

Fenty, I., Willis, J. K., Khazendar, A., Dinardo, S., Forsberg, R., Fukumori, I., Holland, D., Jakobsson, M., Moller, D., Münchow, J. M. A., Rignot, E., Schodlok, M., Thompson, A. F., Tinto, K., Rutherford, M., and Trenholm, N. (2016). Oceans Melting Greenland: Early Results from NASA's Ocean-Ice Mission in Greenland . *Oceanography*, 29.

Ferry, N., Greiner, E., Garric, G., Penduff, T., Treiguier, A.-M., and Reverdin, G. (2008). GLORYS-1 Reference Manual for Stream 1 (2002-2007). GLORYS project report.

Fichefet, T. and Morales Maqueda, M. (1997). Sensitivity of a global sea ice model to the treatment of ice thermodynamics and dynamics. *Journal of Geophysical Research*, 102(C6):12609–12646.

Fratantoni, P. S. and Pickart, R. S. (2007). The western North Atlantic shelfbreak current system in summer. *Journal of Physical Oceanography*, 37(10):2509–2533.

Garcia-Quintana, Y., Courtois, P., Hu, X., Pennelly, C., Kieke, D., and Myers, P. G. (2019). Sensitivity of Labrador Sea Water Formation to Changes in Model Resolution, Atmospheric Forcing, and Freshwater Input. *Journal of Geophysical Research: Oceans*, 124(3):2126–2152.

Gillard, L. C., Hu, X., Myers, P. G., and Bamber, J. L. (2016). Meltwater pathways from marine terminating glaciers of the Greenland Ice Sheet. *Geophysical Research Letters*, 43(20):10,873–10,882.

Gladish, C., Holland, D., and Lee, C. (2015a). Oceanic boundary conditions for Jakobshavn Glacier. Part II: Provenance and sources of variability of disko bay and Ilulissat Icefjord waters, 1990-2011. *Journal of Physical Oceanography*, 45(1):33–63.

Gladish, C., Holland, D., Rosing-Asvid, A., Behrens, J., and Boje, J. (2015b). Oceanic boundary conditions for Jakobshavn Glacier. Part I: Variability and renewal of Ilulissat Icefjord waters, 2001-14. *Journal of Physical Oceanography*, 45(1):3–32.

Grist, J. P., Josey, S. A., Boehme, L., Meredith, M. P., Laidre, K. L., Heide-Jørgensen, M. P., Kovacs, K. M., Lydersen, C., Davidson, F. J. M., Stenson, G. B., Hammill, M. O., Marsh, R., and Coward, A. C. (2014). Seasonal variability of the warm Atlantic water layer in the vicinity of the Greenland shelf break. *Geophysical Research Letters*, 41(23):8530–8537.

Grivault, N., Hu, X., and Myers, P. G. (2017). Evolution of Baffin Bay Water Masses and Transports in a Numerical Sensitivity Experiment under Enhanced Greenland Melt. *Atmosphere-Ocean*, 55(3):169–194.

Hogan, K. A., Cofaigh, C. ., Jennings, A. E., Dowdeswell, J. A., and Hiemstra, J. F. (2016). Deglaciation of a major palaeo-ice stream in Disko Trough, West Greenland. *Quaternary Science Reviews*, 147:5 – 26. Special Issue: PAST Gateways (Palaeo-Arctic Spatial and Temporal Gateways).

Holdsworth, A. M. and Myers, P. G. (2015). The influence of high-frequency atmospheric forcing on the circulation and deep convection of the Labrador Sea. *Journal of Climate*, 28(12):4980–4996.

Holland, D. M. and Jenkins, A. (1999). Modeling Thermodynamic Ice–Ocean Interactions at the Base of an Ice Shelf. *Journal of Physical Oceanography*, 29(8):1787–1800.

Holland, D. M., Thomas, R. H., De Young, B., Ribergaard, M. H., and Lyberth, B. (2008). Acceleration of Jakobshavn Isbrae triggered by warm subsurface ocean waters. *Nature Geoscience*, 1(10):659–664.

Hu, X. and Myers, P. G. (2013). A Lagrangian view of Pacific water inflow pathways in the Arctic Ocean during model spin-up. *Ocean Modelling*, 71:66 – 80.

Inall, M. E., Murray, T., Cottier, F. R., Scharrer, K., Boyd, T. J., Heywood, K. J., and Bevan, S. L. (2014). Oceanic heat delivery via Kangerdlugssuaq Fjord to the south-east Greenland Ice Sheet. *Journal of Geophysical Research: Oceans*, 119(2):631–645.

Jackson, R. H., Straneo, F., and Sutherland, D. A. (2014). Externally forced fluctuations in ocean temperature at Greenland glaciers in non-summer months. *Nature Geoscience*, 7(7):503–508.

Jenkins, A. (2011). Convection-driven melting near the grounding lines of ice shelves and tidewater glaciers. *Journal of Physical Oceanography*, 41(12):2279–2294.

Joughin, I., Alley, R. B., and Holland, D. M. (2012). Ice-Sheet Response to Oceanic Forcing. *Science*, 338(6111):1172–1176.

Karcher, M., Beszczynska-Möller, A., Kauker, F., Gerdes, R., Heyen, S., Rudels, B., and Schauer, U. (2011). Arctic Ocean warming and its consequences for the Denmark Strait overflow. *Journal of Geophysical Research: Oceans*, 116(C2).

Khazendar, A., Fenty, I. G., Carroll, D., Gardner, A. an Lee, C. M., Fukumori, I., Wang, O., Zhang, H., Seroussi, H., Moller, D., Noël, B. P. Y., van den Broeke, M. R., Dinardo, S., and Willis, J. (2019). Interruption of two decades of Jakobshavn Isbrae acceleration and thinning as regional ocean cools. *Nature Geoscience*, 12(4).

Luo, H., Castelao, R. M., Rennermalm, A. K., Tedesco, M., Bracco, A., Yager, P. L., and Mote, T. L. (2016). Oceanic transport of surface meltwater from the southern Greenland Ice Sheet. *Nature Geoscience*.

Madec, G. (2008). NEMO ocean engine. *Note du Pole de modélisation*, (27).

Marson, J. M., Myers, P. G., Hu, X., and Le Sommer, J. (2018). Using Vertically Integrated Ocean Fields to Characterize Greenland Icebergs' Distribution and Lifetime. *Geophysical Research Letters*, 45(9):4208–4217.

Mayer, C., Reeh, N., Jung-Rothenhäusler, F., Huybrechts, P., and Oerter, H. (2000). The subglacial cavity and implied dynamics under Nioghalvfjerdsfjorden Glacier, NE-Greenland. *Geophysical Research Letters*, 27(15):2289–2292.

MEOM (2013). Bathymetry ORCA0.25. http://servdap.legi.grenoble-inp.fr/meom/ORCA025-I/.

Moon, T., Joughin, I., and Smith, B. (2015). Seasonal to multiyear variability of glacier surface velocity, terminus position, and sea ice/ice mélange in northwest Greenland. *Journal of Geophysical Research: Earth Surface*, 120(5):818–833.

Moore, G. W. K., Straneo, F., and Oltmanns, M. (2014). Trend and interannual variability in southeast Greenland Sea Ice: Impacts on coastal Greenland climate variability. *Geophysical Research Letters*, 41(23):8619–8626.

Morlighem, M., Williams, C. N., Rignot, E., An, L., Arndt, J. E., Bamber, J. L., Catania, G., Chauché, N., Dowdeswell, J. A., Dorschel, B., Fenty, I., Hogan, K., Howat, I., Hubbard, A., Jakobsson, M., Jordan, T. M., Kjeldsen, K. K., Millan, R., Mayer, L., Mouginot, J., Noël, B. P. Y., O'Cofaigh, C., Palmer, S., Rysgaard, S., Seroussi, H., Siegert, M. J., Slabon, P., Straneo, F., van den Broeke, M. R., Weinrebe, W., Wood, M., and Zinglersen, K. B. (2017). BedMachine v3: Complete Bed Topography and Ocean Bathymetry Mapping of Greenland From Multibeam Echo Sounding Combined With Mass Conservation. *Geophysical Research Letters*, 44(21):11,051–11,061.

Myers, P. G., Donnelly, C., and Ribergaard, M. H. (2009). Structure and variability of the West Greenland Current in Summer derived from 6 repeat standard sections. *Progress in Oceanography*, 80(1-2):93–112.

Myers, P. G. and Ribergaard, M. H. (2013). Warming of the polar water layer in Disko Bay and potential impact on Jakobshavn Isbrae. *Journal of Physical Oceanography*, 43(12):2629–2640.

National Geophysical Data Cente (2006). 2-minute Gridded Global Relief Data (ETOPO2) v2. National Geophysical Data Center, NOAA. Dataset accessed [2017-05-09].

Pennelly, C., Hu, X., and Myers, P. G. (2019). Cross-Isobath Freshwater Exchange Within the North Atlantic Subpolar Gyre. *Journal of Geophysical Research: Oceans*, 124(10):6831–6853.

Porter, D. F., Tinto, K. J., Boghosian, A., Cochran, J. R., Bell, R. E., Manizade, S. S., and Sonntag, J. G. (2014). Bathymetric control of tidewater glacier mass loss in northwest Greenland. *Earth and Planetary Science Letters*, 401:40 – 46.

Rastner, P., Bolch, T., Mölg, N., Machguth, H., Le Bris, R., and Paul, F. (2012). The first complete inventory of the local glaciers and ice caps on Greenland. *The Cryosphere*, 6(6):1483–1495.

Ribergaard, M. (2014). Oceanographic Investigations off West Greenland 2013. *NAFO Scientific Council Documents*.

Rignot, E., Fenty, I., Xu, Y., Cai, C., Velicogna, I., Cofaigh, C. ., Dowdeswell, J. A., Weinrebe, W., Catania, G., and Duncan, D. (2016a). Bathymetry data reveal glaciers vulnerable to ice-ocean interaction in Uummannaq and Vaigat glacial fjords, west Greenland. *Geophysical Research Letters*, 43(6):2667–2674. 2016GL067832.

Rignot, E. and Kanagaratnam, P. (2006). Changes in the velocity structure of the Greenland Ice Sheet. *Science*, 311(5763):986–990.

Rignot, E. and Mouginot, J. (2012). Ice flow in Greenland for the International Polar Year 2008-2009. *Geophysical Research Letters*, 39(11).

Rignot, E., Xu, Y., Menemenlis, D., Mouginot, J., Scheuchl, B., Li, X., Morlighem, M., Seroussi, H., den Broeke, M. v., Fenty, I., Cai, C., An, L., and Fleurian, B. d. (2016b). Modeling of ocean-induced ice melt rates of five west Greenland glaciers over the past two decades. *Geophysical Research Letters*, 43(12):6374–6382.

Schaffer, J., von Appen, W.-J., Dodd, P. A., Hofstede, C., Mayer, C., de Steur, L., and Kanzow, T. (2017). Warm water pathways toward Nioghalvfjerdsfjorden Glacier, Northeast Greenland. *Journal of Geophysical Research: Oceans*, 122(5):4004–4020.

Seroussi, H., Morlighem, M., Rignot, E., Larour, E., Aubry, D., Ben Dhia, H., and Kristensen, S. S. (2011). Ice flux divergence anomalies on 79north Glacier, Greenland. *Geophysical Research Letters*, 38(9). L09501.

Slabon, P., Dorschel, B., Jokat, W., Myklebust, R., Hebbeln, D., and Gebhardt, C. (2016). Greenland ice sheet retreat history in the northeast Baffin Bay based on high-resolution bathymetry. *Quaternary Science Reviews*, 154:182 – 198.

Smith, G. C., Roy, F., Mann, P., Dupont, F., Brasnett, B., Lemieux, J.-F., Laroche, S., and Bélair, S. (2014). A new atmospheric dataset for forcing ice-ocean models: Evaluation of reforecasts using the Canadian global deterministic prediction system. *Quarterly Journal of the Royal Meteorological Society*, 140(680):881–894.

Smith, W. H. F. and Sandwell, D. T. (1997). Global seafloor topography from satellite altimetry and ship depth soundings. *Science*, 277:1957–1962.

Straneo, F. (2006). Heat and freshwater transport through the central Labrador Sea. *Journal of Physical Oceanography*, 36(4):606–628.

Straneo, F., Hamilton, G., Sutherland, D., Stearns, L. A., Davidson, F., Hammill, M., Stenson, G. B., and A., R. (2010). Rapid circulation of warm subtropical waters in a major glacial fjord in East Greenland. *Nature Geosci*, 3(3):182–186.

Straneo, F. and Heimbach, P. (2013). North Atlantic warming and the retreat of Greenland's outlet glaciers. *Nature*, 504(7478):36–43.

Straneo, F., Sutherland, D. A., Holland, D., Gladish, C., Hamilton, G. S., Johnson, H. L., Rignot, E., Xu, Y., and Koppes, M. (2012). Characteristics of ocean waters reaching Greenland's glaciers. *Annals of Glaciology*, 53(60):202–210.

Sutherland, D. A., Straneo, F., and Pickart, R. S. (2014). Characteristics and dynamics of two major Greenland glacial fjords. *Journal of Geophysical Research: Oceans*, 119(6):3767–3791.

Swingedouw, D., Rodehacke, C. B., Olsen, S. M., Menary, M., Gao, Y., Mikolajewicz, U., and Mignot, J. (2014). On the reduced sensitivity of the Atlantic overturning to Greenland Ice Sheet melting in projections: a multi-model assessment. *Climate Dynamics*.

van den Broeke, M. R., Enderlin, E. M., Howat, I. M., Kuipers Munneke, P., Noël, B. P. Y., van de Berg, W. J., van Meijgaard, E., and Wouters, B. (2016). On the recent contribution of the Greenland Ice Sheet to sea level change. *The Cryosphere*, 10(5):1933–1946.

Weijer, W., Maltrud, M. E., Hecht, M. W., Dijkstra, H. A., and Kliphuis, M. A. (2012). Response of the Atlantic Ocean circulation to Greenland Ice Sheet melting in a strongly-eddying ocean model. *Geophysical Research Letters*, 39(9).

Williams, C. N., Cornford, S. L., Jordan, T. M., Dowdeswell, J. A., Siegert, M. J., Clark, C. D., Swift, D. A., Sole, A., Fenty, I., and Bamber, J. L. (2017). Generating synthetic fjord bathymetry for coastal Greenland. *The Cryosphere*, 11(1):363–380.

Wilson, N. J. and Straneo, F. (2015). Water exchange between the continental shelf and the cavity beneath Nioghalvfjerdsbrae (79 North Glacier). *Geophysical Research Letters*, 42(18):7648–7654.

Wood, M., Rignot, E., Fenty, I., Menemenlis, D., Millan, R., Morlighem, M., Mouginot, J., and Seroussi, H. (2018). Ocean-Induced Melt Triggers Glacier Retreat in Northwest Greenland. *Geophysical Research Letters*, 45(16):8334–8342.

Zurbenko, I., Porter, P. S., Gui, R., Rao, S. T., Ku, J. Y., and Eskridge, R. E. (1996). Detecting Discontinuities in Time Series of Upper-Air Data: Development and Demonstration of an Adaptive Filter Technique. *Journal of Climate*, 9(12):3548–3560.

Chapter 4

The Balance Between Atmospheric and Lateral Buoyancy Fluxes in Labrador Sea Water Formation

Chapter 4 of this thesis is being prepared for publication with authorship of Laura C. Gillard, Clark Pennelly, Helen L. Johnson, and Paul G. Myers. I was responsible for the analysis and ran all of the model experiments. C. Pennelly provided insight, manuscript edits, and performed some of the calculations: the heat flux at Cape Farewell, convective resistance, and buoyancy flux between the atmosphere and ocean surface. H.L. Johnson and P.G. Myers provided advice, insight, and manuscript edits.

Abstract

Labrador Sea Water formation is a balance between atmospheric buoyancy loss and lateral buoyancy exchange, and is notoriously difficult to represent accurately in ocean and climate models. Lateral exchanges of heat and salt between the shelf and the interior are smaller in a regional coupled ocean-sea ice model at higher vertical resolution (75 levels compared with 50 levels), due in part to altered bathymetry along the Greenland shelf. Reduced lateral exchange results in a stronger stratification in the interior of the Labrador Sea, with stronger convection resistance which results in unrealistically shallow mixed layers. The westward fluxes of heat and salt associated with Irminger Water at Cape Farewell are 50 % and 33 % lower, respectively, with higher vertical resolution. Exchanges south of the Labrador Sea from the North Atlantic Current are also smaller, contributing to the reduction in salt and heat import into the Labrador Sea interior. When the high resolution model is forced with a stronger wintertime buoyancy loss at the ocean surface, this weakens the Labrador Sea stratification, allowing

the forcing to break through the freshwater cap and increasing convection, bringing mixed layer depths back to observed values. A strong atmospheric forcing can therefore compensate for a reduction in lateral advection. Therefore, this study suggests that convection and Labrador Sea Water formation is a careful interplay of surface and lateral fluxes, linked to stratification thresholds.

4.1 Introduction

The Labrador Sea is a high-latitude partially enclosed basin of the North Atlantic Ocean. Located between Canada and Greenland and exposed to the mid-latitude storm track (Lau, 1988), winter storms, extreme winds and cold temperatures drive intense heat exchange between the atmosphere and the ocean (Marshall et al., 1998). Winter buoyancy loss to the atmosphere drives deep mixing of the water column (convection) through plumes sinking to 1500 m or more (Yashayaev and Loder, 2017). After convection, the basin interior is restratified by a lateral exchange of heat and freshwater. The product of convection is the Labrador Sea Water (LSW) which is exported at depth through the North Atlantic Ocean (Talley et al., 2003).

The Atlantic Meridional Overturning Circulation (AMOC) is a large-scale, 3D system of ocean currents and a crucial component of the Earth's climate system due to its role in the uptake and redistribution of heat and other climatically important tracers. The importance of LSW formation in determining the variability and strength of the AMOC has been shown in numerous ocean modelling (e.g. Bailey et al., 2005; Feucher et al., 2019) and climate modelling (e.g. Kuhlbrodt et al., 2007) studies. A recent short 21-month time series associated with the Overturning in the Subpolar North Atlantic Program (OSNAP) observing system suggested that the eastern sub-polar gyre, rather than the Labrador Sea, was largely responsible for setting the strength of the overturning in the sub-polar North Atlantic (Lozier et al., 2019). However, the OSNAP record is too short to shed light on LSW-AMOC linkages, requiring a longer decadal time scale. Regardless of the Labrador Sea's role in AMOC variability, LSW formation is still a crucial process for the ventilation of the deep ocean, transporting heat, nutrients, oxygen, and carbon dioxide from the surface layers to depth (MacGilchrist et al., 2020; Rhein et al., 2017). Therefore, the processes that control deep water formation in the Labrador Sea are important to understand.

Many factors are important for deep convection in the Labrador Sea, such as Arctic freshwater export, storm tracks, and air temperature (Våge et al., 2009). This makes understanding the mechanisms for initiating deep convection complicated. Shifts in storm tracks can influence the convection, as strong westerlies off eastern Canada drag cold air over the Labrador Sea. Frequency and intensity of storms play a major role in the heat loss in the Labrador Sea (Schulze et al., 2016; Våge et al., 2009). Cold air temperatures over an open ocean can increase the heat exchange from the ocean to the air, decreasing the temperature at the surface and thereby increasing the density and initiating deep convection (Våge et al., 2009).

Lateral exchange of buoyant waters from the boundary currents around the Labrador Sea to the interior restratifies the basin. The water column is warmed, and its salinity is modified through lateral fluxes from the warm, salty, subsurface Irminger Water as well as from the fresh surface boundary currents (Straneo, 2006; Yashayaev and Loder, 2009). The subsurface warming produces a flux of heat and salt into the surface layers (Straneo, 2006) and the surface boundary currents contain freshwater fluxes from the Arctic, as well as the Greenland Ice Sheet's (GrIS) meltwater (Dukhovskoy et al., 2019).

In the last decade, there has been an increase in freshwater content in the Arctic Ocean (Rabe et al., 2014), an increase in southward freshwater export via Fram Strait (de Steur et al., 2018) and an increase in the GrIS freshwater flux (Bamber et al., 2018). Observational and modelling studies suggest that the Labrador Sea's convection has not yet been impacted by the input of GrIS meltwater (Böning et al., 2016; Dukhovskoy et al., 2019; Rhein et al., 2018; Yashayaev and Loder, 2017), although, model studies have suggested that the GrIS freshwater flux may enter the interior of the Labrador Sea (Böning et al., 2016; Gillard et al., 2016; Luo et al., 2016). Therefore, freshwater anomalies in the Labrador Sea boundary currents in recent years likely include a signal of increased export of Polar Water as well as of the increased flux of GrIS freshwater (Dukhovskoy et al., 2019).

The Labrador Sea convection strength can weaken due to an increase of buoyant waters in the interior of the Labrador Sea in combination with a weak atmospheric forcing (weak winds and mild winters). Wind-driven Ekman transport and eddies transport freshwater from the surface boundary currents along the Greenland shelf and into the basin (Luo et al., 2016; Schulze Chretien and Frajka-Williams, 2018). Eddies try to restratify after convection by flattening the density gradients to reach a stable water column. Irminger Rings contribute to the restratification of the Labrador Sea with their warm salty water at depth and cold seasonally fresh surface water (de Jong et al., 2014; Gelderloos et al., 2011; Katsman et al., 2004). They are the largest type of eddy in this region (11 - 35 km radius) and the most energetic, generated by the barotropic instability of the West Greenland and Irminger Currents off Cape Desolation (Chanut et al., 2008). The other two types of eddy in this region, convective eddies and boundary current eddies, are smaller, on the order of the Rossby deformation radius (about 7 km in the Labrador Sea), and therefore harder for models to resolve. Boundary current eddies play a small role in re-stratifying the region (Chanut et al., 2008; de Jong et al., 2014; Gelderloos et al., 2011; Katsman et al., 2004). The relative importance of convective eddies is still debated (Rieck et al., 2019).

To complicate this process more, the ocean's convection cycle has a memory, with a preconditioning stage which acts as a positive feedback (Schulze et al., 2016; Yashayaev and Loder, 2017). Years with weak convection or large freshwater fluxes into the Labrador Sea create a buoyant cap that makes it harder for heat loss to occur at the surface to break this barrier and initiate convection in subsequent years. The opposite is true as well, as years with relatively strong convection have such a well-mixed water column that during the following convective season the water column is preconditioned to convect easily. Therefore, lateral exchanges of heat and freshwater by wind forcing (Ekman transport) and eddies combine with air-sea heat fluxes in a non-linear way to impact the convection and restratification processes in the Labrador Sea. This makes it a difficult region for ocean and climate models to simulate accurately.

Ocean simulations at eddy-permitting resolutions within the North Atlantic have been plagued with a salinity drift. Models tend to produce mixed layers that are too deep compared with observations in the Labrador Sea (Rattan et al., 2010), and lower resolution models tend to overestimate LSW formation compared to models run at higher resolution (Garcia-Quintana et al., 2019; Hirschi et al., 2020). The additional LSW can be due to under-representation of lateral transport of buoyant waters from the boundary currents either through freshwater anomalies or by the warm salty subsurface Irminger Waters (Rattan et al., 2010; Treguier et al., 2005).

Not only is the horizontal resolution important to consider in an ocean model, but vertical resolution may also play a strong role. Stewart et al. (2017) argue that changing the vertical resolution changes the vertical structure of horizontal flows rather than just vertical motion. However, the best choice of a vertical grid resolution is not clear at this point for an ocean model. Stewart et al. (2017) showed that by increasing the vertical resolution (from 50 levels to 75 levels) of a $1/10^o$ global ocean model the eddy kinetic energy and sea surface height on and surrounding the Antarctic continental shelf and slopes increased. This improved the formation, shelf exchange and sinking of Antarctic Bottom Water. Colombo et al. (2020) found improvements for the representation of overflow waters at Denmark Strait with a combination of increasing vertical resolution as well as horizontal resolution.

Does changing the vertical resolution impact the lateral buoyancy exchange in the Labrador Sea? And how does a stronger air-sea heat flux interact with any changes in lateral exchange? By examining the lateral exchanges from the shelf to the interior of the Labrador Sea, and air-sea heat fluxes, the response of the convective strength in the Labrador Sea and the formation of LSW to a change in vertical resolution of an eddy-permitting forced ocean model will be investigated.

4.2 Methods

4.2.1 Ocean-Sea Ice Coupled Model

A coupled ocean-sea ice general circulation model is utilized in this study, within the Nucleus for European Modelling of the Ocean (NEMO) (Madec, 2008) framework. The ocean model used is Océan PArallélisé for ocean dynamics and thermodynamics and the Louvain-la-Neuve Ice Model is used for sea ice dynamics and thermodynamics (Fichefet and Morales Maqueda, 1997). The regional domain of the model covers the Arctic and Northern Hemisphere Atlantic Oceans (ANHA) and has two open boundaries, one at Bering Strait and the other at the latitude 20^{o}S. The ANHA horizontal grid is extracted from the ORCA global tripolar grid (Barnier et al., 2007) at a 1/4^o resolution with a horizontal grid spacing ranging from around 14 km to 18 km in the Labrador Sea, and the model is therefore eddy-permitting. All simulations start from January 2002 and are integrated to the end of December 2017. Initial and monthly open boundary conditions (potential temperature, salinity, horizontal velocities, sea ice, and sea surface height) are derived from the Global Ocean Reanalyses and Simulations (GLORYS2V3) product (Ferry et al., 2008). Previous work has shown that to account for model adjustment, a 2-year spin-up period is enough, given the simulations start from the reanalysis of GLORYS2v3 (Garcia-Quintana et al., 2019). The model output used in this study is therefore from 2004 to 2017.

River runoff (excluding Greenland) is provided by Dai et al. (2009). The GrIS freshwater flux is provided by Bamber et al. (2018); this includes tundra and ice sheet runoff, and iceberg discharge. The Bamber et al. (2018) data set extends from 2002 to 2016, and 2016 is repeated for the year 2017 in this study. Runoff is injected at the surface and vertically mixed over the top 30 metres of the water column along the coastline. In this study, runoff has a salinity of 0 and the potential temperature of the ocean grid cell that receives it. For the iceberg discharge an iceberg module is used. This module's physical behaviour is based on the original model of Bigg et al. (1997) with improvements from Gladstone et al. (2001); Marsh et al. (2015); Marson et al. (2018); Martin and Adcroft (2010); Merino et al. (2016).

4.2.2 Vertical representation

Although the number of vertical levels and their structure varies greatly across the modelling community, many NEMO based studies use 45-50 levels (Barnier et al., 2007; Masina et al., 2017; Treguier et al., 2005) with other studies having used 75 vertical levels, such as the GLORYS2V3 product (Ferry et al., 2008). Previous work with the ANHA configuration used in this study had 50 vertical levels. Model experiments were able to reproduce observed Labrador Sea mixed layer depths (e.g. Garcia-Quintana et al., 2019); however, there was a tendency for the model drift to lead to excessive convection. Therefore, the configuration required an atmospheric product with relatively weak buoyancy loss over the Labrador Sea (Pennelly and Myers, prep). Our manuscript developed out of a plan to increase the vertical resolution to 75 layers, with the default assumption that the use of additional vertical resolution would improve the quality of the simulation. Note that the 50 level experiments in this study are not twins of those in Garcia-Quintana et al. (2019) and Pennelly and Myers (prep). As well as the changes in vertical resolution (discussed further below), additional model improvements are included: a switch to NEMO v3.6, replacing the GrIS freshwater discharge with a new data set (Bamber et al., 2018) as well as the use of an iceberg module (Marson et al., 2018; Merino et al., 2016).

All experiments here use geopotential z-level coordinates with a partial step option (Bernard et al., 2006). In the vertical, the experiment with 50 vertical levels has the layer thickness increase from 1.05 m at the surface level to 453.1 m in the last level (at a depth of 5958.3 m) (Figure 4.1a). For the 75-level experiment, the layer thickness increases from 1.05 m at the surface to 204 m in the last level (at a depth of 6000 m).

Bathymetry is taken from the existing global ORCA025 bathymetry (Barnier et al., 2006) which is based on a global relief model (ETOPO1) (Amante and Eakins, 2009) and a gridded bathymetric data set (GEBCO) (BODC, 2008) with modifications (Barnier et al., 2007). The BedMachineV3 data set (Morlighem et al., 2017) has been interpolated and averaged onto the grid along the coast of Greenland for the 75-level experiments. This includes major improvements in deep bathymetric features such as troughs and canyons. Therefore, the bathymetry in the 50-level model version is different in structure around Greenland to that in the 75-level model version. These two representations of the bathymetry are compared in the northwest of the North Atlantic Ocean in Figure 4.1. The 75-level bathymetry shows a deepening in the interior of the Labrador Sea as well as a change in structure and steepness of the shelf off the west coast of Greenland. The 75-level bathymetry is deeper throughout most of the northwest corner of the Atlantic Ocean (Figure 4.1d).

The lateral exchange between the shelf and the Labrador Sea interior may be influenced by these changes in bathymetric structure in the Labrador Sea. Changing the vertical resolution may impact the vertical structure of the horizontal flows as Stewart et al. (2017) showed. Lateral exchange processes such as the production of eddies depend in part on the steepness of the bathymetry (Katsman et al., 2004) and so may also differ between 50 and 75 level versions.

4.2.3 Atmospheric Forcing

This study uses two atmospheric forcing data sets with a difference in the strength of the net buoyancy loss over the interior of the Labrador Sea. One data set used is the Canadian Meteorological Centre's global deterministic prediction system (CGRF) which is a relatively high-resolution product providing atmospheric forcing fields to be used for ocean-sea ice models (Smith et al., 2014). The temporal resolution is hourly, and the spatial resolution is 0.45^o longitude and 0.3^o latitude to generate an equal grid spacing of 33 km resolution at 49^o north and south and a maximum longitudinal spacing of 50 km at the Equator.

The data set that will be used to compare with CGRF is the Drakkar Forcing Set 5.2 (DFS) which provides three hourly atmospheric forcing fields at a spatial resolution of nearly 0.7^o ($\sim$ 80 km at the Equator) (Dussin et al., 2016). The DFS data set was generated from ERA-interim, an atmospheric reanalysis produced by the European Centre for Medium Range Weather Forecasting. Corrections have been applied to the ERA-interim surface variables such as radiation fluxes, wind speeds, decreased air temperature and humidity in the Arctic, and liquid precipitation fields; for more details see Dussin et al. (2016) and Barnier et al. (2007). It should be noted that the CGRF data set does not prescribe snowfall, while DFS does, and snowfall must be hardcoded into the simulation as any precipitation prescribed by CGRF at or below freezing at 2 meters. DFS has been shown in a previous study (Pennelly and Myers, prep) to drive a deeper mixed layer depth by removing the largest amount of buoyancy

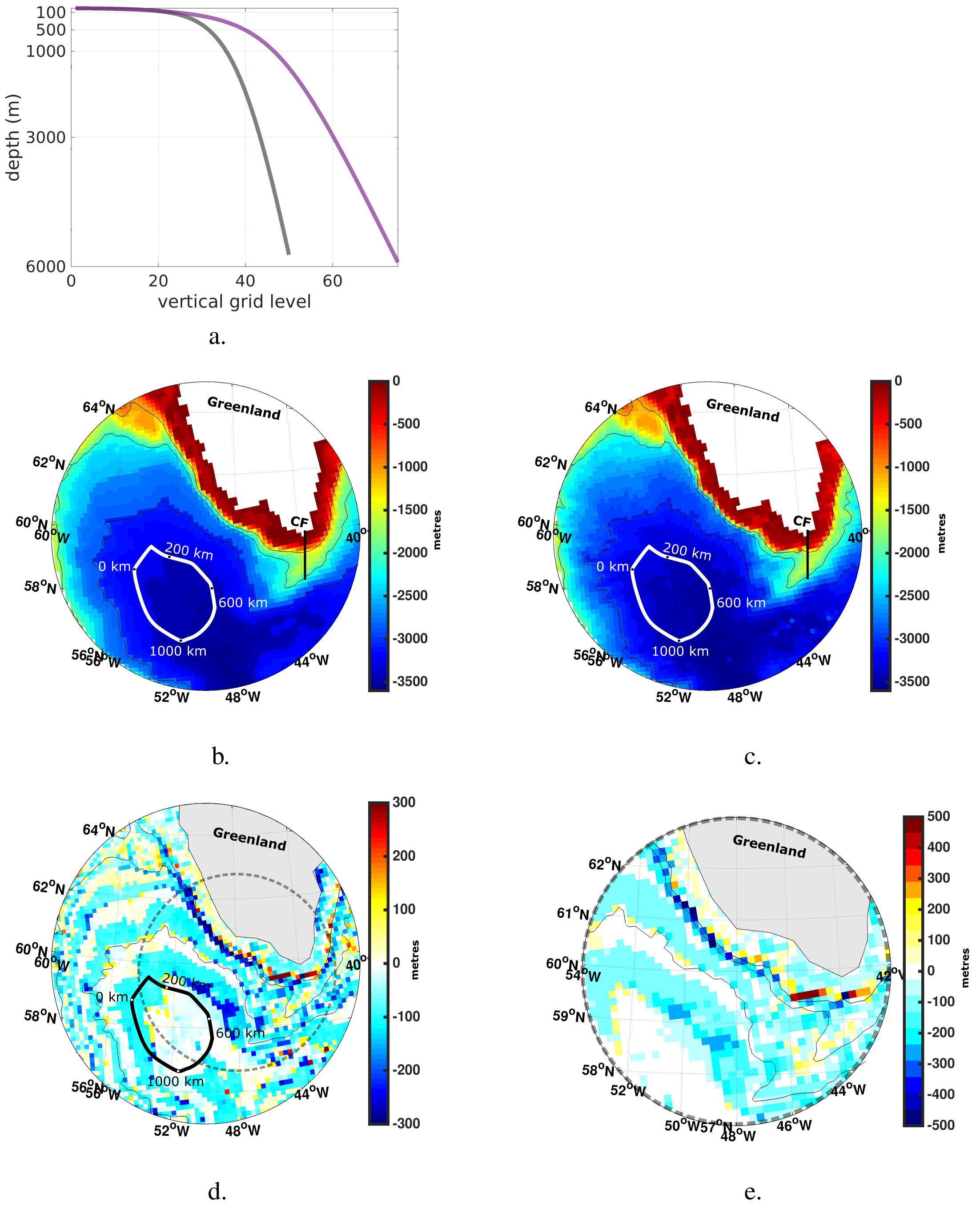

a.

b.

c.

d.

e.

Figure 4.1: Panel a) shows the comparison of the vertical resolution at 50 levels (grey) and 75 levels (purple). Panels b) and c) show the model bathymetry for 50 levels (b) and 75 levels (c). The colour denotes depth in metres. The area of the interior Labrador Sea is shown in the white section. Numbers along the white line indicate kilometre markings along the section. This section was selected following Yashayaev and Loder (2017) and the model study from Garcia-Quintana et al. (2019) following the 3000 m isobath. The Cape Farewell section is indicated by the black line labelled CF. Panel d) shows the difference in bathymetry between the 50 level and the 75 level configuration, where negative numbers show where the 75 level configuration is deeper. Panel e) is a zoom-in of the dashed circle in (d) on the West Greenland Shelf. Black lines show isobaths of 1000 m, 2000 m and 3000 m.

from the ocean in the Labrador Sea when compared to a set of 4 atmospheric products, including CGRF. CGRF was found to have overall less net heat loss over the interior of the Labrador Sea (35 W/m^2) than DFS (43 W/m^2) when averaged from 2002-2015 (Pennelly and Myers, prep).

Experiments using the CGRF atmospheric forcing to drive the NEMO model with 50 vertical levels will be called C50, C75 refers to the 75 vertical level version driven by CGRF, and D75 will have the DFS atmospheric forcing at 75 vertical levels. See Table 4.1 for further details of the three simulations.

4.3 Results and Discussion

4.3.1 Shoaling of the Mixed Layer in the Labrador Sea

The model mixed layer depth, in conjunction with observations from Argo floats, will be evaluated in experiments C50 and C75 (Figure 4.2a). There will be a focus on a small region in the interior of the Labrador Sea (white section in Figure 4.1) where deep convection is observed to occur. Correlation coefficients, denoted as R values, were calculated based on the annual maximum of the mixed layer depth averaged over this region (Figure 4.2b) over 2004-2017 (Table 4.1). The variability of the mixed layer depth in C50 compares better with the Argo observations, with a correlation of 0.80 compared to C75 (correlation of 0.55). The correlations are statistically significant with a P value less than 0.01, i.e. at a 99% confidence level.

During the first 5 years of the analysis period (2004 to 2009), there are only limited discrepancies between the experiments. Following the winter of 2009, when the maximum winter mixed layer depth is deep in both experiments, the winter maximum mixed layer depth in C75 is significantly shallower than that of C50 for every year through to 2017. Other than for the period of 2009-2011, when the maximum winter mixed layer depth from the Argo observations is consistently shallow, there is good correspondence between the maximum winter mixed layer depths from Argo and C50. The Argo floats may underestimate the maximum mixed layer depths in the winters of 2009-2011. Yashayaev and Loder (2016), using multiple data sources, estimate maximum winter mixed layer depths multiple hundreds of metres deeper than from the Argo floats for these years. Looking at the distribution of Argo floats in these years suggests that there were only a limited number of Argo floats in the convection region, offshore of the 3500 m isobaths (not shown).

Focusing on the period of 2012-2017, when deep winter mixed layers were ob-

Table 4.1: Simulations used in this study vary in vertical level (VL) resolution (50 levels vs. 75 levels) and atmospheric forcing (the Canadian Meteorological Centre's global deterministic prediction system (CGRF) (Smith et al., 2014) vs. the Drakkar Forcing Set 5.2 (DFS) (Dussin et al., 2016)). Correlation coefficients of Argo observed mixed layer depth compared with the different simulations from 2004 to 2017 for the Labrador Sea interior (Figure 4.1) are shown in the 4th column. These correlations are statistically highly significant with a P value for all correlations of less than 0.001, therefore at a 99% confidence level. Columns 5 through 7 show the average (2004 to 2017) fluxes of volume (V), temperature (T), and freshwater (FW) (seen in Figure 4.9) through the Cape Farewell section (shown in Figure 4.1), where positive numbers mean westward (or for the freshwater (FW) flux, it means a positive salt flux westward.)

Simulation	VL Resolution	Atmospheric Forcing	Correlation with Argo	V Flux (Sv)	T Flux (TW)	FW Flux (mSv)
C50	50	CGRF	0.80	8.40	210 .23	- 61.63
C75	75	CGRF	0.55	4.45	96.67	- 21.24
D75	75	DFS	0.77	3.03	65.40	- 14.03

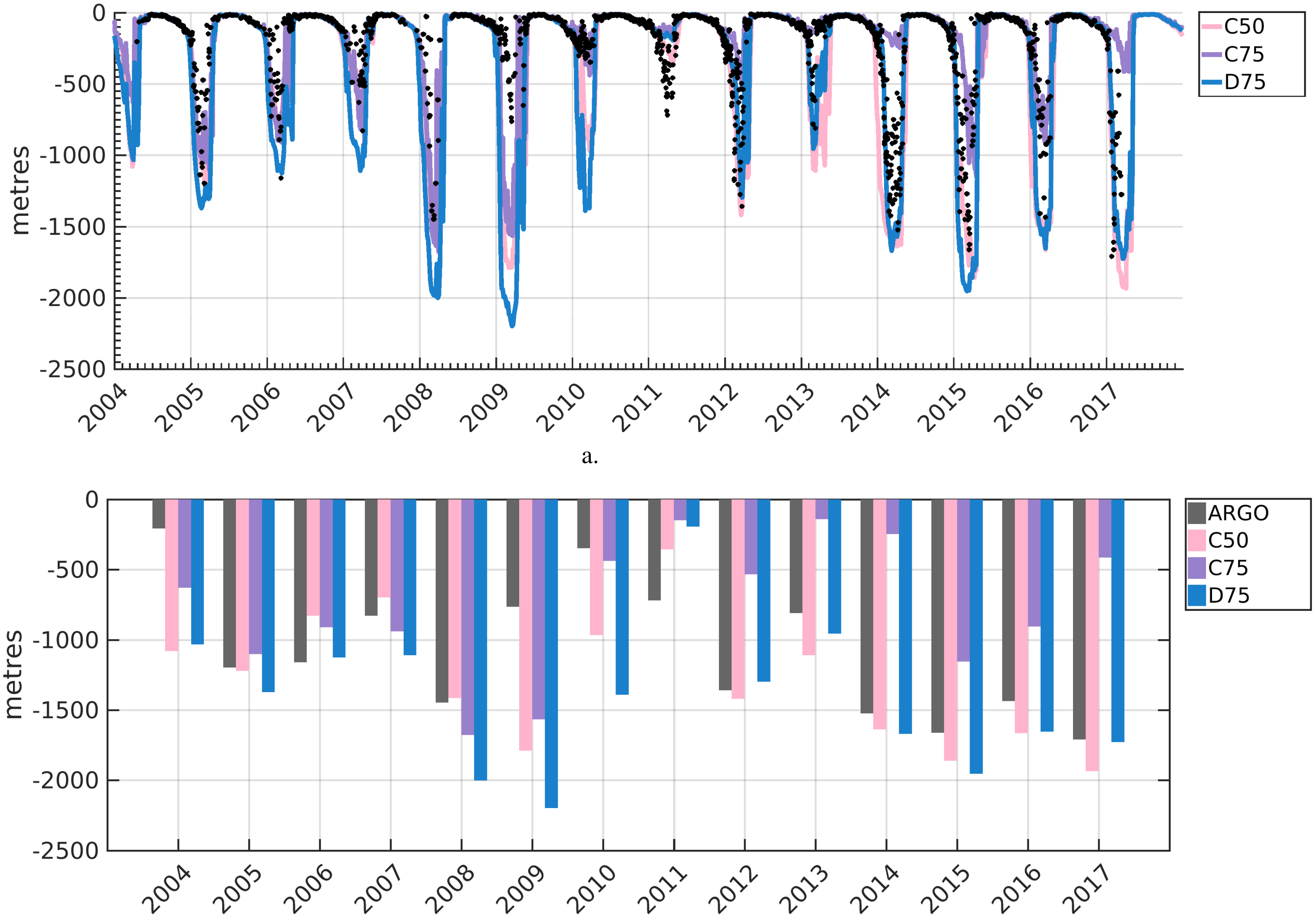

a.

b.

Figure 4.2: The mixed layer depth is averaged over the interior of the Labrador Sea (white section in Figure 4.1). Each experiment's five-day averaged model output of mixed layer depths is averaged spatially over the interior of the Labrador Sea. Argo observations are also averaged over the interior for each day. a) shows the variation of the spatial average for the entire time series, with observations of Argo floats indicated in black circles. b) shows the average's maximum depths over each year.

served in the Labrador Sea (Yashayaev and Loder, 2017), there is a significant difference in the spatial structure of these deep winter mixed layers in C50 compared to C75 (Figure 4.3). Although both experiments find their deepest winter mixed layer depths around 58^oN and 55^oW, in C50 the 400 m and 800 m mixed layer depth contours extend north past 60^oN and east as far as Cape Farewell. Even the 1200 m contour covers a broad region in the central Labrador Sea. Meanwhile, in C75 the winter mixed layer is deeper than 400 m only over a small region in the center of the Labrador Sea (Figure 4.3). For C50, the 2012-2017 average winter mixed layer depth exceeded 1600 m depth, whereas in C75 the average mixed layer does not surpass 600 m. Therefore, while C50's maximum winter mixed layer depth time series (Figure 4.2a and 4.2b) matches closely to the observed, the area covered by deep mixed layers in C50 is too large. While the winter mixed layer depths in C75 are far too shallow, the spatial structure of where those 'deep' mixed layers occur is closer to observed.

The occurrence of convection and deep winter mixed layers depends on the stratification as well as the air-sea buoyancy fluxes. The strength of the stratification in the Labrador Sea, for both experiments (Figure 4.4a and Figure 4.4b), was quantified by determining the water column stability to a depth (h) and quantifying the amount of energy per unit volume (J/m^3) needed to overcome that stratification and mix to that depth (h). This measure is called convection resistance, where high convective resistance indicates the presence of a "barrier to convection" as Bailey et al. (2005) discussed. Convection resistance (CR) is defined in Equation 4.1, based on previous work by Holdsworth and Myers (2015), with concepts of buoyancy anomalies as described in Bailey et al. (2005), and Frajka-Williams et al. (2014):

$$CR(h) = \frac{g}{A} \int \int_A \left[h\sigma_\theta(h) - \int_0^h \sigma_\theta(z) dz \right] dA \tag{4.1}$$

where g is the acceleration due to gravity (9.81m/s^2) and A is the area of each grid cell. The amount of potential energy in a well-mixed column of fluid with a density of $\sigma_\theta(h)$ is compared to that in the modelled water column with a potential density of $\sigma_\theta(z)$ at each depth ($z < h$). Equation 4.1 therefore gives the total amount of energy required to mix the water column to a depth h = 2000 m (which is considered to be the maximum depth of LSW formation in this study; those areas with water depths less than 2000 m are ignored for this analysis).

CR(h)=0 implies a well-mixed fluid, CR(h)>0 implies a stable density stratification, and CR(h)<0 implies an unstable density stratification. There is significantly more convection resistance throughout the Labrador Sea in C75 (Figure 4.4b) than

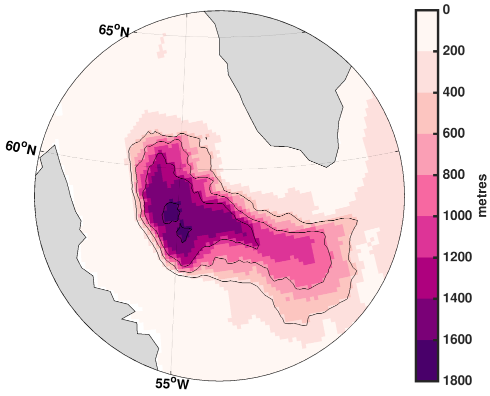

a. C50

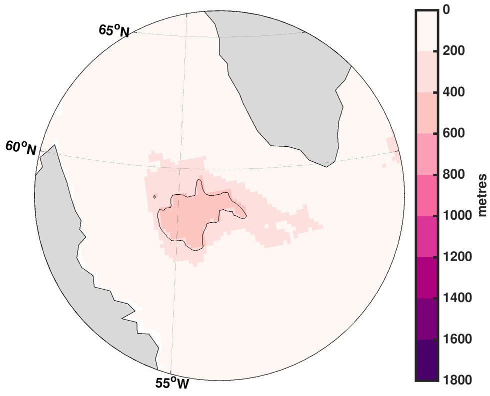

b. C75

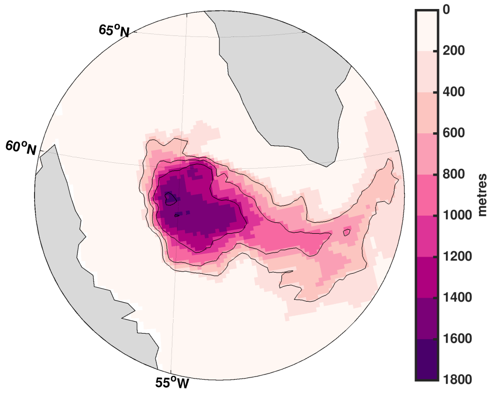

c. D75

Figure 4.3: Mixed layer depths averaged for January, February and March of years 2012 to 2017. Post 2010 years chosen based on known timing of deep mixed layer depths from observations (Argo floats) and where configurations deviate from each other. Each panel shows a different experiment: a) C50, b) C75, and c) D75. Contour lines show intervals of 400 m (400 m, 800 m, 1200 m and 1600 m).

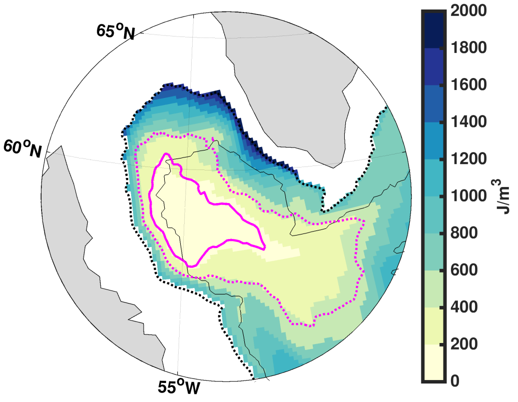

a. C50

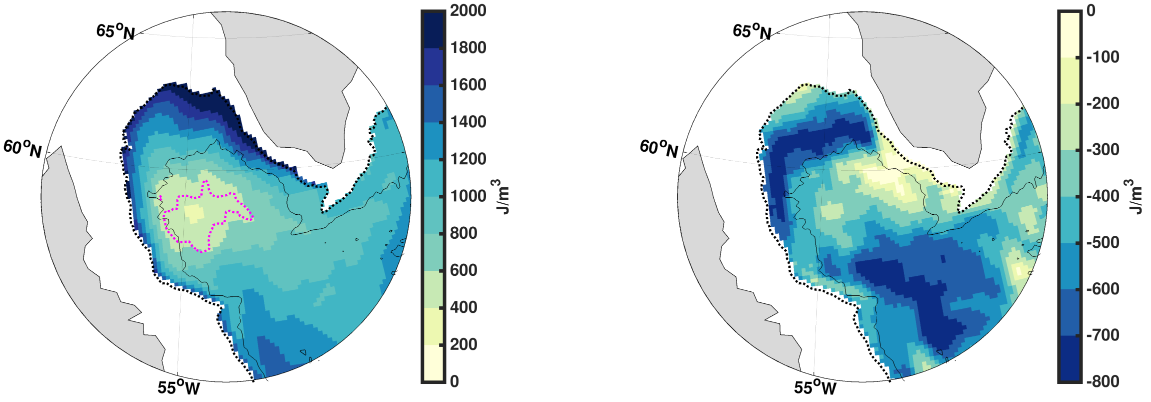

b. C75

c. C50-C75

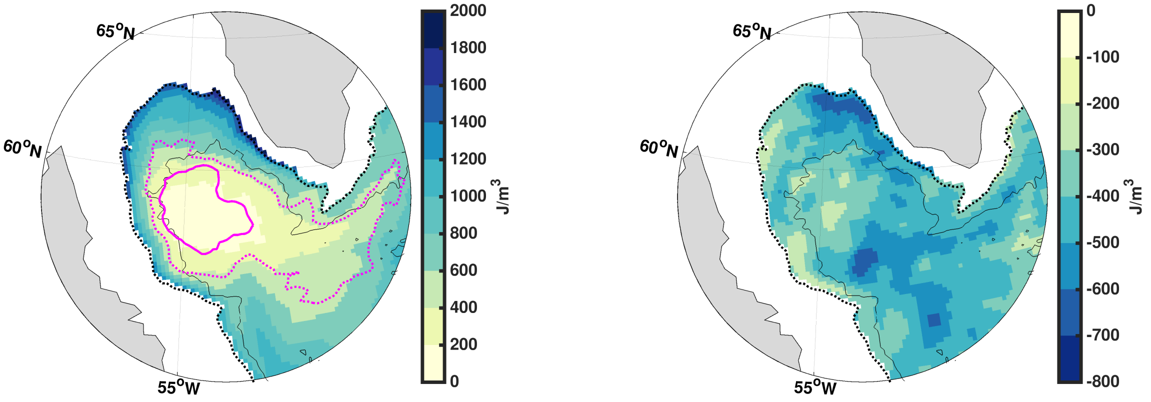

d. D75

e. D75-C75

Figure 4.4: Convective resistance averaged over the period 2012 - 2017 for the winter months of January to March; units are J/m^3. Dashed black line shows 2000 m isobath and solid black line shows 3000 m isobath. Magenta lines show mixed layer depths of 400 m (dashed) and 1200 m (solid). Regions with bathymetry shallower than 2000 m are masked out of the figure. Each configuration is shown: (a) C50, (b) C75, (c) shows the difference between C50 and C75, (d) D75, and (e) shows the difference between D75 and C75.

C50 (Figure 4.4a). In both experiments, the least convection resistance is in the western Labrador Sea, consistent with where the mixed layers are deepest. In C75, the western Labrador Sea is the only portion of the basin with convection resistance less than 600 J/m^3, with the convection resistance increasing from there, almost uniformly, in all directions. In C50, convection resistance remains low over a much larger area, consistent with the 400 m winter mixed layer depth contour. The difference plot of C50-C75 (Figure 4.4c) shows a big increase in convection resistance, exceeding 700 J/m^3, in the north and south of the Labrador Sea with smaller differences in between, approaching 0 J/m^3, reaching offshore from the West Greenland Current.

The large differences in convection resistance between C50 and C75 suggest that there must be significant differences in the water mass properties in the interior of the Labrador Sea between the two experiments. Given the significant differences in winter mixed layer depth, a potential temperature versus salinity plot for the Labrador Sea interior for 2012 to 2017, showing the wintertime water mass properties in C50 and C75 is examined (Figure 4.5). In C75, there is a large amount of cold (T$< 2^o$C), fresh (S < 33), and light water ($\rho < 26.5$ kg/m^3) that is not transformed into dense water. From 2012 to 2017, the upper 450 m in the Labrador Sea is on average significantly saltier (Figure 4.6a) and warmer (Figure 4.6b) in C50 than C75. A depth of 450 m is considered here because it includes both the upper ocean freshwater layer as well as the main core of the Irminger Water.

Another way to examine the property changes is to compute the freshwater and heat content for the interior of the Labrador Sea (Figure 4.7; Equation 4.2 and Equation 4.3). The freshwater content (FWC; units in m^3) relative to a reference salinity S$_{ref}$=34.8 (Aagaard and Carmack, 1989), is:

$$FWC = \int \frac{S_{ref} - S}{S_{ref}} dV \tag{4.2}$$

where S is model salinity. The heat content (HC; in TW) is defined as:

$$HC = \int (T - T_{ref}) \rho_0 C_p 10^{-12} dV \tag{4.3}$$

where T is the model potential temperature, $T_{ref} = -2^oC$ is the reference temperature, ρ_0 is the reference density (1026 kg/m^3; Madec, 2008) and C_p is the specific heat capacity of sea water (3992 J/kg/^{o}C; IOC, SCOR, and IAPSO, 2010).

From 2004 to 2009, there was little difference in the freshwater content between the two experiments with it slowly decreasing with time in all runs, consistent with

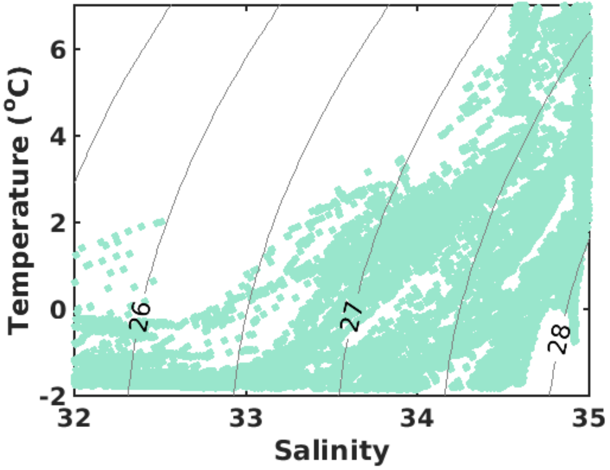

a. C50

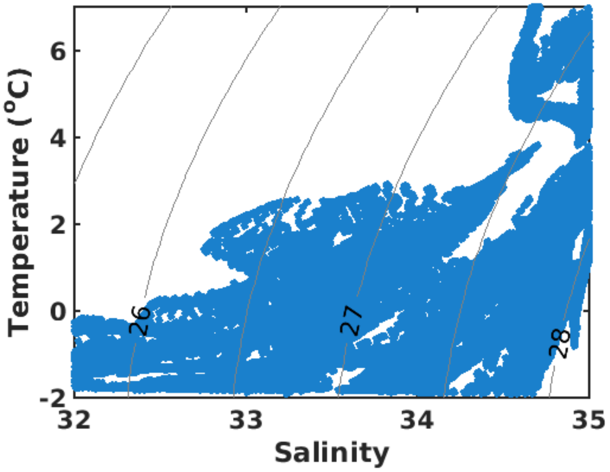

b. C75

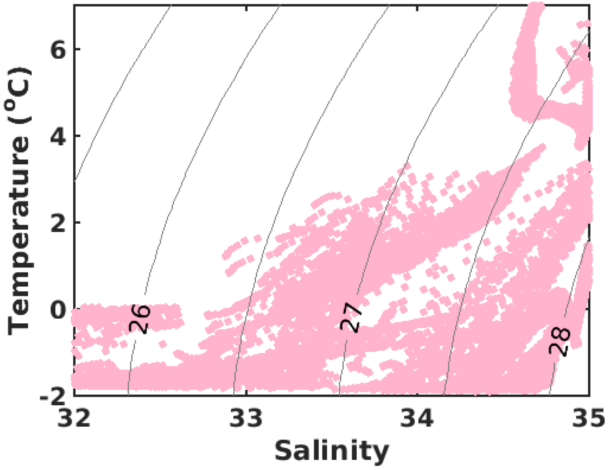

c. D75

Figure 4.5: Potential temperature and salinity plot for the interior of the Labrador Sea. Model fields are plotted the same for all experiments, January to March of 2012 to 2017 within the top 1500 m of the water column. Model fields are subsampled to reduce the number of points plotted by 1/8. Points with a salinity of less than 32 or more than 35, or warmer than 7^oC are excluded. Thin black curved lines are potential density in kg/m^3. Each panel shows a different experiment: a) C50, b) C75, and c) D75.

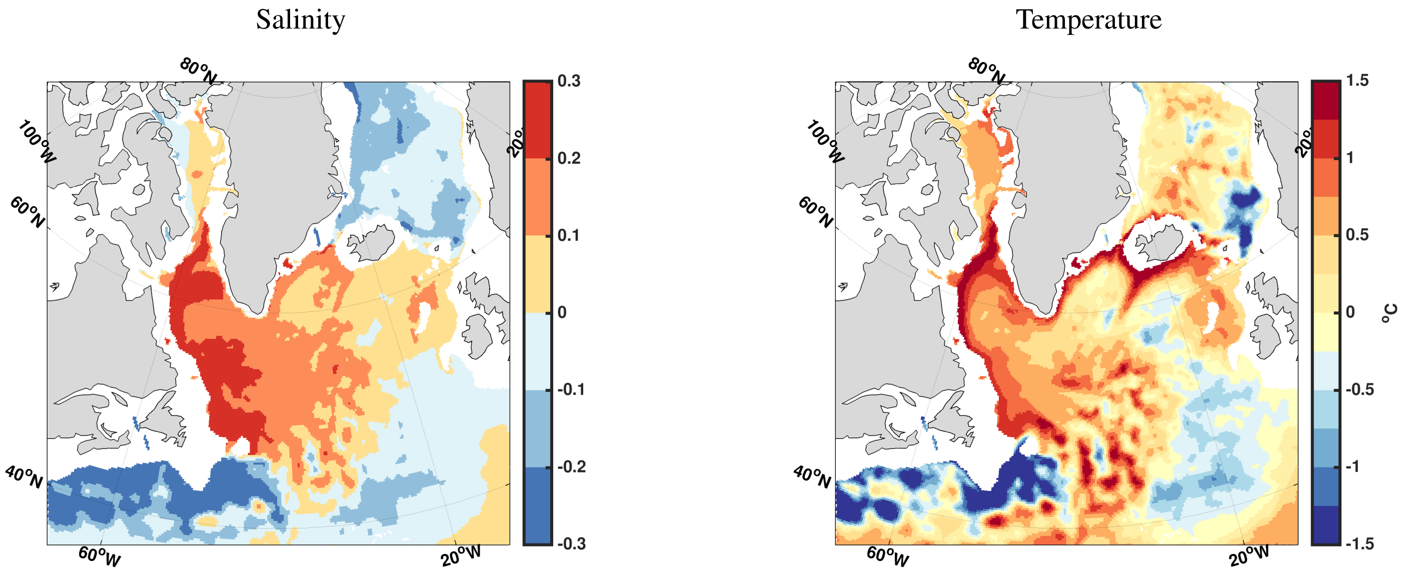

a. C50 - C75

b. C50 - C75

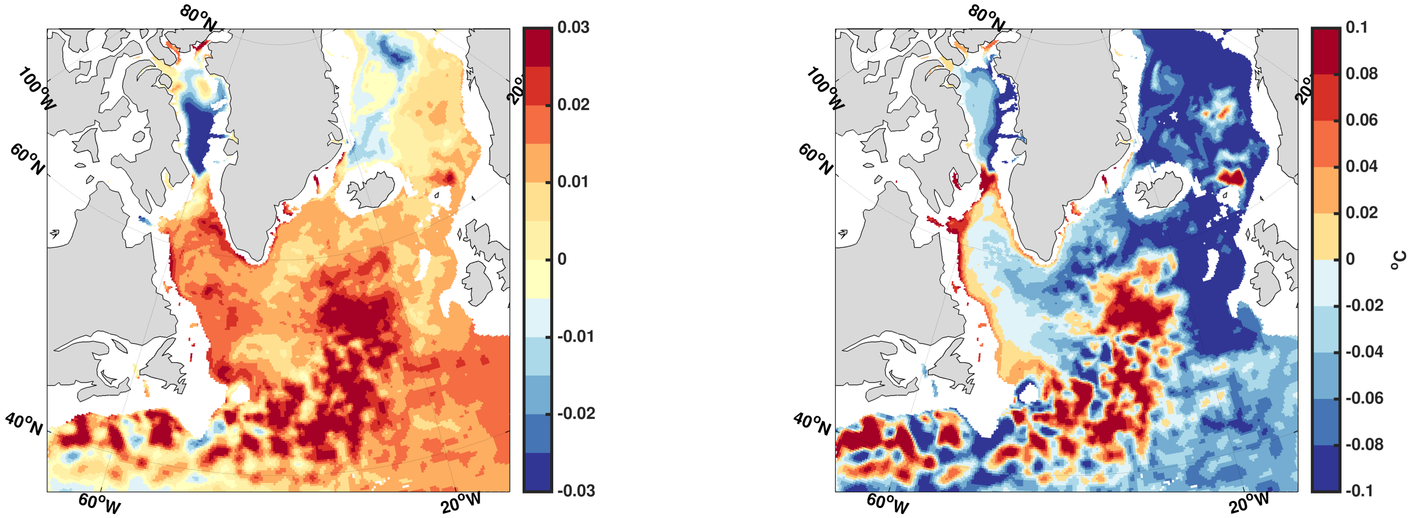

c. D75 - C75

d. D75 - C75

Figure 4.6: Difference in winter-time (Jan.-March, 2012-2017) average salinity (left) and temperature (right) over the upper 450 m of the water column for C50-C75 (top) and D75-C75 (bottom).

model drift (Rattan et al., 2010). However, after 2009 the freshwater content of the runs diverges suddenly and significantly, increasing in C75 while it continues to slowly decline in C50 (Figure 4.7). The heat content begins to diverge earlier, in 2006, with the upper ocean in C50 significantly warmer over time than in C75. The opposing behaviour in freshwater and heat content in the interior for C50/C75 (saltier and warmer in C50 and fresher and colder in C75) may have resulted in little effect on density. However, there would be a greater likelihood of deep mixing if the saltier ocean in C50 could be cooled sufficiently in winter, which is what occurred in that experiment.

4.3.2 Lateral Buoyancy Fluxes Impact on the Labrador Sea Water Formation

Next, where there is significant exchange between boundary and interior of the Labrador Sea will be examined to explain the previous differences in potential temperature and salinity (Figure 4.5) as well as heat and freshwater content (Figure 4.6). The spatial and temporal variability of the exchange between the interior and surrounding regions is shown in Figure 4.8. Exchanges from the west (1000-1400 km) and north (0-200 km) are generally small and similar between the two experiments (C50 and C75). Exchange from the West Greenland Current (200-700 km) and the south (700-1000 km) explain the larger heat and salt content in the interior of the Labrador Sea in C50, as there was continual transport of warm and salty waters into the basin. In C75, these exchanges are much smaller, especially from the West Greenland Current (volume flux of 0.05 Sv compared to volume flux of 0.1 Sv in C50).

Without this source of heat and salt, the interior of the Labrador Sea in C75 freshens (Figure 4.7a) and cools (Figure 4.7b). Exchange of warm water across the southern boundary of the Labrador Sea interior region, in C75, begins around 2012 (1.5 TW; Figure 4.8h) potentially explaining the stabilization of the freshwater and heat content time series after that date (Figure 4.7). Export to the south in C75 is about half of the export in C50 for freshwater transport (-0.5 mSv vs -1 mSv; Figure 4.8e and Figure 4.8d, respectively), and heat transport ($\sim$ 1 TW vs 2 TW; Figure 4.8h and Figure 4.8g, respectively).

The modified Irminger Water transported into the Labrador Sea around Cape Farewell (location shown in Figure 4.1) is an important source of heat and salt for the West Greenland Current. A time series of the westward flux of Irminger Water (defined by $S > 34.8$, $T > 3.5\,^{o}C$, and $\rho < 27.68$ kg/m^3) past Cape Farewell is shown in Figure 4.9. Following 2009, the volume flux is larger in C50 than C75 ($\sim$12 Sv vs $\sim$6 Sv; Figure 4.9a). On average, C50 has a stronger westward salt flux (62 mSv), about three times

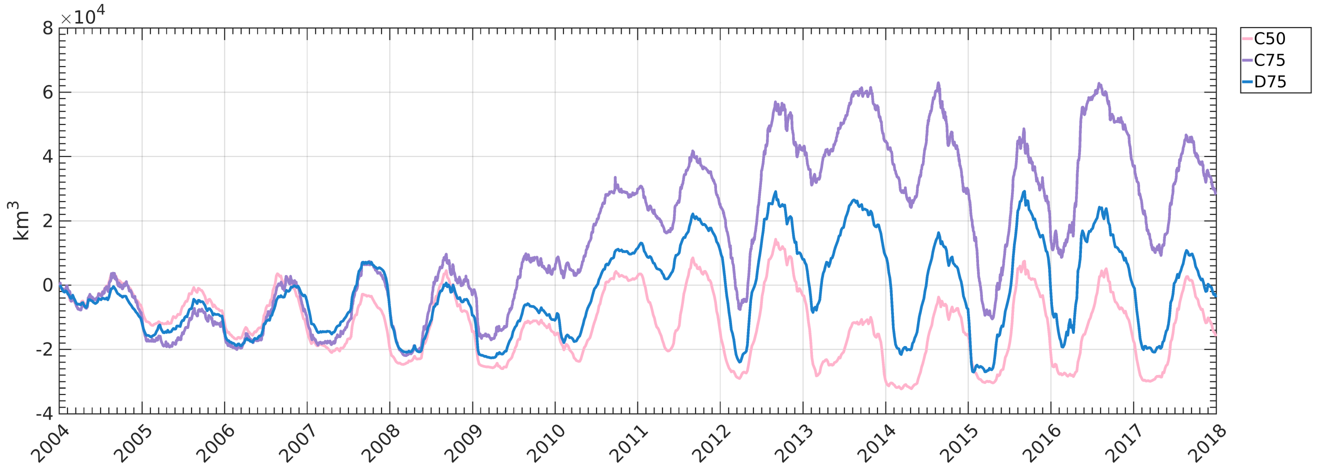

a. Freshwater Content

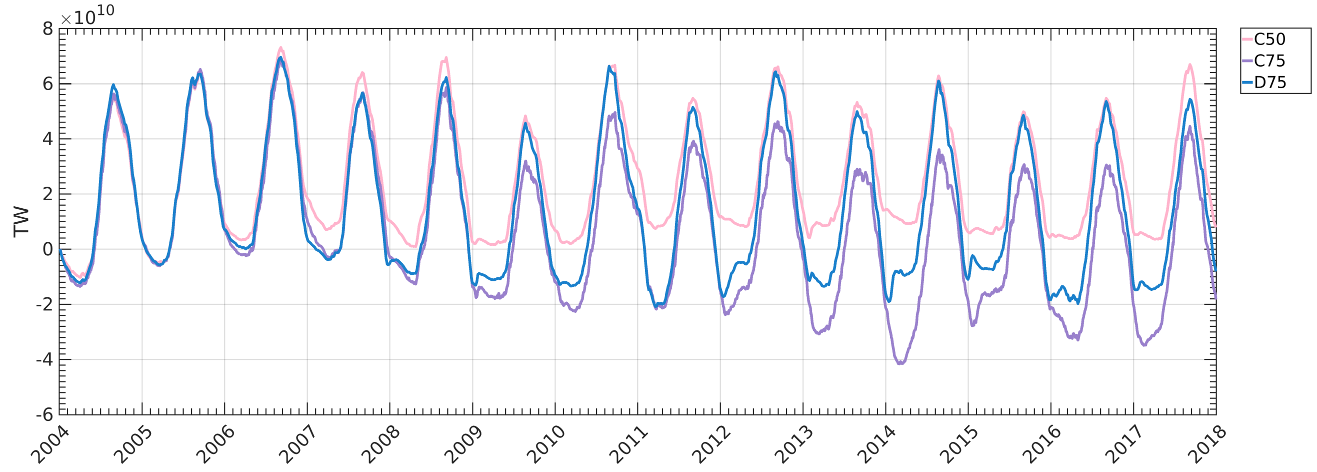

b. Heat Content

Figure 4.7: Interior of the Labrador Sea's freshwater (a) and heat content (b) over the top 1500 m of the water column (Equation 4.2 and Equation 4.3), referenced to the beginning of the time series (5 day average at the start of January 2004).

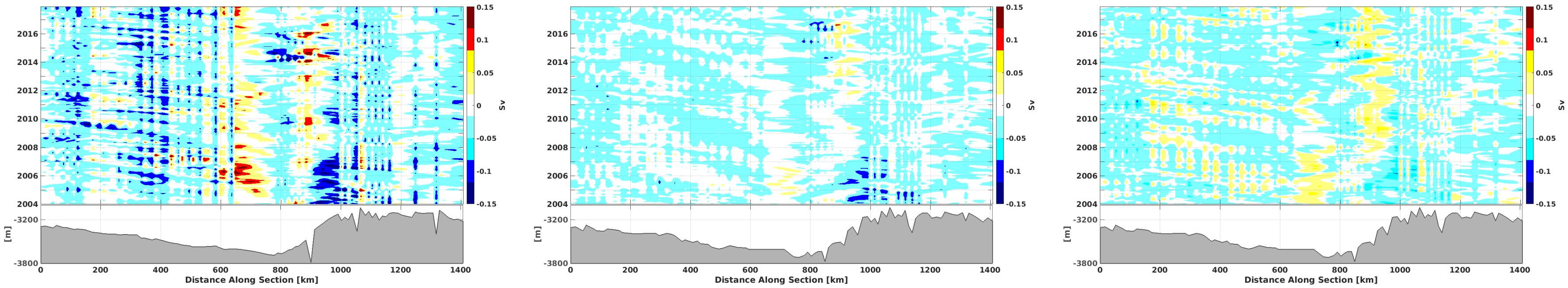

a. C50 Volume Flux b. C75 Volume Flux c. D75 Volume Flux

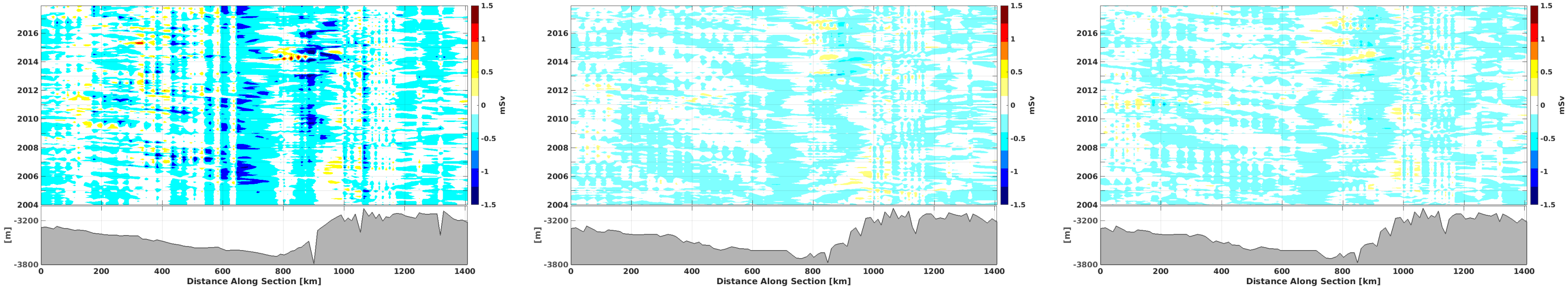

d. C50 Freshwater Flux e. C75 Freshwater Flux f. D75 Freshwater Flux

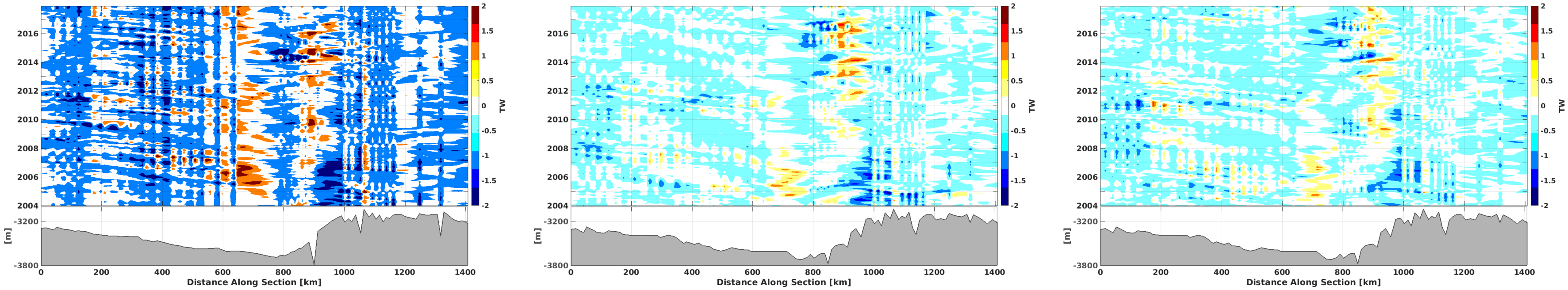

g. C50 Temperature Flux h. C75 Temperature Flux i. D75 Temperature Flux

Figure 4.8: Monthly averaged fluxes into (positive) and out of (negative) the interior of the Labrador Sea. Fluxes are vertically integrated from 0 to 1500 m. Distance markers along the section on the x-axis can be seen in Figure 4.1. A comparison of changing the vertical levels and atmospheric forcing is shown with C50 as the left column and C75 as the centre column and D75 on the right column. Each row shows a different type of flux, the first row shows volume flux in Sv, the second row shows freshwater flux in mSv, and the third row shows temperature flux in TW.

larger than in C75 (21 mSv; Figure 4.9b, Table 4.1). Additionally, C50 has on average a greater temperature flux westward (210 TW), about two times larger than in C75 (97 TW; Figure 4.9c; Table 4.1). But it is not just that more heat and salt are entering the Labrador Sea in C50 than in C75, the strength of eddy kinetic energy (EKE) also differs.

The average EKE (2012 to 2017) of the top 500 m of the water column, in C50 and C75, is shown in Figures 10a and 10b. The monthly EKE was calculated using Equation 4.4; u^2 and v^2 were calculated for every five-day model zonal and meridional velocities and then averaged of the month, and $\bar{u}$ and $\bar{v}$ denote the monthly mean averages.

$$EKE = \frac{(\bar{u^2} - \bar{u}^2) + (\bar{v^2} - \bar{v}^2)}{2} \tag{4.4}$$

Given the horizontal resolution of 1/4^o, it is not surprising that the EKE in these simulations is significantly less than in observations (Fratantoni, 2001); this is a known issue with models that are not eddy-resolving (Chanut et al., 2008; Pennelly et al., 2019).

The differences between the two simulations are shown in Figure 4.10c, where the EKE in C50 has the EKE in C75 subtracted from it. Therefore, positive (negative) values indicate that C50 (C75) has higher EKE values. The EKE in C50 is larger by $\sim$ 20 cm^2/s^2 offshore of the WGC near the 3000 m isobaths, and by $\sim$ 15 cm^2/s^2 in the northwest corner along the 2000 m isobath. The EKE in C75 is larger by $\sim$ 10 cm^2/s^2 along the 2000 m isobath off the south portion of the Canadian shelf. The decrease in the EKE in the 75-level experiment maybe because the 50-level experiment's vertical structure has a sharper gradient (Figure 4.1), which may promote more instabilities and therefore mixing.

The strong transport of warm and salty water into the southern part of the Labrador Sea interior in C50 is consistent with the expanded band of low convection resistance stretching south of Cape Farewell (Figure 4.4a). Without it, as shown in C75, convection resistance remains large in this southern region (Figure 4.4b). A large transport of Irminger Water north in the West Greenland Current, in C50, leads to saltier conditions in the northern Labrador Sea (Figure 4.6). Therefore, low convection resistance (Figure 4.4a) and a broad northward extension of the region of deep winter mixed layers occurs (Figure 4.3a). Although the maximum winter mixed layer depths in C75 are shallower than observed, the spatial extent of deep winter mixed layers is more realistic in C75 than in C50.

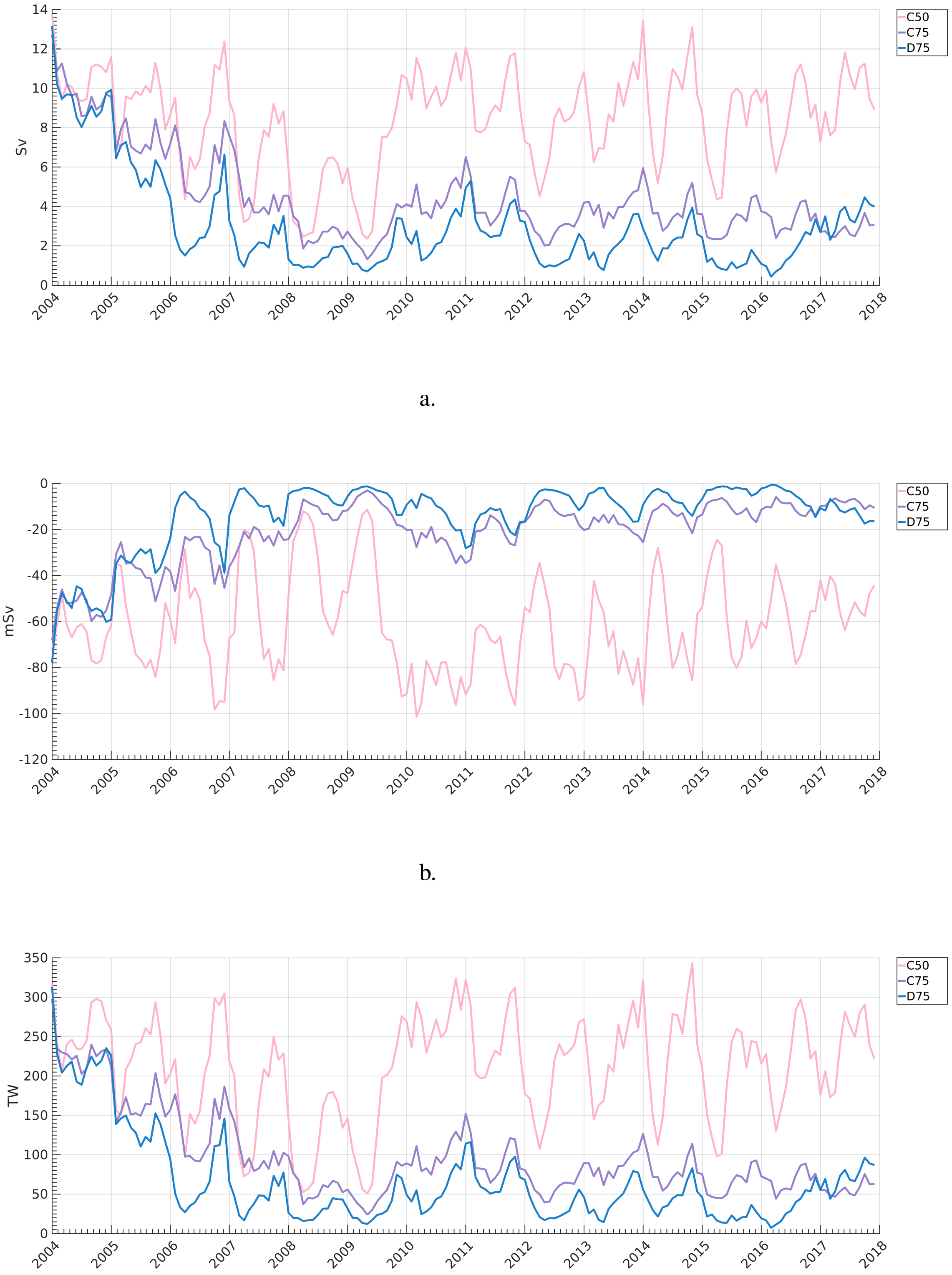

a.

b.

c.

Figure 4.9: Irminger Water mass fluxes at Cape Farewell (location shown in Figure 4.1) of volume (a), freshwater (b), and heat (c). Positive values indicate flux direction to the west. Bounds for the water mass properties are $34.8 < S$, $-5^oC < T^oC$ and $\rho < 27.68 kg/m^3$.

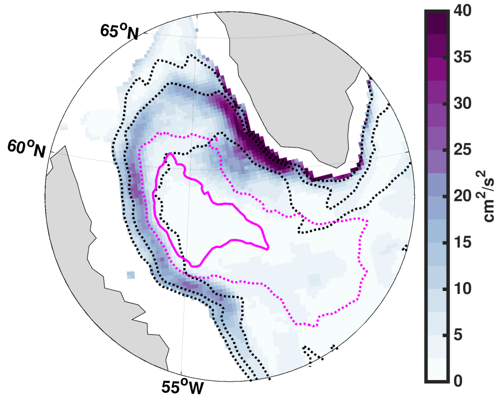

a. C50

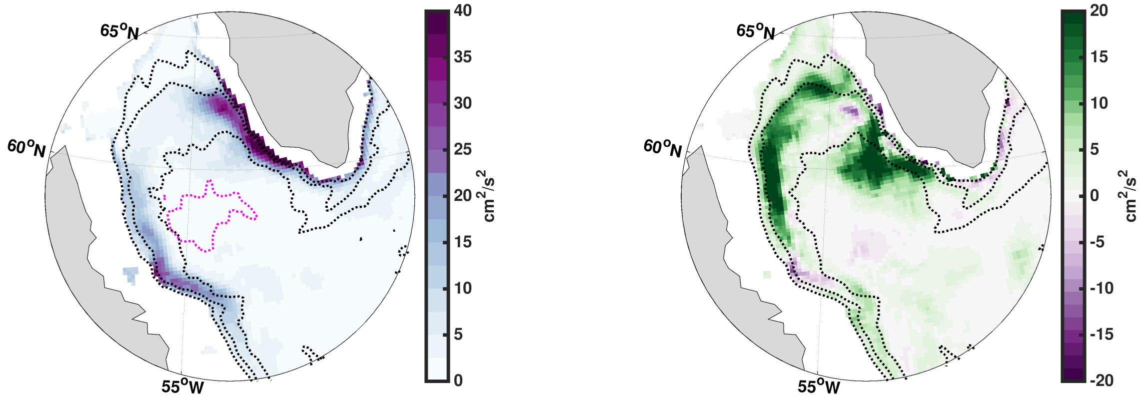

b. C75

c. C50 - C75

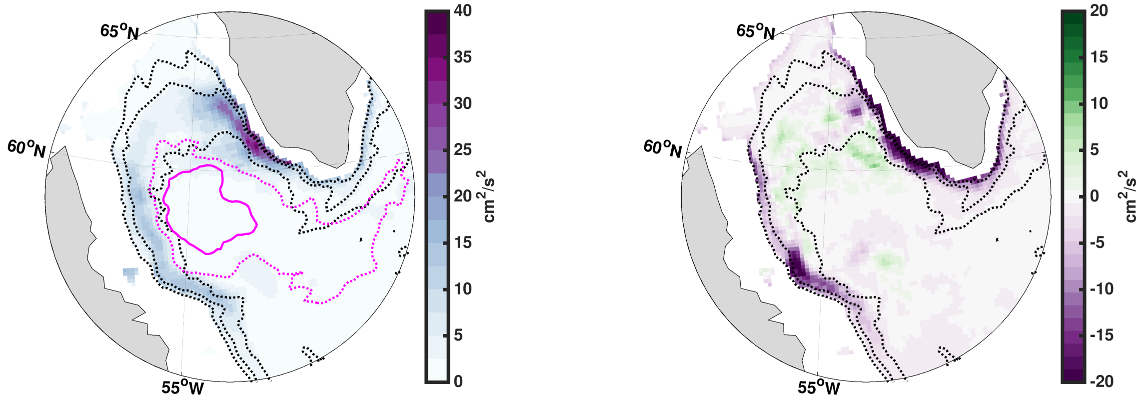

d. D75

e. D75 - C75

Figure 4.10: Average EKE of the top 500m of the water column for the winter months (January to March) of 2012 to 2017. Regions with bathymetry less than 500m are masked out of the figure. Calculated using model velocities in Equation 4.4. Dashed black lines show depth contours of 1000m, 2000m, and 3000m. Magenta lines show average mixed layer depths of 400m (dashed) and 1200 (solid). Each experiment is shown: (a) C50, (c) C75, (c) shows the difference between C50 and C75, (d) D75, and (e) shows the difference between D75 and C75.

4.3.3 Influence of Atmospheric Buoyancy Fluxes on Labrador Sea Water Formation

LSW formation is a balance between atmospheric buoyancy loss and lateral buoyancy exchange from the boundary currents. Section 4.3.2 showed how differences in the lateral exchange between the 50 and 75 level model versions impact the water properties in the interior of the Labrador Sea. In this section, two experiments with different air-sea buoyancy forcing will also be compared.

The average monthly buoyancy flux, B_φ (N/m^{2}s), into the ocean over the interior of the Labrador Sea using an equation from Sathiyamoorthy and Moore (2002) and Gill (1982) that sums the thermal and haline forcing contributions is computed by:

$$\begin{gathered} B_\varphi = b_q + b_s \\ \text{with} \\ b_q = \frac{g\alpha}{C_p}\varphi_q \text{ and } b_s = gS\beta\varphi_s \end{gathered} \tag{4.5}$$

For the buoyancy heat flux (b_q), g is gravity, $\alpha = \rho^{-1}\partial\rho/\partial T$ is the thermal expansion coefficient of seawater at the surface, T is the sea surface temperature, C_p is the specific heat capacity of water (3992 J/kg/^{o}C; IOC, SCOR, and IAPSO, 2010), and φ_q is the heat flux into the ocean at the surface. For the buoyancy salt flux (b_s), S is the salinity of the model at the surface, $\beta = \rho^{-1}\partial\rho/\partial S$ is the saline contraction coefficient and $\varphi_s = (P-E)$ is the ocean salt flux at the surface where P is the precipitation and E is the evaporation. The saline contribution comes from the addition or removal of freshwater. The surface of the ocean gains buoyancy when $B_\varphi > 0$ and thus becomes less dense, while the surface is losing buoyancy and becoming denser when $B_\varphi < 0$.

The time series of the buoyancy forcing over the interior of the Labrador Sea is shown in Figure 4.11. All three experiments show similar seasonality for the surface buoyancy loss and gain over the Labrador Sea. The ocean surface of the Labrador Sea in C75 gains more buoyancy throughout the years than in C50. In C50 the ocean surface gains the least amount of buoyancy and additionally loses similar amounts of buoyancy to the atmosphere than in C75. Therefore, there is stronger net buoyancy loss observed in C50 than in C75. It may seem strange that these two experiments, which use the same atmospheric forcing, have a different wintertime buoyancy loss (see Figure 4.11a, 2011 to 2017). However, the model heat fluxes are computed from bulk formulae (Large and Yeager, 2004) and both the latent and sensible heat components depend on the sea surface temperature. Given the warmer upper ocean in C50 (Figure

4.6b, 4.7b), cold surface air temperatures in winter lead to greater cooling, heat fluxes, and buoyancy loss. Given the stronger buoyancy loss and weak stratification (Figure 4.4a), widespread and deep winter mixed layers can develop across the Labrador Sea in C50. Meanwhile, with cooler pre-winter sea surface temperatures leading to weaker buoyancy loss in C75, the result is that the larger convection resistance in this experiment (Figure 4.4b) cannot be overcome and only shallow and limited convection occurs.

Pennelly and Myers (prep) used a 50 vertical level configuration similar to C50 and forced with the CGRF forcing (Smith et al., 2014); this has been shown to have weaker buoyancy loss over the Labrador Sea than other atmospheric forcing products used in their study. In the 75 vertical level version C75 (which also has different bathymetry along the Greenland shelf), the water mass properties in the interior of the Labrador Sea are different and the CGRF atmospheric forcing does not result in strong enough buoyancy loss to produce realistic LSW. Thus, one of the atmospheric products identified by Pennelly and Myers (prep) with strong buoyancy loss over the Labrador Sea, DFS (Dussin et al., 2016) is considered. Therefore, an equivalent 75 level experiment forced with DFS (this study refers to this model simulation as D75) is carried out. The surface layer of the Labrador Sea in D75 has a different net annual air-sea buoyancy flux, and gains and loses less buoyancy than in C75 (Figure 4.11).

Mixed layer depths in the Labrador Sea are deeper in D75 than C75, with the winter maximums close to C50 (Figure 4.2). The variability in maximum winter mixed layer depth in D75 is now closer to the Argo observations with a correlation of 0.77 (Table 4.1). The spatial structure of the mixed layer shows a broader and deeper structure in D75 than C75 (Figure 4.3). D75 shows a mixed layer of 400 m closer to the Irminger Sea which is more in-line with observations (Yashayaev and Loder, 2017) than the other simulations in this study, as C50 overestimates the depth while C75 underestimates it. Compared to C50, the extent of excessively deep mixed layers north of 60^oN is reduced (Figure 4.3). The convection resistance in the interior of the Labrador Sea is 200 J/m^3 less in D75 than in C75, and there is even more of a difference in convection resistance north (500 J/m^3) and south ($\sim$ 600 J/m^3) of the Labrador Sea core convection region compared to C75 (Figure 4.4e). In the Labrador Sea, a stronger buoyancy loss in D75 created a weaker stratification than in the too strongly stratified C75.

On average in the winter, the top 1500 m of the Labrador Sea's interior in D75 had denser water (greater than 26.5 kg/m^3) than in C75 (Figure 4.5). In D75, there

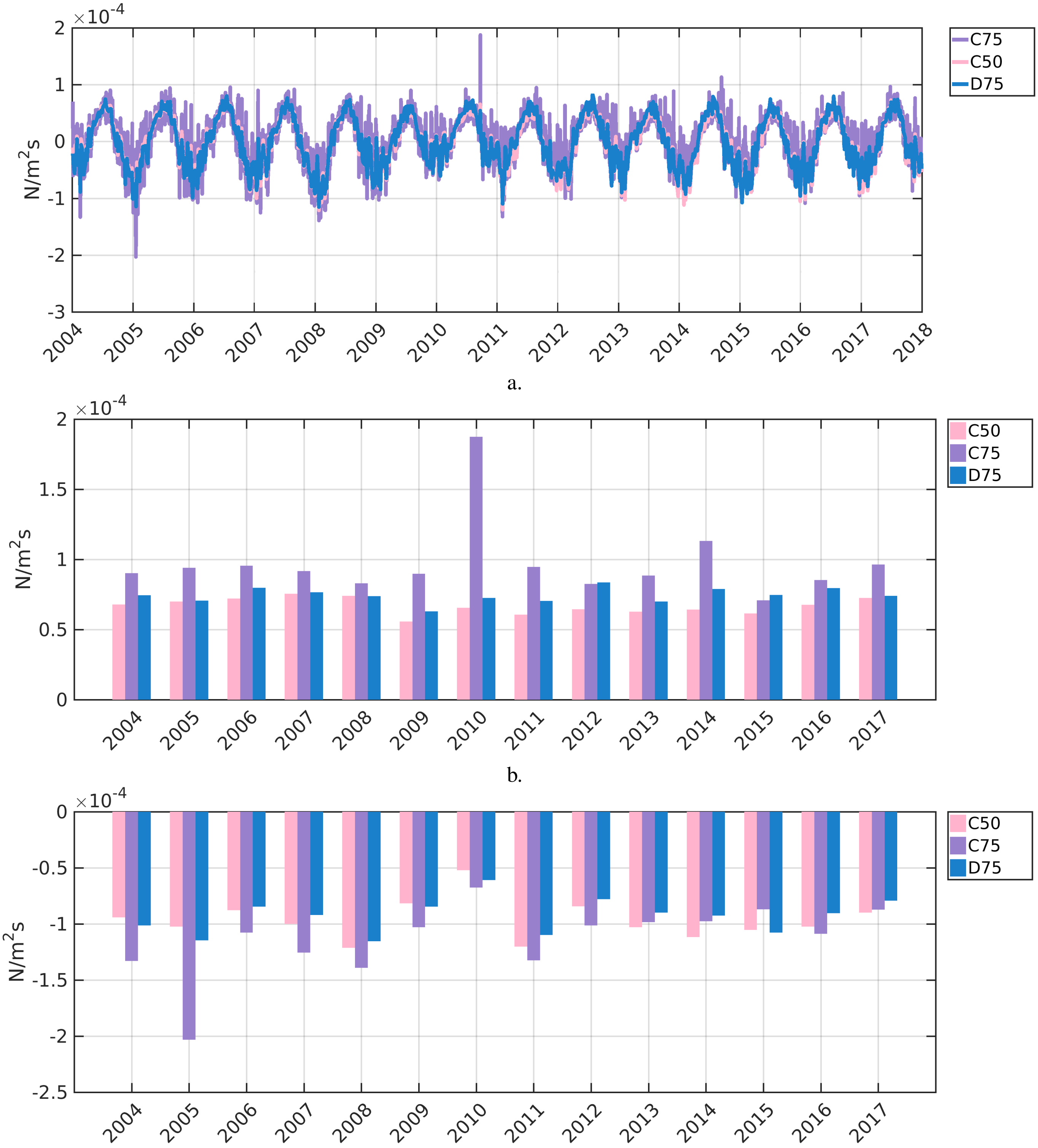

a.

b.

c.

Figure 4.11: Buoyancy flux from the atmosphere to the ocean's surface calculated using Equation 4.5, averaged over the interior of the Labrador Sea (Figure 4.1). This figure shows a comparison of the three experiments with C50 in pink, C75 in purple and D75 in blue. Positive numbers indicate a gain in buoyancy in the ocean surface layer and negative values indicate a loss of buoyancy (denser) in the surface layer. Panel b. shows the surface of the ocean's maximum gain of buoyancy each year. Panel c. shows the surface of the oceans maximum loss of buoyancy each year.

was less cold, fresh, and light water (T$<$ 2^{o}C, S $<$ 33, and ρ $<$ 26.5 kg/m^3) than in C75. Therefore, more of the light upper water mass has been transformed into denser water in D75. The Labrador Sea has a warmer boundary current ($+0.04^oC$) in D75 than in C75, but, due to stronger buoyancy losses, has a saltier and cooler interior ($\Delta S \approx 0.01$, $\Delta T = -0.04^oC$; Figure 4.6), aiding the strengthening of winter convection. The freshwater content in the interior of the Labrador Sea in D75 does not increase as much as in C75 following 2009 (Figure 4.7a). Strong heat loss still occurs in the winter (Figure 4.7b) due to the larger air-sea buoyancy forcing, even though D75's Labrador Sea interior gained more heat content than C75 throughout the period (Figure 4.7).

The salt and heat fluxes into the interior of the Labrador Sea between C75 and D75 are not large when compared to the differences between C75 and C50 (Figure 4.8). The largest differences between D75 and C75 occur in the south of the Labrador Sea, where the North Atlantic Current exchanges warm salty waters with the interior (around km marker 700-900). In C75, the temperature flux is stronger (around 900 km marker) from 2014 to 2017 compared to D75's temperature flux; however, the interior Labrador Sea heat content was higher in D75 (Figure 4.7b). For freshwater flux into the interior (Figure 4.8e. and 4.8f. for C75 and D75), the Hovmöller plot shows a similar structure between the two experiments. Therefore, the behaviour of the salt import is linked to the change in number of vertical levels or representation of the topography, rather than due to a difference in atmospheric forcing fields.

There was less volume transport of Irminger Water westward at Cape Farewell in D75 (3.0 Sv) than in C75 (4.5 Sv) on average (Figure 4.9a; Table 4.1). For the Cape Farewell section in D75 there was also slightly less salt and temperature flux westward than in C75 (Figure 4.9b and Figure 4.9c). Myers et al. (2007) estimated around 4.9 ± 1.1 Sv, 98 ± 22 TW, and 10.9 ± 2.2 mSv for the volume, heat, and salt fluxes, respectively, over 1995-2005. Although in this study the averaging period is different (2004-2017), and there is significant temporal variability in Irminger Water exchange at Cape Farewell, an examination of the relative values can be done to understand more of the model's lateral exchange. The large fluxes (Table 4.1), especially for salt, in C50 suggest that this is the source of much of the warm and salty water that reaches the Labrador Sea interior, reduces stratification, and promotes broad and deep convection. Given the same atmospheric forcing in C75 as C50, the reduced input of Irminger Water at Cape Farewell in C75 must be related to formation or pathway changes in the eastern basin brought about by the change in details of the bathymetry (not explored here). D75 has the salt flux closest to the observed (remembering the different time periods), although weaker volume and temperature fluxes. However, this reduced salt flux appears to be sufficient, in combination with strong atmospheric forcing, to allow for significant and deep Labrador Sea convection.

The magnitude of EKE in the West Greenland Current and along the Labrador Shelf is smaller in D75 compared to C75 (20 cm^2/s^2 less; Figure 4.10e). In D75, the EKE is lower where the boundary currents along the Labrador Sea are warmer than in C75 (Figure 4.6c). The changes in EKE between C75 and D75 indicate that the changes in water mass properties are having a significant effect. Additionally, given the stronger boundary current transport, at Cape Farewell in C75 than D75, there is an increased likelihood of baroclinic instability.

4.4 Conclusion

The role of ocean-atmosphere buoyancy fluxes and lateral buoyancy exchanges in LSW formation and its representation in an eddy-permitting ocean model have been investigated. This study found, as in Stewart et al. (2017), that changing vertical resolution changes the horizontal flows; specifically, in a configuration with 75 levels with modified bathymetry along the Greenland shelf compared with a 50-level configuration. The lateral exchange of buoyancy fluxes from the shelf to the interior were impacted by the change in the details of the bathymetry resulting from the 75-level model's better representation of the Greenland shelf. At higher vertical resolution, the lateral exchanges of heat and salt between the shelf and the interior are smaller. There was a reduction of salt import into the Labrador Sea via the Irminger and North Atlantic Currents in the 75-level model compared with the 50-level model, allowing the Labrador Sea to become more buoyant. At Cape Farewell, there was lower EKE in C75 compared with C50. The westward fluxes of heat and salt associated with Irminger Water at Cape Farewell are 50 % and 33 % lower, respectively.

Without this source of salt and heat the Labrador Sea was able to freshen and cool. And without strong buoyancy loss, deep convection did not occur. This prevented a salinity drift in the model's Labrador Sea which has plagued the 50-level model and resulted in overly deep mixed layers, a common problem in other model simulations too (Garcia-Quintana et al., 2019; Rattan et al., 2010). The different lateral exchange in the 75-level model led to a stronger stratification in the interior of the Labrador Sea with stronger convection resistance which created an unrealistically shallow mixed layer. With cooler pre-winter sea surface temperatures leading to weaker buoyancy loss in the interior of the Labrador Sea for C75, the result is that the greater convection resistance in this experiment could not be overcome and only shallow and limited convection occurred.

Argo observations showed that convection occurred throughout the study period. Therefore, the extreme shallowing of the mixed layer in later years in C75 is not realistic. Applying a strong buoyancy loss over the Labrador Sea with atmospheric forcing from DFS (Dussin et al., 2016) increased the buoyancy loss from the surface of the ocean to the atmosphere with the 75-level model (D75). The Labrador Sea in D75 was able to generate a deeper winter mixed layer than in C75, with convection resistance decreasing, weaker stratification, and stronger buoyancy loss at the surface. Less freshwater content and stronger buoyancy loss created a saltier and cooler, therefore denser, ocean surface in the Labrador Sea interior, compensating for the change in lateral advection. This enabled a break-through of the buoyancy cap and strengthened winter convection generating a realistic deep mixed layer closer to observed values.

This manuscript has highlighted changes in the lateral and air-sea heat fluxes arising due to changes in surface forcing, vertical resolution, and bathymetry have a significant impact on the stratification, and therefore the deep water formation, in the Labrador Sea. This study had multiple configurations tested and identified a way to remove salinity drift. Additionally, at the higher vertical resolution, a reduction in the northward transport of the AMOC (not shown) occurred. Therefore, longer-term climate studies need to be careful with the choice of vertical resolution and bathymetry. The bathymetry along the Greenland shelf, and the lateral exchange of the boundary current may play a critical role in the downstream, larger-scale ocean circulation. This could be especially important for longer-term climate studies, as this study had a relatively low horizontal and temporal resolution (1/4^o and 14 years).

Bibliography

Aagaard, K. and Carmack, E. C. (1989). The role of sea ice and other fresh water in the Arctic circulation. *Journal of Geophysical Research: Oceans*, 94(C10):14485–14498.

Amante, C. and Eakins, B. (2009). ETOPO1 1 Arc-Minute Global Relief Model: Procedures, Data Sources and Analysis. *NOAA Technical Memorandum NESDIS NGDC-24*.

Bailey, D. A., Rhines, P. B., and Häkkinen, S. (2005). Formation and pathways of North Atlantic Deep Water in a coupled ice–ocean model of the Arctic–North Atlantic Oceans. *Climate Dynamics*, 25:497–516.

Bamber, J. L., Tedstone, A. J., King, M. D., Howat, I. M., Enderlin, E. M., van den Broeke, M. R., and Noel, B. (2018). Land Ice Freshwater Budget of the Arctic and North Atlantic Oceans: 1. Data, Methods, and Results. *Journal of Geophysical Research: Oceans*, 123(3):1827–1837.

Barnier, B., Brodeau, L., Le Sommer, J., Molines, J.-M., Penduff, T., Theetten, S., Tréguier, A.-M., Madec, G., Biastoch, A., Böning, C. W., Dengg, J., Gulev, S. K., Bourdallé-Badie, R., Chanut, J., Garric, G., Alderson, S., Coward, A. C., De Cuevas, B., New, A. L., Haines, K., Smith, G. C., Drijfhout, S., Hazeleger, W., Severijns, C. A., and Myers, P. G. (2007). Eddy-permitting ocean circulation hindcasts of past decades. *CLIVAR Exchanges*, 12(42):8–10.

Barnier, B., Madec, G., Penduff, T., Molines, J.-M., Treguier, A.-M., Sommer, J., Beckmann, A., Böning, C., Dengg, J., Derval, C., Durand, E., Gulev, S., Remy, E., Talandier, C., Theetten, S., Maltrud, M., Mcclean, J., and Cuevas, B. (2006). Impact of partial steps and momentum advection schemes in a global ocean circulation model at eddy-permitting resolution. *Ocean Dynamics*, 56.

Bernard, B., Madec, G., Penduff, T., Molines, J.-M., Treguier, A.-M., Le Sommer, J., Beckmann, A., Biastoch, A., Böning, C., Dengg, J., Derval, C., Durand, E., Gulev, S., Remy, E., Talandier, C., Theetten, S., Maltrud, M., McClean, J., and De Cuevas, B. (2006). Impact of partial steps and momentum advection schemes in a global ocean circulation model at eddy-permitting resolution. *Ocean Dynamics*, 56(5):543–567.

Bigg, G. R., Wadley, M. R., Stevens, D. P., and Johnson, J. A. (1997). Modelling the dynamics and thermodynamics of icebergs. *Cold Regions Science and Technology*, 26(2):113 – 135.

BODC (2008). British Oceanographic Data Center's General Bathymetric Chart of the Oceans. http://www.gebco.net/data_and_products/gridded_bathymetry_data/.

Böning, C. W., Behrens, E., Biastoch, A., Getzlaff, K., and Bamber, J. L. (2016). Emerging impact of Greenland meltwater on deepwater formation in the North Atlantic Ocean. *Nature Geosci*, 9(7):523–527.

Chanut, J., Barnier, B., Large, W., Debreu, L., Penduff, T., Molines, J. M., and Mathiot, P. (2008). Mesoscale Eddies in the Labrador Sea and Their Contribution to Convection and Restratification. *Journal of Physical Oceanography*, 38(8):1617–1643.

Colombo, P., Barnier, B., Penduff, T., Chanut, J., Deshayes, J., Molines, J.-M., Sommer, J., Verezemskaya, P., Gulev, S., and Treguier, A.-M. (2020). Representation of the Denmark Strait overflow in a z -coordinate eddying configuration of the NEMO (v3.6) ocean model: resolution and parameter impacts. *Geoscientific Model Development*, 13:3347–3371.

Dai, A., Qian, T., Trenberth, K. E., and Milliman, J. D. (2009). Changes in continental freshwater discharge from 1948 to 2004. *Journal of Climate*, 22(10):2773–2792.

de Jong, M. F., Bower, A. S., and Furey, H. H. (2014). Two Years of Observations of Warm-Core Anticyclones in the Labrador Sea and Their Seasonal Cycle in Heat and Salt Stratification. *Journal of Physical Oceanography*, 44(2):427–444.

de Steur, L., Peralta-Ferriz, C., and Pavlova, O. (2018). Freshwater Export in the East Greenland Current Freshens the North Atlantic. *Geophysical Research Letters*, 45(24):13,359–13,366.

Dukhovskoy, D. S., Yashayaev, I., Proshutinsky, A., Bamber, J. L., Bashmachnikov, I. L., Chassignet, E. P., Lee, C. M., and Tedstone, A. J. (2019). Role of Greenland Freshwater Anomaly in the Recent Freshening of the Subpolar North Atlantic. *Journal of Geophysical Research: Oceans*, 124(5):3333–3360.

Dussin, R., Barnier, B., and Brodeau, L. (2016). The making of Drakkar forcing set DFS5. Grenoble,612 France: LGGE.

Ferry, N., Greiner, E., Garric, G., Penduff, T., Treiguier, A.-M., and Reverdin, G. (2008). GLORYS-1 Reference Manual for Stream 1 (2002-2007). GLORYS project report.

Feucher, C., Garcia-Quintana, Y., Yashayaev, I., Hu, X., and Myers, P. G. (2019). Labrador Sea Water Formation Rate and Its Impact on the Local Meridional Overturning Circulation. *Journal of Geophysical Research: Oceans*, 124(8):5654–5670.

Fichefet, T. and Morales Maqueda, M. (1997). Sensitivity of a global sea ice model to the treatment of ice thermodynamics and dynamics. *Journal of Geophysical Research*, 102(C6):12609–12646.

Frajka-Williams, E., Rhines, P. B., and Eriksen, C. C. (2014). Horizontal Stratification during Deep Convection in the Labrador Sea. *Journal of Physical Oceanography*, 44(1):220–228.

Fratantoni, D. M. (2001). North atlantic surface circulation during the 1990's observed with satellite-tracked drifters. *Journal of Geophysical Research: Oceans*, 106(C10):22067–22093.

Garcia-Quintana, Y., Courtois, P., Hu, X., Pennelly, C., Kieke, D., and Myers, P. G. (2019). Sensitivity of Labrador Sea Water Formation to Changes in Model Resolution, Atmospheric Forcing, and Freshwater Input. *Journal of Geophysical Research: Oceans*, 124(3):2126–2152.

Gelderloos, R., Katsman, C. A., and Drijfhout, S. S. (2011). Assessing the Roles of Three Eddy Types in Restratifying the Labrador Sea after Deep Convection. *Journal of Physical Oceanography*, 41(11):2102–2119.

Gill, A. E. (1982). Atmosphere-Ocean Dynamics. page 662. Academic Press.

Gillard, L. C., Hu, X., Myers, P. G., and Bamber, J. L. (2016). Meltwater pathways from marine terminating glaciers of the Greenland Ice Sheet. *Geophysical Research Letters*, 43(20):10,873–10,882.

Gladstone, R. M., Bigg, G. R., and Nicholls, K. W. (2001). Iceberg trajectory modeling and meltwater injection in the Southern Ocean. *Journal of Geophysical Research: Oceans*, 106(C9):19903–19915.

Hirschi, J. J.-M., Barnier, B., Böning, C., Biastoch, A., Blaker, A. T., Coward, A., Danilov, S., Drijfhout, S., Getzlaff, K., Griffies, S. M., Hasumi, H., Hewitt, H., Iovino, D., Kawasaki, T., Kiss, A. E., Koldunov, N., Marzocchi, A., Mecking, J. V., Moat, B., Molines, J.-M., Myers, P. G., Penduff, T., Roberts, M., Treguier, A.-M., Sein, D. V., Sidorenko, D., Small, J., Spence, P., Thompson, L., Weijer, W., and Xu, X. (2020). The Atlantic Meridional Overturning Circulation in High-Resolution Models. *Journal of Geophysical Research: Oceans*, 125(4):e2019JC015522. e2019JC015522 2019JC015522.

Holdsworth, A. M. and Myers, P. G. (2015). The influence of high-frequency atmospheric forcing on the circulation and deep convection of the Labrador Sea. *Journal of Climate*, 28(12):4980–4996.

IOC, SCOR, and IAPSO (2010). *The international thermodynamic equation of seawater - 2010 : Calculation and use of thermodynamic properties*. Intergovernmental Oceanographic Commission, Manuals and Guides No. 56, UNESCO (English).

Katsman, C. A., Spall, M. A., and Pickart, R. S. (2004). Boundary Current Eddies and Their Role in the Restratification of the Labrador Sea. *Journal of Physical Oceanography*, 34(9):1967–1983.

Kuhlbrodt, T., Griesel, A., Montoya, M., Levermann, A., Hofmann, M., and Rahmstorf, S. (2007). On the driving processes of the Atlantic Meridional Overturning Circulation. *Reviews of Geophysics*, 45(2).

Large, W. G. and Yeager, S. G. (2004). Diurnal to decadal global forcing for ocean and sea-ice models: the datasets and flux climatologies.

Lau, N.-C. (1988). Variability of the Observed Midlatitude Storm Tracks in Relation to Low-Frequency Changes in the Circulation Pattern. *Journal of the Atmospheric Sciences*, 45(19):2718–2743.

Lozier, M. S., Li, F., Bacon, S., Bahr, F., Bower, A. S., Cunningham, S. A., de Jong, M. F., de Steur, L., deYoung, B., Fischer, J., Gary, S. F., Greenan, B. J. W., Holliday, N. P., Houk, A., Houpert, L., Inall, M. E., Johns, W. E., Johnson, H. L., Johnson, C., Karstensen, J., Koman, G., Le Bras, I. A., Lin, X., Mackay, N., Marshall, D. P., Mercier, H., Oltmanns, M., Pickart, R. S., Ramsey, A. L., Rayner, D., Straneo, F., Thierry, V., Torres, D. J., Williams, R. G., Wilson, C., Yang, J., Yashayaev, I., and Zhao, J. (2019). A sea change in our view of overturning in the subpolar North Atlantic. *Science*, 363(6426):516–521.

Luo, H., Castelao, R. M., Rennermalm, A. K., Tedesco, M., Bracco, A., Yager, P. L., and Mote, T. L. (2016). Oceanic transport of surface meltwater from the southern Greenland Ice Sheet. *Nature Geoscience*.

MacGilchrist, G. A., Johnson, H. L., Marshall, D. P., Lique, C., Thomas, M., Jackson, L. C., and Wood, R. A. (2020). Locations and Mechanisms of Ocean Ventilation in the High-Latitude North Atlantic in an Eddy-Permitting Ocean Model. *Journal of Climate*, 33.

Madec, G. (2008). NEMO ocean engine. *Note du Pole de modélisation*, (27).

Marsh, R., Ivchenko, V. O., Skliris, N., Alderson, S., Bigg, G. R., Madec, G., Blaker, A. T., Aksenov, Y., Sinha, B., Coward, A. C., Le Sommer, J., Merino, N., and Zalesny, V. B. (2015). NEMO-ICB (v1.0): interactive icebergs in the NEMO ocean model globally configured at eddy-permitting resolution. *Geoscientific Model Development*, 8(5):1547–1562.

Marshall, J., Dobson, F., Moore, K., Rhines, P., Visbeck, M., D'Asaro, E., Bumke, K., Chang, S., Davis, R., Fischer, K., Garwood, R., Guest, P., Harcourt, R., Herbaut, C., Holt, T., Lazier, J., Legg, S., McWilliams, J., Pickart, R., Prater, M., Renfrew, I., Schott, F., Send, U., and Smethie, W. (1998). The Labrador Sea Deep Convection Experiment. *Bulletin of the American Meteorological Society*, 79(10):2033–2058.

Marson, J. M., Myers, P. G., Hu, X., and Le Sommer, J. (2018). Using Vertically Integrated Ocean Fields to Characterize Greenland Icebergs' Distribution and Lifetime. *Geophysical Research Letters*, 45(9):4208–4217.

Martin, T. and Adcroft, A. (2010). Parameterizing the fresh-water flux from land ice to ocean with interactive icebergs in a coupled climate model. *Ocean Modelling*, 34(3):111 – 124.

Masina, S., Storto, A., Storto, A., Ferry, N., Valdivieso, M., Haines, K., Balmaseda, M., Zuo, H., Drevillon, M., and Parent, L. (2017). An ensemble of eddy-permitting global ocean reanalyses from the MyOcean project. *Climate Dynamics*, 49(3):813–841.

Merino, N., Sommer, J. L., Durand, G., Jourdain, N. C., Madec, G., Mathiot, P., and Tournadre, J. (2016). Antarctic icebergs melt over the Southern Ocean: Climatology and impact on sea ice. *Ocean Modelling*, 104:99 – 110.

Morlighem, M., Williams, C. N., Rignot, E., An, L., Arndt, J. E., Bamber, J. L., Catania, G., Chauché, N., Dowdeswell, J. A., Dorschel, B., Fenty, I., Hogan, K., Howat, I., Hubbard, A., Jakobsson, M., Jordan, T. M., Kjeldsen, K. K., Millan, R., Mayer, L., Mouginot, J., Noël, B. P. Y., O'Cofaigh, C., Palmer, S., Rysgaard, S., Seroussi, H., Siegert, M. J., Slabon, P., Straneo, F., van den Broeke, M. R., Weinrebe, W., Wood, M., and Zinglersen, K. B. (2017). BedMachine v3: Complete Bed Topography and Ocean Bathymetry Mapping of Greenland From Multibeam Echo Sounding Combined With Mass Conservation. *Geophysical Research Letters*, 44(21):11,051–11,061.

Myers, P., Kulan, N., and Ribergaard, M. (2007). Irminger Water variability in the West Greenland Current. *Geophys. Res. Lett*, 34.

Pennelly, C., Hu, X., and Myers, P. G. (2019). Cross-Isobath Freshwater Exchange Within the North Atlantic Subpolar Gyre. *Journal of Geophysical Research: Oceans*, 124(10):6831–6853.

Pennelly, C. and Myers, Paul, G. (In prep). Impact of Different Atmospheric Forcing Sets on Modelling Labrador Sea Water Production.

Rabe, B., Karcher, M., Kauker, F., Schauer, U., Toole, J. M., Krishfield, R. A., Pisarev, S., Kikuchi, T., and Su, J. (2014). Arctic Ocean basin liquid freshwater storage trend 1992–2012. *Geophysical Research Letters*, 41(3):961–968.

Rattan, S., Myers, P. G., Treguier, A. ., Theetten, S., Biastoch, A., and Böning, C. (2010). Towards an understanding of Labrador Sea salinity drift in eddy-permitting simulations. *Ocean Modelling*, 35(1-2):77–88.

Rhein, M., Steinfeldt, R., Huhn, O., Sültenfuß, J., and Breckenfelder, T. (2018). Greenland Submarine Melt Water Observed in the Labrador and Irminger Sea. *Geophysical Research Letters*, 45(19):10,570–10,578.

Rhein, M., Steinfeldt, R., Kieke, D., Stendardo, I., and Yashayaev, I. (2017). Ventilation variability of Labrador Sea Water and its impact on oxygen and anthropogenic carbon: a review. *Philosophical Transactions of the Royal Society A: Mathematical, Physical and Engineering Sciences*, 375(2102):20160321.

Rieck, J., Böning, C., and Getzlaff, K. (2019). The Nature of Eddy Kinetic Energy in the Labrador Sea: Different Types of Mesoscale Eddies, Their Temporal Variability, and Impact on Deep Convection. *Journal of Physical Oceanography*, 49.

Sathiyamoorthy, S. and Moore, G. W. K. (2002). Buoyancy Flux at Ocean Weather Station Bravo. *Journal of Physical Oceanography*, 32(2):458–474.

Schulze, L. M., Pickart, R. S., and Moore, G. W. K. (2016). Atmospheric forcing during active convection in the Labrador Sea and its impact on mixed-layer depth. *Journal of Geophysical Research: Oceans*, 121(9):6978–6992.

Schulze Chretien, L. M. and Frajka-Williams, E. (2018). Wind-driven transport of fresh shelf water into the upper 30 m of the Labrador Sea. *Ocean Science*, 14(5):1247–1264.

Smith, G. C., Roy, F., Mann, P., Dupont, F., Brasnett, B., Lemieux, J.-F., Laroche, S., and Bélair, S. (2014). A new atmospheric dataset for forcing ice-ocean models: Evaluation of reforecasts using the Canadian global deterministic prediction system. *Quarterly Journal of the Royal Meteorological Society*, 140(680):881–894.

Stewart, K., Hogg, A., Griffies, S., Heerdegen, A., Ward, M., Spence, P., and England, M. (2017). Vertical resolution of baroclinic modes in global ocean models. *Ocean Modelling*, 113:50 – 65.

Straneo, F. (2006). Heat and freshwater transport through the central Labrador Sea. *Journal of Physical Oceanography*, 36(4):606–628.

Talley, L. D., Reid, J. L., and Robbins, P. E. (2003). Data-Based Meridional Overturning Streamfunctions for the Global Ocean. *Journal of Climate*, 16(19):3213–3226.

Treguier, A. M., Theetten, S., Chassignet, E. P., Penduff, T., Smith, R., Talley, L., Beismann, J. O., and Böning, C. (2005). The North Atlantic Subpolar Gyre in Four High-Resolution Models. *Journal of Physical Oceanography*, 35(5):757–774.

V*å*ge, K., Pickart, R. S., Thierry, V., Reverdin, G., Lee, C. M., Petrie, B., Agnew, T. A., Wong, A., and Ribergaard, M. H. (2009). Surprising return of deep convection to the subpolar North Atlantic Ocean in winter 2007–2008. *Nature Geoscience*, 2:67–72.

Yashayaev, I. and Loder, J. W. (2009). Enhanced production of Labrador Sea Water in 2008. *Geophysical Research Letters*, 36(1).

Yashayaev, I. and Loder, J. W. (2016). Recurrent replenishment of Labrador Sea Water and associated decadal-scale variability. *Journal of Geophysical Research: Oceans*, 121(11):8095–8114.

Yashayaev, I. and Loder, J. W. (2017). Further intensification of deep convection in the Labrador Sea in 2016. *Geophysical Research Letters*, 44(3):1429–1438.

Chapter 5

The Fate of Greenland's Glacial Melt and Iceberg Discharge

Chapter 5 of this thesis is being prepared for publication with the authorship of Laura C. Gillard, Juliana M. Marson, Helen L. Johnson, and Paul G. Myers. I was responsible for the analysis and ran all of the model experiments. J.M. Marson taught me how to implement icebergs into the model and provide methods for analysis on iceberg variables and manuscript edits. H.L. Johnson provided insight to the project. P.G. Myers provided insight, advice and manuscript edits.

Abstract

As the Greenland Ice Sheet (GrIS) continues to lose large amounts of mass, the importance of the fate of the discharged icebergs and runoff increases. Many freshwater flux (FWF) estimates of the GrIS are available, but it is not clear when to use one over the other when forcing an ocean general circulation model. This study compares three different GrIS FWF products using an eddy-permitting general ocean circulation model. Using different products changes the amount of meltwater and iceberg accumulation throughout the Arctic and Sub-Arctic Oceans. Additionally, the representation of the seasonality of the runoff and iceberg discharge impacts the freshwater accumulation in basins near Greenland. Iceberg calving maps representing the magnitude of a few large marine-terminating glaciers (MtG) versus many smaller MtG was shown to impact the fate of iceberg discharge in the ocean model. The eastern Arctic's heat content varied by about 10 GJ between experiments, which could have the energy to melt 30 tonnes of fresh ice. Additionally, the freshwater content varied by more than 10 000 km^3 through Baffin Bay, Irminger Sea, Greenland Sea, Nordic Sea, and the eastern Sub Polar Gyre. Despite the variation in meltwater and iceberg discharge of

the GrIS FWF products, for a decade long study period at eddy-permitting resolution, none of the three estimates have impacted the Labrador Sea convection or the Atlantic Meridional Overturning Circulation yet.

5.1 Introduction

The Greenland Ice Sheet (GrIS) has lost 3902 ± 342 Gt of ice to the ocean since 1992 (Shepherd et al., 2020). Though the GrIS mass loss slowed in 2017 and 2018, the GrIS has remained on an increasing mass loss trend since the late 1990s (Rignot et al., 2008; Sasgen et al., 2020). The increase in the ice sheet mass loss rate has been linked to a warming climate with warmer summer atmospheric temperatures (Hanna et al., 2008, 2012; Rignot et al., 2008). The 2019 melt season showed a record mass loss of 532 ± 50 Gt/year due to a stronger anticyclonic circulation that advected warm air along Greenland's west coast (Sasgen et al., 2020; Tedesco and Fettweis, 2020). Additionally, enhanced mass loss is linked to the increasing presence of relatively warm ocean waters contacting the ice sheet (Holland et al., 2008; Jackson et al., 2014; Myers and Ribergaard, 2013; Straneo and Heimbach, 2013). From 1992 to 2018, the GrIS contributed to a mean sea-level rise of 10.8 ± 0.9 millimetres (Shepherd et al., 2020) and has the potential to increase it by 7.42 ± 0.05 metres if the entire ice sheet were to melt (Morlighem et al., 2017).

The GrIS is situated between two large oceans, the Arctic and the North Atlantic, and has gateways between these two basins on either side of it (Figure 5.1). The Arctic Ocean is stratified with cold polar surface water overlaying relatively warm and saline waters (Rudels, 2015). Pacific waters enter the Chukchi Sea via Bering Strait and flow southeastward along the boundary of the Canadian Basin, below the surface waters and mixed layer (Rudels et al., 1996). The surface water in the Canadian Basin governed by the strength of the anticyclonic Beaufort Gyre (Rudels, 2015). Along the Lomonosov Ridge, separating the Eurasian and Canadian basins, the Transpolar Drift connects waters from the Siberian Shelf through to Fram Strait, northeast of Greenland (Steele et al., 2004). Modified Atlantic water is transported northward through Fram Strait, then travels cyclonically around the continental margin, providing the Arctic Ocean with additional heat (Polyakov et al., 2005). The polar water from the Arctic Ocean and meltwater from Greenland travels southward along the east Greenland shelf as the East Greenland Coastal Current (Bacon et al., 2002). Farther off the shelf, the East Greenland Current also travels southward through Fram Strait (Aagaard and Carmack, 1989), and has been known to increase in freshwater transport and freshen the North Atlantic Ocean (de Steur et al., 2018).

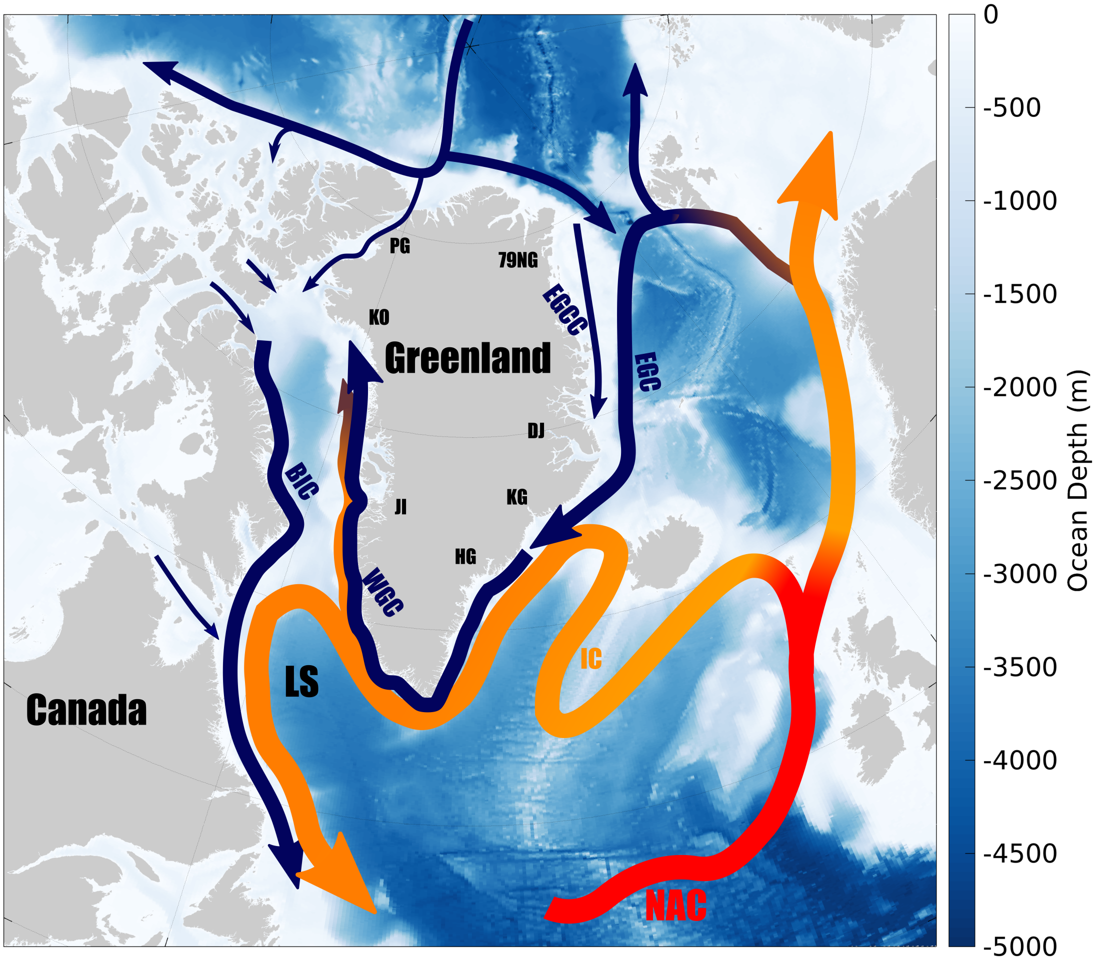

Figure 5.1: Realtively warm Atlantic waters are seen in red and change to orange as they get mixed and modified along the North Atlantic Current (NAC), Irminger Current (IC), and West Greenland Current (WGC). Arctic water and freshwater pathways are shown in blue lines. These currents include the East Greenland Coastal Current (EGCC), East Greenland Current (EGC), and Baffin Island Current (BIC). The Labrador Sea (LS) is located in the western Subpolar Gyre. Melville Bay (MVB) is located along the northwest coast of Greenland. Notable marine-terminating glaciers are indicated on Greenland: Petermann Glacier (PG), Kong Oscar Glacier (KO), Jakobshavn Isbrae (JI), Helheim Glacier (HG), Kangerlussuaq Glacier (KG), Daugaard-Jensen Glacier (DJ), and Nioghalvfjerdsbrae (79NG).

The East Greenland Current merges with the warm and salty Irminger Current once it rounds Cape Farewell and becomes the West Greenland Current (WGC) (Pickart et al., 2005). Along the west coast of Greenland, the WGC splits into two currents: one travelling north through Davis Strait and the other travelling westward, shedding eddies into the Labrador Sea before joining a southward flowing Baffin Island Current at Davis Strait (Fratantoni and Pickart, 2007; Myers et al., 2009). The Baffin Island Current contains a mixture of polar water exported south through the Canadian Arctic Archipelago (CAA) and melt from Greenland (Tang et al., 2004). The relatively fresh water exported south through Davis Strait flows along the Labrador Coast as the Labrador Current; the boundary current for the Labrador Sea (Myers et al., 2009; Straneo and Saucier, 2008).

Though increased melt from the GrIS may impact local ecosystems and regions near the GrIS (Arrigo et al., 2017; Hawkings et al., 2016), larger climate impacts may occur as well. Labrador Sea convection is sensitive to atmosphere heat loss as well as freshwater input (e.g. Chapter 4; Aagaard and Carmack, 1989; Marshall et al., 1998). Several model studies have investigated the fate of GrIS discharge (e.g. Böning et al., 2016; Dukhovskoy et al., 2016; Gillard et al., 2016; Luo et al., 2016; Marson et al., 2018), and showed that meltwater and icebergs originating from the south coast of the GrIS accumulate in the Labrador Sea. Although no impact on the Labrador Sea convection linked to the increasing discharge from the GrIS has been observed so far (Rhein et al., 2018; Yashayaev and Loder, 2017), deep convection may reduce as the GrIS continues to melt.

The Labrador Sea's winter heat loss to the atmosphere drives convection, producing the Labrador Sea Water which is exported at depth through the North Atlantic Ocean (Talley et al., 2003). The Labrador Sea Water formation feeds into the Atlantic Meridional Overturning Circulation (AMOC) and contributes to its strength and variability (Bailey et al., 2005; Feucher et al., 2019; Kuhlbrodt et al., 2007). A shallowing of the deep water formation in the Labrador Sea may impact the AMOC, influencing how the Earth distributes heat, impacting the concentration of dissolved gases such as oxygen and carbon dioxide, and altering ecosystems (Böning et al., 2016; Swingedouw et al., 2014; Weijer et al., 2012). However, a climate model study (Menary et al., 2020) suggests the role of convection that occurs in the eastern subpolar gyre (Irminger Sea) may have stronger control over the variability and strength of the AMOC. This has also been seen in a short 21-month observation study (OSNAP; Lozier et al., 2019).

In the past, ocean model studies have used incomplete GrIS freshwater flux (FWF) data, which included only runoff and excluded icebergs. Some ocean modelling studies which did not include an iceberg module (Dukhovskoy et al., 2016; Gillard et al., 2020) converted solid discharge to liquid and merged it with the liquid FWF, creating one total liquid FWF. Dukhovskoy et al. (2019) used Bamber et al. (2012) data up until 2010 and then switched to Bamber et al. (2018) from 2011 to 2016. However, these studies do not tell the whole story of the GrIS FWF impact on the ocean as they are missing solid ice discharge (icebergs). Marson et al. (2018) used an ocean model coupled to an iceberg module wherein icebergs account for 54 % of the total mass loss on the GrIS, as estimated by Bamber et al. (2012). Marson et al. (2018) found that most icebergs ($\sim$ 60 %) which crossed into the Labrador Sea interior were generated from Greenland's southeast coast. Marsh et al. (2018), in a first attempt for forecasting icebergs, showed the need for studies to focus on implementing icebergs into an ocean model as the increase in calving of icebergs from GrIS will be important for navigation in the Arctic and Sub-Arctic ocean.

The majority of the above-listed studies are based on numerical models. Their results are directly influenced by the amount, distribution, and type of discharge prescribed as forcing fields. Some of the products used in these studies to prescribe GrIS FWF come from Bamber et al. (2012, 2018), and an idealized forcing strategy for icebergs (for more details see Marsh et al. (2018)). To our knowledge, there have not yet been any sensitivity studies, using a consistent model framework, to assess the ocean's response in the Labrador Sea to different well-known Greenland discharge products (liquid and iceberg). Therefore, an assessment of the GrIS' impact on the large-scale ocean circulation using an eddy-permitting numerical model will be conducted. The Greenland discharge products used in this study come from Bamber et al. (2012), Bamber et al. (2018), and Lenaerts et al. (2015), all of which will be fully described in the next section.

5.2 Methods

5.2.1 Ocean-Sea Ice Coupled Model

The coupled ocean-sea ice general circulation model utilized in this study is the Nucleus for European Modelling of the Ocean version 3.6 (NEMO) framework (Madec, 2008). The Océan PArallélisé (OPA) model is used for ocean dynamics and thermodynamics and the Louvain-la-Neuve Ice Model (LIM2) is used for sea ice dynamics and thermodynamics (Fichefet and Morales Maqueda, 1997). The regional domain of the model covers the Arctic and Northern Hemisphere Atlantic Oceans (ANHA) and has two open boundaries: one at Bering Strait and the other at the latitude 20^oS. The ANHA horizontal grid is extracted from the ORCA global tripolar grid (Barnier et al., 2007) at a $1/4^o$ resolution, which corresponds to approximately 11 to 15 km around

Greenland.

All simulations start from January 2002 and are integrated to the end of December 2016. Initial and monthly open boundary conditions (temperature, salinity, horizontal velocities, and sea surface height) are derived from the Global Ocean Reanalyses and Simulations (GLORYS2V3) product (Ferry et al., 2008). Previous work showed that a 2-year model adjustment period is enough for the model to reach a steady state (spin-up), given the simulation starts from the reanalysis of GLORYS2v3 (Garcia-Quintana et al., 2019). Therefore, the model output used in this study was from 2004 to 2016 as the first two years (2002 to 2004) were considered the adjustment period.

All experiments here use geopotential z-level coordinates with a partial step option (Bernard et al., 2006) enabled at 75 levels. In the vertical, the experiments have the layer thickness increased from 1.05 m at the surface level to 204 m in the last level (at a depth of 6000 m). Bathymetry is taken from the existing global ORCA025 bathymetry (Barnier et al., 2006) which is based on a global relief model (ETOPO1) (Amante and Eakins, 2009) and a gridded bathymetry dataset (GEBCO) (BODC, 2008) with modifications (Barnier et al., 2007). The BedMachineV3 dataset (Morlighem et al., 2017) has been interpolated and averaged onto the grid along the coast of Greenland. This includes major improvements in deep bathymetric features such as troughs and canyons.

The experiments are forced with the Drakkar Atmospheric Forcing Set 5.2 (DFS) which provides atmospheric forcing fields at a three hour time step with a spatial resolution of nearly 0.7^o ($\sim$ 40 km in the Labrador Sea) (Dussin et al., 2016). The DFS dataset was generated by atmospheric reanalysis carried out at the European Centre for Medium Range Weather Forecast (ECMWF). DFS was created to drive ocean hindcast simulations based on the ERA-interim reanalysis and ECMWF real-time analyses. Adjustments and corrections have been applied to the following ERA-interim surface variables: radiation fluxes; wind speeds; air temperature and humidity in the Arctic; and liquid precipitation fields. For more details see Dussin et al. (2016).

In the configuration's domain, river runoff (not including Greenland) is provided by Dai et al. (2009). Runoff is injected at the surface and then mixed over the top 30 m of the water column through enhanced mixing at the river mouths. The runoff is assumed to be fresh (0 psu) and has the temperature of the grid cell that it is added to. The volume of the water column does not change due to the addition of runoff but is instead diluted (linear free surface; Madec, 2008). Therefore, a salt flux, which equals the volume of the runoff, is removed from the model domain where the runoff was injected.

5.2.2 Greenland Ice Sheet Estimates

An iceberg module is used for the solid discharge based on the original model of Bigg et al. (1997) and improvements from Gladstone et al. (2001), Martin and Adcroft (2010), Marsh et al. (2015), and Merino et al. (2016). The iceberg module takes into account the influence of the vertical profile of the ocean currents and temperature (rather than just the surface fields), allowing for a more accurate representation of the distribution and lifetime of icebergs (Marson et al., 2018; Merino et al., 2016). Icebergs are grouped in numbers, which depend on their classification (i.e. size and mass), to form a Lagrangian particle that will be tracked by the model (Martin and Adcroft, 2010). At each grid point along the coast of Greenland and at each model timestep, a test is performed in the model to see if there is enough ice mass to calve a particle. When there is enough mass, a new particle is spawned, and the total stored mass is reduced (Madec, 2008).

The GrIS solid ice discharge in Lenaerts et al. (2015) is constructed from remote sensing for 2000-2012 (Enderlin et al., 2014). However, the solid ice discharge rates are assumed to be constant in time. In Lenaerts et al. (2015) the liquid runoff portion of the GrIS freshwater forcing originates from the runoff from Regional Atmospheric Climate Model version 2.1 (hereafter, RACMO2.1; Meijgaard et al., 2008). The RACMO2.1 has a spatial resolution of $\sim$ 11 km, is forced by ERA-Interim fields at its lateral boundaries, has a GrIS surface mass balance (van Angelen et al., 2014), and improvements for the climate over Greenland (Ettema et al., 2010).

Runoff is given spatial variability by the subdivision into eight basins. The historical scenario calculates runoff based on RACMO2.1 (1960–2012) for each basin. This also includes runoff from the melting of seasonal snow covering the tundra area that surrounds the GrIS. For the meltwater calculations beyond 2012, the regional climate model is forced with an atmospheric circulation climate model HadGEM2-ES. Runoff is distributed evenly to the ocean grid points along each individual basin and assimilated into the coupled land-atmosphere-ocean climate model Community Earth System Model (CESM, version 1.1.2). The CESM is used to simulate 6 different scenarios, two of which have been used in this study: a historical (1850-2005) and future climate scenario (2006-2200; forced by the climate scenario RCP2.6). In the RCP2.6 scenario, global emissions were supressed in the 21st century and atmospheric temperatures increase slightly ($\sim 2^{o}$C) over the GrIS until 2100 (Lenaerts et al., 2015).

In Lenaerts et al. (2015), the seasonal cycle of runoff for 1850-2200 is determined from the mean RACMO2.1 seasonal cycle for the period 1960–2012. The monthly seasonal cycle has a runoff peak in summer and a very slight amount of runoff in the winter. The expansive period (1850-2200) of GrIS freshwater forcing from Lenaerts et al. (2015) provides climate model studies (e.g. Bakker et al., 2016; Ivanovic et al., 2018)) a product to use to look at the impact the GrIS may have on the AMOC strength in various climate change scenarios.

The GrIS liquid FWF from Bamber et al. (2012) was created from a 53-year reconstruction (1958–2010) of the surface mass balance model of the GrIS (Ettema et al., 2009) coupled with RACMO2.1 (Meijgaard et al., 2008). The GrIS solid ice discharge in Bamber et al. (2012) was created from regional estimates of ice motion for thirty-seven drainage basins calculated from surface velocity measurements multiplied by the ice thickness across the grounding line. The velocity and ice thickness measurements were calculated a few kilometres upstream of the grounding line and therefore required a surface mass balance correction (Rignot and Kanagaratnam, 2006). This product has been used for numerous ocean model studies (Dukhovskoy et al., 2016; Garcia-Quintana et al., 2019; Gillard et al., 2016, 2020; Grivault et al., 2017; Marson et al., 2018).

Bamber et al. (2018) have updated and extended the product from Bamber et al. (2012) to the end of 2016. This extension of data into more recent years is important for understanding recent Labrador Sea convection observations and the impact of the rapidly changing GrIS on the subpolar ocean. For the GrIS liquid runoff, Bamber et al. (2018) used RACMO version 2.3 (RACMO2.3 hereafter; Noël et al., 2015), an updated version from RACMO2.1. RACMO2.3 has an updated physics package which improved the surface mass balance estimates over Greenland due to improvements of cloud cover and precipitation estimates. Additionally, Bamber et al. (2018) has higher runoff rates than Bamber et al. (2012) due to downscaling RACMO2.3 to 1 km, improving resolution, and therefore the representation of the glaciers, ice caps, and the ablation zone on GrIS. The GrIS solid ice discharge is estimated using satellite-based observations of surface velocity and ice thickness (Morlighem et al., 2017).

5.2.3 Greenland Ice Sheet Experiments

In the present experiments, the GrIS liquid FWF is represented by the sum of tundra and ice sheet runoff, and the solid FWF (estimates represent calving and subglacial melt) is discharged in the form of icebergs. One experiment used GrIS FWF provided

Table 5.1: Model simulations used in this study. All experiments use interannual river discharge from Dai et al. (2009) except for the Greenland region, whose freshwater flux is provided by Bamber et al. (2012), Bamber et al. (2018), and Lenaerts et al. (2015). All simulations use the same atmospheric forcing, DFS (Dussin et al., 2016). The experiments five-day average mixed layer depth in the interior Labrador Sea were calculated between 2004-2016 and their correlation with Argo observations are presented in the third column (Figure 5.11c). These correlations are statistically highly significant with a P value for all correlations is less than 0.001, therefore at a 99% confidence level.

Simulation	Greenland Ice Sheet Dataset	Correlation with Argo
B12	Bamber et al. (2012)	0.75
B18	Bamber et al. (2018)	0.77
L15	Lenaerts et al. (2015)	0.74

by Bamber et al. (2012) for 2002-2010, with the 2010 runoff rates repeated from 2010 to 2016. Since this product did not provide separate FWF by source, the liquid runoff and solid ice discharge portions were generated by taking 46 % and 54 % fractions, respectively, from the total FWF. This is based on the 1961-1990 average rates of surface runoff and solid ice discharge provided in Bamber et al. (2012). The second experiment used the GrIS FWF from Bamber et al. (2018) from 2002 to 2016. In this new dataset, separate variables for runoff, tundra melt, and ice discharge were provided, rather than a combined FWF variable that needed to be fractioned into liquid and solid phases. Consequently, iceberg and liquid discharge sites and time variability did not coincide like in the experiment forced by Bamber et al. (2012). The third experiment used the GrIS FWF product of Lenaerts et al. (2015) from 2002 to 2016.

From Lenaerts et al. (2015), historical data was used from 2002 to 2005 and then from 2006 to 2016 their climate scenario using RCP2.6 was used. Iceberg discharge was held essentially constant because since it did not vary significantly in Lenaerts et al. (2015) study period (1850 to 2200). A comparison of these three products will be done and the associated numerical experiments are thus named B12 for using Bamber et al. (2012), B18 for Bamber et al. (2018), and L15 for Lenaerts et al. (2015) (details listed in Table 5.1).

Passive tracers were used to track the pathways and understand the overall distribution of liquid FWF and iceberg melt. The passive tracers were released from 1 January 2004 (and updated at every time step) in the same proportion and location as their sources. Along the coast of Greenland, five different passive tracers tag meltwater for the north, northwest, northeast, southeast, and southwest sectors (Figure 5.2).

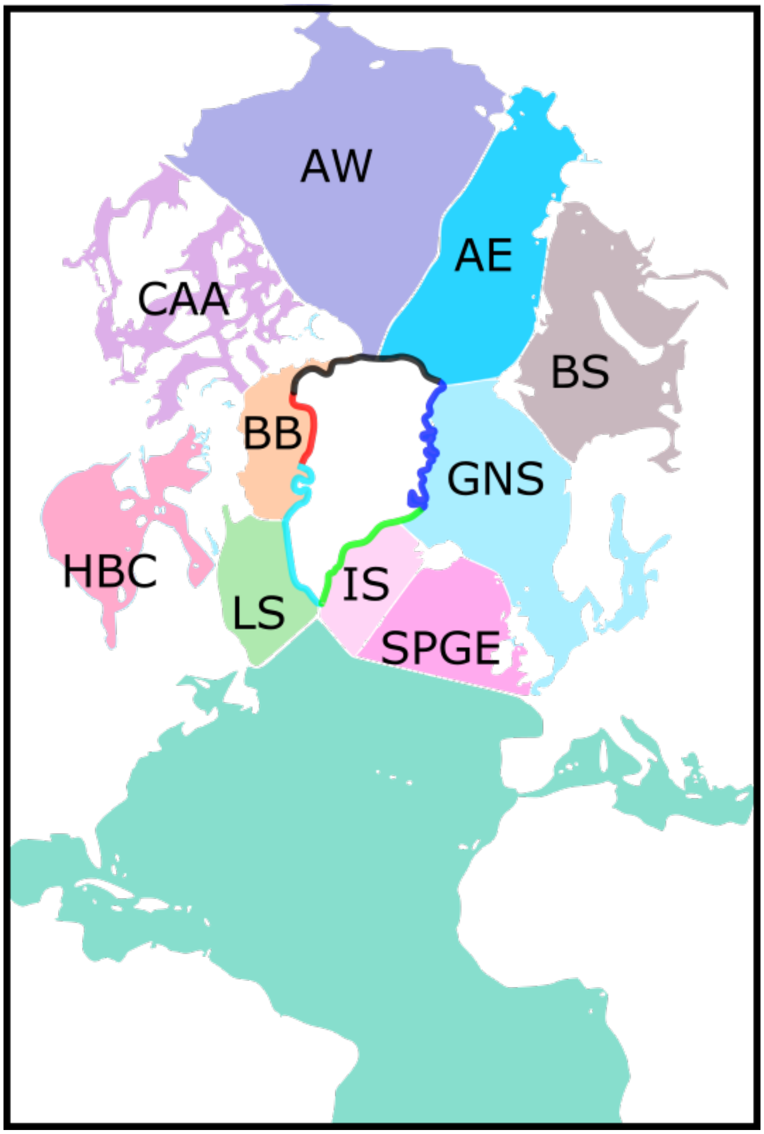

Figure 5.2: Map of separated regions. West Arctic (AW), East Arctic (AE), Irminger Sea (IS), Labrador Sea (LS), Hudson Bay Complex (HBC), Baffin Bay (BB), Canadian Arctic Archipelago (CAA), Greenland and Nordic Sea (GNS), Subpolar Gyre East (SPGE), Barents and Kara Sea (BS). Passive tracers that tag the GrIS runoff are shown in different colours along the coastline. Locations include north (black), northwest (red), northeast (blue), southeast (green) and southwest (cyan).

5.2.4 Freshwater Flux Amounts

Annual and seasonal liquid FWF from the GrIS is shown in Figures 5.3a and 5.3b. The average liquid FWF for the period of 2002 – 2016 in B12 is 527 km^3/year, while for B18 it is 638 km^3/year, and for L15 869 km^3/year. Up until 2006, the three experiments have similar annual liquid FWF, though B12 has the lowest, and L15 the highest. In 2006, there was a liquid FWF increase in all three datasets, followed by a decline in 2007. The increase of L15 liquid FWF from 2006 onward occurs because of the switch from historical data to L15's RCP2.6 data in that year. After 2007, L15 rapidly increases from 583 km^3/year to about 1153 km^3/year in 2009. L15 remains with the highest amount of liquid FWF out of the three experiments. The liquid FWF decreases under 1000 km^3/year for 2010 to 2012, followed by a steady increase until 2014, when it decreases below 1000 km^3/year for the remainder of the period. After 2007, B18 liquid FWF varies between 827 km^3/year in 2012 and 467 km^3/year in 2013, the lowest rate out of all three experiments. For the most part, B12 has the lowest liquid FWF and is constant after 2010 because of the dataset ending in that year.

The seasonality of the liquid FWF from all three sources behaves similarly. The summer months have the highest discharge values (starting in April/May and ending in September/October). Summer discharge peaked in July with averages of 118 mSv for L15, 109 mSv for B18 and 43 mSv for B12 (Figure 5.3b). B12 has the lowest amount of summer melt but it also has the largest rates of winter melt (December to March average) with 9 mSv compared to 0.6 mSv for B18 and 2.1 mSv L15.

Annual and seasonal solid FWF from the GrIS is shown in Figure 5.3c and 5.3d There is, in general, a small inter-annual variability in the solid FWF (hereafter called iceberg discharge) throughout the time series (Figure 5.3c). The average annual iceberg discharge for the period of 2002 to 2016 was 710 km^3/year for B12, 492 km^3/year for B18, and 604 km^3/year for L15. However, B12 varies the most year to year, peaking in 2008 at 752 km^3/year and reaching a low of 607 km^3/year in 2009. For B12, iceberg discharge rates were not provided separately. Therefore, the total FWF dataset had to be manually split into the two FWF components with the ratio of 46 % for liquid and 54 % for solid. Whereas for B18 and L15 the liquid FWF and iceberg discharge were stored in different variables. This issue of post-processing the data and breaking down the dataset into each component also shows in the seasonality of iceberg discharge (Figure 5.3d). The seasonality of the iceberg discharge for B12 behaves proportionally to the seasonality of liquid FWF, with a minimum of 382 km^3/year in the winter months (December to March) and a maximum of 1819 km^3/year in July. How-

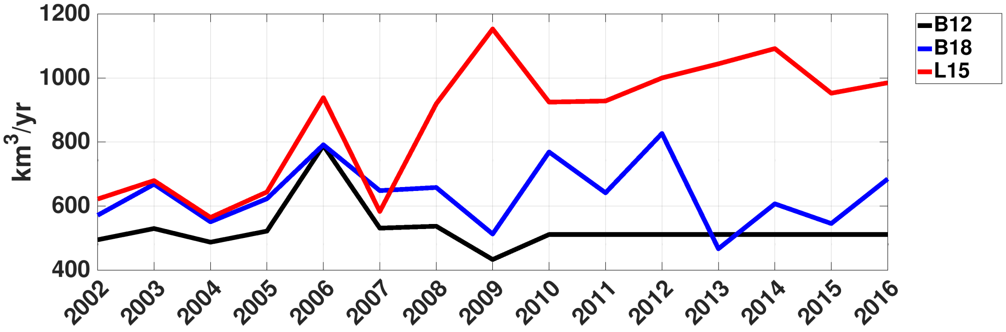

a. Annual Liquid Freshwater Flux

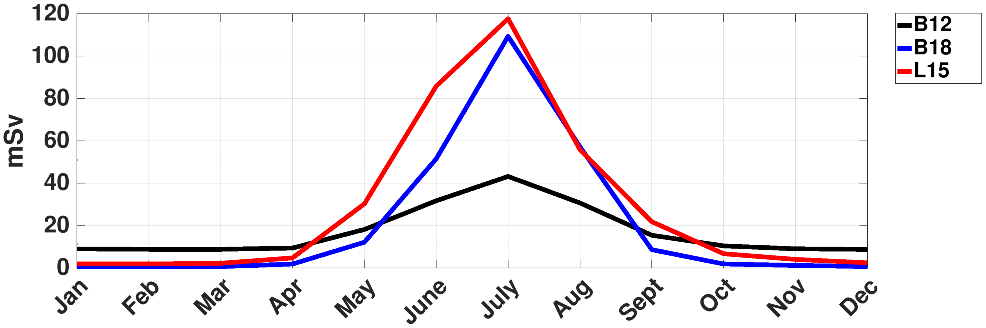

b. Seasonality of the Liquid Freshwater Flux

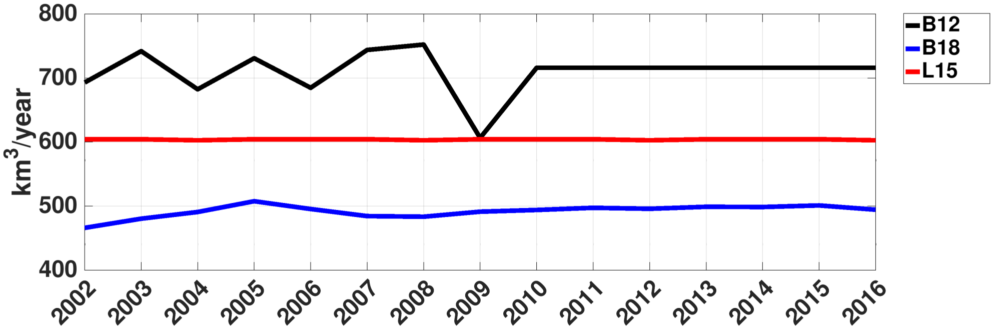

c. Annual Solid Freshwater Flux

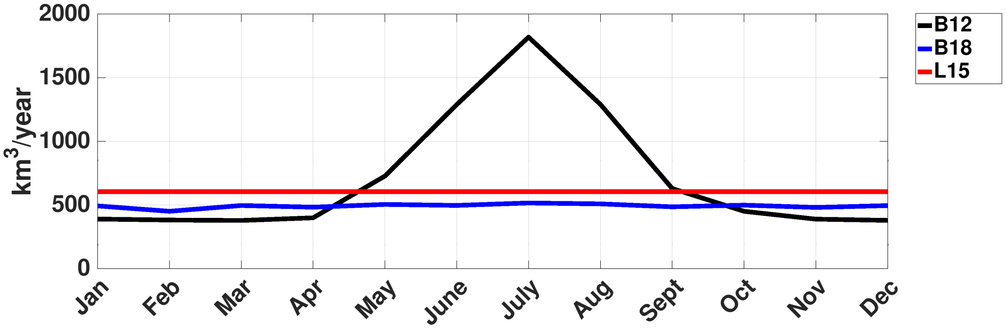

d. Seasonal Solid Freshwater Flux

Figure 5.3: Liquid and solid freshwater flux off of Greenland inputted into the experiments throughout the time-series. Products from L15 is in red, B12 in black and B18 in blue. Panels a. and b. show the annual sum and seasonal average of liquid FWF from 2002 to 2016. Panels c. and d. shows the annual sum and season average of solid FWF from 2002 to 2016.

ever, B18 and L15 have no seasonal cycle (L15 at its constant rate of 604 km^3/year and B18 hovering around 500 km^3/year, with a winter average of 483 km^3/year and maximum in July at 515 km^3/year). As previously mentioned, the solid FWF is measured from both calving processes and subglacial melt. Therefore, representation of the seasonality of the solid FWF is not exactly obvious since the icebergs are released along the coastline, outside of the fjords. Calving events depends on the dynamics and thermodynamics of a glacial front; however, a seasonality of icebergs could exist by the behaviour and seasonality of the breakup of ice melanges which allows icebergs to exit through the fjords (Amundson et al., 2010; Howat et al., 2010). Additionally, subglacial melt, discharge of surface runoff at the base of the glacier, does have a seasonality as it very sensitive to air temperatures (Sciascia et al., 2013).

Liquid FWF discharge sites (Figure 5.4) in the north have, on average, very low magnitudes in B12 (Figure 5.4; Table 5.2), while B18 and L15 have larger magnitudes for some discharge sites. In the northwest, in Baffin Bay, B18 has the smallest meltwater rates, whereas B12 has few points approaching 10 Gt/year (average $\sim$ 0.5 Gt/year), and L15 has several points close to or reaching 10 Gt/year (average $\sim$ 1.7 Gt/year). The Northeast region, facing the Nordic Seas, has smaller magnitudes of melt for B12 ($\sim$ 0.22 Gt/year) and larger in B18 ($\sim$ 0.44 Gt/year). L15 has the largest melt along the northeast coast ($\sim$ 1.2 Gt/year). However, for iceberg discharge in the northeast, B12 has the most locations where discharge/calving occurs but the smallest rates, whereas B18 and L15 have fewer points but larger values. In the southern regions (southwest and southeast), L15 has the smallest number of liquid FWF discharge sites (257) compared to B12 (530) and B18 (515), but L15 has larger average magnitudes of liquid FWF discharge per site. For iceberg discharge, L15 and B18 have fewer data points than B12 (39, 56, and 530, respectively) at a much higher discharge rate (Table 5.2).

B12's setup doesn't give an accurate representation of iceberg calving rates and locations compared to B18 and L15 which work from specific calving masks. The representation of larger marine-terminating glaciers around Greenland, indicated in Figure 5.1, can be seen by the larger magnitudes in the mean solid discharge maps in Figures 5.4d and 5.4f. On the north coast there is Petermann Glacier. On the northwest coast there is Kong Oscar Glacier, and further south along the coast in Disko Bay, there is Jakobshavn Isbrae. Along the northeast coast there is Nioghalvfjerdsbrae (79NG) and Daugaard-Jensen Glacier, which terminates into Scoresby Sund. On the southeast coast there is Helheim Glacier and Kangerlussuaq Glacier (Figures 5.4d and 5.4f).

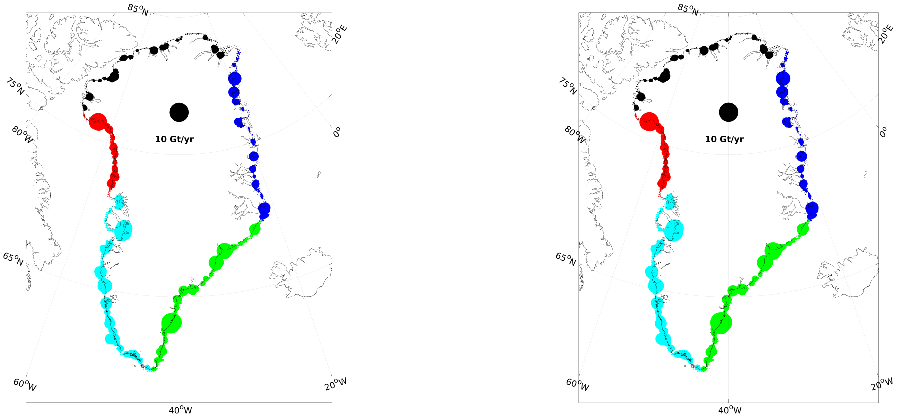

a. B12 Mean Liquid Discharge (2002 - 2010) b. B12 Mean Solid Discharge (2002-2010)

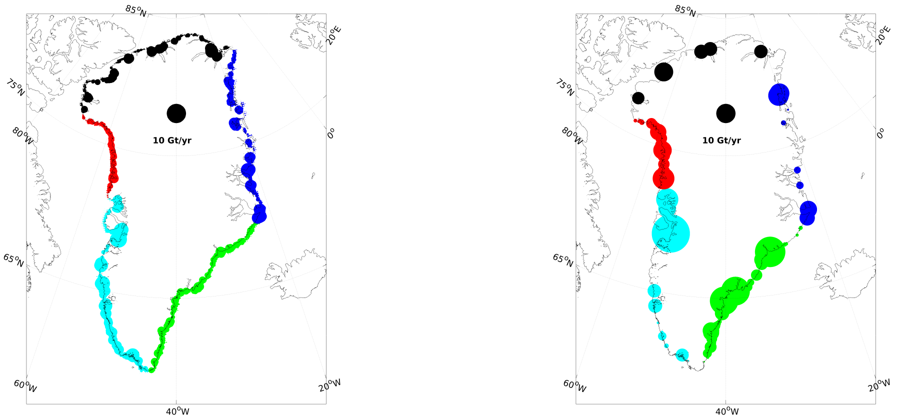

c. B18 Mean Liquid Discharge (2002-2016) d. B18 Mean Solid Discharge (2002-2016)

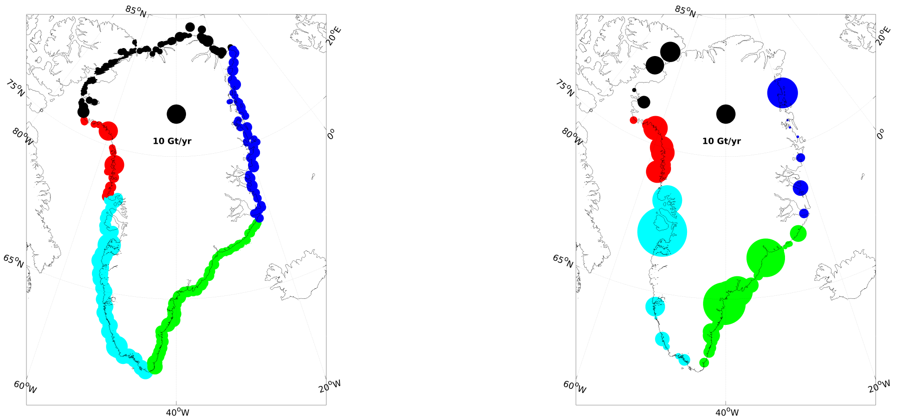

e. L15 Mean Liquid Discharge (2002 -2016) f. L15 Mean Solid Discharge (2002 - 2016)

Figure 5.4: Average rates of the GrIS freshwater flux (FWF) for the liquid and solid discharge for B12 (a. and b.), B18 (c. and d.) and L15 (e. and f.) averaged from 2002-2010 for B12 and 2002 - 2016 for L15 and B18. The circle in the middle of Greenland denotes the reference scale for magnitude of discharge rates in Gt/year. Colours denote separate regions for evaluation of the discharge sites (Table 5.2).

Table 5.2: Average rates of liquid and solid FWF per location (Gt/year) and site for different Greenland Ice Sheet (GrIS) products (Figure 5.4). Averaged from 2002-2010 for B12 and 2002 - 2016 for L15 and B18 The third and forth columns show the number of discharge sites per region and the average discharge per site in each region.

GrIS Region	Dataset	Runoff		Solid	
		Number	Average	Number	Average
North	B12	287	0.1365	287	0.1602
	B18	283	0.3845	6	5.5545
	L15	292	0.3223	8	5.1275
Northwest	B12	154	0.4568	154	0.5363
	B18	139	0.3388	29	2.8652
	L15	34	1.6917	11	8.5501
Southwest	B12	311	0.5490	311	0.6445
	B18	294	0.7984	17	5.8150
	L15	120	2.3419	11	11.6303
Southeast	B12	219	0.7575	219	0.8892
	B18	221	0.4663	39	4.1671
	L15	137	1.1099	28	8.1422
Northeast	B12	292	0.2221	292	0.2607
	B18	300	0.4422	8	5.0475
	L15	86	1.2391	8	4.7205

5.2.5 Freshwater and Heat Content

The freshwater content (FWC; units in m^3), relative to a reference salinity S_{ref}=34.8 (Aagaard and Carmack, 1989), over each region (Figure 5.2) can be calculated as:

$$FWC = \int \frac{S_{ref} - S}{S_{ref}} dV \tag{5.1}$$

where S is the salinity of the model output at each grid point. The heat content (HC; units in TW) is defined as:

$$HC = \int (T - T_{ref}) \rho_0 C_p 10^{-12} dV \tag{5.2}$$

where T is the temperature of the model output over the at each grid point, $T_{ref} = -2^oC$ is the reference temperature, ρ_0 is the reference density (1026 kg/m^3; Madec, 2008) and C_p is the specific heat capacity of seawater (3992 J/kg/^{o}C; IOC, SCOR, and IAPSO, 2010).

5.3 Results and Discussion

5.3.1 Spatial Distribution of Iceberg Discharge

The differences in iceberg distribution and their discharge rates were examined further by investigating the occurrence of icebergs and their accumulated mass. This was done by counting the number of icebergs and their total mass in each ocean grid cell at each time step. The accumulated mass includes the mass of icebergs as well as bergy bits (large, floating glacial ice spawned from disintegrated icebergs). B18 will be used as a control experiment in the comparison of iceberg accumulation over the entire period (Figure 5.5a and Figure 5.6a). The majority of the icebergs remain along the coastlines of the Greenland shelf, off the northwest coast of Greenland into Melville Bay, in the interior of Baffin Bay, and off the Baffin Island Shelf (Figure 5.5a and Figure 5.6a). Icebergs from the GrIS have the potential to travel throughout the majority of the western subpolar gyre (including the Labrador Sea) as well as Baffin Bay, which can have significant impacts on navigation through these waters (Figure 5.6a). If an individual iceberg was slow or stuck and remained in the same ocean grid cell for more than one model time step, it was counted twice. By calculating the accumulation of icebergs, regardless if they are a unique iceberg or the same iceberg, indicates where potential grounding zones are. The accumulated mass highlights where the larger icebergs (or perhaps many smaller icebergs) travel (Figure 5.5a), which can also be important for navigation and is crucial for thinking about freshwater dispersal, which will be discussed more in a later section.

By the end of the period, the distribution of the iceberg mass (including bergy bits) between B18 and B12 (Figure 5.5b) showed that there was about 10 Pt more mass accumulated from B18 on the northwest Greenland shelf (east Baffin Bay), as well as along the Canadian Shelf. There were $\sim$ 800 more icebergs in B18 than in B12 around specific regions along the Greenland coastline: the northwest, and two specific spots along the northeast and southeast, near 79NG and Helheim Glacier, respectively (Figure 5.6b). B18 also had $\sim$ 200 more icebergs along the Canadian Shelf, and $\sim$ 400 more off Baffin Island. B12 had $\sim$ 800 more icebergs than B18 along the southwest coast and eastern coast of Greenland.

The comparison of iceberg distribution between B18 and L15 (Figure 5.5c) showed that there was about 10 Pt more accumulated mass from L15 in Baffin Bay, Labrador Current, and into the Subpolar Gyre. B18 had more iceberg mass closer to the southeast, north, and northeast coasts as well as into the Arctic. Looking at the occurrence

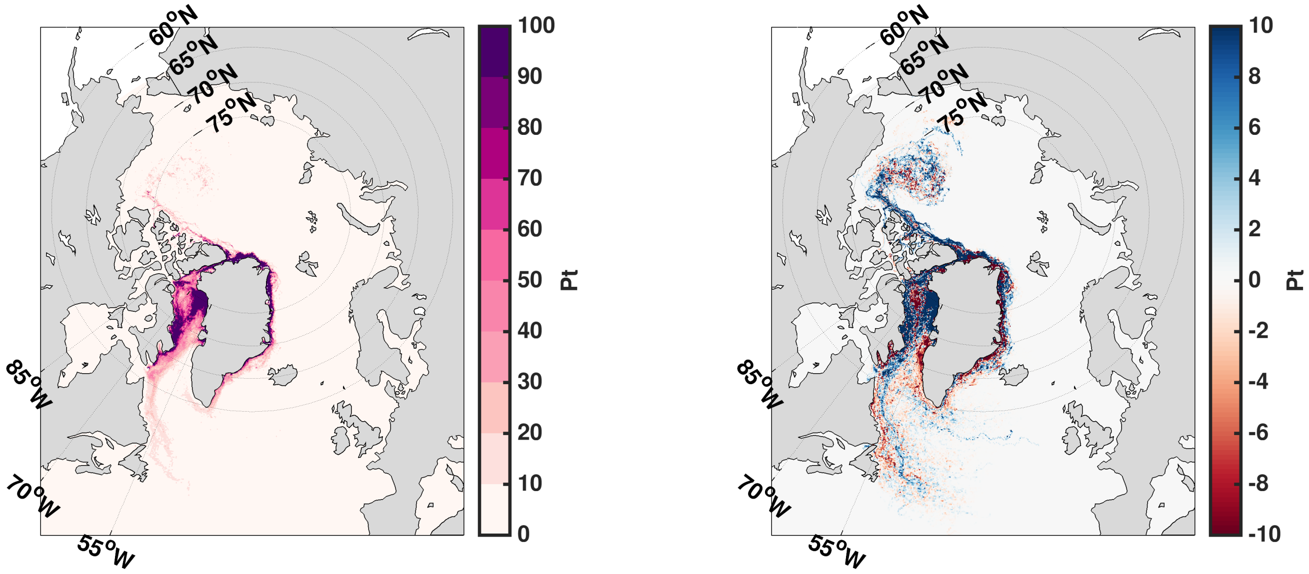

a. B18 b. B18 minus B12

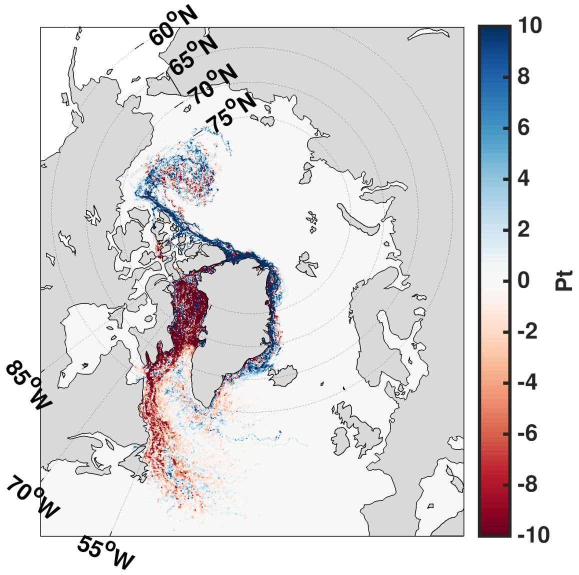

c. B18 minus L15

Figure 5.5: Difference between iceberg mass (including bergy bits) that have been accumulated through the experiments grid cells, during 2002-2016 (Pt = $1x10^{15}$ kg), regardless if they are unique icebergs or the same iceberg. Panel a. shows the iceberg mass and bergy bits for B18, panel b. shows the difference between B18 and B12, panel c. shows the difference between B18 and L15.

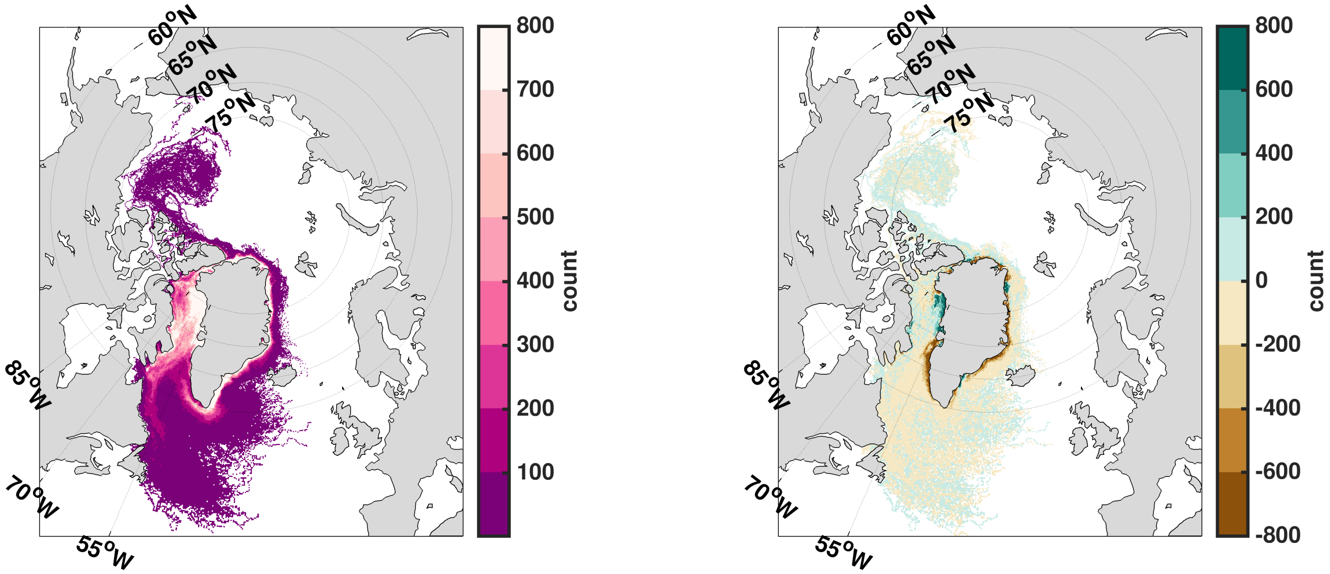

a. B18

b. B18 minus B12

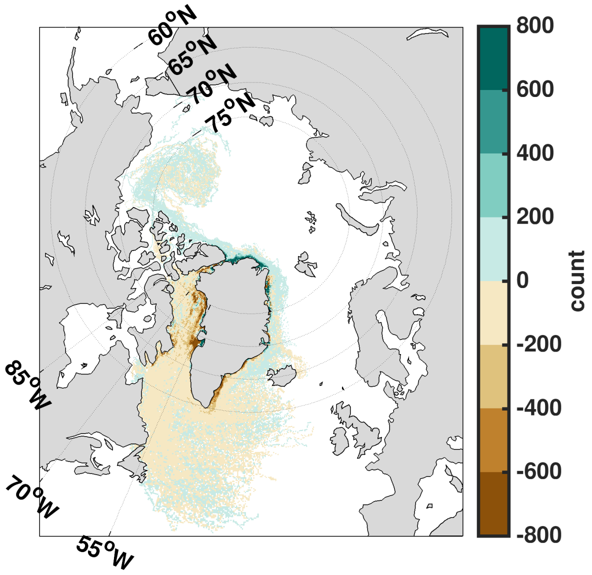

c. B18 minus L15

Figure 5.6: Difference between the number of iceberg particles that have been accounted for in the experiments grid cells, during 2002-2016, regardless if they are unique icebergs or the same iceberg. Panel a. shows the iceberg particle count for B18, panel b. shows the difference between B18 and B12, panel c. shows the difference between B18 and L15.

of icebergs (Figure 5.6c), L15 had 800 or more icebergs in Baffin Bay, especially along the northwest shelf break and southeast coast of Greenland. B18 showed 800 or more icebergs inside Disko Bay and generally along the north and northeast coast (near 79NG and Scoresby Sund). In the Subpolar Gyre, L15 had about 200 more icebergs, whereas in the Arctic, B18 had about 200 more icebergs.

5.3.2 Spatial Distribution of Meltwater

Figure 5.7 compares the Greenland passive tracers that collected in each region over the entire water column for the three experiments. Since the tracers are proportional to the amount of meltwater, they can represent the meltwater thickness in the water column in metres. B18 will be used as a control experiment in the comparison of the passive tracers.

Iceberg Melt

An additional passive tracer is added as the icebergs melt and, thereafter, advected as a liquid tracer. The melt of icebergs in B18 collected mostly along the northwest coast of Greenland, in Davis Strait, and the western subpolar gyre. This contrasts with the distribution seen for the solid iceberg trajectory (Figure 5.5a and Figure 5.6a). Thus, the iceberg melt collects in regions where icebergs may not reach themselves. Therefore, the impact of icebergs has two components: the distribution of the solid ice, which is important for navigation, and the advection of iceberg meltwater (which will be discussed in Section 5.3.3).

In B12 (Figure 5.7b), the iceberg meltwater accumulated and formed a thicker meltwater layer near Disko Bay (0.6 m), Davis Strait (0.6 m), Hudson Strait (0.4 m) and Labrador Current (0.4 m) compared to B18. This may be because more of the icebergs accumulated along the southwest coast of Greenland in B12 than in B18 (Figure 5.5b and Figure 5.5b). Additionally, B12 had a greater number of iceberg discharge locations further south than in B18, albeit with smaller magnitudes (Figure 5.4, Table 5.2) as well as differences in seasonality (Figure 5.3d).

L15 had similar seasonality and solid iceberg discharge locations to B18, but had more iceberg accumulation in Baffin Bay, the Labrador Current, and the Labrador Sea (Figure 5.5c and Figure 5.6c). The iceberg meltwater distribution varied very little from B18, with a thickness increase of only 0.2 m for the meltwater layer throughout the region. Therefore, B12 highlights that it might be the number of discharge sites, and not necessarily the magnitude of the discharge (as it is higher in L15 and B18) which is important for the dispersion of the iceberg's meltwater. This study only looks at icebergs released all along the coast whereas Marson et al. (2018) studied the fate of icebergs divided by the five regions along the coastline. Marson et al. (2018) found that of the icebergs which entered the interior of the Labrador Sea, 60 % of them originated from the southeast region.

Southeast

Liquid FWF released from the southeast region of Greenland travelled throughout the entire North Atlantic Subpolar Gyre (in all experiments; Figures 5.7d, 5.7e, and 5.7f). In B18, approximately a 0.4 m to 0.5 m layer of meltwater accumulated along the WGC, along the boundary of the Labrador Sea, and in the Labrador Current off the Canadian Shelf reaching the Flemish Cap. Most of the meltwater bypassed the central Labrador Sea, though some became entrained.

L15 had approximately 0.1m more melt accumulation scattered throughout the entire North Atlantic region, with 0.3 m more accumulation near the southeast coast of Greenland, western Labrador basin, and the Flemish Cap than in B18 (Figure 5.7f). Recall that L15 had fewer discharge sites than B18, but the thicker meltwater layer near the southeast coast could be due to the larger magnitude of discharge in that region (Figure 5.4; Table 5.2). Similarly, B12 had more melt accumulated throughout the North Atlantic region (Figure 5.7e) than in B18. B12 had a meltwater layer 0.2 m thicker near the Flemish Cap, 0.3 m in the Labrador Sea, 0.4 m on the south coast of Greenland, 0.1 m on the west Greenland shelf, and 0.1 m into Hudson Strait. As discussed above regarding iceberg melt, B12 showed larger amounts of meltwater accumulation in the Labrador Sea, as seen in Gillard et al. (2016) which used similar runoff and discharge sites Bamber et al. (2012). B12 has slightly fewer runoff discharge sites, but at a greater magnitude of discharge (Table 5.2). Even though the annual liquid FWF is higher in B18 (Figure 5.3a), the seasonality is quite different. B12 had a lower seasonal average in the summer months but a higher seasonal average in the winter months (Figure 5.3b).

It is likely that more meltwater accumulated in the Labrador Sea in B12 than B18 due to the higher runoff in winter months in B12 and the greater magnitude of FWF per discharge site. This is in contrast to how the iceberg meltwater was shown to enter the Labrador Sea. For icebergs, the greater number of discharge sites may have caused the icebergs to spread out more, leading to an even larger dispersion of the iceberg melt. However, for meltwater injected off the southeast sector, the magnitude of runoff, not the number of discharge sites, increased the accumulation in the Labrador Sea. Gillard et al. (2016) also found that meltwater from the southern regions of Greenland penetrated the interior of the Labrador Sea, with around 80 % of the accumulated meltwater coming from the southeast coast. The amount of meltwater accumulated per region will be discussed later.

Northeast

In B18, most of the liquid FWF released from the northeast region of Greenland stayed close to the eastern Greenland shelf with a meltwater layer of 1 m. Some meltwater became entrained in the Labrador Sea and reached the Flemish Cap with a meltwater layer of approximately 0.4 m thick. B18 had a meltwater layer 2 m thicker along the east coast than in B12 (Figure 5.7h) and about 1.5 m thicker than in L15 (Figure 5.7i). In the northeast, B18 has a higher magnitude of FWF per discharge site on average than B12 but not L15; however, B18 does have more discharge sites than L15 (Figure 5.4; Table 5.2).

North

In B18, most of the liquid FWF released from the north region of Greenland travelled westward through Nares Strait with a meltwater layer of 1 m (Figure 5.7j). There was an accumulation in northern Baffin Bay, into Jones Sound and central Baffin Bay of about 0.75 to 1 m. An accumulation of approximately 0.6 m on the west coast of Baffin Bay and west side Davis Strait with 0.3 m in the Labrador Current.

B18 had a meltwater accumulation along Nares Strait and near Lancaster Sound approximately 1 m thicker than in B12 (Figure 5.7k). The meltwater thickness in B18 was larger than in B12 by about 0.4 m in Baffin Bay and about 0.2 m in the Labrador Current. B18 also had a thicker meltwater layer than in L15 along the north coast by about 1 m, and by about 0.2 m in Baffin Bay, Davis Strait, and in the Labrador Current (Figure 5.7l). Gillard et al. (2016) used ARIANE, an offline tracking tool (Blanke et al., 1999; Blanke and Raynaud, 1997), to show the dispersion of particles released from Greenland's coast. They showed that particles released from the north coast tend to accumulate in the interior of Baffin Bay and Canadian Shelf, with a low percentage of them reaching as far as the Nordic Seas. However, while ARIANE only calculates the advection of particles with diffusion and mixing processes handled by the ocean model's output velocity fields, passive tracers are treated as a physical quantity and their transport is dictated both by advection and diffusion equations.

Northwest

In B18, the liquid FWF released from the northwest region of Greenland typically stayed within Baffin Bay, with a 1.5 m-thick meltwater layer close to Disko Bay and a 0.6m-thick meltwater layer in Davis Strait (Figure 5.7m). B12 had more melt accumulated than B18 in certain regions, resulting in a meltwater layer that was 0.5 m thicker along the northwest coast of Greenland and in Disko Bay, and 0.1 m thicker in the interior Baffin Bay (Figure 5.7n). B18 had a meltwater layer more than 0.3 m thicker than in B12 just north of Disko Bay. Comparing L15 and B18, B18 had a meltwater layer 0.5m thicker north of and within Disko Bay. L15 had a meltwater layer along western Baffin Bay that was thicker than in B18 by about 0.3 m to 0.5 m (Figure 5.7o). In fact, B18 had the lowest meltwater discharge rates in the northwest area (Figure 5.4; Table 5.2), whereas B12 and L15 showed higher magnitude discharge rates close to Kong Oscar and Hayes Glacier. These differences may have caused the changes close to and north of Disko Bay and in Melville Bay.

Southwest

In B18, the liquid FWF released from the southwest region (including the coastline up to Uummannaq Fjord) of Greenland formed a meltwater layer of 1m in Davis Strait and a layer of 0.4 m in the Labrador Current (Figure 5.7p). The meltwater layer was generally thicker (by $\sim$ 0.1 m) in B18 than in B12 throughout the North Atlantic Ocean, reaching a 0.4 m difference near Disko Bay (Figure 5.7q). L15 had a meltwater layer that was 0.1 to 0.6 m thicker than in B18 throughout the entire region (Figure 5.7r). Recall that L15 had fewer discharge sites than both B12 and B18, though larger average magnitudes of FWF (Figure 5.4; Table 5.2). The higher discharge rates in L15 were located near Uummannaq Fjord and Disko Bay (close to where Rink Glacier and Jakobshavn Isbrae terminate), whereas in B12 the discharge in those regions were the lowest among the three products. This is most likely why there was more meltwater dispersion from the southwest sector in L15 compared to B18 (and in B18 compared to in B12).

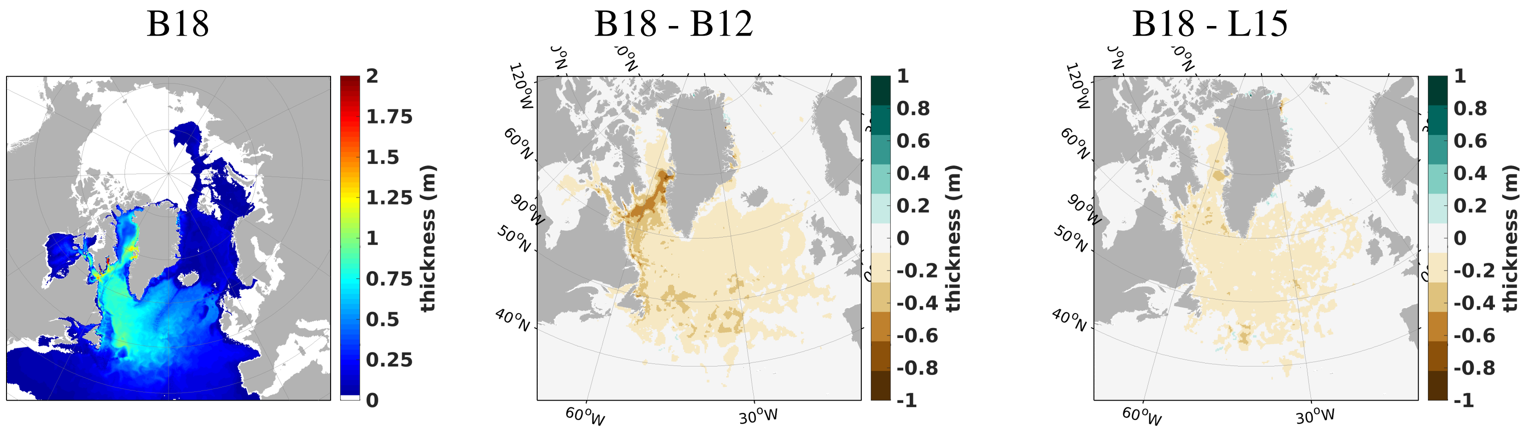

a. b. c.

Iceberg Melt

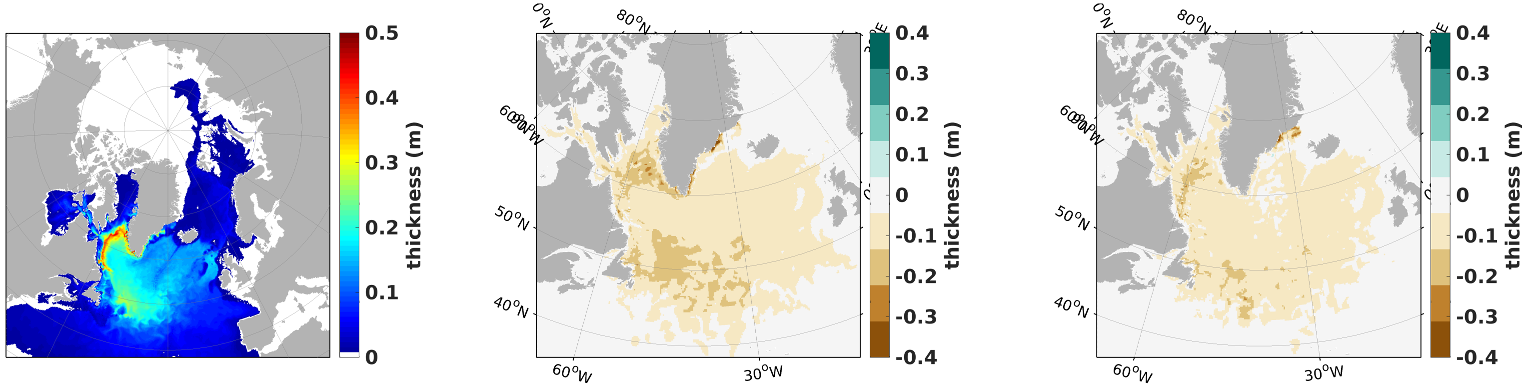

d. e. f.

Southeast

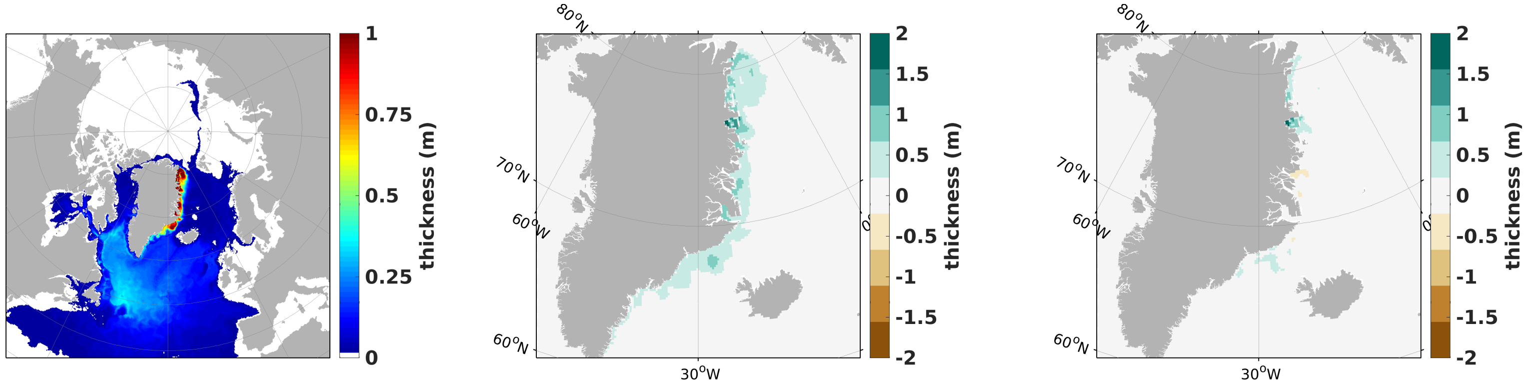

g. h. i.

Northeast

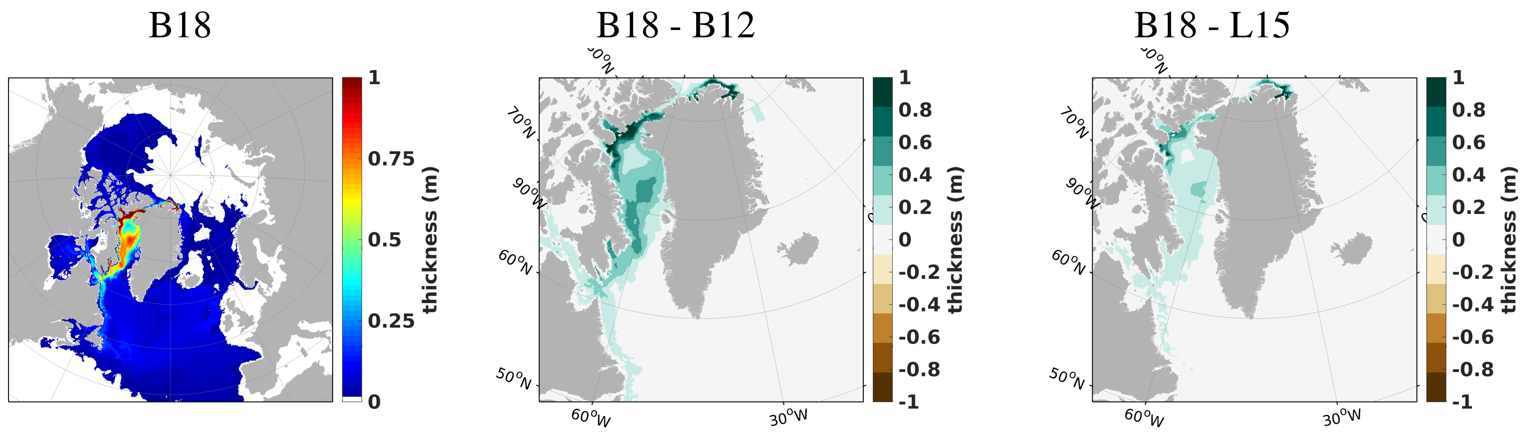

j.

k.

l.

North

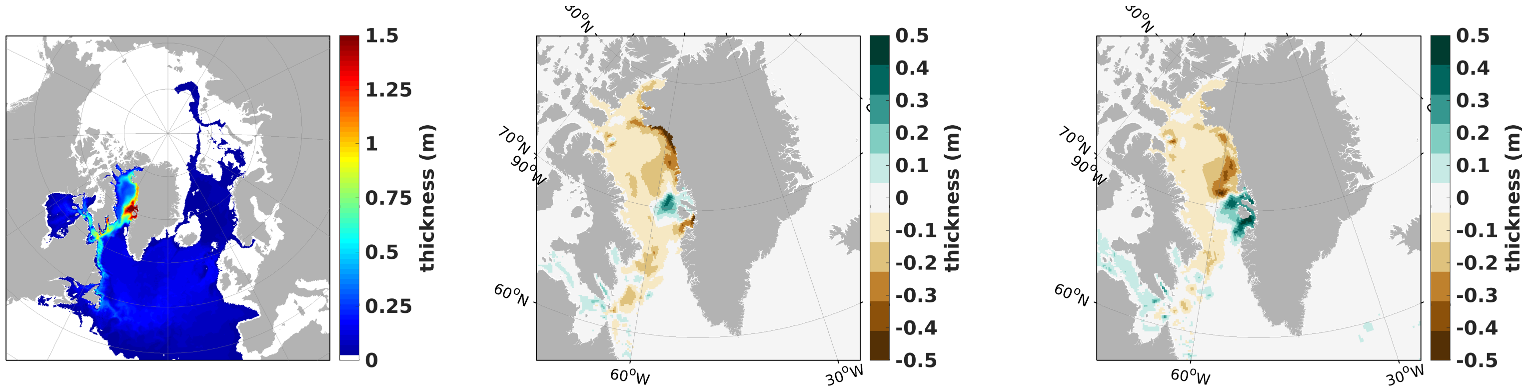

m.

n.

o.

Northwest

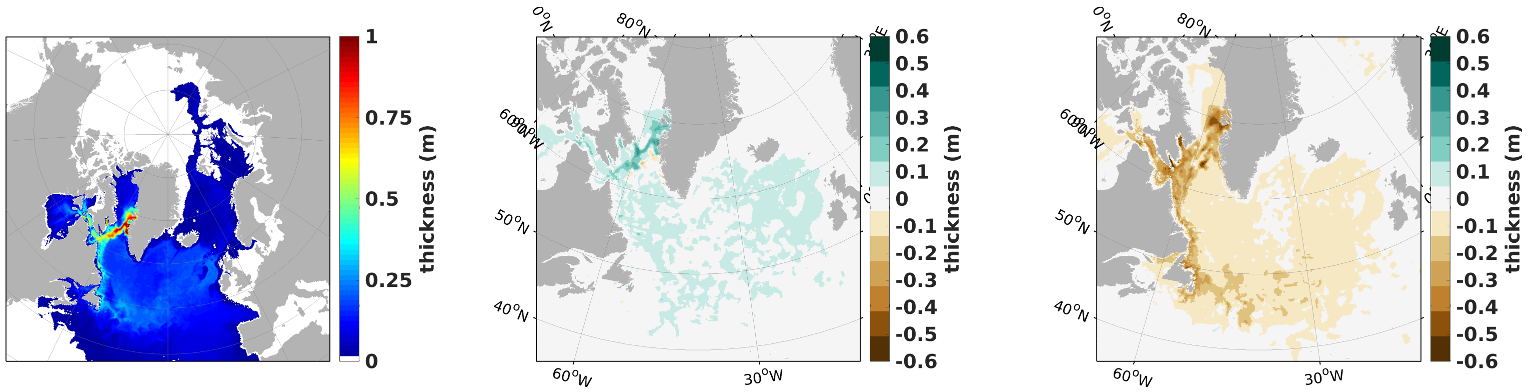

p.

q.

r.

Southwest

Figure 5.7: The evolution of passive tracers that have been tagged with different melt locations and datasets at the end of the experiment run (December 31st, 2016). The passive tracers are collected over the entire depth of the water column. The first row the evolution of B18's passive tracers while the rest of the rows show the difference between the experiments.

5.3.3 Storage of Meltwater

The amount of meltwater accumulated by the end of the simulation period (Dec. 31st, 2016) has been calculated (Figure 5.8) to determine potential implications of iceberg melt and liquid FWF from the 5 sectors of the GrIS to different regions in the ocean. The region's major source of meltwater will be discussed.

Entire Region

The total accumulation of melt throughout all of the study domain (Figure 5.2) highlights the consistency of the previous discussion on the GrIS melt tagged by passive tracers (Figure 5.7). B18 had the lowest amount of iceberg melt accumulation over all of the study domain (Figure 5.8a), which is consistent with B18 having the lowest amount of annual solid FWF (Figure 5.3c) and the smallest spatial distribution of iceberg melt (Figure 5.7a). Depending on which GrIS FWF product was used, the GrIS sector that contributed the most melt varied. For B12, melt from the north and northeast sectors of the GrIS had the least amount of runoff melt accumulated throughout the study domain; GrIS northeast and north sectors had minimal spread (Figure 5.7h and 5.7k, respectively). For B18, melt from the southeast led to least amount of melt accumulated, which again did not spread extensively (Figure 5.7d). For L15, melt from the southwest had the largest amount of accumulated melt, and was also more broadly distributed (Figure 5.7r). Each study domain (Figure 5.2) will be analysed separately to assess the iceberg melt and main source of liquid FWF among the five GrIS sectors.

Hudson Bay Complex

From all three experiments, melt released off the west coast of Greenland had a higher likelihood of entering the Hudson Bay Complex (Figure 5.8b). For L15, 205 Gt of meltwater from the southwest GrIS entered the Hudson Bay Complex, whereas in B18 and B12 the main source of meltwater (159 GT and 150 GT, respectively) was the northwest sector of Greenland. The amount of iceberg melt varied between the three experiments, with 322 Gt in B12, 272 Gt in L15, and 237 Gt in B18. A difference of about 100 Gt of meltwater (summation of iceberg melt and main source of melt from liquid FWF) over the 13-year study period is not a significant difference since, in comparison, the HBC receives about 900 Gt of river runoff annually (Shiklomanov and Shiklomanov, 2003). However, now knowing that GrIS meltwater and iceberg melt enter the HBC, this may become an important contribution of freshwater in the future as the GrIS continues to lose mass.

Baffin Bay

In Baffin Bay, there is not a significant amount of meltwater accumulation from the southeast and northeast sectors of Greenland, with less than 40 Gt per region, in any of the three experiments (Figure 5.8c). For L15, the sectors of Greenland that contributed the most meltwater to Baffin Bay were the northwest with a total of 431 Gt, which resides in Baffin Bay, and the north with 291 Gt, which follows the general circulation to the west through the Lincoln Sea and Nares Strait (Aksenov et al., 2010). For B18, the regions of Greenland that contributed the most meltwater to Baffin Bay were the north with a total of 420 Gt and the northwest with 387 Gt. For B12, most of the meltwater, with a total of 457 Gt, came from the northwest coast of Greenland. The total amount of iceberg melt accumulated in Baffin Bay was 513 Gt in B12, 489 Gt in L15 and 417 Gt in B18. Melt from the northwest appeared to have the greatest impact on Baffin Bay, which is expected given the proximity. However, whether the north or southwest melt accumulated more depended on the product used. Modelling studies (Castro de la Guardia et al., 2015; Gillard et al., 2020; Grivault et al., 2017) showed that an increase in GrIS liquid FWF increased the heat content within Baffin Bay. Future researchers looking at Baffin Bays dynamics may want to consider which GrIS FWF product to use to force the ocean model as it may impact the following: freshwater and heat content; sea ice conditions; surface circulation patterns; and air to sea surface heat loss.

Canadian Arctic Archipelago

Overall, the accumulated mass of GrIS meltwater in the CAA was two orders of magnitude smaller compared to the values obtained for the entire region (Figure 5.8d). In the CAA, the most meltwater came from the north sector with 60 Gt stored in B18, 48 Gt in L15, and only 20 Gt in B12 (Figure 5.8d). The meltwater from the north sector could reach the CAA through two currents: one current that travels west across the Lincoln Sea to the north coastline of the CAA, and another one that travels along the eastern CAA and heads westward in Jones Sound (Figure 5.7j-l). The iceberg melt accumulated in the CAA remained low ($\sim$ 11 to 17 Gt) because not many icebergs travelled into the region (Figure 5.6). The addition of freshwater in this region may increase the sea surface height and lead to a reduction of the pressure gradient between the Arctic Ocean and Baffin Bay, which would reduce the transport of Arctic waters through the CAA (Castro de la Guardia et al., 2015).

Arctic West

In the western Arctic, the north sector of Greenland contributed with the highest amount of meltwater in B18 and in L15, storing 95 Gt each; in B12, only 28 Gt of meltwater from the north were stored (Figure 5.8e). This is expected as portions of the north coast resides in the western Arctic region (Figure 5.2), which includes the Lincoln Sea. In the Lincoln Sea, there is a westward current (Aksenov et al., 2010) which may have aided in mixing the meltwater into the western Arctic. The storage of iceberg melt in this region is relatively low: 8 Gt in L15, 19 Gt in B18, and 20 Gt in B12. The accumulation of meltwater in the western Arctic is relatively low compared to the other regions (Figure 5.7j). Therefore, depending on the experiment, the total accumulation of meltwater (glacial meltwater and iceberg meltwater) in the western Arctic varies between experiment and is lowest, by about half, in B12.

Arctic East

In the eastern Arctic region, the leading source of GrIS liquid FWF depended on the GrIS FWF product used (Figure 5.8f). For L15, the highest contribution of meltwater to the east part of the Arctic was 42 Gt from the southwest and 36 Gt from the north sectors of Greenland. For B18, the north sector had the highest contribution of meltwater with 63 Gt. B12 had similar contributions of meltwater from three different sectors: 23 Gt from the southeast, 24 Gt from the northwest, and 21 Gt from the southwest. It is worth remembering that B12 had the lowest number of runoff discharge sites from the north sector compared to B18 and L15. For solid discharge, on the other hand, B12 had the highest number of discharge sites, though very low FWF magnitudes (Table 5.2). As a result, B12 had the highest accumulated iceberg melt of 89 Gt, followed by 87 Gt in L15 and 72 Gt in B18. Since a portion of the north coast of Greenland resides in the eastern Arctic region, it is expected that meltwater from this sector would be a major contributor. However, the contributions from the west and south sectors of Greenland are surprising, since the meltwater had to travel through the North Atlantic Subpolar Gyre, recirculate northward through Iceland-Scotland ridge, and bypass Fram Strait, Barents Sea, and Kara Sea.

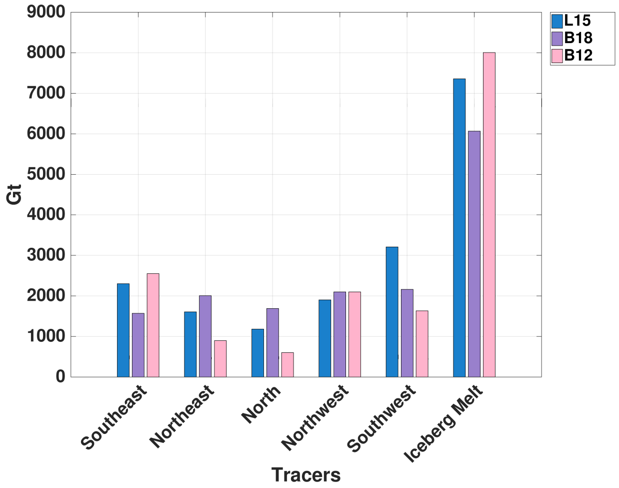

a. Entire Region

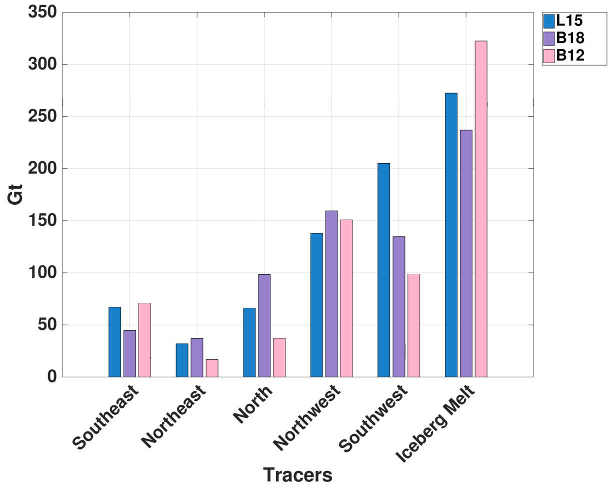

b. Hudson Bay Complex

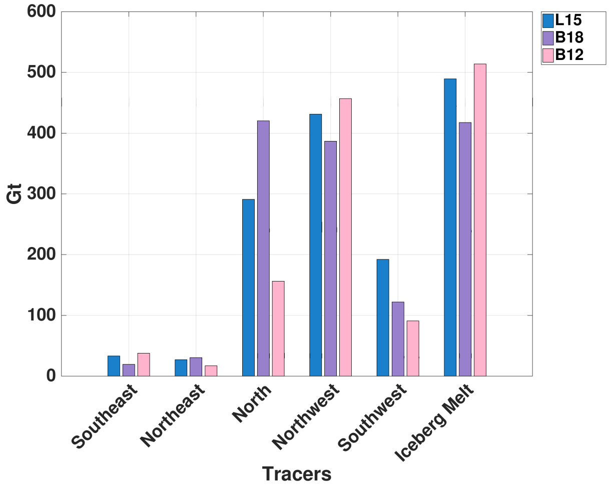

c. Baffin Bay

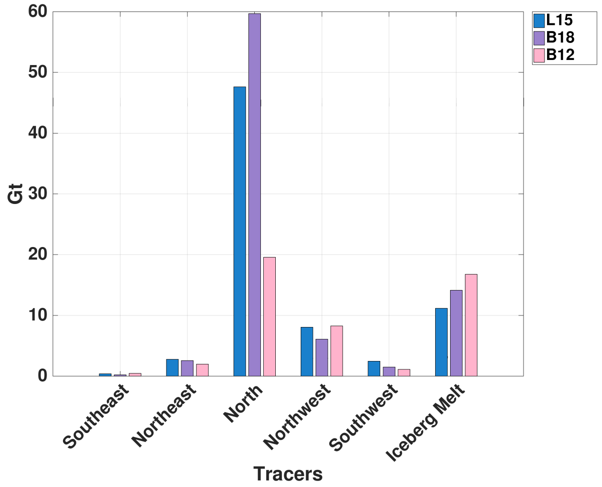

d. CAA

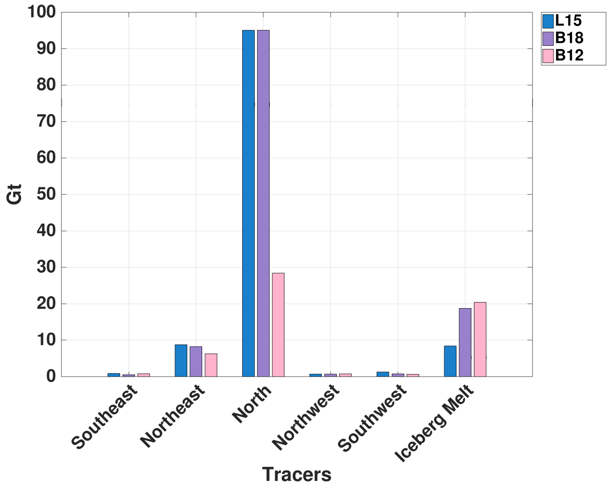

e. Arctic West

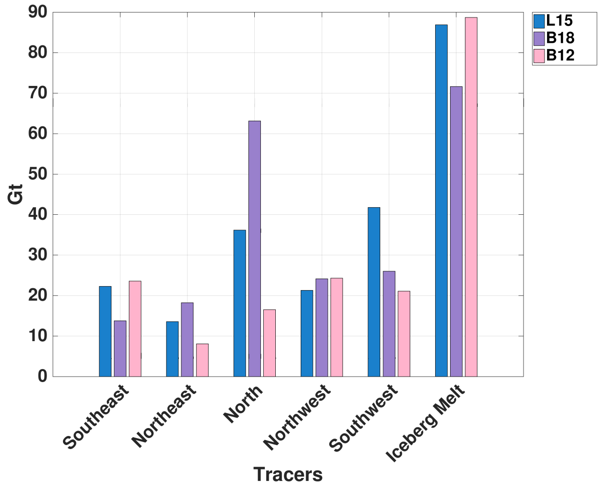

f. Arctic East

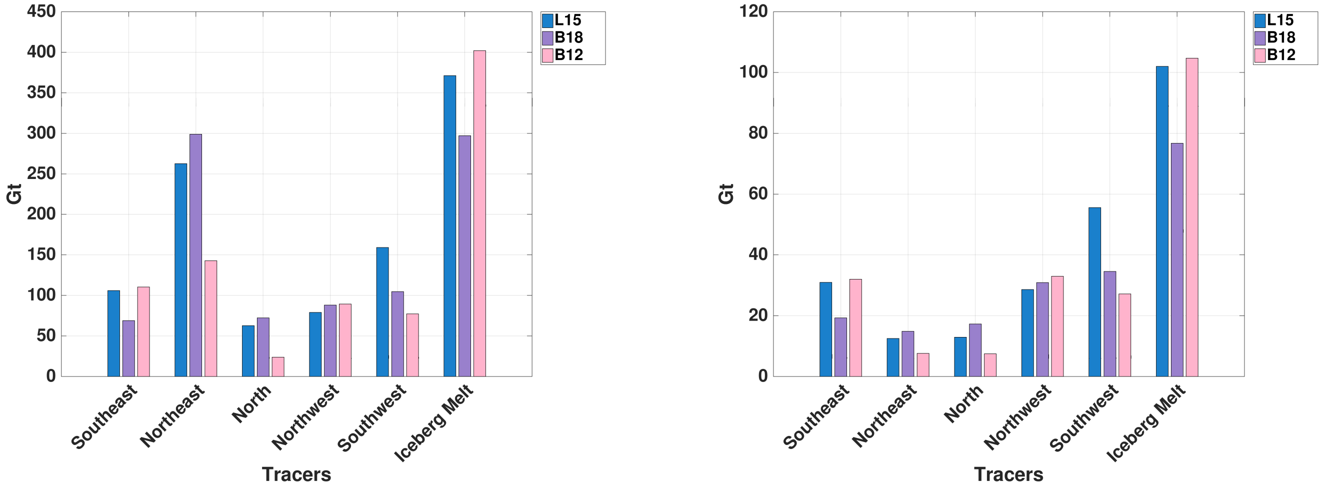

g. Greenland and Nordic Seas

h. Barents and Kara Seas

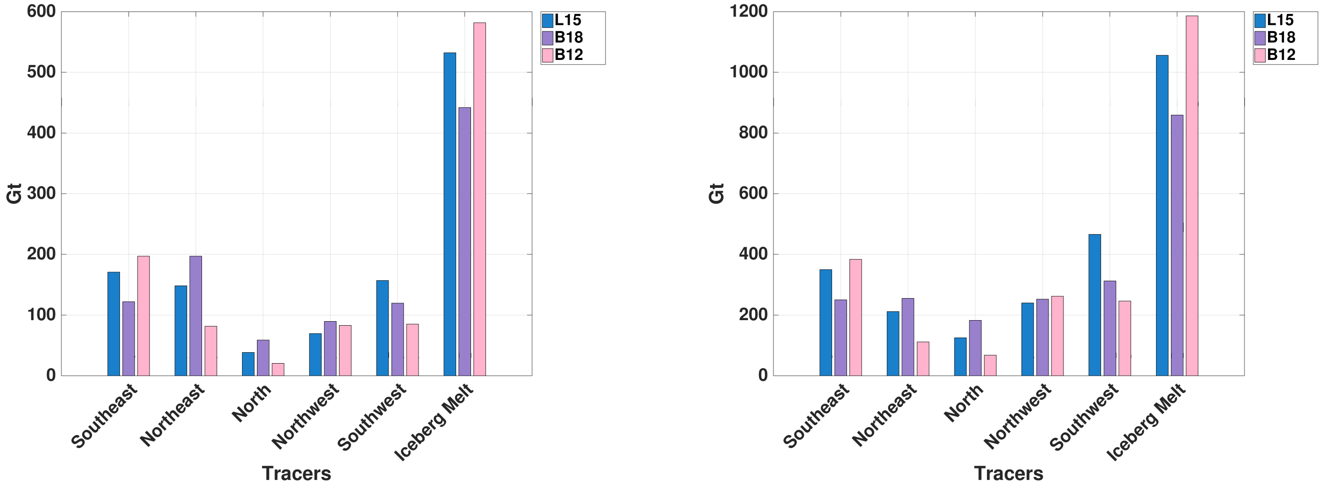

i. Irminger Sea

j. Labrador Sea

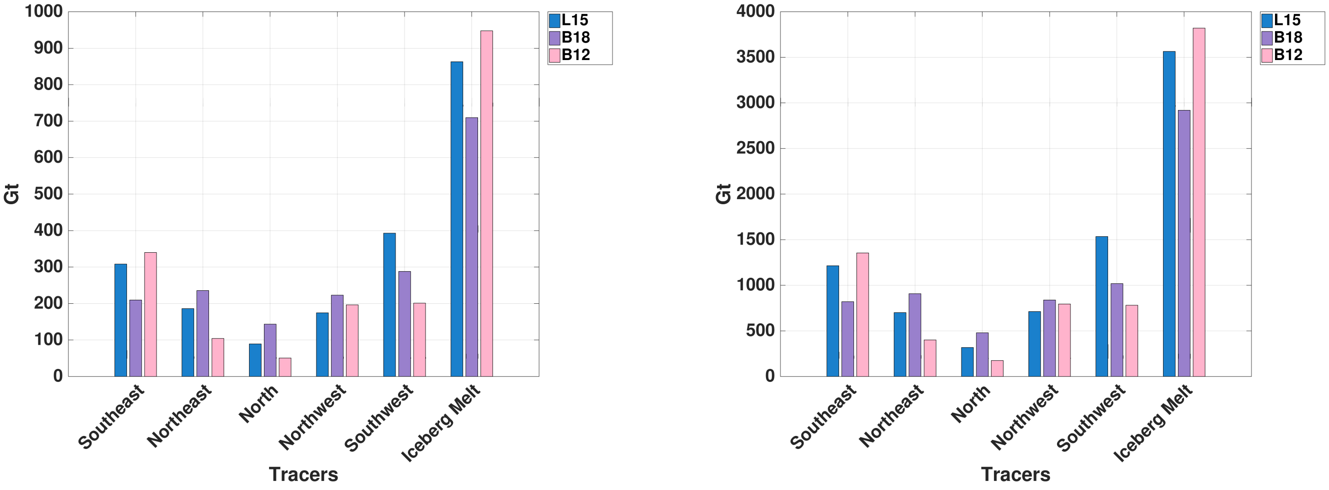

k. Subpolar Gyre East

l. South

Figure 5.8: Accumulated mass of tagged meltwater (passive tracers) at the end of the time series (December 31st, 2016) per region (Figure 5.2). L15 tracers are in blue, B18 tracers in purple and B12 tracers pink.

Greenland and Nordic Seas

In the Greenland and Nordic Seas (GNS), the northeast sector was the leading contributor of liquid FWF with 299 Gt in B18 and 263 Gt in L15 (Figure 5.8g). For B12, the main sources were the northeast sector with 143 Gt and the southeast sector with 110 Gt. This is because B12 liquid FWF discharge rates in the northeast have the lowest magnitude on average (though the number of discharge sites is high) compared to the other experiments (Table 5.2). Since the northeast coast of Greenland resides in the GNS, it would be expected that meltwater from this sector would accumulate the most in this region. The lowest thickness of meltwater is in the interior of the GNS region (Figure 5.7g) which is also seen in Dukhovskoy et al. (2016): passive tracers released from Greenland show that, over time, the tracer content increases in the Nordic Seas, but take longer to circulate into the interior of the Greenland Sea. In the case of iceberg melt, although B12 has the lowest magnitudes of discharge rates on average, it has the largest number of solid discharge sites compared to the other two experiments. Consequently, B12 had the highest accumulated iceberg melt of around 402 Gt, followed by L15 with under 371 Gt, and B18 with 297 Gt.

Barents and Kara Seas

In the Barents and Kara Seas, the total amount of meltwater was quite low relative to the entire region, which may be a function of its relative distance to the GrIS and the general ocean circulation (Figure 5.8h). The source of meltwater varied with the different experiments. In L15, 56 Gt came from the southwest; in B18, 35 Gt came from the southwest and 31 Gt came from the northwest; and in B12, 32 Gt came from the southeast, 33 Gt from the northwest, and 27 Gt from the southwest. B12 had the highest accumulation of iceberg melt (105 Gt), followed closely by 102 Gt from L15, and then a larger drop to 77 Gt from B18.

Irminger Sea

In L15 and B12, most meltwater came from the southeast sector of the GrIS (171 Gt and 197 Gt, respectively). Given the proximity between the GrIS southeast coast and the Irminger Sea, and the fast-following marine terminating glaciers that discharge into this region, it was expected that the southeast coast would be the highest contributor of melt to the Irminger Sea. However, for B18, the northeast sector meltwater dominated with 197 Gt (Figure 5.8i). The melt from the northeast coast could have travelled south with the EGC to be recirculated into the interior of the Irminger Sea by either travelling westward around the Labrador Sea or topographically steered away from Cape Farewell along the Eirik Ridge (Holliday et al., 2007). In terms of iceberg melt, B12 had the highest accumulated mass of 582 Gt, followed by 532 Gt in L15, and 442 Gt in B18.

Melt from the GrIS which enters the Irminger Sea may inhibit convection in this region. Recent studies have begun to investigate the role of convection in the Irminger Sea and its part in contributing to the variability and strength of the AMOC (Lozier et al., 2019; Menary et al., 2020). Therefore, the freshwater accumulation in the Irminger Sea from the GrIS may have the potential to impact and alter the large-scale ocean circulation. Studies looking at Irminger Sea convection should take into account melt from the southeast and northeast of GrIS, as when large marine terminating glaciers (e.g. 79NG and Zachariae Isstrom) start to accelerate they may add much more melt into this region than ever recorded.

Labrador Sea

All three experiments of this study agrees with previous works (e.g. Gillard et al., 2016; Luo et al., 2016; Marson et al., 2018)) that melt from south (southeast and southwest) Greenland is the largest contributor to GrIS meltwater in the Labrador Sea (Figure 5.8j). For B12, 383 Gt of meltwater in the Labrador Sea came from the southeast. For L15, 466 Gt of meltwater came from the southwest and 350 Gt from the southeast. For B18, the southwest sector had the greatest contribution (312 Gt) and GrIS remaining sectors contributed with similar amounts. For the iceberg melt, B12 had the largest accumulation of melt at around 1187 Gt, followed by L15 with 1056 Gt, and B18 with 859 Gt. The model used in Gillard et al. (2016) did not include iceberg representation, so it was limited to the analysis of liquid FWF only. Marson et al. (2018) found that solid discharge from the southeast was also an important contributor of meltwater to the Labrador Sea. The current study shows that the iceberg melt adds another contribution to the freshwater accumulation within the Labrador Sea region. Out of all regions, the Labrador Sea has the largest amount of melt accumulation. This highlights the importance of liquid and solid FWF from the southeast coast of Greenland for the freshwater variability in the Labrador Sea.

Subpolar Gyre East

In the eastern subpolar gyre (SPGE), the majority of the meltwater came from the southwest sector in L15 and B18 (393 Gt and 289 Gt, respectively) and from the southeast coast for B12 (340 Gt) (Figure 5.8k). For iceberg melt, B12 had the highest amount of meltwater at 948 Gt, followed by 863 Gt for L15 and 710 Gt for B18. Melt from the GrIS that entered the SPGE would have had to travel along the boundary currents (EGC, WGC, and Labrador Current) and then recirculated towards the SPGE.

South

This final region is located south outside all the other regions mentioned previously. The highest amount of meltwater came from the southwest in L15 at 1535 Gt, southeast in B12 with 1355 Gt, and B18 with multiple sectors contributing with the largest from the southwest at 1017 Gt (Figure 5.8l). Many icebergs travel south and export large amounts of melt as they travel, bringing low density (fresh) waters to southern (relatively salty) oceans. For the iceberg melt, B12 had the highest accumulation with 3820 Gt, whereas L15 had accumulated 3565 Gt and B18 accumulated 2920 Gt.

Freshwater and Heat Content

The regional source of meltwater and iceberg melt in the different regions was previously discussed (Figure 5.2). Another way to examine the property changes in the experiments is to compute the freshwater and heat content for the different regions (Figure 5.2; Equation 5.1 and Equation 5.2).

The only region that showed a difference in heat content was the eastern Arctic region (Figure 5.9; Table 5.3). Therefore, only the east Arctic region will be discussed. From 2004 to the end of 2016 the overall variability of heat content was similar throughout the three experiments. The differences among the experiments started to stand out in 2008 (Figure 5.9). B18 reached the highest heat content at 2.29×10^{12} TW, whereas B12 and L15 reached 2.28×10^{12} TW. B12, B18, and L15 had the minimum heat content at 2.11×10^{12} TW. A difference of 0.01×10^{12} TW is equivalent to 10 GJ, an amount of energy capable of melting 30 tonnes of fresh ice.

There are only a few regions that showed a difference in the FWC (Figure 5.10; Table 5.3). In Baffin Bay, between 2010 to 2016, the FWC average was 1.66×10^{7} km^3 among all experiments with only small differences (Figure 5.10a). The FWC of the Greenland and Nordic Seas varied slightly among the three experiments from 2010

Table 5.3: Comparing experiments' heat content and freshwater content per regions of Eastern Arctic (AE), Baffin Bay (BB), Greenland and Nordic Sea (GNS), Irminger Sea (IS), and Subploar Gyre East (SPGE). Third and fourth coloumn show the maximum and minimum heat content (HC; units TW) over the entire period (2004-2016). The fifth column shows the average freshwater content (FWC; units km^3) over a select period.

Simulation	Region	Maximum HC (TW)	Minimum HC (TW)	Average FWC (km^3)
B12	AE	2.28×10^{12}	2.11×10^{12}	
	BB	–	–	1.66×10^{7} (2010 - 2016)
	GNS	–	–	8.13×10^{7} (2010 - 2016)
	IS	–	–	3.26×10^{7} (2004 - 2016)
	SPGE	–	–	6.10×10^{7} (2010 - 2015)
B18	AE	2.29×10^{12}	2.11×10^{12}	
	BB	–	–	1.66×10^{7} (2010 - 2016)
	GNS	–	–	8.12×10^{7} (2010 - 2016)
	IS	–	–	3.26×10^{7} (2004 - 2016)
	SPGE	–	–	6.10×10^{7} (2010 - 2015)
L15	AE	2.28×10^{12}	2.11×10^{12}	
	BB	–	–	1.66×10^{7} (2010 - 2016)
	GNS	–	–	8.12×10^{7} (2010 - 2016)
	IS	–	–	3.26×10^{7} (2004 - 2016)
	SPGE	–	–	6.11×10^{7} (2010 - 2015)

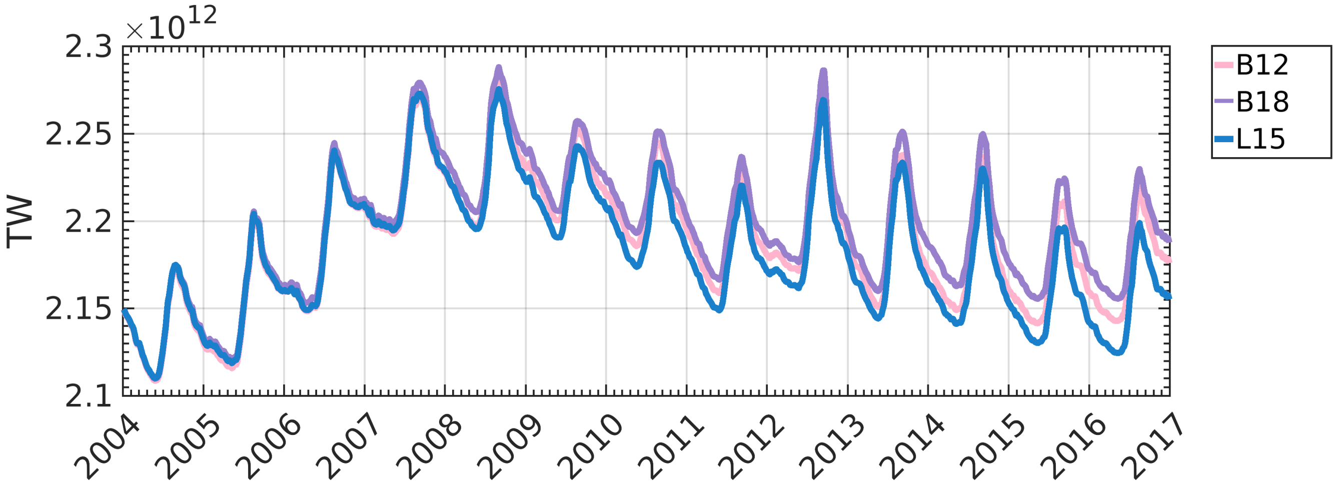

Figure 5.9: Heat content (TW) evaluation from 2002 to the end of 2016. A comparison between the different GrIS products (B12 in pink, B18 in purple, and L15 in blue) in the eastern Arctic region (Figure 5.2).

to the end of 2016, with averages of approximately of 8.1×10^7 km^3. L15 and B18 had a FWC average of 8.12×10^7 km^3 and B12 had a FWC average of 8.13 $\times10^7$ km^3 (Figure 5.10b). For the Irminger Sea, the FWC changed slightly throughout the entire period; however, all experiments FWC average was 3.26×10^7 km^3 (Figure 5.10c). For the subpolar gyre east region, the FWC changes slightly throughout the entire period, with the largest differences occurring from 2010 to 2015; however, all experiments FWC average was 6.10×10^7 km^3 (Figure 5.10d).

The FWC is calculated over the entire water column and varies slightly in all three experiments. However, a change on the order of magnitude of 0.001×10^7 km^3 (10000 km^3) of freshwater (relative to 34.8) is equivalent to the amount of freshwater that entered the sub-Arctic seas in the late 1960s to early 1970s (the Great Salinity Anomaly, Curry and Mauritzen (2005), which proved to be capable of reducing the deep water formation in the Labrador and Nordic Seas. However, Böning et al. (2016) showed that the GrIS discharge had not yet altered the variability or strength of the AMOC. Our study agrees with Boning et al. (2016), as the AMOC (Figure S5.1) has not shown any sensitivity to the three different GrIS FWF products. Therefore, the variation in FWC in these regions discussed in this section (Baffin Bay, GNS, Irminger Sea, SPGE) are not significant for the AMOC. Future climate studies should look at how changes in GrIS FWF products alter the FWC in these regions on a longer time scale, as it could become significant to the strength of convection and overflow of dense waters that feed the AMOC.

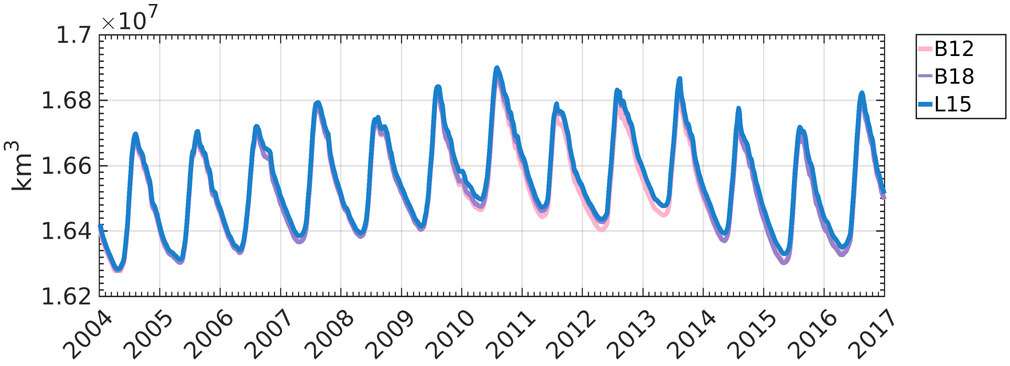

a. Baffin Bay

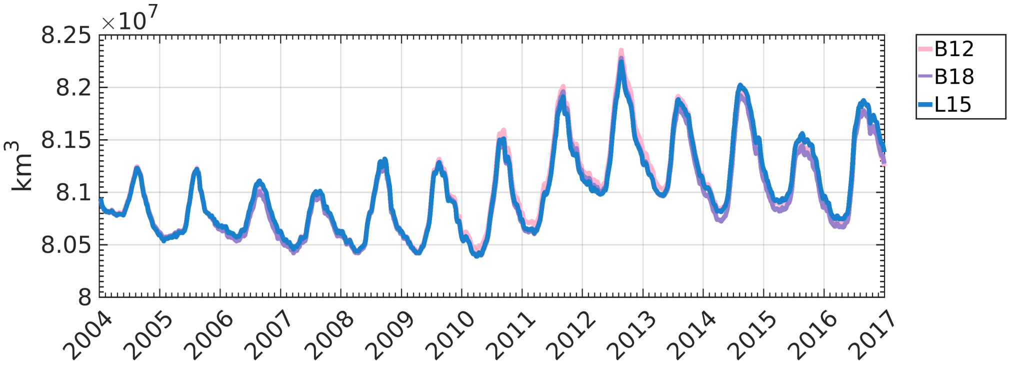

b. Greenland and Nordic Seas

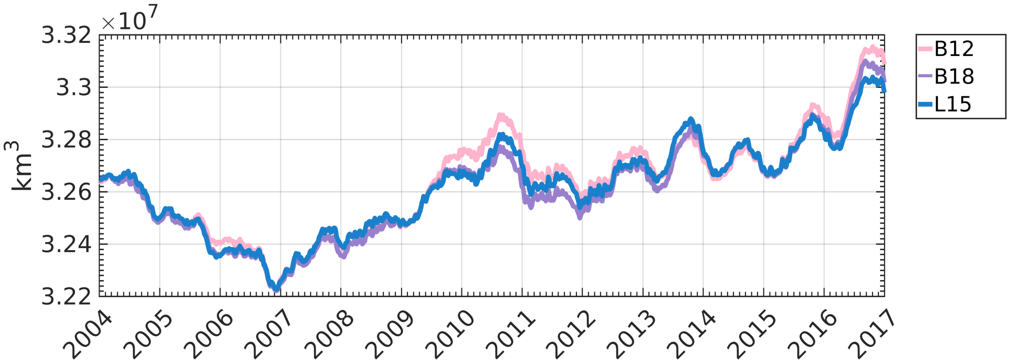

c. Irminger Sea

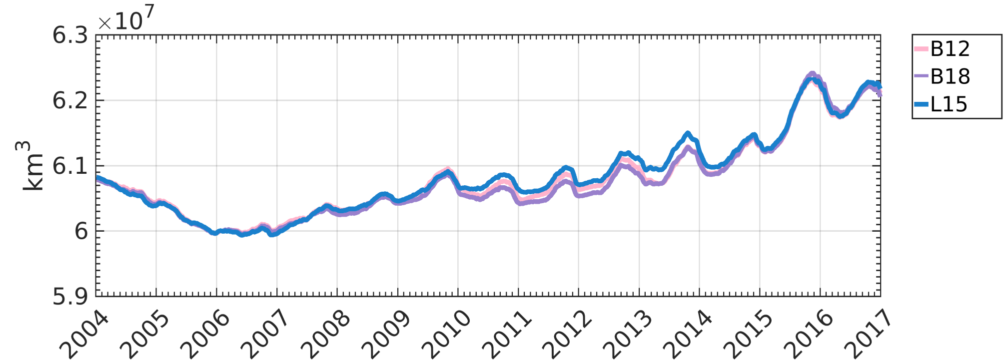

d. Subpolar Gyre East

Figure 5.10: Freshwater content (km^3) evaluation from 2002 to the end of 2016. Each panel shows a comparison between the different GrIS products (B12 in pink, B18 in purple, and L15 in blue) in different basins (Figure 5.2).

5.3.4 Potential Implications on the Labrador Sea Water Formation

The Labrador Sea (Figure 5.8j), out of all regions examined, had the largest amount of melt accumulation from the GrIS, especially from the southeast coast. Therefore, the liquid and solid FWF from the southeast coast of Greenland has the greatest potential to impact the freshwater variability in the Labrador Sea, consistent with other studies (Gillard et al., 2016; Luo et al., 2016; Marson et al., 2018). However, the FWC in the Labrador Sea has not yet had a significant response to the change in FWF products in this relatively short-term (13 year) model study (Figure 5.11), as previous studies have shown (Böning et al., 2016; Dukhovskoy et al., 2019; Rhein et al., 2018; Yashayaev and Loder, 2017).

An evaluation of the model mixed layer depth (MLD) was done in conjunction with observations from Argo floats in all three experiments (Figure 5.11). The analysis was done over a small region in the interior of the Labrador Sea (white section in Figure 5.11c) where deep convection has been observed to occur. Correlations between each experiment and the observations are from the annual MLD maximums over 2004-2016 (Figure 5.11b; Table 5.1). The variability of the mixed layer depth in all three experiments did not show a large difference. The correlation between the experiments and Argo mixed layer depths differed little with 0.74 in L15, 0.75 in B12, and 0.77 for B18. The correlations are statistically significant, with a P value of less than 0.001 and a 99 % confidence level. Therefore, varying the GrIS FWF rates, spatial resolution, and seasonality did not have an impact on the mixed layer depth within this 13-year study period.

From 2004 through to the end of 2016, there are only a few differences among the experiments' MLD. In the winter of 2007, there was an overestimation of the MLD in L15 (1580 m), while the other experiments matched closer to the observed value of about 829 m (1178 m in B12 and 1113 m in B18). In the winters of 2009 and 2010, Argo observed depths of 763 m and 348 m, respectively. For these two years, all three experiments overestimated the winter mixed layer depth (2151 m and 1224 m for L15, 2198 m and 1307 m for B12, and 2029 m and 1048 m for B18). It is possible that the Argo floats may underestimate the maximum mixed layer depths in the winters of 2009 and 2010, as Chapter 4 discusses. A study was done by Yashayaev and Loder (2016), using multiple data sources, which estimated maximum winter mixed layer depths several hundreds of metres greater than from the Argo floats in these years. In the winters of 2011 to 2013, it appears that all experiments underestimate the maximum depths. Following 2013, a deepening in the observations as well as in the experiments

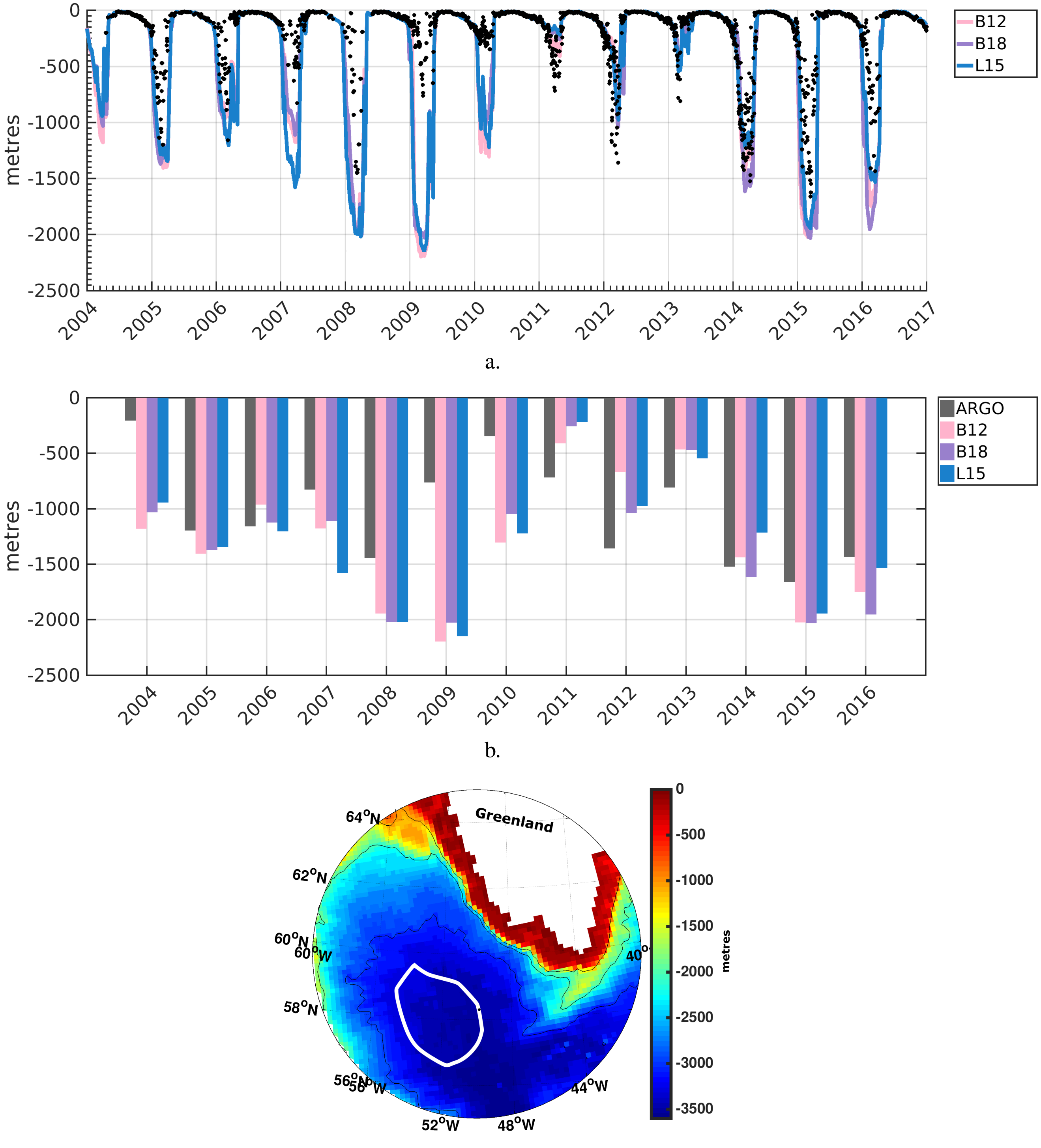

a.

b.

c.

Figure 5.11: Mixed layer depth averaged over the interior of the Labrador Sea (white section Panel C). Each experiment's five-day averaged model output of mixed layer depths is averaged spatially over the interior of the Labrador Sea. Argo observations are also averaged over the interior for each day. A) shows the variation of the spatial average for the entire time series, with observations of Argo floats indicated in black circles. B) shows the average's maximum depths over each year of the average. C) shows the model bathymetry. The colour denotes depth in metres. Area of interior Labrador Sea is shown in white section. This section was selected following Yashayaev and Loder (2017) and model study from Garcia-Quintana et al. (2019).

occurred throughout the rest of the period. In 2016, L15 estimated a mixed layer depth of 1533 m, which was similar to the depth of 1435 m recorded by the ARGO floats. B12 and B18 overestimated the maximum mixed layer depth, predicting depths of 1750 m and 1955 m, respectively. The differences in the maximum mixed layer depth among the three experiments are not significant. Therefore, at this ocean model's temporal and spatial resolution, using any of the three GrIS FWF products will not significantly alter the production of Labrador Sea water.

5.4 Conclusion

This study used a consistent model framework to explore the ocean's response to different Greenland FWF products (including both liquid and solid FWF components). The assessment was done of the GrIS' impact on the large-scale ocean circulation using an eddy-permitting numerical model. The Greenland discharge products used in this study were from well-known products: Bamber et al. (2012, 2018); Lenaerts et al. (2015).

The use of different GrIS FWF products varied the liquid and solid discharge rates and points of origin. The representation of substantial marine-terminating glaciers in the datasets may have impacted the ultimate distribution of meltwater in the ocean (Figure 5.4; Figure 5.7). In the northwest, B12 and L15 showed liquid and solid FWF discharge rates which have much higher magnitudes near Kong Oscar and Hayes Glacier. These differences may have caused the changes in the thickness of the meltwater layer close to and north of Disko Bay and in Melville Bay (Figure 5.7m-o). L15 has very high magnitudes for solid FWF discharge sites close to where Rink Glacier and Jakobshavn Isbrae terminate (Figure 5.4f). The difference in discharge rates caused an increase in meltwater thickness layer near Uummannaq Fjord and Disko Bay and more meltwater dispersion from the southwest sector in L15 (Figure 5.7r).

For icebergs, the larger number of discharge sites from the GrIS FWF datasets may have increased the spread of icebergs (Figure 5.4 and Figure 5.6), which lead to an even larger dispersion of iceberg melt (Figure 5.7). The number of discharge sites is more important than the magnitude of the discharge (if the differences are not of orders of magnitude). Fewer sites with higher rates will produce particles with large icebergs. More discharge sites with lower rates will form a large number of smaller icebergs. More smaller icebergs can increase the spatial distribution in the ocean model, as one particle will only have one path, but 10 particles may follow different paths. Additionally, smaller icebergs may melt sooner than larger ones; therefore, the melt may accumulate closer to its location that it was released. Melt off icebergs will disperse and collect in regions where icebergs may not frequently travel. The distribution of the solid ice is important for the safety of Arctic marine navigation as well as the deposition of materials impacting local ecosystems (Arrigo et al., 2017; Hawkings et al., 2016).

The change in GrIS liquid meltwater seasonality, as well as the magnitude of the discharge rate at each point, changed the amount of freshwater accumulated in a given region. For meltwater injected off the southeast coast, the seasonality and the discharge rate of runoff (Figure 5.3b, Figure 5.4, and Table 5.2), not the number of discharge sites, increased the accumulation in the Labrador Sea. Melt from south (southeast and southwest) Greenland, in all three experiments, accumulated more in the Labrador Sea than all other regions (Figure 5.8j). Despite the varied amounts of meltwater in the Labrador Sea among all three experiments, at this time and resolution scale, the GrIS FWF does not yet appear to have an impact on the mixed layer depth of that basin (Figure 5.11), as previous studies have shown (Böning et al., 2016; Dukhovskoy et al., 2019; Rhein et al., 2018; Yashayaev and Loder, 2017). The mass loss on the south coast (where there are substantial marine-terminating glaciers, Helheim and Kangerlussuaq Glacier) could have drastic implications on large-scale ocean circulation and climate as Greenland continues to melt. Potential aspects which other studies could explore are the implications in nutrient concentration, biological productivity, and hydrography.

This study showed that the heat and freshwater content in different basins did not vary significantly among the three products. Therefore, the variation of GrIS FWF product in this study's 13-year analysis, had not impacted the AMOC (Figure S5.1). Long climate studies may want to consider their choice of GrIS FWF product and the potential impact it may have on the variability of dense water overflow, deep convection, and the AMOC. This study might not have been long enough to fully capture the impact the GrIS may have on larger spatial and temporal scales. However, this paper has shown how the different GrIS products represent discharge from substantial marine-terminating glaciers. Therefore, depending on the researcher's interests, (i.e. whether it is small scale and regional versus long climate global studies) caution and careful examination should be used when considering a GrIS FWF product.

5.5 Supplementary

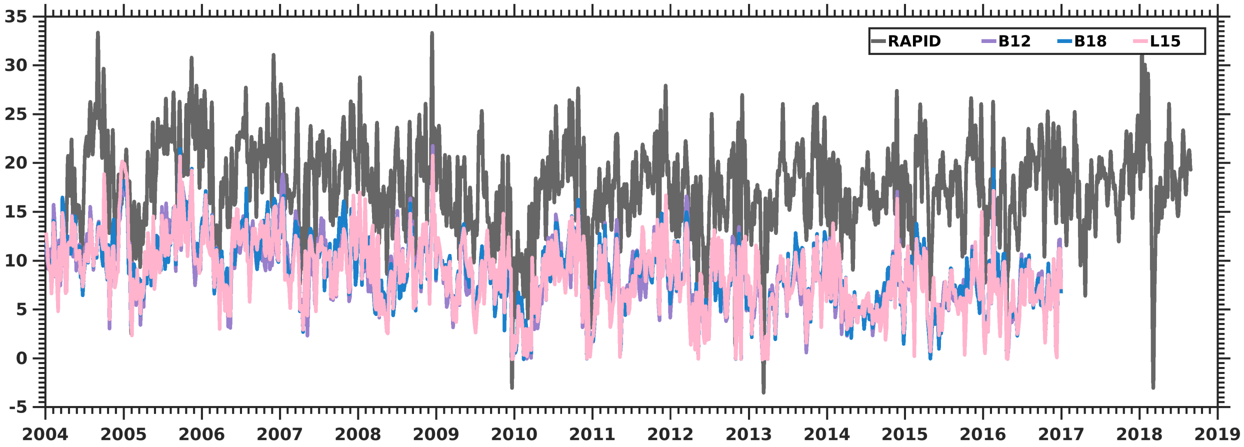

Figure S5.1: The time-series of the volume transport in units of *Sv* at 26.5 N (AMOC index). Rapid array is shown in grey, L15 in pink, B12 in purple, and B18 in blue.

Bibliography

Aagaard, K. and Carmack, E. C. (1989). The role of sea ice and other fresh water in the Arctic circulation. *Journal of Geophysical Research: Oceans*, 94(C10):14485–14498.

Aksenov, Y., Bacon, S., Coward, A. C., and Holliday, N. P. (2010). Polar outflow from the Arctic Ocean: A high resolution model study . *Journal of Marine Systems*, 83(1–2):14 – 37.

Amante, C. and Eakins, B. (2009). ETOPO1 1 Arc-Minute Global Relief Model: Procedures, Data Sources and Analysis. *NOAA Technical Memorandum NESDIS NGDC-24*.

Amundson, J., Fahnestock, M., Truffer, M., Brown, J., Lüthi, M., and Motyka, R. (2010). Ice mélange dynamics and implications for terminus stability, Jakobshavn Isbrae, Greenland. *J. Geophys. Res*, 115:F01005.

Arrigo, K. R., van Dijken, G. L., Castelao, R. M., Luo, H., Rennermalm, A. K., Tedesco, M., Mote, T. L., Oliver, H., and Yager, P. L. (2017). Melting glaciers stimulate large summer phytoplankton blooms in southwest Greenland waters. *Geophysical Research Letters*, 44(12):6278–6285.

Bacon, S., Reverdin, G., Rigor, I. G., and Snaith, H. M. (2002). A freshwater jet on the east Greenland shelf. *Journal of Geophysical Research: Oceans*, 107(C7):5–1–5–16.

Bailey, D. A., Rhines, P. B., and Häkkinen, S. (2005). Formation and pathways of North Atlantic Deep Water in a coupled ice–ocean model of the Arctic–North Atlantic Oceans. *Climate Dynamics*, 25:497–516.

Bakker, P., Schmittner, A., Lenaerts, J. T. M., Abe-Ouchi, A., Bi, D., van den Broeke, M. R., Chan, W.-L., Hu, A., Beadling, R. L., Marsland, S. J., Mernild, S. H., Saenko, O. A., Swingedouw, D., Sullivan, A., and Yin, J. (2016). Fate of the Atlantic Meridional Overturning Circulation: Strong decline under continued warming and Greenland melting. *Geophysical Research Letters*, 43(23):12,252–12,260.

Bamber, J., Van Den Broeke, M., Ettema, J., Lenaerts, J., and Rignot, E. (2012). Recent large increases in freshwater fluxes from Greenland into the North Atlantic. *Geophysical Research Letters*, 39(19).

Bamber, J. L., Tedstone, A. J., King, M. D., Howat, I. M., Enderlin, E. M., van den Broeke, M. R., and Noel, B. (2018). Land Ice Freshwater Budget of the Arctic and North Atlantic Oceans: 1. Data, Methods, and Results. *Journal of Geophysical Research: Oceans*, 123(3):1827–1837.

Barnier, B., Brodeau, L., Le Sommer, J., Molines, J.-M., Penduff, T., Theetten, S., Tréguier, A.-M., Madec, G., Biastoch, A., Böning, C. W., Dengg, J., Gulev, S. K., Bourdallé-Badie, R., Chanut, J., Garric, G., Alderson, S., Coward, A. C., De Cuevas, B., New, A. L., Haines, K., Smith, G. C., Drijfhout, S., Hazeleger, W., Severijns, C. A., and Myers, P. G. (2007). Eddy-permitting ocean circulation hindcasts of past decades. *CLIVAR Exchanges*, 12(42):8–10.

Barnier, B., Madec, G., Penduff, T., Molines, J.-M., Treguier, A.-M., Sommer, J., Beckmann, A., Böning, C., Dengg, J., Derval, C., Durand, E., Gulev, S., Remy, E., Talandier, C., Theetten, S., Maltrud, M., Mcclean, J., and Cuevas, B. (2006). Impact of partial steps and momentum advection schemes in a global ocean circulation model at eddy-permitting resolution. *Ocean Dynamics*, 56.

Bernard, B., Madec, G., Penduff, T., Molines, J.-M., Treguier, A.-M., Le Sommer, J., Beckmann, A., Biastoch, A., Böning, C., Dengg, J., Derval, C., Durand, E., Gulev, S., Remy, E., Talandier, C., Theetten, S., Maltrud, M., McClean, J., and De Cuevas, B. (2006). Impact of partial steps and momentum advection schemes in a global ocean circulation model at eddy-permitting resolution. *Ocean Dynamics*, 56(5):543–567.

Bigg, G. R., Wadley, M. R., Stevens, D. P., and Johnson, J. A. (1997). Modelling the dynamics and thermodynamics of icebergs. *Cold Regions Science and Technology*, 26(2):113 – 135.

Blanke, B., Arhan, M., Madec, G., and Roche, S. (1999). Warm water paths in the equatorial Atlantic as diagnosed with a general circulation model. *Journal of Physical Oceanography*, 29(11):2753–2768.

Blanke, B. and Raynaud, S. (1997). Kinematics of the Pacific Equatorial Undercurrent: An Eulerian and Lagrangian approach from GCM results. *Journal of Physical Oceanography*, 27(6):1038–1053.

BODC (2008). British Oceanographic Data Center's General Bathymetric Chart of the Oceans. http://www.gebco.net/data_and_products/gridded_bathymetry_data/.

Böning, C. W., Behrens, E., Biastoch, A., Getzlaff, K., and Bamber, J. L. (2016). Emerging impact of Greenland meltwater on deepwater formation in the North Atlantic Ocean. *Nature Geosci*, 9(7):523–527.

Castro de la Guardia, L., Hu, X., and Myers, P. G. (2015). Potential positive feedback between Greenland Ice Sheet melt and Baffin Bay heat content on the west Greenland shelf. *Geophysical Research Letters*, 42(12):4922–4930.

Curry, R. and Mauritzen, C. (2005). Dilution of the Northern North Atlantic Ocean in Recent Decades. *Science (New York, N.Y.)*, 308:1772–4.

Dai, A., Qian, T., Trenberth, K. E., and Milliman, J. D. (2009). Changes in continental freshwater discharge from 1948 to 2004. *Journal of Climate*, 22(10):2773–2792.

de Steur, L., Peralta-Ferriz, C., and Pavlova, O. (2018). Freshwater Export in the East Greenland Current Freshens the North Atlantic. *Geophysical Research Letters*, 45(24):13,359–13,366.

Dukhovskoy, D. S., Myers, P. G., Platov, G., Timmermans, M.-L., Curry, B., Proshutinsky, A., Bamber, J. L., Chassignet, E., Hu, X., Lee, C. M., and Somavilla, R. (2016). Greenland freshwater pathways in the sub-Arctic Seas from model experiments with passive tracers. *Journal of Geophysical Research: Oceans*.

Dukhovskoy, D. S., Yashayaev, I., Proshutinsky, A., Bamber, J. L., Bashmachnikov, I. L., Chassignet, E. P., Lee, C. M., and Tedstone, A. J. (2019). Role of Greenland Freshwater Anomaly in the Recent Freshening of the Subpolar North Atlantic. *Journal of Geophysical Research: Oceans*, 124(5):3333–3360.

Dussin, R., Barnier, B., and Brodeau, L. (2016). The making of Drakkar forcing set DFS5. Grenoble,612 France: LGGE.

Enderlin, E. M., Howat, I. M., Jeong, S., Noh, M. ., Van Angelen, J. H., and Van Den Broeke, M. R. (2014). An improved mass budget for the Greenland Ice Sheet. *Geophysical Research Letters*, 41(3):866–872.

Ettema, J., van den Broeke, M. R., van Meijgaard, E., van de Berg, W. J., Bamber, J. L., Box, J. E., and Bales, R. C. (2009). Higher surface mass balance of the Greenland ice sheet revealed by high-resolution climate modeling. *Geophysical Research Letters*, 36(12).

Ettema, J., van den Broeke, M. R., van Meijgaard, E., van de Berg, W. J., Box, J. E., and Steffen, K. (2010). Climate of the Greenland ice sheet using a high-resolution climate model – Part 1: Evaluation. *The Cryosphere*, 4(4):511–527.

Ferry, N., Greiner, E., Garric, G., Penduff, T., Treiguier, A.-M., and Reverdin, G. (2008). GLORYS-1 Reference Manual for Stream 1 (2002-2007). GLORYS project report.

Feucher, C., Garcia-Quintana, Y., Yashayaev, I., Hu, X., and Myers, P. G. (2019). Labrador Sea Water Formation Rate and Its Impact on the Local Meridional Overturning Circulation. *Journal of Geophysical Research: Oceans*, 124(8):5654–5670.

Fichefet, T. and Morales Maqueda, M. (1997). Sensitivity of a global sea ice model to the treatment of ice thermodynamics and dynamics. *Journal of Geophysical Research*, 102(C6):12609–12646.

Fratantoni, P. S. and Pickart, R. S. (2007). The western North Atlantic shelfbreak current system in summer. *Journal of Physical Oceanography*, 37(10):2509–2533.

Garcia-Quintana, Y., Courtois, P., Hu, X., Pennelly, C., Kieke, D., and Myers, P. G. (2019). Sensitivity of Labrador Sea Water Formation to Changes in Model Resolution, Atmospheric Forcing, and Freshwater Input. *Journal of Geophysical Research: Oceans*, 124(3):2126–2152.

Gillard, L. C., Hu, X., Myers, P. G., and Bamber, J. L. (2016). Meltwater pathways from marine terminating glaciers of the Greenland Ice Sheet. *Geophysical Research Letters*, 43(20):10,873–10,882.

Gillard, L. C., Hu, X., Myers, P. G., Ribergaard, M. H., and Lee, C. M. (2020). Drivers for Atlantic-origin waters abutting Greenland. *The Cryosphere*, 14(8):2729–2753.

Gladstone, R. M., Bigg, G. R., and Nicholls, K. W. (2001). Iceberg trajectory modeling and meltwater injection in the Southern Ocean. *Journal of Geophysical Research: Oceans*, 106(C9):19903–19915.

Grivault, N., Hu, X., and Myers, P. G. (2017). Evolution of Baffin Bay Water Masses and Transports in a Numerical Sensitivity Experiment under Enhanced Greenland Melt. *Atmosphere-Ocean*, 55(3):169–194.

Hanna, E., Cappelen, J., Allan, R., Jonsson, T., Blancq, F., Lillington, T., and Hickey, K. (2008). New Insights into North European and North Atlantic Surface Pressure

Variability, Storminess, and Related Climatic Change since 1830. *Journal of Climate*, 21:6739–6766.

Hanna, E., Mernild, S. H., Cappelen, J., and Steffen, K. (2012). Recent warming in Greenland in a long-term instrumental (1881–2012) climatic context: I. Evaluation of surface air temperature records. *Environmental Research Letters*, 7(4):045404.

Hawkings, J., Wadham, J., Tranter, M., Telling, J., Bagshaw, E., Beaton, A., Simmons, S., Chandler, D., Tedstone, A., and Nienow, P. (2016). The Greenland Ice Sheet as a hot spot of phosphorus weathering and export in the Arctic. *Global Biogeochemical Cycles*.

Holland, D. M., Thomas, R. H., De Young, B., Ribergaard, M. H., and Lyberth, B. (2008). Acceleration of Jakobshavn Isbrae triggered by warm subsurface ocean waters. *Nature Geoscience*, 1(10):659–664.

Holliday, N. P., Meyer, A., Bacon, S., Alderson, S. G., and de Cuevas, B. (2007). Retroflection of part of the East Greenland Current at Cape Farewell. *Geophysical Research Letters*, 34(7). L07609.

Howat, I., Box, J., Ahn, Y., Herrington, A., and McFadden, E. (2010). Seasonal variability in the dynamics of marine-terminating outlet glaciers in Greenland. *Journal of Glaciology*, 56:601–613.

IOC, SCOR, and IAPSO (2010). *The international thermodynamic equation of seawater - 2010 : Calculation and use of thermodynamic properties*. Intergovernmental Oceanographic Commission, Manuals and Guides No. 56, UNESCO (English).

Ivanovic, R. F., Gregoire, L. J., Burke, A., Wickert, A. D., Valdes, P. J., Ng, H. C., Robinson, L. F., McManus, J. F., Mitrovica, J. X., Lee, L., and Dentith, J. E. (2018). Acceleration of Northern Ice Sheet Melt Induces AMOC Slowdown and Northern Cooling in Simulations of the Early Last Deglaciation. *Paleoceanography and Paleoclimatology*, 33(7):807–824.

Jackson, R. H., Straneo, F., and Sutherland, D. A. (2014). Externally forced fluctuations in ocean temperature at Greenland glaciers in non-summer months. *Nature Geoscience*, 7(7):503–508.

Kuhlbrodt, T., Griesel, A., Montoya, M., Levermann, A., Hofmann, M., and Rahmstorf, S. (2007). On the driving processes of the Atlantic Meridional Overturning Circulation. *Reviews of Geophysics*, 45(2).

Lenaerts, J. T. M., Le Bars, D., van Kampenhout, L., Vizcaino, M., Enderlin, E. M., and van den Broeke, M. R. (2015). Representing Greenland ice sheet freshwater fluxes in climate models. *Geophysical Research Letters*, 42(15):6373–6381.

Lozier, M. S., Li, F., Bacon, S., Bahr, F., Bower, A. S., Cunningham, S. A., de Jong, M. F., de Steur, L., deYoung, B., Fischer, J., Gary, S. F., Greenan, B. J. W., Holliday, N. P., Houk, A., Houpert, L., Inall, M. E., Johns, W. E., Johnson, H. L., Johnson, C., Karstensen, J., Koman, G., Le Bras, I. A., Lin, X., Mackay, N., Marshall, D. P., Mercier, H., Oltmanns, M., Pickart, R. S., Ramsey, A. L., Rayner, D., Straneo, F., Thierry, V., Torres, D. J., Williams, R. G., Wilson, C., Yang, J., Yashayaev, I., and Zhao, J. (2019). A sea change in our view of overturning in the subpolar North Atlantic. *Science*, 363(6426):516–521.

Luo, H., Castelao, R. M., Rennermalm, A. K., Tedesco, M., Bracco, A., Yager, P. L., and Mote, T. L. (2016). Oceanic transport of surface meltwater from the southern Greenland Ice Sheet. *Nature Geoscience*.

Madec, G. (2008). NEMO ocean engine. *Note du Pole de modélisation*, (27).

Marsh, R., Bigg, G., Zhao, Y., Martin, M., Blundell, J. R., Josey, S., Hanna, E., and Ivchenko, V. (2018). Prospects for seasonal forecasting of iceberg distributions in the North Atlantic. *Nat Hazards*, 91:447–471.

Marsh, R., Ivchenko, V. O., Skliris, N., Alderson, S., Bigg, G. R., Madec, G., Blaker, A. T., Aksenov, Y., Sinha, B., Coward, A. C., Le Sommer, J., Merino, N., and Zalesny, V. B. (2015). NEMO-ICB (v1.0): interactive icebergs in the NEMO ocean model globally configured at eddy-permitting resolution. *Geoscientific Model Development*, 8(5):1547–1562.

Marshall, J., Dobson, F., Moore, K., Rhines, P., Visbeck, M., D'Asaro, E., Bumke, K., Chang, S., Davis, R., Fischer, K., Garwood, R., Guest, P., Harcourt, R., Herbaut, C., Holt, T., Lazier, J., Legg, S., McWilliams, J., Pickart, R., Prater, M., Renfrew, I., Schott, F., Send, U., and Smethie, W. (1998). The Labrador Sea Deep Convection Experiment. *Bulletin of the American Meteorological Society*, 79(10):2033–2058.

Marson, J. M., Myers, P. G., Hu, X., and Le Sommer, J. (2018). Using Vertically Integrated Ocean Fields to Characterize Greenland Icebergs' Distribution and Lifetime. *Geophysical Research Letters*, 45(9):4208–4217.

Martin, T. and Adcroft, A. (2010). Parameterizing the fresh-water flux from land ice to ocean with interactive icebergs in a coupled climate model. *Ocean Modelling*, 34(3):111 – 124.

Meijgaard, E., Ulft, L., Berg, W., Bosvelt, F., Hurk, B., Lenderink, G., and Siebesma, A. (2008). The KNMI regional atmospheric model RACMO version 2.1. *Tech. Rep. 302, KNMI.*

Menary, M. B., Jackson, L. C., and Lozier, M. S. (2020). Reconciling the Relationship Between the AMOC and Labrador Sea in OSNAP Observations and Climate Models. *Geophysical Research Letters*, 47(18):e2020GL089793. e2020GL089793 10.1029/2020GL089793.

Merino, N., Sommer, J. L., Durand, G., Jourdain, N. C., Madec, G., Mathiot, P., and Tournadre, J. (2016). Antarctic icebergs melt over the Southern Ocean: Climatology and impact on sea ice. *Ocean Modelling*, 104:99 – 110.

Morlighem, M., Williams, C. N., Rignot, E., An, L., Arndt, J. E., Bamber, J. L., Catania, G., Chauché, N., Dowdeswell, J. A., Dorschel, B., Fenty, I., Hogan, K., Howat, I., Hubbard, A., Jakobsson, M., Jordan, T. M., Kjeldsen, K. K., Millan, R., Mayer, L., Mouginot, J., Noël, B. P. Y., O'Cofaigh, C., Palmer, S., Rysgaard, S., Seroussi, H., Siegert, M. J., Slabon, P., Straneo, F., van den Broeke, M. R., Weinrebe, W., Wood, M., and Zinglersen, K. B. (2017). BedMachine v3: Complete Bed Topography and Ocean Bathymetry Mapping of Greenland From Multibeam Echo Sounding Combined With Mass Conservation. *Geophysical Research Letters*, 44(21):11,051–11,061.

Myers, P. G., Donnelly, C., and Ribergaard, M. H. (2009). Structure and variability of the West Greenland Current in Summer derived from 6 repeat standard sections. *Progress in Oceanography*, 80(1-2):93–112.

Myers, P. G. and Ribergaard, M. H. (2013). Warming of the polar water layer in Disko Bay and potential impact on Jakobshavn Isbrae. *Journal of Physical Oceanography*, 43(12):2629–2640.

Noël, B., van de Berg, W. J., van Meijgaard, E., Kuipers Munneke, P., van de Wal, R. S. W., and van den Broeke, M. R. (2015). Evaluation of the updated regional climate model RACMO2.3: summer snowfall impact on the Greenland Ice Sheet. *The Cryosphere*, 9(5):1831–1844.

Pickart, R., Torres, D., and Fratantoni, P. (2005). The East Greenland Spill Jet. *Journal of Physical Oceanography*, 35.

Polyakov, I. V., Beszczynska, A., Carmack, E. C., Dmitrenko, I. A., Fahrbach, E., Frolov, I. E., Gerdes, R., Hansen, E., Holfort, J., Ivanov, V. V., Johnson, M. A., Karcher, M., Kauker, F., Morison, J., Orvik, K. A., Schauer, U., Simmons, H. L., Skagseth, y., Sokolov, V. T., Steele, M., Timokhov, L. A., Walsh, D., and Walsh, J. E. (2005). One more step toward a warmer Arctic. *Geophysical Research Letters*, 32(17).

Rhein, M., Steinfeldt, R., Huhn, O., Sültenfuß, J., and Breckenfelder, T. (2018). Greenland Submarine Melt Water Observed in the Labrador and Irminger Sea. *Geophysical Research Letters*, 45(19):10,570–10,578.

Rignot, E., Box, J. E., Burgess, E., and Hanna, E. (2008). Mass balance of the Greenland ice sheet from 1958 to 2007. *Geophysical Research Letters*, 35(20).

Rignot, E. and Kanagaratnam, P. (2006). Changes in the velocity structure of the Greenland Ice Sheet. *Science*, 311(5763):986–990.

Rudels, B. (2015). Arctic Ocean circulation, processes and water masses: A description of observations and ideas with focus on the period prior to the International Polar Year 2007-2009 . *Progress in Oceanography*, 132(0):22 – 67.

Rudels, B., Anderson, L., and Jones, E. (1996). Formation and evolution of the surface mixed layer and halocline of the Arctic Ocean. *Journal of Geophysical Research C: Oceans*, 101(C4):8807–8821.

Sasgen, I., Wouters, B., Gardner, A., King, M., Tedesco, M., Landerer, F., Dahle, C., Save, H., and Fettweis, X. (2020). Return to rapid ice loss in Greenland and record loss in 2019 detected by the GRACE-FO satellites. *Commun Earth Environ*, 1(8).

Sciascia, R., Straneo, F., Cenedese, C., and Heimbach, P. (2013). Seasonal variability of submarine melt rate and circulation in an East Greenland fjord. *Journal of Geophysical Research: Oceans*, 118(5):2492–2506.

Shepherd, A., Ivins, E., Rignot, E., Smith, B., van den Broeke, M., Velicogna, I., Whitehouse, P., Briggs, K., Joughin, I., Krinner, G., Nowicki, S., Payne, T., Scambos, T., Schlegel, N., Geruo, A., Agosta, C., Ahlstrøm, A., Babonis, B., Barletta, V., Bjørk, A., Blazquez, A., Bonin, J., Colgan, W., Csatho, B., Cullather, R., Engdahl, M., Felikson, D., Fettweis, X., Forsberg, R., Hogg, A., Gallee, H., Gardner, A., Gilbert, L., Gourmelen, N., Groh, A., Gunter, B., Hanna, E., Harig, C., Helm, V., Horvath, A., Horwath, M., Khan, S., Kjeldsen, K., Konrad, H., Langen, P., Lecavalier, B., Loomis, B., Luthcke, S., McMillan, M., Melini, D., Mernild, S., Mohajerani, Y., Moore, P., Mottram, R., Mouginot, J., Moyano, G., Muir, A., Nagler, T., Nield, G., Nilsson, J., Noël, B., Otosaka, I., Pattle, M., Peltier, W., Pie, N., Rietbroek, R., Rott, H., Sørensen, L., Sasgen, I., Save, H., Scheuchl, B., Schrama, E., Schröder, L., Seo, K., Simonsen, S., Slater, T., Spada, G., Sutterley, T., Talpe, M., Tarasov, L., van de Berg, W., van der Wal, W., van Wessem, M., Vishwakarma, B., Wiese, D., Wilton, D., Wagner, T., Wouters, B., and Wuite, J. (2020). Mass balance of the Greenland Ice Sheet from 1992 to 2018. *Nature*, 579:233–239.

Shiklomanov, I. and Shiklomanov, A. (2003). Climatic Change and the Dynamics of River Runoff into the Arctic Ocean. *Water Resources*, 30:593–601.

Steele, M., Morison, J., Ermold, W., Rigor, I., Ortmeyer, M., and Shimada, K. (2004). Circulation of summer Pacific halocline water in the Arctic Ocean. *Journal of Geophysical Research: Oceans*, 109(C2).

Straneo, F. and Heimbach, P. (2013). North Atlantic warming and the retreat of Greenland's outlet glaciers. *Nature*, 504(7478):36–43.

Straneo, F. and Saucier, F. (2008). The outflow from Hudson Strait and its contribution to the Labrador Current . *Deep Sea Research Part I: Oceanographic Research Papers*, 55(8):926 – 946.

Swingedouw, D., Rodehacke, C. B., Olsen, S. M., Menary, M., Gao, Y., Mikolajewicz, U., and Mignot, J. (2014). On the reduced sensitivity of the Atlantic overturning to Greenland Ice Sheet melting in projections: a multi-model assessment. *Climate Dynamics*.

Talley, L. D., Reid, J. L., and Robbins, P. E. (2003). Data-Based Meridional Overturning Streamfunctions for the Global Ocean. *Journal of Climate*, 16(19):3213–3226.

Tang, C. C. L., Ross, C. K., Yao, T., Petrie, B., DeTracey, B. M., and Dunlap, E. (2004). The circulation, water masses and sea-ice of Baffin Bay. *Progress in Oceanography*, 63:183–228.

Tedesco, M. and Fettweis, X. (2020). Unprecedented atmospheric conditions (1948–2019) drive the 2019 exceptional melting season over the Greenland ice sheet. *The Cryosphere*, 14(4):1209–1223.

van Angelen, J., van den Broeke, M., Wouters, B., and Lenaerts, J. T. M. (2014). Contemporary (1960–2012) Evolution of the Climate and Surface Mass Balance of the Greenland Ice Sheet. *Surv Geophys*, 35:1155–1174.

Weijer, W., Maltrud, M. E., Hecht, M. W., Dijkstra, H. A., and Kliphuis, M. A. (2012). Response of the Atlantic Ocean circulation to Greenland Ice Sheet melting in a strongly-eddying ocean model. *Geophysical Research Letters*, 39(9).

Yashayaev, I. and Loder, J. W. (2016). Recurrent replenishment of Labrador Sea Water and associated decadal-scale variability. *Journal of Geophysical Research: Oceans*, 121(11):8095–8114.

Yashayaev, I. and Loder, J. W. (2017). Further intensification of deep convection in the Labrador Sea in 2016. *Geophysical Research Letters*, 44(3):1429–1438.

Chapter 6

Conclusion

Communities in Arctic and coastal environments are at the highest risk for future climatic hazards caused by humans and their ventures (Abram et al., 2019). The ocean is pivotal in managing the Earth's climate by behaving as a carbon sink (Sarmiento and Gruber, 2002) and transporting heat through ocean currents (Srokosz et al., 2012). The cryosphere also plays an important role in climate regulation by amplifying Arctic warming through albedo feedbacks (Lindsay and Zhang, 2005) and increasing the global mean sea level (Shepherd et al., 2020), and has the potential to impact the ocean circulation.

The Greenland Ice Sheet (GrIS) is the second-largest storage of fresh ice on Earth. From 1992 to 2018 the GrIS has contributed to a mean sea-level rise by 10.8 $\pm$ 0.9 millimetres (Shepherd et al., 2020). If the entire ice sheet were to melt, the global mean sea level could increase by 7.42 $\pm$ 0.05 metres (Morlighem et al., 2017). As oceans warm, there is a potential to increase ocean-induced undercutting of marine-terminating glaciers which may have a strong control over the future of the ice sheet. It has not yet been observed that the GrIS has had any impact on the Labrador Sea convection (Rhein et al., 2018; Yashayaev and Loder, 2017). However, several model studies have found that melt and icebergs from the south coast of the GrIS can enter the Labrador Sea (e.g. Böning et al., 2016; Dukhovskoy et al., 2016; Gillard et al., 2016; Luo et al., 2016; Marson et al., 2018). The future influence that the GrIS may have on large-scale ocean circulations like the Labrador Sea convection is still not completely understood. Many GrIS freshwater flux estimates exist; however, it is not clear how different estimates may influence ocean processes.

In this thesis, a series of numerical modelling ocean configurations were used to explore the potential relationship between Greenland and the surrounding oceans. This thesis has investigated how oceans may impact the mass loss of the GrIS and how the freshwater flux from the GrIS may, in turn, impact the ocean. The main objectives of this thesis were:

Objective 1: To examine the processes that drive the delivery of oceanic heat towards the coastline of Greenland through troughs that connect to fjords with marine-terminating glaciers.

Objective 2: To investigate the response of the Labrador Sea Water formation due to atmospheric and lateral buoyancy fluxes.

Objective 3: To explore the consequences of using various estimates of the Greenland Ice Sheet's freshwater flux in an ocean model.

In the following section, more details will be provided on the main questions, findings, limitations, and recommended future work.

6.1 Principal Findings

Objective 1: To examine the processes that drive the delivery of oceanic heat towards the coastline of Greenland through troughs that connect to fjords with marine-terminating glaciers.

Greenland's marine-terminating glaciers drain most of the ice sheet (Rignot and Mouginot, 2012). Chapter 3 looked at the processes that drive ocean heat towards troughs that are connected to fjords with large marine-terminating glaciers. The heat from the ocean may accelerate the mass loss of the ice sheet by flowing through deep troughs and making contact with marine-terminating glaciers. This undercutting of marine-terminating glaciers is suggested to have a considerable influence on the grounding-line stability, iceberg calving, and overall GrIS mass balance (Rignot et al., 2015; Schaffer et al., 2020). Onshore heat transport through six sections (troughs) around Greenland with marine-terminating glaciers and deep bathymetric features was investigated with an ocean model.

This study showed that the processes which drive the delivery of ocean heat respond differently by region to increasing GrIS meltwater, the origin of the warm water, how the water travels and is transformed, and local processes such as heat loss to the atmosphere. Heat fluxes were examined using a reference temperature of -1.5^{o}C to consider the effects of boundary layer salinity and pressure on the freezing point. Therefore, the heat present in the troughs is not simply modified Irminger Water. The seasonality of the maximum onshore heat flux through troughs around the GrIS differs as the distance from the Irminger Sea increases.

Relatively warm water can extend into Baffin Bay, reaching as far north as Melville Bay. Therefore, oceanic forcing may have a larger control over marine-terminating glaciers in regions further north than previously thought. Oceanic heat may have driven mass loss of these glaciers and have the potential to continue to drive mass loss in the future. The results also captured an increase in onshore heat flux in Disko Bay (2004 to 2006), coinciding with the timing of the disintegration of Jakobshavn Isbrae's floating ice tongue and within the period of observed oceanic heat increase in Disko Bay (from 1997 to 2007) (Holland et al., 2008). Ocean temperatures near the northwestern coast respond differently to changes in meltwater from Greenland than all other regions. Increased meltwater generated a positive feedback. With a doubling of the GrIS meltwater, Baffin Bay troughs transported $\approx 20\%$ more heat towards the coast, which then has the potential to further increase mass loss from the ice sheet.

Along the southeastern coast, ocean temperatures were influenced by storms. Fewer storms resulted in a doubling of onshore heat through Helheim Glacier's trough. These results demonstrate the regional variability of onshore heat transport through troughs and its potential influence on the GrIS.

Limitations and Future Work

Due to the model resolution and model bathymetry under-representing the depth of these troughs, this study may be underestimating the amount of ocean heat available to enter these troughs. The model used in this study could not resolve small scale processes such as fjord circulation. Therefore, the exchange between fjords and troughs could not be examined. Instead, there is an assumption in place that the water characteristics that exist in the troughs will match those in the fjords due to the dynamics of cross-shelf exchanges (Jackson et al., 2014; Sutherland et al., 2014). Additionally, the study only looked at the impact of the liquid freshwater flux component from the GrIS as an iceberg module was not yet been compatible with the model at the time of this work. Therefore, this study did not capture the full impact that the GrIS melt may have on renewing heat transport towards the shelves, as solid iceberg discharge was not included in this investigation. The use of a higher resolution model would help look at smaller scale features, such as exchanges from shelf to fjord, to understand when and how warm water mixes to the fjords as well as how freshwater and icebergs are exported.

Objective 2: To investigate the response of the Labrador Sea Water formation due to atmospheric and lateral buoyancy fluxes.

The Labrador Sea Water Formation is a very important process for the ventilation of the deep ocean, transporting heat, nutrients, oxygen, and carbon dioxide from the surface layers to depths (Rhein et al., 2017). However, the Labrador Sea's deep water formation can be a difficult process for ocean and climate models to represent accurately. Exchanges of heat and freshwater fluxes by wind and ocean forcing can impact deep convection and restratification processes in the Labrador Sea (V*å*ge et al., 2009). Ocean simulations tend to produce mixed layer depths that are too deep compared with observations in the Labrador Sea (salinity drift; Rattan et al., 2010) and lower horizontal resolution models tend to overestimate the Labrador Sea Water formation (Garcia-Quintana et al., 2019; Hirschi et al., 2020). Chapter 4 investigated the lateral exchanges from the shelf to the interior of the Labrador Sea, air-sea heat fluxes, and the response of the convective strength and the formation of Labrador Sea Water in an eddy-permitting forced ocean model.

This study found that increasing the vertical resolution, from 50 to 75 vertical levels, in the ocean experiments altered the horizontal flows. This decreased the import of buoyant, fresh boundary current water and warm, saline Atlantic water into the interior of the Labrador Sea. There was also a reduction of heat and salt into the interior of the Labrador Sea from two currents: decreased import of modified Irminger Water at Cape Farewell and decreased modified Atlantic water from the North Atlantic Current, south of the interior. This created more buoyant waters in the Labrador Sea with a stronger stratification which led to unrealistically shallow mixed layers. Therefore, a salinity drift in the Labrador Sea did not occur, which is a common problem in the lower resolution, 50-vertical level model experiments (Garcia-Quintana et al., 2019; Rattan et al., 2010).

Due to the 75-vertical level experiment having a greater convective resistance, this experiment could not overcome the buoyancy cap at the surface and the Labrador Sea deep water formation did not occur. Therefore, a stronger buoyancy loss was applied over the Labrador Sea. With a stronger buoyancy loss at the surface, convection resistance decreased and there was weaker stratification. The ocean surface for the Labrador Sea interior became denser and strengthened winter convection, compensating for the change in lateral advection. The experiment at a higher vertical resolution with a stronger atmospheric forcing allowed a break-through the buoyancy cap at the surface and allowed for denser water to exist, generating a realistic mixed layer depth, close to observed values.

Limitations and Future Work

This study found that with changes in model vertical structure there were significant impacts on the deep-water formation in the Labrador Sea. Additionally, at the higher vertical resolution there was a reduction of northward transport of the Atlantic Meridional Overturning Circulation. Therefore, future researchers should be mindful of their reasons for choosing their vertical and horizontal resolutions. This could be especially important for longer-term climate studies, as our study had a relatively low horizontal and temporal resolution (1/4^o and 14 years). This study had multiple configurations tested and identified a way to remove salinity drift. Therefore, with the setup used in this study, one could use a more expensive, higher horizontal resolution (eddy resolving) model. This could investigate small scale processes such as horizontal mixing around the Labrador Sea, lateral exchange off the Greenland shelf, and horizontal and vertical mixing in the interior of the Labrador Sea.

Objective 3: To explore the consequences of using various estimates of the Greenland Ice Sheet's freshwater flux in an ocean model.

As the GrIS continues to lose large amounts of freshwater, the fate of its icebergs and meltwater are important questions. As well as increasing sea-level, the addition of freshwater into the ocean adds buoyancy, impacts dynamics, and modifies stratification and winter-time convection. Additionally, increasing numbers of icebergs are important for navigation in the Arctic and Sub-Arctic ocean. Chapter 5 investigated the oceanic response to varying GrIS freshwater flux products.

The representation of the seasonality of runoff and iceberg discharge impacts the freshwater accumulation and dispersion in basins near the GrIS. Freshwater content varied by more than 10 000 km^3 for the Irminger, Greenland, and Nordic Seas, Baffin Bay, and the eastern Sub Polar Gyre. Based on a decade-long study period with an eddy-permitting ocean model, the GrIS has not yet impacted large-scale ocean circulations such as the Labrador Sea convection or the Atlantic Meridional Overturning Circulation.

Limitations and Future Work

GrIS meltwater is currently only discharged at the surface of the ocean grid cell and is then mixed down to 30 metres. This is not a true representation of the water column in the fjord (Carroll et al., 2016; Mortensen et al., 2013; Straneo et al., 2011). Future model studies that wish to represent marine-terminating glaciers and their interconnection with the ocean should inject meltwater at the surface as well as at a specific depth to try and represent the structure of the plume dynamics (Jenkins, 2011; Mortensen et al., 2013).

6.2 Thesis Summary

The work accomplished in this thesis focused on the interconnected response that the GrIS and the ocean have on each other. First, Chapter 3 looked at the oceanic forcing and potential implications the ocean can have on the GrIS. Chapter 3 showed that there were many factors that impacted the heat flux in Greenland's offshore troughs. Heat flux amounts are dependent on the location of the trough and source of warm water. The southeast coast was more vulnerable to storms. Fewer storms decreased the offshore winds, reduced upwelling along the shelf, and decreased the offshore exchange of heat flux. Therefore, a reduction of storms in this region may increase the overall onshore heat flux. Increased meltwater from the GrIS increased the heat flux into troughs with marine-terminating glaciers in Baffin Bay. This demonstrated the sensitivity an ocean system can have to an increase in GrIS melt.

Chapter 4 demonstrated that a combination of air-sea heat fluxes and lateral exchanges from the shelf to the interior of the Labrador Sea impacted the convective strength and the formation of Labrador Sea Water. Increased vertical resolution created an unrealistically shallow mixed layer with a buoyancy cap that could not be overcome by 'weak' air-sea fluxes. Therefore, stronger buoyancy loss at the surface was needed to weaken the stratification and generate a realistic mixed layer depth.

Chapter 5 showed the way in which ocean systems nearby to the GrIS may respond to varying freshwater flux estimates. Glacier meltwater, icebergs, and melt from icebergs each dispersed in different ways and had their own unique fates. This study found that large scale ocean circulation, such as the Labrador Sea convection or the AMOC, were not yet affected.

In summary, the interconnection between the GrIS and the ocean is a complicated system. Work accomplished in this thesis provided an insight into this relationship while highlighting where further work needs to be done. Oceanic heat has the potential to continue to increase the mass loss of the GrIS in the future. The iceberg discharge and meltwater from the GrIS has the capability to alter ocean circulation. Therefore, the full impact of this network on the climate system is still to be determined.

Bibliography

Abram, N., Gattuso, J.-P., Prakash, A., Cheng, L., Chidichimo, M., Crate, S., Enomoto, H., M., G., Gruber, N., Harper, S., Holland, E., Kudela, R., Rice, J., Steffen, K., and von Schuckmann, K. (2019). 2019: Framing and Context of the Report . *IPCC Special Report on the Ocean and Cryosphere in a Changing Climate*.

Böning, C. W., Behrens, E., Biastoch, A., Getzlaff, K., and Bamber, J. L. (2016). Emerging impact of Greenland meltwater on deepwater formation in the North Atlantic Ocean. *Nature Geosci*, 9(7):523–527.

Carroll, D., Sutherland, D., Hudson, B., Moon, T., Catania, G., Shroyer, E., Nash, J., Bartholomaus, T., Felikson, D., Stearns, L., Noël, B., and Van den Broeke, M. (2016). The impact of glacier geometry on meltwater plume structure and submarine melt in Greenland fjords: Glacier Geometry Controls Plumes. *Geophysical Research Letters*, 43.

Dukhovskoy, D. S., Myers, P. G., Platov, G., Timmermans, M.-L., Curry, B., Proshutinsky, A., Bamber, J. L., Chassignet, E., Hu, X., Lee, C. M., and Somavilla, R. (2016). Greenland freshwater pathways in the sub-Arctic Seas from model experiments with passive tracers. *Journal of Geophysical Research: Oceans*.

Garcia-Quintana, Y., Courtois, P., Hu, X., Pennelly, C., Kieke, D., and Myers, P. G. (2019). Sensitivity of Labrador Sea Water Formation to Changes in Model Resolution, Atmospheric Forcing, and Freshwater Input. *Journal of Geophysical Research: Oceans*, 124(3):2126–2152.

Gillard, L. C., Hu, X., Myers, P. G., and Bamber, J. L. (2016). Meltwater pathways from marine terminating glaciers of the Greenland Ice Sheet. *Geophysical Research Letters*, 43(20):10,873–10,882.

Hirschi, J. J.-M., Barnier, B., Böning, C., Biastoch, A., Blaker, A. T., Coward, A., Danilov, S., Drijfhout, S., Getzlaff, K., Griffies, S. M., Hasumi, H., Hewitt, H., Iovino, D., Kawasaki, T., Kiss, A. E., Koldunov, N., Marzocchi, A., Mecking, J. V., Moat, B., Molines, J.-M., Myers, P. G., Penduff, T., Roberts, M., Treguier, A.-M., Sein, D. V., Sidorenko, D., Small, J., Spence, P., Thompson, L., Weijer, W., and Xu, X. (2020). The Atlantic Meridional Overturning Circulation in High-Resolution Models. *Journal of Geophysical Research: Oceans*, 125(4):e2019JC015522. e2019JC015522 2019JC015522.

Holland, D. M., Thomas, R. H., De Young, B., Ribergaard, M. H., and Lyberth, B. (2008). Acceleration of Jakobshavn Isbrae triggered by warm subsurface ocean waters. *Nature Geoscience*, 1(10):659–664.

Jackson, R. H., Straneo, F., and Sutherland, D. A. (2014). Externally forced fluctuations in ocean temperature at Greenland glaciers in non-summer months. *Nature Geoscience*, 7(7):503–508.

Jenkins, A. (2011). Convection-driven melting near the grounding lines of ice shelves and tidewater glaciers. *Journal of Physical Oceanography*, 41(12):2279–2294.

Lindsay, R. and Zhang, J. (2005). The Thinning of Arctic Sea Ice, 1988–2003: Have We Passed a Tipping Point? *Journal of Climate*, 18:4879–4894.

Luo, H., Castelao, R. M., Rennermalm, A. K., Tedesco, M., Bracco, A., Yager, P. L., and Mote, T. L. (2016). Oceanic transport of surface meltwater from the southern Greenland Ice Sheet. *Nature Geoscience*.

Marson, J. M., Myers, P. G., Hu, X., and Le Sommer, J. (2018). Using Vertically Integrated Ocean Fields to Characterize Greenland Icebergs' Distribution and Lifetime. *Geophysical Research Letters*, 45(9):4208–4217.

Morlighem, M., Williams, C. N., Rignot, E., An, L., Arndt, J. E., Bamber, J. L., Catania, G., Chauché, N., Dowdeswell, J. A., Dorschel, B., Fenty, I., Hogan, K., Howat, I., Hubbard, A., Jakobsson, M., Jordan, T. M., Kjeldsen, K. K., Millan, R., Mayer, L., Mouginot, J., Noël, B. P. Y., O'Cofaigh, C., Palmer, S., Rysgaard, S., Seroussi, H., Siegert, M. J., Slabon, P., Straneo, F., van den Broeke, M. R., Weinrebe, W., Wood, M., and Zinglersen, K. B. (2017). BedMachine v3: Complete Bed Topography and Ocean Bathymetry Mapping of Greenland From Multibeam Echo Sounding Combined With Mass Conservation. *Geophysical Research Letters*, 44(21):11,051–11,061.

Mortensen, J., Bendtsen, J., Motyka, R., Lennert, K., Truffer, M., Fahnestock, M., and Rysgaard, S. (2013). On the seasonal freshwater stratification in the proximity of fast-flowing tidewater outlet glaciers in a sub-Arctic sill fjord. *Journal of Geophysical Research: Oceans*, 118(3):1382–1395.

Rattan, S., Myers, P. G., Treguier, A. ., Theetten, S., Biastoch, A., and Böning, C. (2010). Towards an understanding of Labrador Sea salinity drift in eddy-permitting simulations. *Ocean Modelling*, 35(1-2):77–88.

Rhein, M., Steinfeldt, R., Huhn, O., Sültenfuß, J., and Breckenfelder, T. (2018). Greenland Submarine Melt Water Observed in the Labrador and Irminger Sea. *Geophysical Research Letters*, 45(19):10,570–10,578.

Rhein, M., Steinfeldt, R., Kieke, D., Stendardo, I., and Yashayaev, I. (2017). Ventilation variability of Labrador Sea Water and its impact on oxygen and anthropogenic carbon: a review. *Philosophical Transactions of the Royal Society A: Mathematical, Physical and Engineering Sciences*, 375(2102):20160321.

Rignot, E., Fenty, I., Xu, Y., Cai, C., and Kemp, C. (2015). Undercutting of marine-terminating glaciers in West Greenland. *Geophysical Research Letters*, 42.

Rignot, E. and Mouginot, J. (2012). Ice flow in Greenland for the International Polar Year 2008-2009. *Geophysical Research Letters*, 39(11).

Sarmiento, J. and Gruber, N. (2002). Sinks for Anthropogenic Carbon. *Physics Today*, 55:30–36.

Schaffer, J., Kanzow, T., von Appen, W.-J., von Albedyll, L., Arndt, J. E., and Roberts, D. (2020). Bathymetry constrains ocean heat supply to Greenland's largest glacier tongue. *Nature Geoscience*, 13:1–5.

Shepherd, A., Ivins, E., Rignot, E., Smith, B., van den Broeke, M., Velicogna, I., Whitehouse, P., Briggs, K., Joughin, I., Krinner, G., Nowicki, S., Payne, T., Scambos, T., Schlegel, N., Geruo, A., Agosta, C., Ahlstrøm, A., Babonis, B., Barletta, V., Bjørk, A., Blazquez, A., Bonin, J., Colgan, W., Csatho, B., Cullather, R., Engdahl, M., Felikson, D., Fettweis, X., Forsberg, R., Hogg, A., Gallee, H., Gardner, A., Gilbert, L., Gourmelen, N., Groh, A., Gunter, B., Hanna, E., Harig, C., Helm, V., Horvath, A., Horwath, M., Khan, S., Kjeldsen, K., Konrad, H., Langen, P., Lecavalier, B., Loomis, B., Luthcke, S., McMillan, M., Melini, D., Mernild, S., Mohajerani, Y., Moore, P., Mottram, R., Mouginot, J., Moyano, G., Muir, A., Nagler, T., Nield, G., Nilsson, J., Noël, B., Otosaka, I., Pattle, M., Peltier, W., Pie, N., Rietbroek, R., Rott, H., Sørensen, L., Sasgen, I., Save, H., Scheuchl, B., Schrama, E., Schröder, L., Seo, K., Simonsen, S., Slater, T., Spada, G., Sutterley, T., Talpe, M., Tarasov, L., van de Berg, W., van der Wal, W., van Wessem, M., Vishwakarma, B., Wiese, D., Wilton, D., Wagner, T., Wouters, B., and Wuite, J. (2020). Mass balance of the Greenland Ice Sheet from 1992 to 2018. *Nature*, 579:233–239.

Srokosz, M., Baringer, M., Bryden, H., Cunningham, S., Delworth, T., Lozier, M., Marotzke, J., and Sutton, R. (2012). Past, Present, and Future Changes in the Atlantic Meridional Overturning Circulation. *Bulletin of the American Meteorological Society*, 93:1663–1676.

Straneo, F., Curry, R. G., Sutherland, D. A., Hamilton, G. S., Cenedese, C., V*å*ge, K., and Stearns, L. A. (2011). Impact of fjord dynamics and glacial runoff on the circulation near Helheim Glacier. *Nature Geoscience*, 4(5):322–327.

Sutherland, D. A., Straneo, F., and Pickart, R. S. (2014). Characteristics and dynamics of two major Greenland glacial fjords. *Journal of Geophysical Research: Oceans*, 119(6):3767–3791.

V*å*ge, K., Pickart, R. S., Thierry, V., Reverdin, G., Lee, C. M., Petrie, B., Agnew, T. A., Wong, A., and Ribergaard, M. H. (2009). Surprising return of deep convection to the subpolar North Atlantic Ocean in winter 2007–2008. *Nature Geoscience*, 2:67–72.

Yashayaev, I. and Loder, J. W. (2017). Further intensification of deep convection in the Labrador Sea in 2016. *Geophysical Research Letters*, 44(3):1429–1438.

Bibliography

Aagaard, K. and Carmack, E. C. (1989). The role of sea ice and other fresh water in the Arctic circulation. *Journal of Geophysical Research: Oceans*, 94(C10):14485–14498.

Abram, N., Gattuso, J.-P., Prakash, A., Cheng, L., Chidichimo, M., Crate, S., Enomoto, H., M., G., Gruber, N., Harper, S., Holland, E., Kudela, R., Rice, J., Steffen, K., and von Schuckmann, K. (2019). 2019: Framing and Context of the Report . *IPCC Special Report on the Ocean and Cryosphere in a Changing Climate*.

Aksenov, Y., Bacon, S., Coward, A. C., and Holliday, N. P. (2010). Polar outflow from the Arctic Ocean: A high resolution model study . *Journal of Marine Systems*, 83(1–2):14 – 37.

Amante, C. and Eakins, B. (2009). ETOPO1 1 Arc-Minute Global Relief Model: Procedures, Data Sources and Analysis. *NOAA Technical Memorandum NESDIS NGDC-24*.

Amundson, J., Fahnestock, M., Truffer, M., Brown, J., Lüthi, M., and Motyka, R. (2010). Ice mélange dynamics and implications for terminus stability, Jakobshavn Isbrae, Greenland. *J. Geophys. Res*, 115:F01005.

An, L., Rignot, E., Elieff, S., Morlighem, M., Millan, R., Mouginot, J., Holland, D. M., Holland, D., and Paden, J. (2017). Bed elevation of Jakobshavn Isbrae, West Greenland, from high-resolution airborne gravity and other data. *Geophysical Research Letters*, 44(8):3728–3736. 2017GL073245.

Arrigo, K. R., van Dijken, G. L., Castelao, R. M., Luo, H., Rennermalm, A. K., Tedesco, M., Mote, T. L., Oliver, H., and Yager, P. L. (2017). Melting glaciers stimulate large summer phytoplankton blooms in southwest Greenland waters. *Geophysical Research Letters*, 44(12):6278–6285.

Asselin, R. (1972). Frequency Filter for Time Integrations. *Monthly Weather Review*, 100(6):487–490.

Azetsu-Scott, K. and Tan, F. C. (1997). Oxygen isotope studies from Iceland to an East Greenland Fjord: behaviour of glacial meltwater plume. *Marine Chemistry*, 56(3):239 – 251. Modern Chemical and Biological Oceanography: The Influence of Peter J. Wangersky.

Bacon, S., Marshall, A., Holliday, N. P., Aksenov, Y., and Dye, S. R. (2014). Seasonal variability of the East Greenland Coastal Current. *Journal of Geophysical Research: Oceans*, 119(6):3967–3987.

Bacon, S., Reverdin, G., Rigor, I. G., and Snaith, H. M. (2002). A freshwater jet on the east Greenland shelf. *Journal of Geophysical Research: Oceans*, 107(C7):5–1–5–16.

Bailey, D. A., Rhines, P. B., and Häkkinen, S. (2005). Formation and pathways of North Atlantic Deep Water in a coupled ice–ocean model of the Arctic–North Atlantic Oceans. *Climate Dynamics*, 25:497–516.

Bakker, P., Schmittner, A., Lenaerts, J. T. M., Abe-Ouchi, A., Bi, D., van den Broeke, M. R., Chan, W.-L., Hu, A., Beadling, R. L., Marsland, S. J., Mernild, S. H., Saenko, O. A., Swingedouw, D., Sullivan, A., and Yin, J. (2016). Fate of the Atlantic Meridional Overturning Circulation: Strong decline under continued warming and Greenland melting. *Geophysical Research Letters*, 43(23):12,252–12,260.

Bamber, J., Van Den Broeke, M., Ettema, J., Lenaerts, J., and Rignot, E. (2012). Recent large increases in freshwater fluxes from Greenland into the North Atlantic. *Geophysical Research Letters*, 39(19).

Bamber, J. L., Griggs, J. A., Hurkmans, R. T. W. L., Dowdeswell, J. A., Gogineni, S. P., Howat, I., Mouginot, J., Paden, J., Palmer, S., Rignot, E., and Steinhage, D. (2013). A new bed elevation dataset for Greenland. *The Cryosphere*, 7(2):499–510.

Bamber, J. L., Tedstone, A. J., King, M. D., Howat, I. M., Enderlin, E. M., van den Broeke, M. R., and Noel, B. (2018). Land Ice Freshwater Budget of the Arctic and North Atlantic Oceans: 1. Data, Methods, and Results. *Journal of Geophysical Research: Oceans*, 123(3):1827–1837.

Barnier, B., Brodeau, L., Le Sommer, J., Molines, J.-M., Penduff, T., Theetten, S., Tréguier, A.-M., Madec, G., Biastoch, A., Böning, C. W., Dengg, J., Gulev, S. K., Bourdallé-Badie, R., Chanut, J., Garric, G., Alderson, S., Coward, A. C., De Cuevas, B., New, A. L., Haines, K., Smith, G. C., Drijfhout, S., Hazeleger, W., Severijns, C. A., and Myers, P. G. (2007). Eddy-permitting ocean circulation hindcasts of past decades. *CLIVAR Exchanges*, 12(42):8–10.

Barnier, B., Madec, G., Penduff, T., Molines, J.-M., Treguier, A.-M., Sommer, J., Beckmann, A., Böning, C., Dengg, J., Derval, C., Durand, E., Gulev, S., Remy, E., Talandier, C., Theetten, S., Maltrud, M., Mcclean, J., and Cuevas, B. (2006). Impact of partial steps and momentum advection schemes in a global ocean circulation model at eddy-permitting resolution. *Ocean Dynamics*, 56.

Bartholomaus, T. C., Stearns, L. A., Sutherland, D. A., Shroyer, E. L., Nash, J. D., Walker, R. T., Catania, G., Felikson, D., Carroll, D., Fried, M. J., and et al. (2016). Contrasts in the response of adjacent fjords and glaciers to ice-sheet surface melt in West Greenland. *Annals of Glaciology*, 57(73):25–38.

Beaird, N., Straneo, F., and Jenkins, W. (2017). Characteristics of meltwater export from Jakobshavn Isbræ and Ilulissat Icefjord. *Annals of Glaciology*, 58(74):107–117.

Beaird, N. L., Straneo, F., and Jenkins, W. (2018). Export of Strongly Diluted Greenland Meltwater From a Major Glacial Fjord. *Geophysical Research Letters*, 45(9):4163–4170.

Bernard, B., Madec, G., Penduff, T., Molines, J.-M., Treguier, A.-M., Le Sommer, J., Beckmann, A., Biastoch, A., Böning, C., Dengg, J., Derval, C., Durand, E., Gulev, S., Remy, E., Talandier, C., Theetten, S., Maltrud, M., McClean, J., and De Cuevas, B. (2006). Impact of partial steps and momentum advection schemes in a global ocean circulation model at eddy-permitting resolution. *Ocean Dynamics*, 56(5):543–567.

Beszczynska-Möller, A., Fahrbach, E., Schauer, U., and Hansen, E. (2012). Variability in Atlantic water temperature and transport at the entrance to the Arctic Ocean, 1997–2010. *ICES Journal of Marine Science: Journal du Conseil*.

Bigg, G. R., Wadley, M. R., Stevens, D. P., and Johnson, J. A. (1996). Prediction of iceberg trajectories for the North Atlantic and Arctic oceans. *Geophysical Research Letters*, 23(24):3587–3590.

Bigg, G. R., Wadley, M. R., Stevens, D. P., and Johnson, J. A. (1997). Modelling the dynamics and thermodynamics of icebergs. *Cold Regions Science and Technology*, 26(2):113 – 135.

Blanke, B., Arhan, M., Madec, G., and Roche, S. (1999). Warm water paths in the equatorial Atlantic as diagnosed with a general circulation model. *Journal of Physical Oceanography*, 29(11):2753–2768.

Blanke, B. and Raynaud, S. (1997). Kinematics of the Pacific Equatorial Undercurrent: An Eulerian and Lagrangian approach from GCM results. *Journal of Physical Oceanography*, 27(6):1038–1053.

BODC (2008). British Oceanographic Data Center's General Bathymetric Chart of the Oceans. http://www.gebco.net/data_and_products/gridded_bathymetry_data/.

Böning, C. W., Behrens, E., Biastoch, A., Getzlaff, K., and Bamber, J. L. (2016). Emerging impact of Greenland meltwater on deepwater formation in the North Atlantic Ocean. *Nature Geosci*, 9(7):523–527.

Bouillon, S., Ángel Morales Maqueda, M., Legat, V., and Fichefet, T. (2009). An elastic–viscous–plastic sea ice model formulated on Arakawa B and C grids. *Ocean Modelling*, 27(3):174 – 184.

Box, J. E., Yang, L., Bromwich, D. H., and Bai, L. (2009). Greenland Ice Sheet surface air temperature variability: 1840–2007. *Journal of Climate*, 22(14):4029–4049.

Cai, C., Rignot, E., Menemenlis, D., and Nakayama, Y. (2017). Observations and modeling of ocean-induced melt beneath Petermann Glacier Ice Shelf in northwestern Greenland. *Geophysical Research Letters*.

Carroll, D., Sutherland, D., Hudson, B., Moon, T., Catania, G., Shroyer, E., Nash, J., Bartholomaus, T., Felikson, D., Stearns, L., Noël, B., and Van den Broeke, M. (2016). The impact of glacier geometry on meltwater plume structure and submarine melt in Greenland fjords: Glacier Geometry Controls Plumes. *Geophysical Research Letters*, 43.

Carroll, D., Sutherland, D. A., Curry, B., Nash, J. D., Shroyer, E. L., Catania, G. A., Stearns, L. A., Grist, J. P., Lee, C. M., and de Steur, L. (2018). Subannual and Seasonal Variability of Atlantic-Origin Waters in Two Adjacent West Greenland Fjords. *Journal of Geophysical Research: Oceans*, 123(9):6670–6687.

Castro de la Guardia, L., Hu, X., and Myers, P. G. (2015). Potential positive feedback between Greenland Ice Sheet melt and Baffin Bay heat content on the west Greenland shelf. *Geophysical Research Letters*, 42(12):4922–4930.

Chanut, J., Barnier, B., Large, W., Debreu, L., Penduff, T., Molines, J. M., and Mathiot, P. (2008). Mesoscale Eddies in the Labrador Sea and Their Contribution to Convection and Restratification. *Journal of Physical Oceanography*, 38(8):1617–1643.

Christoffersen, P., Mugford, R. I., Heywood, K. J., Joughin, I., Dowdeswell, J. A., Syvitski, J. P. M., Luckman, A., and Benham, T. J. (2011). Warming of waters in an East Greenland fjord prior to glacier retreat: Mechanisms and connection to large-scale atmospheric conditions. *Cryosphere*, 5(3):701–714.

Colombo, P., Barnier, B., Penduff, T., Chanut, J., Deshayes, J., Molines, J.-M., Sommer, J., Verezemskaya, P., Gulev, S., and Treguier, A.-M. (2020). Representation of the Denmark Strait overflow in a z -coordinate eddying configuration of the NEMO (v3.6) ocean model: resolution and parameter impacts. *Geoscientific Model Development*, 13:3347–3371.

Csatho, B. M., Schenk, A. F., van der Veen, C. J., Babonis, G., Duncan, K., Rezvanbehbahani, S., van den Broeke, M. R., Simonsen, S. B., Nagarajan, S., and van Angelen, J. H. (2014). Laser altimetry reveals complex pattern of Greenland Ice Sheet dynamics. *Proceedings of the National Academy of Sciences*, 111(52):18478–18483.

Curry, B., Lee, C., Petrie, B., Moritz, R., and Kwok, R. (2014). Multiyear volume, liquid freshwater, and sea ice transports through Davis Strait, 2004-10. *Journal of Physical Oceanography*, 44(4):1244–1266.

Curry, B., Lee, C. M., and Petrie, B. (2011). Volume, Freshwater, and Heat Fluxes through Davis Strait, 2004–05. *Journal of Physical Oceanography*, 41(3):429–436.

Curry, R. and Mauritzen, C. (2005). Dilution of the Northern North Atlantic Ocean in Recent Decades. *Science (New York, N.Y.)*, 308:1772–4.

Dai, A., Qian, T., Trenberth, K. E., and Milliman, J. D. (2009). Changes in continental freshwater discharge from 1948 to 2004. *Journal of Climate*, 22(10):2773–2792.

de Jong, M. F., Bower, A. S., and Furey, H. H. (2014). Two Years of Observations of Warm-Core Anticyclones in the Labrador Sea and Their Seasonal Cycle in Heat and Salt Stratification. *Journal of Physical Oceanography*, 44(2):427–444.

de Steur, L., Peralta-Ferriz, C., and Pavlova, O. (2018). Freshwater Export in the East Greenland Current Freshens the North Atlantic. *Geophysical Research Letters*, 45(24):13,359–13,366.

Dmitrenko, I. A., Kirillov, S. A., Rudels, B., Babb, D. G., Myers, P. G., Stedmon, C. A., Bendtsen, J., Ehn, J. K., Pedersen, L. T., Rysgaard, S., and Barber, D. G. (2019). Variability of the Pacific-Derived Arctic Water Over the Southeastern Wandel Sea Shelf (Northeast Greenland) in 2015–2016. *Journal of Geophysical Research: Oceans*, 124(1):349–373.

Dukhovskoy, D. S., Myers, P. G., Platov, G., Timmermans, M.-L., Curry, B., Proshutinsky, A., Bamber, J. L., Chassignet, E., Hu, X., Lee, C. M., and Somavilla, R. (2016). Greenland freshwater pathways in the sub-Arctic Seas from model experiments with passive tracers. *Journal of Geophysical Research: Oceans*.

Dukhovskoy, D. S., Yashayaev, I., Proshutinsky, A., Bamber, J. L., Bashmachnikov, I. L., Chassignet, E. P., Lee, C. M., and Tedstone, A. J. (2019). Role of Greenland Freshwater Anomaly in the Recent Freshening of the Subpolar North Atlantic. *Journal of Geophysical Research: Oceans*, 124(5):3333–3360.

Dussin, R., Barnier, B., and Brodeau, L. (2016). The making of Drakkar forcing set DFS5. Grenoble,612 France: LGGE.

Enderlin, E. M., Howat, I. M., Jeong, S., Noh, M. ., Van Angelen, J. H., and Van Den Broeke, M. R. (2014). An improved mass budget for the Greenland Ice Sheet. *Geophysical Research Letters*, 41(3):866–872.

Eskridge, R. E., Ku, J. Y., Rao, S. T., Porter, P. S., and Zurbenko, I. G. (1997). Separating Different Scales of Motion in Time Series of Meteorological Variables. *Bulletin of the American Meteorological Society*, 78(7):1473–1484.

Ettema, J., van den Broeke, M. R., van Meijgaard, E., van de Berg, W. J., Bamber, J. L., Box, J. E., and Bales, R. C. (2009). Higher surface mass balance of the Greenland ice sheet revealed by high-resolution climate modeling. *Geophysical Research Letters*, 36(12).

Ettema, J., van den Broeke, M. R., van Meijgaard, E., van de Berg, W. J., Box, J. E., and Steffen, K. (2010). Climate of the Greenland ice sheet using a high-resolution climate model – Part 1: Evaluation. *The Cryosphere*, 4(4):511–527.

Felikson, D., Bartholomaus, T. C., Catania, G. A., Korsgaard, N. J., Kjær, K. H., Morlighem, M., Noël, B., van den Broeke, M., Stearns, L. A., Shroyer, E. L., Sutherland, D. A., and Nash, J. D. (2017). Inland thinning on the Greenland Ice Sheet controlled by outlet glacier geometry. *Nature Geoscience*, 10:366–369.

Fenty, I., Willis, J. K., Khazendar, A., Dinardo, S., Forsberg, R., Fukumori, I., Holland, D., Jakobsson, M., Moller, D., Münchow, J. M. A., Rignot, E., Schodlok, M., Thompson, A. F., Tinto, K., Rutherford, M., and Trenholm, N. (2016). Oceans Melting Greenland: Early Results from NASA's Ocean-Ice Mission in Greenland . *Oceanography*, 29.

Ferry, N., Greiner, E., Garric, G., Penduff, T., Treiguier, A.-M., and Reverdin, G. (2008). GLORYS-1 Reference Manual for Stream 1 (2002-2007). GLORYS project report.

Feucher, C., Garcia-Quintana, Y., Yashayaev, I., Hu, X., and Myers, P. G. (2019). Labrador Sea Water Formation Rate and Its Impact on the Local Meridional Overturning Circulation. *Journal of Geophysical Research: Oceans*, 124(8):5654–5670.

Fichefet, T. and Morales Maqueda, M. (1997). Sensitivity of a global sea ice model to the treatment of ice thermodynamics and dynamics. *Journal of Geophysical Research*, 102(C6):12609–12646.

Frajka-Williams, E., Rhines, P. B., and Eriksen, C. C. (2014). Horizontal Stratification during Deep Convection in the Labrador Sea. *Journal of Physical Oceanography*, 44(1):220–228.

Fratantoni, D. M. (2001). North atlantic surface circulation during the 1990's observed with satellite-tracked drifters. *Journal of Geophysical Research: Oceans*, 106(C10):22067–22093.

Fratantoni, P. S. and Pickart, R. S. (2007). The western North Atlantic shelfbreak current system in summer. *Journal of Physical Oceanography*, 37(10):2509–2533.

Garcia-Quintana, Y., Courtois, P., Hu, X., Pennelly, C., Kieke, D., and Myers, P. G. (2019). Sensitivity of Labrador Sea Water Formation to Changes in Model Resolution, Atmospheric Forcing, and Freshwater Input. *Journal of Geophysical Research: Oceans*, 124(3):2126–2152.

Gelderloos, R., Katsman, C. A., and Drijfhout, S. S. (2011). Assessing the Roles of Three Eddy Types in Restratifying the Labrador Sea after Deep Convection. *Journal of Physical Oceanography*, 41(11):2102–2119.

Gill, A. E. (1982). Atmosphere-Ocean Dynamics. page 662. Academic Press.

Gillard, L. C., Hu, X., Myers, P. G., and Bamber, J. L. (2016). Meltwater pathways from marine terminating glaciers of the Greenland Ice Sheet. *Geophysical Research Letters*, 43(20):10,873–10,882.

Gillard, L. C., Hu, X., Myers, P. G., Ribergaard, M. H., and Lee, C. M. (2020). Drivers for Atlantic-origin waters abutting Greenland. *The Cryosphere*, 14(8):2729–2753.

Gladish, C., Holland, D., and Lee, C. (2015a). Oceanic boundary conditions for Jakobshavn Glacier. Part II: Provenance and sources of variability of disko bay and Ilulissat Icefjord waters, 1990-2011. *Journal of Physical Oceanography*, 45(1):33–63.

Gladish, C., Holland, D., Rosing-Asvid, A., Behrens, J., and Boje, J. (2015b). Oceanic boundary conditions for Jakobshavn Glacier. Part I: Variability and renewal of Ilulissat Icefjord waters, 2001-14. *Journal of Physical Oceanography*, 45(1):3–32.

Gladstone, R. M., Bigg, G. R., and Nicholls, K. W. (2001). Iceberg trajectory modeling and meltwater injection in the Southern Ocean. *Journal of Geophysical Research: Oceans*, 106(C9):19903–19915.

Griffies, S. (2004). Fundamentals of ocean climate models. *Princeton University Press*.

Grist, J. P., Josey, S. A., Boehme, L., Meredith, M. P., Laidre, K. L., Heide-Jørgensen, M. P., Kovacs, K. M., Lydersen, C., Davidson, F. J. M., Stenson, G. B., Hammill, M. O., Marsh, R., and Coward, A. C. (2014). Seasonal variability of the warm Atlantic water layer in the vicinity of the Greenland shelf break. *Geophysical Research Letters*, 41(23):8530–8537.

Grivault, N., Hu, X., and Myers, P. G. (2017). Evolution of Baffin Bay Water Masses and Transports in a Numerical Sensitivity Experiment under Enhanced Greenland Melt. *Atmosphere-Ocean*, 55(3):169–194.

Hanna, E., Cappelen, J., Allan, R., Jonsson, T., Blancq, F., Lillington, T., and Hickey, K. (2008). New Insights into North European and North Atlantic Surface Pressure Variability, Storminess, and Related Climatic Change since 1830. *Journal of Climate*, 21:6739–6766.

Hanna, E., Fettweis, X., Mernild, S., Cappelen, J., Ribergaard, M., Shuman, C., Steffen, K., Wood, L., and Mote, T. (2014). Atmospheric and oceanic climate forcing of the exceptional Greenland Ice Sheet surface melt in summer 2012.

Hanna, E., Mernild, S. H., Cappelen, J., and Steffen, K. (2012). Recent warming in Greenland in a long-term instrumental (1881–2012) climatic context: I. Evaluation of surface air temperature records. *Environmental Research Letters*, 7(4):045404.

Hawkings, J., Wadham, J., Tranter, M., Telling, J., Bagshaw, E., Beaton, A., Simmons, S., Chandler, D., Tedstone, A., and Nienow, P. (2016). The Greenland Ice Sheet as a hot spot of phosphorus weathering and export in the Arctic. *Global Biogeochemical Cycles*.

Hibler, W. D. (1979). A Dynamic Thermodynamic Sea Ice Model. *Journal of Physical Oceanography*, 9(4):815–846.

Hirschi, J. J.-M., Barnier, B., Böning, C., Biastoch, A., Blaker, A. T., Coward, A., Danilov, S., Drijfhout, S., Getzlaff, K., Griffies, S. M., Hasumi, H., Hewitt, H., Iovino, D., Kawasaki, T., Kiss, A. E., Koldunov, N., Marzocchi, A., Mecking, J. V., Moat, B., Molines, J.-M., Myers, P. G., Penduff, T., Roberts, M., Treguier, A.-M., Sein, D. V., Sidorenko, D., Small, J., Spence, P., Thompson, L., Weijer, W., and Xu, X. (2020). The Atlantic Meridional Overturning Circulation in High-Resolution Models. *Journal of Geophysical Research: Oceans*, 125(4):e2019JC015522. e2019JC015522 2019JC015522.

Hogan, K. A., Cofaigh, C. ., Jennings, A. E., Dowdeswell, J. A., and Hiemstra, J. F. (2016). Deglaciation of a major palaeo-ice stream in Disko Trough, West Greenland. *Quaternary Science Reviews*, 147:5 – 26. Special Issue: PAST Gateways (Palaeo-Arctic Spatial and Temporal Gateways).

Holdsworth, A. M. and Myers, P. G. (2015). The influence of high-frequency atmospheric forcing on the circulation and deep convection of the Labrador Sea. *Journal of Climate*, 28(12):4980–4996.

Holland, D. M. and Jenkins, A. (1999). Modeling Thermodynamic Ice–Ocean Interactions at the Base of an Ice Shelf. *Journal of Physical Oceanography*, 29(8):1787–1800.

Holland, D. M., Thomas, R. H., De Young, B., Ribergaard, M. H., and Lyberth, B. (2008). Acceleration of Jakobshavn Isbrae triggered by warm subsurface ocean waters. *Nature Geoscience*, 1(10):659–664.

Holliday, N. P., Meyer, A., Bacon, S., Alderson, S. G., and de Cuevas, B. (2007). Retroflection of part of the East Greenland Current at Cape Farewell. *Geophysical Research Letters*, 34(7). L07609.

Howat, I., Box, J., Ahn, Y., Herrington, A., and McFadden, E. (2010). Seasonal variability in the dynamics of marine-terminating outlet glaciers in Greenland. *Journal of Glaciology*, 56:601–613.

Hu, X. and Myers, P. G. (2013). A Lagrangian view of Pacific water inflow pathways in the Arctic Ocean during model spin-up. *Ocean Modelling*, 71:66 – 80.

Hunke, E. C. and Dukowicz, J. K. (1997). An Elastic–Viscous–Plastic Model for Sea Ice Dynamics. *Journal of Physical Oceanography*, 27(9):1849–1867.

Inall, M. E., Murray, T., Cottier, F. R., Scharrer, K., Boyd, T. J., Heywood, K. J., and Bevan, S. L. (2014). Oceanic heat delivery via Kangerdlugssuaq Fjord to the south-east Greenland Ice Sheet. *Journal of Geophysical Research: Oceans*, 119(2):631–645.

IOC, SCOR, and IAPSO (2010). *The international thermodynamic equation of seawater - 2010 : Calculation and use of thermodynamic properties*. Intergovernmental Oceanographic Commission, Manuals and Guides No. 56, UNESCO (English).

Ivanovic, R. F., Gregoire, L. J., Burke, A., Wickert, A. D., Valdes, P. J., Ng, H. C., Robinson, L. F., McManus, J. F., Mitrovica, J. X., Lee, L., and Dentith, J. E. (2018). Acceleration of Northern Ice Sheet Melt Induces AMOC Slowdown and Northern Cooling in Simulations of the Early Last Deglaciation. *Paleoceanography and Paleoclimatology*, 33(7):807–824.

Jackson, R. H., Straneo, F., and Sutherland, D. A. (2014). Externally forced fluctuations in ocean temperature at Greenland glaciers in non-summer months. *Nature Geoscience*, 7(7):503–508.

Jenkins, A. (2011). Convection-driven melting near the grounding lines of ice shelves and tidewater glaciers. *Journal of Physical Oceanography*, 41(12):2279–2294.

Joughin, I., Alley, R. B., and Holland, D. M. (2012). Ice-Sheet Response to Oceanic Forcing. *Science*, 338(6111):1172–1176.

Karcher, M., Beszczynska-Möller, A., Kauker, F., Gerdes, R., Heyen, S., Rudels, B., and Schauer, U. (2011). Arctic Ocean warming and its consequences for the Denmark Strait overflow. *Journal of Geophysical Research: Oceans*, 116(C2).

Katsman, C. A., Spall, M. A., and Pickart, R. S. (2004). Boundary Current Eddies and Their Role in the Restratification of the Labrador Sea. *Journal of Physical Oceanography*, 34(9):1967–1983.

Khazendar, A., Fenty, I. G., Carroll, D., Gardner, A. an Lee, C. M., Fukumori, I., Wang, O., Zhang, H., Seroussi, H., Moller, D., Noël, B. P. Y., van den Broeke, M. R., Dinardo, S., and Willis, J. (2019). Interruption of two decades of Jakobshavn Isbrae acceleration and thinning as regional ocean cools. *Nature Geoscience*, 12(4).

Kuhlbrodt, T., Griesel, A., Montoya, M., Levermann, A., Hofmann, M., and Rahmstorf, S. (2007). On the driving processes of the Atlantic Meridional Overturning Circulation. *Reviews of Geophysics*, 45(2).

Large, W. G. and Yeager, S. G. (2004). Diurnal to decadal global forcing for ocean and sea-ice models: the datasets and flux climatologies.

Lau, N.-C. (1988). Variability of the Observed Midlatitude Storm Tracks in Relation to Low-Frequency Changes in the Circulation Pattern. *Journal of the Atmospheric Sciences*, 45(19):2718–2743.

Lenaerts, J. T. M., Le Bars, D., van Kampenhout, L., Vizcaino, M., Enderlin, E. M., and van den Broeke, M. R. (2015). Representing Greenland ice sheet freshwater fluxes in climate models. *Geophysical Research Letters*, 42(15):6373–6381.

Lindsay, R. and Zhang, J. (2005). The Thinning of Arctic Sea Ice, 1988–2003: Have We Passed a Tipping Point? *Journal of Climate*, 18:4879–4894.

Lozier, M. S., Li, F., Bacon, S., Bahr, F., Bower, A. S., Cunningham, S. A., de Jong, M. F., de Steur, L., deYoung, B., Fischer, J., Gary, S. F., Greenan, B. J. W., Holliday, N. P., Houk, A., Houpert, L., Inall, M. E., Johns, W. E., Johnson, H. L., Johnson, C., Karstensen, J., Koman, G., Le Bras, I. A., Lin, X., Mackay, N., Marshall, D. P., Mercier, H., Oltmanns, M., Pickart, R. S., Ramsey, A. L., Rayner, D., Straneo, F., Thierry, V., Torres, D. J., Williams, R. G., Wilson, C., Yang, J., Yashayaev, I., and Zhao, J. (2019). A sea change in our view of overturning in the subpolar North Atlantic. *Science*, 363(6426):516–521.

Luo, H., Castelao, R. M., Rennermalm, A. K., Tedesco, M., Bracco, A., Yager, P. L., and Mote, T. L. (2016). Oceanic transport of surface meltwater from the southern Greenland Ice Sheet. *Nature Geoscience*.

MacGilchrist, G. A., Johnson, H. L., Marshall, D. P., Lique, C., Thomas, M., Jackson, L. C., and Wood, R. A. (2020). Locations and Mechanisms of Ocean Ventilation in the High-Latitude North Atlantic in an Eddy-Permitting Ocean Model. *Journal of Climate*, 33.

Madec, G. (2008). NEMO ocean engine. *Note du Pole de modélisation*, (27).

Marsh, R., Bigg, G., Zhao, Y., Martin, M., Blundell, J. R., Josey, S., Hanna, E., and Ivchenko, V. (2018). Prospects for seasonal forecasting of iceberg distributions in the North Atlantic. *Nat Hazards*, 91:447–471.

Marsh, R., Ivchenko, V. O., Skliris, N., Alderson, S., Bigg, G. R., Madec, G., Blaker, A. T., Aksenov, Y., Sinha, B., Coward, A. C., Le Sommer, J., Merino, N., and Zalesny, V. B. (2015). NEMO-ICB (v1.0): interactive icebergs in the NEMO ocean model globally configured at eddy-permitting resolution. *Geoscientific Model Development*, 8(5):1547–1562.

Marshall, J., Dobson, F., Moore, K., Rhines, P., Visbeck, M., D'Asaro, E., Bumke, K., Chang, S., Davis, R., Fischer, K., Garwood, R., Guest, P., Harcourt, R., Herbaut, C., Holt, T., Lazier, J., Legg, S., McWilliams, J., Pickart, R., Prater, M., Renfrew, I., Schott, F., Send, U., and Smethie, W. (1998). The Labrador Sea Deep Convection Experiment. *Bulletin of the American Meteorological Society*, 79(10):2033–2058.

Marson, J. M., C., G. L., Myers, P. G., and Le Sommer, J. (In prep). Prescribing Greenland discharge in ocean models: solid versus liquid and their corresponding impacts on the subpolar North Atlantic. *Ocean Modelling*.

Marson, J. M., Myers, P. G., Hu, X., and Le Sommer, J. (2018). Using Vertically Integrated Ocean Fields to Characterize Greenland Icebergs' Distribution and Lifetime. *Geophysical Research Letters*, 45(9):4208–4217.

Martin, T. and Adcroft, A. (2010). Parameterizing the fresh-water flux from land ice to ocean with interactive icebergs in a coupled climate model. *Ocean Modelling*, 34(3):111 – 124.

Masina, S., Storto, A., Storto, A., Ferry, N., Valdivieso, M., Haines, K., Balmaseda, M., Zuo, H., Drevillon, M., and Parent, L. (2017). An ensemble of eddy-permitting global ocean reanalyses from the MyOcean project. *Climate Dynamics*, 49(3):813–841.

Mayer, C., Reeh, N., Jung-Rothenhäusler, F., Huybrechts, P., and Oerter, H. (2000). The subglacial cavity and implied dynamics under Nioghalvfjerdsfjorden Glacier, NE-Greenland. *Geophysical Research Letters*, 27(15):2289–2292.

Meijgaard, E., Ulft, L., Berg, W., Bosvelt, F., Hurk, B., Lenderink, G., and Siebesma, A. (2008). The KNMI regional atmospheric model RACMO version 2.1. *Tech. Rep. 302, KNMI.*

Menary, M. B., Jackson, L. C., and Lozier, M. S. (2020). Reconciling the Relationship Between the AMOC and Labrador Sea in OSNAP Observations and Climate Models. *Geophysical Research Letters*, 47(18):e2020GL089793. e2020GL089793 10.1029/2020GL089793.

MEOM (2013). Bathymetry ORCA0.25. http://servdap.legi.grenoble-inp.fr/meom/ORCA025-I/.

Merino, N., Sommer, J. L., Durand, G., Jourdain, N. C., Madec, G., Mathiot, P., and Tournadre, J. (2016). Antarctic icebergs melt over the Southern Ocean: Climatology and impact on sea ice. *Ocean Modelling*, 104:99 – 110.

Mesinger, F. and Arakawa, A. (1976). Numerical methods used in atmospheric models. *GARP Publication Series No. 17*, I:64.

Moon, T., Joughin, I., and Smith, B. (2015). Seasonal to multiyear variability of glacier surface velocity, terminus position, and sea ice/ice mélange in northwest Greenland. *Journal of Geophysical Research: Earth Surface*, 120(5):818–833.

Moore, G. W. K., Straneo, F., and Oltmanns, M. (2014). Trend and interannual variability in southeast Greenland Sea Ice: Impacts on coastal Greenland climate variability. *Geophysical Research Letters*, 41(23):8619–8626.

Morlighem, M., Williams, C. N., Rignot, E., An, L., Arndt, J. E., Bamber, J. L., Catania, G., Chauché, N., Dowdeswell, J. A., Dorschel, B., Fenty, I., Hogan, K., Howat, I., Hubbard, A., Jakobsson, M., Jordan, T. M., Kjeldsen, K. K., Millan, R., Mayer, L., Mouginot, J., Noël, B. P. Y., O'Cofaigh, C., Palmer, S., Rysgaard, S., Seroussi, H., Siegert, M. J., Slabon, P., Straneo, F., van den Broeke, M. R., Weinrebe, W., Wood, M., and Zinglersen, K. B. (2017). BedMachine v3: Complete Bed Topography and Ocean Bathymetry Mapping of Greenland From Multibeam Echo Sounding Combined With Mass Conservation. *Geophysical Research Letters*, 44(21):11,051–11,061.

Mortensen, J., Bendtsen, J., Motyka, R., Lennert, K., Truffer, M., Fahnestock, M., and Rysgaard, S. (2013). On the seasonal freshwater stratification in the proximity of fast-flowing tidewater outlet glaciers in a sub-Arctic sill fjord. *Journal of Geophysical Research: Oceans*, 118(3):1382–1395.

Myers, P., Kulan, N., and Ribergaard, M. (2007). Irminger Water variability in the West Greenland Current. *Geophys. Res. Lett*, 34.

Myers, P. G., Donnelly, C., and Ribergaard, M. H. (2009). Structure and variability of the West Greenland Current in Summer derived from 6 repeat standard sections. *Progress in Oceanography*, 80(1-2):93–112.

Myers, P. G. and Ribergaard, M. H. (2013). Warming of the polar water layer in Disko Bay and potential impact on Jakobshavn Isbrae. *Journal of Physical Oceanography*, 43(12):2629–2640.

National Geophysical Data Cente (2006). 2-minute Gridded Global Relief Data (ETOPO2) v2. National Geophysical Data Center, NOAA. Dataset accessed [2017-05-09].

Nghiem, S., Hall, D., Mote, T., Tedesco, M., Albert, M., Keegan, K., Shuman, C., DiGirolamo, N., and Neumann, G. (2012). The extreme melt across the Greenland Ice Sheet in 2012. *Geophys. Res. Lett.*, 39.

Noël, B., van de Berg, W. J., van Meijgaard, E., Kuipers Munneke, P., van de Wal, R. S. W., and van den Broeke, M. R. (2015). Evaluation of the updated regional climate model RACMO2.3: summer snowfall impact on the Greenland Ice Sheet. *The Cryosphere*, 9(5):1831–1844.

Pennelly, C., Hu, X., and Myers, P. G. (2019). Cross-Isobath Freshwater Exchange Within the North Atlantic Subpolar Gyre. *Journal of Geophysical Research: Oceans*, 124(10):6831–6853.

Pennelly, C. and Myers, Paul, G. (In prep). Impact of Different Atmospheric Forcing Sets on Modelling Labrador Sea Water Production.

Pickart, R., Torres, D., and Fratantoni, P. (2005). The East Greenland Spill Jet. *Journal of Physical Oceanography*, 35.

Polyakov, I. V., Beszczynska, A., Carmack, E. C., Dmitrenko, I. A., Fahrbach, E., Frolov, I. E., Gerdes, R., Hansen, E., Holfort, J., Ivanov, V. V., Johnson, M. A., Karcher, M., Kauker, F., Morison, J., Orvik, K. A., Schauer, U., Simmons, H. L., Skagseth, y., Sokolov, V. T., Steele, M., Timokhov, L. A., Walsh, D., and Walsh, J. E. (2005). One more step toward a warmer Arctic. *Geophysical Research Letters*, 32(17).

Porter, D. F., Tinto, K. J., Boghosian, A., Cochran, J. R., Bell, R. E., Manizade, S. S., and Sonntag, J. G. (2014). Bathymetric control of tidewater glacier mass loss in northwest Greenland. *Earth and Planetary Science Letters*, 401:40 – 46.

Rabe, B., Karcher, M., Kauker, F., Schauer, U., Toole, J. M., Krishfield, R. A., Pisarev, S., Kikuchi, T., and Su, J. (2014). Arctic Ocean basin liquid freshwater storage trend 1992–2012. *Geophysical Research Letters*, 41(3):961–968.

Rastner, P., Bolch, T., Mölg, N., Machguth, H., Le Bris, R., and Paul, F. (2012). The first complete inventory of the local glaciers and ice caps on Greenland. *The Cryosphere*, 6(6):1483–1495.

Rattan, S., Myers, P. G., Treguier, A. ., Theetten, S., Biastoch, A., and Böning, C. (2010). Towards an understanding of Labrador Sea salinity drift in eddy-permitting simulations. *Ocean Modelling*, 35(1-2):77–88.

Rhein, M., Steinfeldt, R., Huhn, O., Sültenfuß, J., and Breckenfelder, T. (2018). Greenland Submarine Melt Water Observed in the Labrador and Irminger Sea. *Geophysical Research Letters*, 45(19):10,570–10,578.

Rhein, M., Steinfeldt, R., Kieke, D., Stendardo, I., and Yashayaev, I. (2017). Ventilation variability of Labrador Sea Water and its impact on oxygen and anthropogenic carbon: a review. *Philosophical Transactions of the Royal Society A: Mathematical, Physical and Engineering Sciences*, 375(2102):20160321.

Ribergaard, M. (2014). Oceanographic Investigations off West Greenland 2013. *NAFO Scientific Council Documents*.

Rieck, J., Böning, C., and Getzlaff, K. (2019). The Nature of Eddy Kinetic Energy in the Labrador Sea: Different Types of Mesoscale Eddies, Their Temporal Variability, and Impact on Deep Convection. *Journal of Physical Oceanography*, 49.

Rignot, E., Box, J. E., Burgess, E., and Hanna, E. (2008). Mass balance of the Greenland ice sheet from 1958 to 2007. *Geophysical Research Letters*, 35(20).

Rignot, E., Fenty, I., Xu, Y., Cai, C., and Kemp, C. (2015). Undercutting of marine-terminating glaciers in West Greenland. *Geophysical Research Letters*, 42.

Rignot, E., Fenty, I., Xu, Y., Cai, C., Velicogna, I., Cofaigh, C. ., Dowdeswell, J. A., Weinrebe, W., Catania, G., and Duncan, D. (2016a). Bathymetry data reveal glaciers vulnerable to ice-ocean interaction in Uummannaq and Vaigat glacial fjords, west Greenland. *Geophysical Research Letters*, 43(6):2667–2674. 2016GL067832.

Rignot, E. and Kanagaratnam, P. (2006). Changes in the velocity structure of the Greenland Ice Sheet. *Science*, 311(5763):986–990.

Rignot, E., Koppes, M., and Velicogna, I. (2010). Rapid submarine meting of the calving faces of West Greenland glaciers. *Nature Geoscience*, 3:187–191.

Rignot, E. and Mouginot, J. (2012). Ice flow in Greenland for the International Polar Year 2008-2009. *Geophysical Research Letters*, 39(11).

Rignot, E., Xu, Y., Menemenlis, D., Mouginot, J., Scheuchl, B., Li, X., Morlighem, M., Seroussi, H., den Broeke, M. v., Fenty, I., Cai, C., An, L., and Fleurian, B. d. (2016b). Modeling of ocean-induced ice melt rates of five west Greenland glaciers over the past two decades. *Geophysical Research Letters*, 43(12):6374–6382.

Robert, A. J. (1966). The Integration of a Low Order Spectral Form of the Primitive Meteorological Equations. *Journal of the Meteorological Society of Japan. Ser. II*, 44(5):237–245.

Roullet, G. and Madec, G. (2000). Salt conservation, free surface, and varying levels: A new formulation for ocean general circulation models. *Journal of Geophysical Research: Oceans*, 105(C10):23927–23942.

Rudels, B. (2015). Arctic Ocean circulation, processes and water masses: A description of observations and ideas with focus on the period prior to the International Polar Year 2007-2009 . *Progress in Oceanography*, 132(0):22 – 67.

Rudels, B., Anderson, L., and Jones, E. (1996). Formation and evolution of the surface mixed layer and halocline of the Arctic Ocean. *Journal of Geophysical Research C: Oceans*, 101(C4):8807–8821.

Sarmiento, J. and Gruber, N. (2002). Sinks for Anthropogenic Carbon. *Physics Today*, 55:30–36.

Sasgen, I., Wouters, B., Gardner, A., King, M., Tedesco, M., Landerer, F., Dahle, C., Save, H., and Fettweis, X. (2020). Return to rapid ice loss in Greenland and record loss in 2019 detected by the GRACE-FO satellites. *Commun Earth Environ*, 1(8).

Sathiyamoorthy, S. and Moore, G. W. K. (2002). Buoyancy Flux at Ocean Weather Station Bravo. *Journal of Physical Oceanography*, 32(2):458–474.

Savage, S. (2001). *Aspects of Iceberg Deterioration and Drift*, pages 279–318. Springer Berlin Heidelberg, Berlin, Heidelberg.

Schaffer, J., Kanzow, T., von Appen, W.-J., von Albedyll, L., Arndt, J. E., and Roberts, D. (2020). Bathymetry constrains ocean heat supply to Greenland's largest glacier tongue. *Nature Geoscience*, 13:1–5.

Schaffer, J., von Appen, W.-J., Dodd, P. A., Hofstede, C., Mayer, C., de Steur, L., and Kanzow, T. (2017). Warm water pathways toward Nioghalvfjerdsfjorden Glacier, Northeast Greenland. *Journal of Geophysical Research: Oceans*, 122(5):4004–4020.

Schulze, L. M., Pickart, R. S., and Moore, G. W. K. (2016). Atmospheric forcing during active convection in the Labrador Sea and its impact on mixed-layer depth. *Journal of Geophysical Research: Oceans*, 121(9):6978–6992.

Schulze Chretien, L. M. and Frajka-Williams, E. (2018). Wind-driven transport of fresh shelf water into the upper 30 m of the Labrador Sea. *Ocean Science*, 14(5):1247–1264.

Sciascia, R., Straneo, F., Cenedese, C., and Heimbach, P. (2013). Seasonal variability of submarine melt rate and circulation in an East Greenland fjord. *Journal of Geophysical Research: Oceans*, 118(5):2492–2506.

Seroussi, H., Morlighem, M., Rignot, E., Larour, E., Aubry, D., Ben Dhia, H., and Kristensen, S. S. (2011). Ice flux divergence anomalies on 79north Glacier, Greenland. *Geophysical Research Letters*, 38(9). L09501.

Serreze, M. and Francis, J. (2006). The Arctic Amplification Debate. *Climatic Change*, 76:241–264.

Shepherd, A., Ivins, E., Rignot, E., Smith, B., van den Broeke, M., Velicogna, I., Whitehouse, P., Briggs, K., Joughin, I., Krinner, G., Nowicki, S., Payne, T., Scambos, T., Schlegel, N., Geruo, A., Agosta, C., Ahlstrøm, A., Babonis, B., Barletta, V., Bjørk, A., Blazquez, A., Bonin, J., Colgan, W., Csatho, B., Cullather, R., Engdahl, M., Felikson, D., Fettweis, X., Forsberg, R., Hogg, A., Gallee, H., Gardner, A., Gilbert, L., Gourmelen, N., Groh, A., Gunter, B., Hanna, E., Harig, C., Helm, V., Horvath, A., Horwath, M., Khan, S., Kjeldsen, K., Konrad, H., Langen, P., Lecavalier, B., Loomis, B., Luthcke, S., McMillan, M., Melini, D., Mernild, S., Mohajerani, Y., Moore, P., Mottram, R., Mouginot, J., Moyano, G., Muir, A., Nagler, T., Nield, G., Nilsson, J., Noël, B., Otosaka, I., Pattle, M., Peltier, W., Pie, N., Rietbroek, R., Rott, H., Sørensen, L., Sasgen, I., Save, H., Scheuchl, B., Schrama, E., Schröder, L., Seo, K., Simonsen, S., Slater, T., Spada, G., Sutterley, T., Talpe, M., Tarasov, L., van de Berg, W., van der Wal, W., van Wessem, M., Vishwakarma, B., Wiese, D., Wilton, D., Wagner, T., Wouters, B., and Wuite, J. (2020). Mass balance of the Greenland Ice Sheet from 1992 to 2018. *Nature*, 579:233–239.

Shiklomanov, I. and Shiklomanov, A. (2003). Climatic Change and the Dynamics of River Runoff into the Arctic Ocean. *Water Resources*, 30:593–601.

Slabon, P., Dorschel, B., Jokat, W., Myklebust, R., Hebbeln, D., and Gebhardt, C. (2016). Greenland ice sheet retreat history in the northeast Baffin Bay based on high-resolution bathymetry. *Quaternary Science Reviews*, 154:182 – 198.

Smith, G. C., Roy, F., Mann, P., Dupont, F., Brasnett, B., Lemieux, J.-F., Laroche, S., and Bélair, S. (2014). A new atmospheric dataset for forcing ice-ocean models: Evaluation of reforecasts using the Canadian global deterministic prediction system. *Quarterly Journal of the Royal Meteorological Society*, 140(680):881–894.

Smith, W. H. F. and Sandwell, D. T. (1997). Global seafloor topography from satellite altimetry and ship depth soundings. *Science*, 277:1957–1962.

Srokosz, M., Baringer, M., Bryden, H., Cunningham, S., Delworth, T., Lozier, M., Marotzke, J., and Sutton, R. (2012). Past, Present, and Future Changes in the Atlantic Meridional Overturning Circulation. *Bulletin of the American Meteorological Society*, 93:1663–1676.

Steele, M., Morison, J., Ermold, W., Rigor, I., Ortmeyer, M., and Shimada, K. (2004). Circulation of summer Pacific halocline water in the Arctic Ocean. *Journal of Geophysical Research: Oceans*, 109(C2).

Stewart, K., Hogg, A., Griffies, S., Heerdegen, A., Ward, M., Spence, P., and England, M. (2017). Vertical resolution of baroclinic modes in global ocean models. *Ocean Modelling*, 113:50 – 65.

Straneo, F. (2006). Heat and freshwater transport through the central Labrador Sea. *Journal of Physical Oceanography*, 36(4):606–628.

Straneo, F., Curry, R. G., Sutherland, D. A., Hamilton, G. S., Cenedese, C., V*å*ge, K., and Stearns, L. A. (2011). Impact of fjord dynamics and glacial runoff on the circulation near Helheim Glacier. *Nature Geoscience*, 4(5):322–327.

Straneo, F., Hamilton, G., Sutherland, D., Stearns, L. A., Davidson, F., Hammill, M., Stenson, G. B., and A., R. (2010). Rapid circulation of warm subtropical waters in a major glacial fjord in East Greenland. *Nature Geosci*, 3(3):182–186.

Straneo, F. and Heimbach, P. (2013). North Atlantic warming and the retreat of Greenland's outlet glaciers. *Nature*, 504(7478):36–43.

Straneo, F. and Saucier, F. (2008). The outflow from Hudson Strait and its contribution to the Labrador Current . *Deep Sea Research Part I: Oceanographic Research Papers*, 55(8):926 – 946.

Straneo, F., Sutherland, D. A., Holland, D., Gladish, C., Hamilton, G. S., Johnson, H. L., Rignot, E., Xu, Y., and Koppes, M. (2012). Characteristics of ocean waters reaching Greenland's glaciers. *Annals of Glaciology*, 53(60):202–210.

Sutherland, D. A., Straneo, F., and Pickart, R. S. (2014). Characteristics and dynamics of two major Greenland glacial fjords. *Journal of Geophysical Research: Oceans*, 119(6):3767–3791.

Swingedouw, D., Rodehacke, C. B., Olsen, S. M., Menary, M., Gao, Y., Mikolajewicz, U., and Mignot, J. (2014). On the reduced sensitivity of the Atlantic overturning to Greenland Ice Sheet melting in projections: a multi-model assessment. *Climate Dynamics*.

Talley, L. D., Reid, J. L., and Robbins, P. E. (2003). Data-Based Meridional Overturning Streamfunctions for the Global Ocean. *Journal of Climate*, 16(19):3213–3226.

Tang, C. C. L., Ross, C. K., Yao, T., Petrie, B., DeTracey, B. M., and Dunlap, E. (2004). The circulation, water masses and sea-ice of Baffin Bay. *Progress in Oceanography*, 63:183–228.

Tedesco, M. and Fettweis, X. (2020). Unprecedented atmospheric conditions (1948–2019) drive the 2019 exceptional melting season over the Greenland ice sheet. *The Cryosphere*, 14(4):1209–1223.

Timmermann, R., Goosse, H., Madec, G., Fichefet, T., Ethe, C., and Dulière, V. (2005). On the representation of high latitude processes in the ORCA-LIM global coupled sea ice-ocean model. *Ocean Modelling*, 8(1-2):175–201.

Treguier, A. M., Theetten, S., Chassignet, E. P., Penduff, T., Smith, R., Talley, L., Beismann, J. O., and Böning, C. (2005). The North Atlantic Subpolar Gyre in Four High-Resolution Models. *Journal of Physical Oceanography*, 35(5):757–774.

van Angelen, J., van den Broeke, M., Wouters, B., and Lenaerts, J. T. M. (2014). Contemporary (1960–2012) Evolution of the Climate and Surface Mass Balance of the Greenland Ice Sheet. *Surv Geophys*, 35:1155–1174.

van den Broeke, M. R., Enderlin, E. M., Howat, I. M., Kuipers Munneke, P., Noël, B. P. Y., van de Berg, W. J., van Meijgaard, E., and Wouters, B. (2016). On the recent contribution of the Greenland Ice Sheet to sea level change. *The Cryosphere*, 10(5):1933–1946.

Vancoppenolle, M., Fichefet, T., Goosse, H., Bouillon, S., Madec, G., and Morales Maqueda, M. (2009). Simulating the mass balance and salinity of Arctic and Antarctic sea ice. 1. Model description and validation. *Ocean Modelling*, 27(1):33 – 53.

V*å*ge, K., Pickart, R. S., Thierry, V., Reverdin, G., Lee, C. M., Petrie, B., Agnew, T. A., Wong, A., and Ribergaard, M. H. (2009). Surprising return of deep convection to the subpolar North Atlantic Ocean in winter 2007–2008. *Nature Geoscience*, 2:67–72.

Warren, C. R. (1991). Terminal environment, topographic control and fluctuations of West Greenland glaciers. *Boreas*, 20(1):1–15.

Weijer, W., Maltrud, M. E., Hecht, M. W., Dijkstra, H. A., and Kliphuis, M. A. (2012). Response of the Atlantic Ocean circulation to Greenland Ice Sheet melting in a strongly-eddying ocean model. *Geophysical Research Letters*, 39(9).

Williams, C. N., Cornford, S. L., Jordan, T. M., Dowdeswell, J. A., Siegert, M. J., Clark, C. D., Swift, D. A., Sole, A., Fenty, I., and Bamber, J. L. (2017). Generating synthetic fjord bathymetry for coastal Greenland. *The Cryosphere*, 11(1):363–380.

Wilson, N. J. and Straneo, F. (2015). Water exchange between the continental shelf and the cavity beneath Nioghalvfjerdsbrae (79 North Glacier). *Geophysical Research Letters*, 42(18):7648–7654.

Wood, M., Rignot, E., Fenty, I., Menemenlis, D., Millan, R., Morlighem, M., Mouginot, J., and Seroussi, H. (2018). Ocean-Induced Melt Triggers Glacier Retreat in Northwest Greenland. *Geophysical Research Letters*, 45(16):8334–8342.

Yashayaev, I. and Loder, J. W. (2009). Enhanced production of Labrador Sea Water in 2008. *Geophysical Research Letters*, 36(1).

Yashayaev, I. and Loder, J. W. (2016). Recurrent replenishment of Labrador Sea Water and associated decadal-scale variability. *Journal of Geophysical Research: Oceans*, 121(11):8095–8114.

Yashayaev, I. and Loder, J. W. (2017). Further intensification of deep convection in the Labrador Sea in 2016. *Geophysical Research Letters*, 44(3):1429–1438.

Zurbenko, I., Porter, P. S., Gui, R., Rao, S. T., Ku, J. Y., and Eskridge, R. E. (1996). Detecting Discontinuities in Time Series of Upper-Air Data: Development and Demonstration of an Adaptive Filter Technique. *Journal of Climate*, 9(12):3548–3560.